Fall 2022

Use of DIC Measurements With Finite Element Models For Direct Heterogeneous Material Property Determination and Wrinkle Formation During Automated Fiber Placement

Sreehari Rajan Kattil

USE OF DIC MEASUREMENTS WITH FINITE ELEMENT MODELS FOR DIRECT HETEROGENEOUS MATERIAL PROPERTY DETERMINATION AND WRINKLE FORMATION DURING AUTOMATED FIBER PLACEMENT

by

Sreehari Rajan Kattil

Bachelor of Technology
University of Calicut 2007

Master of Technology
Indian Institute of Technology Bombay 2010

Submitted in Partial Fulfillment of the Requirements

for the Degree of Doctor of Philosophy in

Mechanical Engineering

College of Engineering and Computing

University of South Carolina

2022

Accepted by:

Michael A. Sutton, Major Professor

Subramani Sockalingam, Committee Member

Addis Kidane, Committee Member

Dimitris Rizos, Committee Member

Cheryl L. Addy, Interim Vice Provost and Dean of the Graduate School

Dedication

To my wife Sruthi, my daughter Shriya and my parents Rajan and Shobha for their sacrifices, prayers and endless love.

Acknowledgments

I would like to express my deepest appreciation to my advisor Dr. Michael A. Sutton for his guidance and advice during my PhD studies. His enthusiasm and immense knowledge have inspired me throughout the course of the research process. This dissertation would not have been possible without his support, insight, and encouragement.

I would like to thank my committee members Dr. Subramani Sockalingam, Dr. Addis Kidane, and Dr. Rizos Dimitris for their valuable comments and suggestions and encouragement. I am grateful to each of the committee members for their guidance during the preparation of this dissertation.

The help and support of Dr. Tusit Weerasooriya and Stephen Alexander for providing access to their experimental data for the deformations in a bone specimen undergoing compressive loading is greatly appreciated. Completion of this work would not have been possible without the support of my colleagues and faculty members in the McNair Aerospace center, University of South Carolina, including Dr. Brian Tatting and Dr. Zafer Gurdal. A special thanks to my colleague Dr. Roudy Wehbe for his technical assistance and support during our AFP experiments. Technical support of the McNair technical staff, Mr. Burton Rhodes, Jr., is greatly appreciated. I would like to express my gratitude to Ms. Eileen Miller at Boeing, Charleston for providing AFP composite samples. Funding provided by Army Research Laboratory, Adelphi, Maryland under Cooperative Agreement Number W911NF-20-2-0231, Boeing Research Contract SSOWBRTW0915000 and associated matching funds provided by University of South Carolina Vice President for Finance Edward Walton via 15540

E250 are deeply appreciated.

I am grateful to my fellow lab mates Troy Mayers, William McMakin, Farzana Yasmeen, Vijendra Gupta, and Chisoba Emanuel for their friendship and support. My gratitude is extended to our Mechanical Engineering Shop supervisor, Mr. Bill Bradley, and our Departmental Electronics Technician, Mr. David Westbury, for their kind assistance. Last but not least, I would like to thank my family for their love and support.

Abstract

In this work, application of DIC in combination with finite element modeling is demonstrated for efficient material characterization for complex heterogeneous materials and tow wrinkle formation during automated fiber placement.

The first part of the work describes the integration of DIC measurements with finite element models for direct property identification in heterogeneous material systems. The material property identification is based on solving partial differential equations (PDE) of equilibrium for unknown elastic material properties with known boundary conditions and full field strain data (Eg. DIC). The PDEs are solved numerically using Petrov-Galerkin finite element procedure. The classical Bubnov-Galerkin method is shown to exhibit spurious oscillations in the result for noisy strain input and for problem involving discontinuous elastic modulus distribution. The formulation is developed for uniaxial applications using basic theoretical constructs, resulting in a computational framework that has a matrix form $[A]\{E\} = \{R\}$, where the $[A]$ matrix components are known functions of measured axial strains and axial positions, components of the vector $\{R\}$ are known functions of axial body forces, applied loads and reactions and components of the vector $\{E\}$ are the unknown elastic material properties at discrete locations along the length of the specimen. For a series of 1D material property identification procedure with known axial strains at discrete locations and various levels of random noise, results are presented to demonstrate the accuracy and noise sensitivity of the methodology. Finally, experimental measurements for a heterogeneous bone specimen are compared to our one-dimensional model predictions, demonstrating that the predictions at each load level of interest

are in very good agreement with independent estimates at each location along the specimen length.

In the second part, an experimental investigation using StereoDIC to measure out-of-plane wrinkle formation and in-plane deformations in a prepreg slit tape during automated fiber placement (AFP) is described. Based on observations made during the experiments, additional experiments are performed using a rigid double cantilever beam specimen and StereoDIC to measure the Mode I and Mode II traction-separation relationships for tow-to-tow bonding. These were followed by two additional sets of experiments to quantify the viscoelastic response of the tow matrix material.

Results from simulations and experiments for automated fiber placement (AFP) of prepreg slit tape (tow) on a flat surface with different tow path radii of curvature are presented with emphasis on characterization of wrinkle formation. AFP simulations modeled bonding of the slit tape using the "sticky contact" definition in Abaqus and the measured mixed mode cohesive traction-separation relationships. Comparison of the measured and predicted wrinkle shapes, amplitudes and wavelengths to experimental measurements shows excellent agreement for a 6.35 mm wide IM7/8552-1 prepreg tow placed on a flat surface using four different radii of curvature. In addition, the simulations are shown to be capable of capturing the mechanism of wrinkle formation using a generally accepted damage model. Careful inspection of the stress and deformation conditions at the tow-substrate interface under the compaction roller reveals a combination of Mode II and Mode III tractions, with significant damage predicted under the roller due to the mixed mode conditions.

Table of Contents

List of Tables

List of Figures

Chapter 1

INTRODUCTION

Developments in the previous millennium that resulted in the broad distribution of robust, accurate digital image correlation methods to obtain full-field deformation measurements (Chu, Ranson, and Sutton 1985; Luo, Chao, Sutton, and Peters 1993; Schreier, Braasch, and Sutton 2000; Helm, Sutton, and McNeill 2003a; Helm, Sutton, and McNeill 2003b; Sutton, Orteu, and Schreier 2009) has led to increasing interest in novel ways to utilize the dense sets of DIC data that were previously unavailable. In particular, the methodology has been investigated for material property identification, especially in heterogeneous and anisotropic material systems that are more difficult to characterize.

Automated fiber placement(AFP) process for manufacturing of advanced composites is another field where DIC measurements have the potential to reduce lead time for material development and increase product quality. For example, StereoDIC measurements can be used to measure tow surface shapes and deformations during AFP processing, providing data for validation of AFP models. Importance of additive manufacturing of composite structures using AFP is justified by the improvements in weight reduction, higher corrosion resistance and lower maintenance cost of the manufactured composite parts compared to conventional manufacturing processes. Though advanced composite materials with superior mechanical properties have existed for more than six decades, their use has been limited to a small spectrum of advanced military aircraft, primarily due to higher manufacturing costs associated with composite materials. Recently, the commercial aircraft industry has developed

a generation of advanced composite aerostructures to replace conventional aluminum components.

Major roadblocks to rapid expansion and deployment of composite-based structures are difficulties associated with manufacturing of high quality, complex-shaped parts using existing manufacturing technology. Some of the earliest manufacturing approaches, such as conventional hand layup methods are painstakingly slow and thus unsuitable for the high production rate demands. However, the recent introduction of computer aided prepreg placement processes, such as automated tape layup and automated fiber placement, have resolved many of the difficulties in manufacturing of high-quality composite material parts at faster production rates. These developments have led to a shift in interest for some manufacturers in automotive, sports and particularly commercial aircraft industry to exploit many of the superior mechanical properties offered by composite materials.

A typical AFP system is shown in Figure 1.1, consisting of a computer controlled robotic arm to place and adhere bands of tows (8 to 32 bands) having widths ranging from 3 mm to 12 mm along predefined paths (Qureshi, Swait, Scaife, and El-Dessouky 2014). The tows are heated while they are being placed on the mold and the placement head applies pressure to ensure proper adherence of tows to the current substrate surface. The AFP process has the flexibility to cut, restart and independently control the feed rate on individual tows, reducing wastage of materials. By individually controlling the feed rate of tows, differential payout of adjacent tows can be performed, allowing the robotic arm to move along curvilinear paths to obtain advantageous variable stiffness properties. In fact, the ability to steer tows at a preferred orientation opens a wide range of design option for tailoring properties of composite laminates. For example, orienting fibers within each lamina along optimal paths can result in favorable stress distributions and improved performance of a laminate for specific applications (Lopes, Gürdal, and Camanho 2008; Abdi, Gürdal, and Huang 2017)

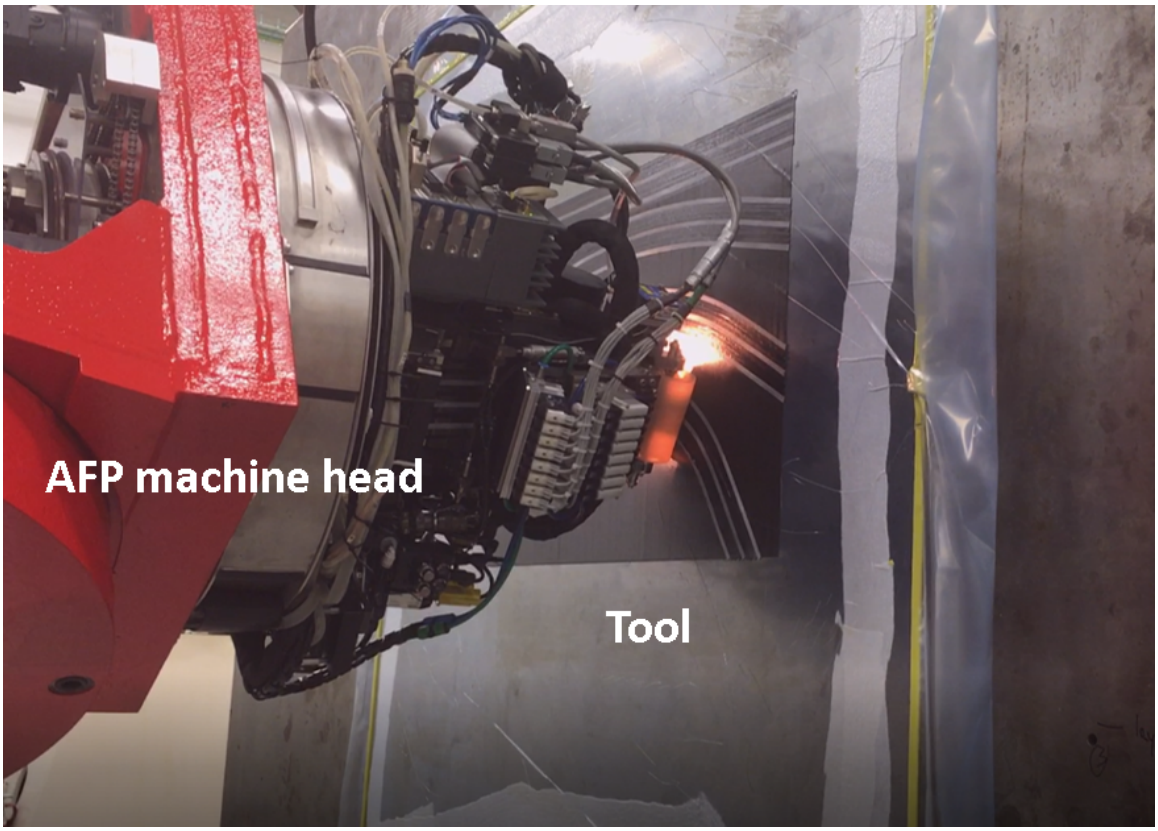

Figure 1.1 Photograph of the AFP head and tool

without addition of material, with further weight reduction possible. In this regard, buckling analysis performed by Chen, Wu, Nie, and Weaver (2018) and Wu, Raju, and Weaver (2018) for variable angle tow composites positioned along the optimal tow paths has shown that buckling resistance can be significantly improved by optimizing the tow path.

1.1 BACKGROUND AND MOTIVATION

1.1.1 DIRECT MATERIAL PROPERTY IDENTIFICATION

With the recent advancement in additive manufacturing, complex material system are increasingly being used in special application for obtaining desirable properties. For example Ajdari, Nayeb-Hashemi, and Vaziri (2011) showed that functionally graded cellular structures offer better energy absorption. An extensive review on

the multiscale design of functionally graded 3D printed material can be found in Li et al. (2020). Modeling of naturally occurring heterogeneous materials such as bone and tissue has attracted attention in recent years (Alexander, Gunnarsson, Rafaels, and Weerasooriya 2020). Characterization of such complex material systems poses challenges due to heterogeneity in the material response. Thanks to the development of DIC methods for full-field, non-contacting deformation measurements, a large data set can be generated in a single experiment. As noted by Hild and Roux (2006), DIC methods are necessary to obtain full field measurements for characterization of the spatial distribution in material properties. Development of a robust method for transforming the measured displacements (strains) into model parameters (material properties) is important in a range of heterogeneous material applications.

1.1.2 AUTOMATED FIBER PLACEMENT

In recent years, the commercial aircraft industry has increased the use of composite materials for aircraft structures. For example, advanced composites account for over 50% of the weight in a Boeing 787 aircraft (*AERO-Boeing 787 from the ground up* 2016), resulting in a 20% weight reduction compared to conventional aluminum airframe. In order to take full advantage of AFP, tows are usually placed along curvilinear paths resulting in stress concentration reduction around cutouts and reduced material wastage. However, as tow path curvature increases beyond a critical value, various defects can occur in the as-placed tows (Rajan et al. 2019b). One of the major defects observed in the AFP placed tows is out-of-plane wrinkling. Figure 1.2 shows an as-placed tow that has experienced out-of-plane wrinkling during AFP processing. These defects can affect fatigue life and increase part rejection due to inferior quality.

Various process parameters affect wrinkle formation during AFP processing, including tow path curvature, prepreg tack (bonding strength) and elastic moduli. Since the matrix material is viscoelastic, various properties of the tow are time and tem-

perature dependent. For example, tackiness of the uncured epoxy within a typical thermoset tow is observed to be a function of layup temperature and layup speed. Tow wrinkle formation is observed to be a function of tow tackiness. Thus, a method for quantifying tow tackiness for use in simulations capable of predicting AFP defects is essential for design of optimal tow paths that minimize defect formation.

Though several research publications have focused on modeling wrinkle formation during thermo-forming process of thermoplastic prepregs (Sargent et al. 2010; Sherwood et al. 2010; Boisse, Hamila, and Madeo 2016), there are a limited number of published articles focused on understanding the deformation mechanisms and subsequent occurrence of wrinkle formation during AFP placement of uncured thermoset tows. Manufacturing of quality composite parts using AFP processing requires a deeper understanding of the mechanisms resulting in defect formation and the effect of various process parameters on the defect formation. In this work, a finite element-based tow placement and bonding model is developed to simulate the AFP process

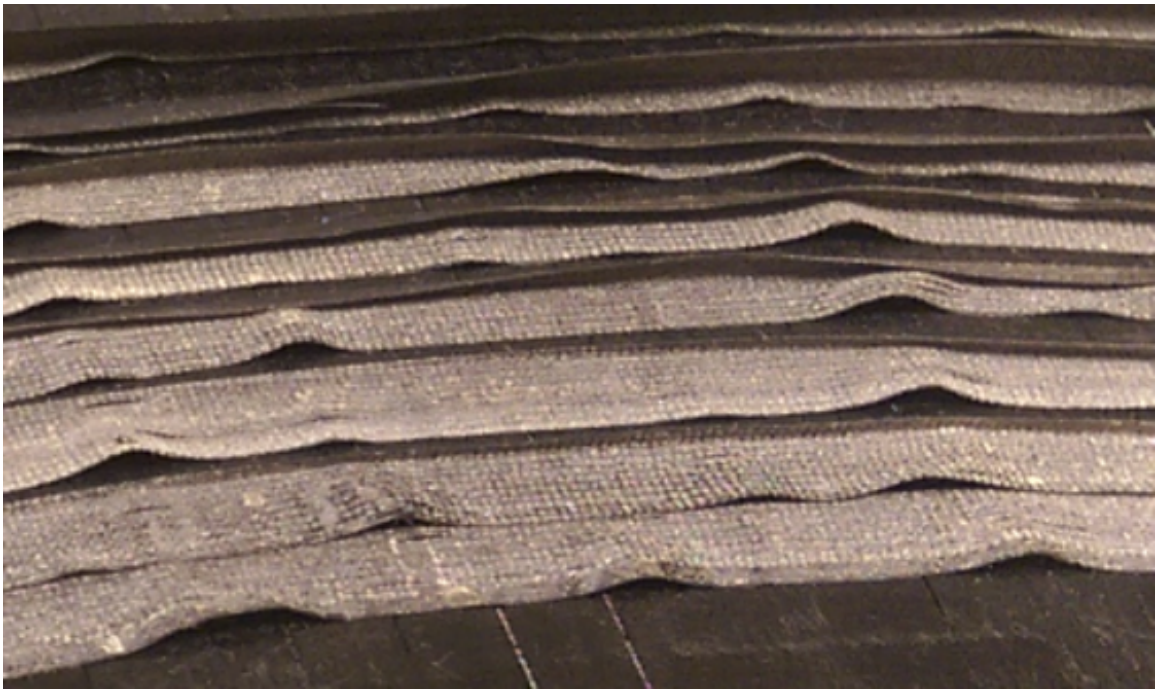

Figure 1.2 Out-of-plane wrinkle defects in tows after AFP processing

along curvilinear paths for thermoset tows. The simulations incorporate experimental results for Mode I and Mode II traction-separation laws in the cohesive interaction property of the tow-substrate interface to predict out-of-plane wrinkles during AFP processing.

1.2 ORGANIZATION OF THE DISSERTATION

The rest of this dissertation is organized as follows. Chapter 2 discusses direct material property identification in heterogeneous material systems. Chapter 3 focus on the development of a stereoDIC setup for identification of wrinkle defects in as-placed tows and measurement of wrinkle amplitude and wavelength of tows placed along four different paths. Chapter 4 introduces our development of theoretical formulation for extracting Mode I and Mode II traction versus separation relationship of tow-tow bonding using a modified rigid cantilever beam specimen. A complete description of the finite element model along with material properties employed in the simulations is discussed in Chapter 5. A summary and recommendations for future work are given in Chapter 6. Appendix A presents results from a series of composite tow experiments to quantify how the degree of polymer aging (oftentimes termed "low-temperature cure") and the glass transition temperature are affected by time at room temperature. Appendix B shows results from an additional set of experiments performed to measure tow viscoelastic bending modulus for different temperatures.

Chapter 2

DIRECT MATERIAL PROPERTY DETERMINATION UTILIZING FULL-FIELD DEFORMATION MEASUREMENTS

A direct approach is described to determine the elastic modulus distribution in a nominally heterogeneous material. The approach is based on solving partial differential equations (PDE) of equilibrium for unknown material properties with known boundary conditions and full field strain data (Eg. DIC). The PDEs are solved numerically using a Prtrov-Galerkin finite element procedure. The Bubnov-Galerkin method is shown to exhibit spurious oscillations for noisy strain input and for problems with discontinuities in elastic material properties. The formulation is developed for uniaxial applications using basic theoretical constructs, resulting in a computational framework that has a matrix form [A]{E} = {R}, where the [A] matrix components are known functions of measured axial strains and axial positions, {R} is a vector with components that are known functions of axial body forces, applied loads and reactions and {E} is a vector with components representing the unknown elastic moduli at discrete locations along the length of the specimen. For a series of 1D material property identification procedures with known axial strains at discrete locations and various levels of random noise, results are presented to demonstrate the accuracy and noise sensitivity of the methodology. Finally, experimental measurements for a heterogeneous bone specimen are compared to our one-dimensional model predictions, demonstrating that the predictions are in very good agreement

with independent estimates along the length of the specimen at each load level of interest.

2.1 INTRODUCTION

Developments in the previous millennium that resulted in the broad distribution of robust, accurate digital image correlation methods to obtain full-field deformation measurements (Chu, Ranson, and Sutton 1985; Luo, Chao, Sutton, and Peters 1993; Schreier, Braasch, and Sutton 2000; Helm, Sutton, and McNeill 2003a; Helm, Sutton, and McNeill 2003b; Sutton, Orteu, and Schreier 2009) has led to increasing interest in novel ways to utilize the dense sets of DIC data that were previously unavailable. In particular, the methodology has been investigated for material property identification, especially in heterogeneous and anisotropic material systems that are more difficult to characterize.

Prior to the development of DIC methods, a common approach was to bond strain gauges to specimens and use the discrete strain measurements with global stress estimates to estimate material properties. Since strain gauges are not appropriate for soft materials, a few years before the ascent of DIC methods for full-field measurements, researchers in the medical imaging field began studying approaches to determine material properties in soft tissues using ultrasound images. In 1994, Raghavan and Yagle (1994) used ultrasound images to determine through-thickness strains at various locations in a tissue sample when subjected to mechanical loads. By rearranging a set of finite difference equations for equilibrium in an elastic material, the authors indicated that they were successful in obtaining elastic properties. Kallel and Bertrand (1996) published one of the first "correlation-based" articles for material property determination, describing how to estimate the elastic properties of biological tissues. In his study, the author combined (a) property updating in an elastic finite element model for nominally "known" loads with (b) ultrasound-based image correlation mo-

tion measurements on the tissue. During the analysis process, the authors noted that forces should be "measured" at the boundary nodes; issues with boundary conditions were also noted in Raghavan and Yagle (1994). Since the use of micro-scale load cells was impractical for the soft tissue specimens, the authors suggested using a known material between the specimen and the loading surface. By applying load to the known material, while simultaneously obtaining full-field strains on the material during loading, the strain data could be used to determine the surface stresses (and hence forces) on the specimen. Once all required conditions were known, the authors minimized the difference between the measured and predicted displacements by iteratively updating the material properties to obtain optimal property estimates. Finally, noting concerns regarding ill-conditioning of the matrices, the authors used Tikhonov regularization as a compromise between fidelity to the observed data and a priori information regarding the range of elastic properties in the tissue, with convergence in the regularized solution occurring within a few iterations for an echo-cardiogram image set.

Near the turn of the millennium, Chasiotis and Knauss (2002) demonstrated the use of Atomic Force Microscopy (AFM) with 2D-DIC for regions on the order of 100 μm in size to obtain full-field deformation measurements that could be used to obtain highly localized material property estimates. In the mid-2000's, two review articles focusing on the use of full-field methods for material property identification were published (Hild and Roux 2006; Avril et al. 2008). In particular, Hild and Roux (2006) stated that DIC methods were needed to obtain elastic properties in heterogeneous materials where single measurements are not sufficient to fully characterize the material property distribution. In their review, the authors noted that minimization of the difference between measurements and theoretical predictions using the material parameters provides an iterative methodology for optimal property identification. In a more detailed follow-on review Avril et al. (2008) noted that a direct finite element

approach would result in matrix form, $[K(\theta)]\{U\} = \{F\}$ where [K] is the stiffness matrix that is a function of the material parameters, θ, {U} is the nodal displacement vector and {F} is the force vector. A variety of methods were discussed that could be used to determine material properties, including finite element method updating, virtual fields method, equilibrium gap and related approaches that minimize a specific function to determine an optimal set of material parameters.

When using full field measurements with computational models, as noted by Kallel and Bertrand (1996), ill-posed matrices may complicate the inversion process necessary to determine an optimal set of material properties. One approach that was described for fracture problems by Réthoré, Roux, and Hild (2008) is to require least noise sensitivity for the parameter of interest during the optimization process. A global DIC-based method, commonly known as integrated DIC (IDIC) has been developed and extensively applied for parameter identification in recent years. For example, Neggers, Hoefnagels, Geers, Hild, and Roux (2015) showed that time resolved IDIC can be applied for material property identification by combining the finite element method with DIC measurements at all time increments. Bertin et al. (2016) applied the IDIC method for material property identification of an elasto-plastic material using biaxial experimental data. In another study, Hoefnagels, Bertin, Du, and Hild (2018) applied the IDIC method using 3D surface displacement data, load history and confocal microscopy to measure the height profile at the micro-scale to estimate crystal plasticity parameters (Hoefnagels, Bertin, Du, and Hild 2018).

In this chapter, the concepts described in Avril et al. (2008) are utilized to develop a direct solution method for the distribution of Young's modulus in a heterogeneous, nominally one-dimensional component subjected to either tension or compression loading. The method does not require iterative updating, thereby reducing computational overhead, especially when a large number of parameters are to be determined. Compared to the IDIC method, the direct approach shown in this work has no re-

striction on the type of measurement method used to obtain the strain data while also allowing some flexibility in the element size based on the strain resolution and noise in the measured data. Though the method is readily applied to dynamic situations where specimen accelerations are measured, the focus in this study is on development and validation of the quasi-static formulation. To obtain the basic equations, a direct approach based on a Petrov-Galerkin finite element formulation is employed. Direct approach was also developed using the Bubnov-Galerkin method, with results using this approach shown to exhibit spurious oscillations for noisy strain input and spatially discontinuous elastic modulus distribution. When given either measured displacements or strains, along with a measured force at either end, the resulting linear set of equations is then solved to determine the unknown material property distribution along the entire length of the specimen.

The remainder of Chapter 2 is organized as follows. First, Section 2.2 describes the basic theory and the 1D material property identification equations are presented. Section 2.3 presents results from the material property identification procedure using synthetic displacement and strain data with Gaussian random noise. Section 2.4 presents results when applying the methodology to a nominally one-dimensional bone specimen that is subjected to uniaxial compression loading. Section 2.5 provides discussion of results.

2.2 THEORETICAL FORMULATION

2.2.1 One Dimensional Formulation

A schematic of the one-dimensional problem considered in this work including the coordinate system, applied axial loading and specimen dimensions, are shown in Figure 2.1.

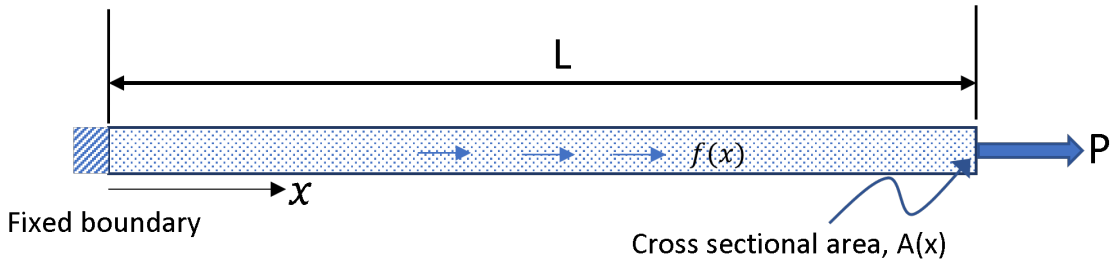

Figure 2.1 One dimensional bar undergoing loading due to point load (P) and body force per unit volume (f)

The equation of equilibrium for a 1-D bar can be written as

$$\frac{d\sigma}{dx} + f(x) = 0, \tag{2.1}$$

where f(x) is the body force per unit volume, σ is the axial stress and x is distance along the bar axis. The force boundary condition can be written in terms of the axial stress as

$$\sigma(x = L) = P/A(x = L), \tag{2.2}$$

where A(x) is the cross-sectional area and P is the equilibrated axial static load. Assuming a linear elastic constitutive relationship, Equations (2.1) and (2.2) can be written in terms of Young's modulus, E, and axial strain, ϵ, as follows:

$$\frac{d(E(x)\epsilon(x)}{dx} + f(x) = 0; E(x = L) = \frac{p}{\epsilon(x)A(x)}, \tag{2.3}$$

where $\epsilon(x) = du/dx$, u(x) is the axial displacement and P/A(x) = $\sigma(x)$. A solution for Equation (2.3), with E(x) as the unknown variable, is sought using the finite element method. The weak form for Equation (2.3) can be written as

$$\int_0^L \left[\frac{d(E(x)\epsilon(x)}{dx} + f(x)\right] w(x)A(x)dx = 0, \tag{2.4}$$

where w(x) is a weighting function (or test function). Using integration by parts, Equation (2.4) can be written as

$$w(x)E(x)\epsilon(x)A(x)|_{x=0}^{x=L} - \int_0^L \frac{dw(x)}{dx} E(x)\epsilon(x)A(x)dx + \int_0^L f(x)w(x)A(x)dx = 0. \tag{2.5}$$

Comparison of Equation (2.4) to the virtual fields method shows similar forms, with the weighting function related to kinematically admissible virtual field displacements. In the enclosed study, the weighting functions are assumed to be piecewise continuous functions across all elements. Reordering the terms, Equation (2.5) can be written as

$$\int_0^L \frac{dw(x)}{dx} E(x)\epsilon(x)A(x)dx = w(x)E(x)\epsilon(x)A(x)|_{x=0}^{x=L} + \int_0^L f(x)w(x)A(x)dx. \quad (2.6)$$

2.2.2 FINITE ELEMENT FORMULATION

Figure 2.2 shows discretization of the domain into n elements. The element level equations for the i^{th} element are shown in terms of natural coordinates and local node numbers. Assuming a linear shape function for the approximate solution in each element, the Young's modulus distribution in each element can be expressed as

$$E(\xi^{e_i}) = E_i(1 - \xi^{e_i}) + E_{i+1}(\xi^{e_i}), \quad (2.7)$$

where i represents element number, ξ^{e_i} is the local natural coordinate of the element as shown in Figure 2.3 ($\xi^{e_i} = 0$ at node 1 and $\xi^{e_i} = 1$ at node 2 in element i), E_i and E_{i+1} are the nodal values of the Young's modulus at nodes i and i+1, respectively. The shape functions are also shown in Figure 2.3, with $N_1 = (1 - \xi^{e_i})$ and $N_2 = \xi^{e_i}$.

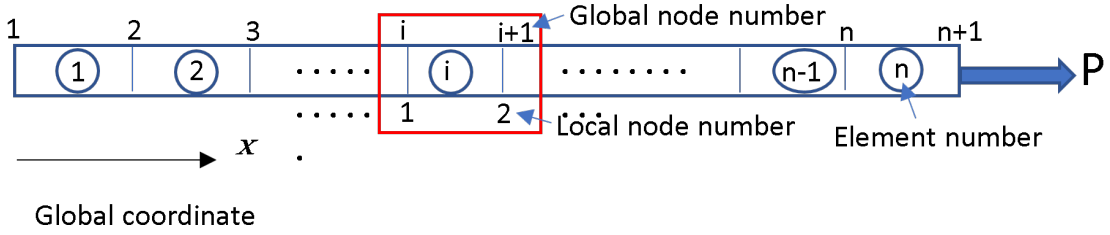

Figure 2.2 Finite element discretization of the one-dimensional bar loaded in tension

The global to natural coordinate system transformation is written as

$$X(\xi^{e_i}) = x_i(1 - \xi^{e_i}) + x_{i+1}(\xi^{e_i}), \quad (2.8)$$

where x_i and x_{i+1} are coordinates of nodes 1 and 2 in element i in the global coordinate system. Here the shape functions for an element (sub domain) are $N_1^{e_i} = (1 - \xi^{e_i})$

and $N_2^{e_i} = \xi^{e_i}$. In the Bubnov-Galerkin method the weight functions are chosen from

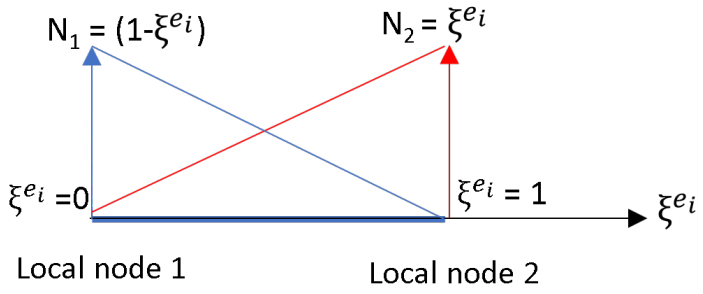

Figure 2.3 Local element coordinate system and shape function for a linear element

the same function space as the shape functions. However referring Equation (2.6), it can be observed that shape function regularity requirements are lower than that for the weight functions (the first derivative of the weight functions should exist). It is well known that PDEs with odd order differentials are susceptible to oscillations in the solution due to small perturbations in input data (Stenger 1974). Hence the weight functions are chosen from different function spaces with piecewise quadratic basis functions (Petrov-Galerkin method). The selected weight functions (shown in Figure 2.4) for a two node element are

$$w_1^{e_i} = (1 - \xi^{e_i})^2, w_2^{e_i} = (2 - \xi^{e_i})\xi^{e_i}. \tag{2.9}$$

Substituting the shape functions and weight functions into the weak form of the equilibrium equation in Equation (2.6) and using the transformation equation given in Equation (2.8)

$$\int_0^1 \left[(J^{e_i})^{-1} \frac{dw_1^{e_i}(x)}{d\xi^{e_i}} (E_i N_1^{e_i} + E_{i+1} N_2^{e_i}) \right] \epsilon(\xi^{e_i}) A(\xi^{e_i}) J^{e_i} d\xi^{e_i} = w_1^{e_i} E(\xi^{e_i}) \epsilon(\xi^{e_i}) A(\xi^{e_i}) |_{\xi^{e_i}=0}^{\xi^{e_i}=1} + \int_0^1 f(\xi^{e_i}) w_1^{e_i} A(\xi^{e_i}) J^{e_i} d\xi^{e_i}, \tag{2.10}$$

$$\int_0^1 \left[(J^{e_i})^{-1} \frac{dw_2^{e_i}(x)}{d\xi^{e_i}} (E_i N_1^{e_i} + E_{i+1} N_2^{e_i}) \right] \epsilon(\xi^{e_i}) A(\xi^{e_i}) J^{e_i} d\xi^{e_i} = w_2^{e_i} E(\xi^{e_i}) \epsilon(\xi^{e_i}) A(\xi^{e_i}) |_{\xi^{e_i}=0}^{\xi^{e_i}=1} + \int_0^1 f(\xi^{e_i}) w_2^{e_i} A(\xi^{e_i}) J^{e_i} d\xi^{e_i}, \tag{2.11}$$

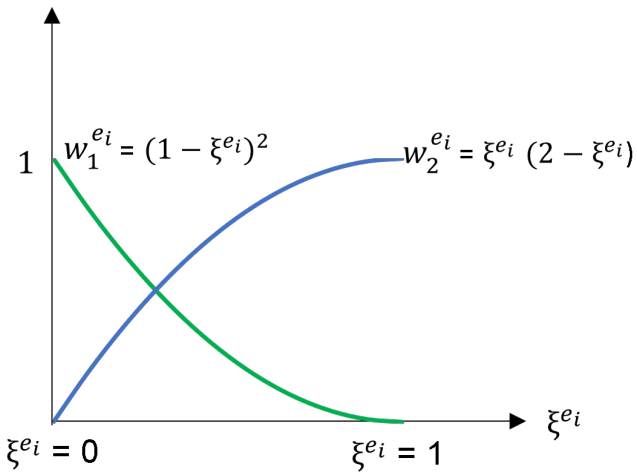

Figure 2.4 Quadratic polynomial weight functions selected in the Petrov-Galerkin formulation

where global derivative is converted to derivative with respect to natural coordinates using Jacobian, J^{e_i}. The global derivative in natural coordinate is given by

$$\frac{d}{dx} = (J^{e_i})^{-1}\frac{d}{d\xi^{e_i}}. \tag{2.12}$$

The term $E(\xi^{e_i})\epsilon(\xi^{e_i})$ on the right hand side of Equations (2.10) and (2.11) can be replaced by $\sigma(\xi^{e_i})$ where σ is the Cauchy stress in the axial direction, so that Equations (2.10) and (2.11) can be written as

$$\int_0^1 \left[(J^{e_i})^{-1}\frac{dw_1^{e_i}(x)}{d\xi^{e_i}}(E_i N_1^{e_i} + E_{i+1}N_2^{e_i}\right]\epsilon(\xi^{e_i})A(\xi^{e_i})J^{e_i}d\xi^{e_i} = w_1^{e_i}\sigma(\xi^{e_i})A(\xi^{e_i})|_{\xi^{e_i}=0}^{\xi^{e_i}=1} + \int_0^1 f(\xi^{e_i})w_1^{e_i}A(\xi^{e_i})J^{e_i}d\xi^{e_i}, \tag{2.13}$$

$$\int_0^1 \left[(J^{e_i})^{-1}\frac{dw_2^{e_i}(x)}{d\xi^{e_i}}(E_i N_1^{e_i} + E_{i+1}N_2^{e_i}\right]\epsilon(\xi^{e_i})A(\xi^{e_i})J^{e_i}d\xi^{e_i} = w_2^{e_i}\sigma(\xi^{e_i})A(\xi^{e_i})|_{\xi^{e_i}=0}^{\xi^{e_i}=1} + \int_0^1 f(\xi^{e_i})w_2^{e_i}A(\xi^{e_i})J^{e_i}d\xi^{e_i}. \tag{2.14}$$

The weight functions at local nodes 1 and 2 are given by

$$w_1^{e_i}|_{\xi^{e_i}=1} = w_2^{e_i}|_{\xi^{e_i}=0} = 0,$$
$$w_1^{e_i}|_{\xi^{e_i}=0} = w_2^{e_i}|_{\xi^{e_i}=1} = 1. \tag{2.15}$$

Substituting Equation (2.15) into Equations (2.13) and (2.14) gives

$$E_i \int_0^1 \frac{dw_1^{e_i}(x)}{d\xi^{e_i}} N_1^{e_i} \epsilon(\xi^{e_i}) A(\xi^{e_i}) d\xi^{e_i} + E_{i+1} \int_0^1 \frac{dw_1^{e_i}(x)}{d\xi^{e_i}} N_2^{e_i} \epsilon(\xi^{e_i}) A(\xi^{e_i}) d\xi^{e_i} = -F_1^{e_i} + \int_0^1 f(\xi^{e_i}) w_1^{e_i} A(\xi^{e_i}) J^{e_i} d\xi^{e_i}, \quad (2.16)$$

$$E_i \int_0^1 \frac{dw_2^{e_i}(x)}{d\xi^{e_i}} N_1^{e_i} \epsilon(\xi^{e_i}) A(\xi^{e_i}) d\xi^{e_i} + E_{i+1} \int_0^1 \frac{dw_2^{e_i}(x)}{d\xi^{e_i}} N_2^{e_i} \epsilon(\xi^{e_i}) A(\xi^{e_i}) d\xi^{e_i} = F_2^{e_i} + \int_0^1 f(\xi^{e_i}) w_2^{e_i} A(\xi^{e_i}) J^{e_i} d\xi^{e_i}, \quad (2.17)$$

where $F_1^{e_i}$ and $F_2^{e_i}$ are the internal forces at local nodes 1 and node 2 in element i, respectively, ($F_1^{e_i} = \sigma(\xi^{e_i} = 0) A(\xi^{e_i} = 0)$ and $F_2^{e_i} = \sigma(\xi^{e_i} = 1) A(\xi^{e_i} = 1)$. Hence the element matrix equation for the i^{th} element is given by

$$\begin{bmatrix} \int_0^1 \frac{dw_1^{e_i}(x)}{d\xi^{e_i}} N_1^{e_i} \epsilon(\xi^{e_i}) A(\xi^{e_i}) d\xi^{e_i} & \int_0^1 \frac{dw_1^{e_i}(x)}{d\xi^{e_i}} N_2^{e_i} \epsilon(\xi^{e_i}) A(\xi^{e_i}) d\xi^{e_i} \\ \int_0^1 \frac{dw_2^{e_i}(x)}{d\xi^{e_i}} N_1^{e_i} \epsilon(\xi^{e_i}) A(\xi^{e_i}) d\xi^{e_i} & \int_0^1 \frac{dw_2^{e_i}(x)}{d\xi^{e_i}} N_2^{e_i} \epsilon(\xi^{e_i}) A(\xi^{e_i}) d\xi^{e_i} \end{bmatrix} \begin{bmatrix} E_i \\ E_{i+1} \end{bmatrix} = \begin{bmatrix} -F_1^{e_i} + \int_0^1 f(\xi^{e_i}) w_1^{e_i} A(\xi^{e_i}) J^{e_i} d\xi^{e_i} \\ F_2^{e_i} + \int_0^1 f(\xi^{e_i}) w_2^{e_i} A(\xi^{e_i}) J^{e_i} d\xi^{e_i} \end{bmatrix}. \quad (2.18)$$

To obtain direct equations for the unknown Young's moduli in each element, the element equations are assembled to form the global equation as shown in Equation (2.19):

$$\begin{bmatrix} A_{11} & \cdots & A_{1n} \\ \vdots & \ddots & \vdots \\ A_{n1} & \cdots & A_{nn} \end{bmatrix} \begin{bmatrix} E_1 \\ \vdots \\ E_n \end{bmatrix} = \begin{bmatrix} -F_1^{e_1} + \int_0^1 f(\xi^{e_1}) w_1^{e_1} A(\xi^{e_1}) J^{e_1} d\xi^{e_1} \\ \vdots \\ -F_1^{e_n} + F_2^{e_{n-1}} + \int_0^1 f(\xi^{e_n}) w_1^{e_n} A(\xi^{e_n}) J^{e_n} d\xi^{e_n} + \\ \int_0^1 f(\xi^{e_{n-1}}) w_2^{e_{n-1}} A(\xi^{e_{n-1}}) J^{e_{n-1}} d\xi^{e_{n-1}} \end{bmatrix}. \quad (2.19)$$

Equation (2.19) can be solved with the boundary condition at the right, $E_{n+1} = P/[A(x = L)\epsilon_{n+1}]$. For comparison of the result with Bubnov-Galerkin method, Equation (2.19) is also solved for the weighting functions corresponding to Bubnov-Galerkin method. The Bubnov-Galerkin and Petrov-Galerkin weight functions are shown in Table 2.1.

Table 2.1 Bubnov-Galerkin and Petrov-Galerkin weight functions

Bubnov-Galerkin weight functions	Petrov-Galerkin weight functions
$w_1^{e_i} = (1-\xi^{e_i})^2$	$w_1^{e_i} = (1-\xi^{e_i})$
$w_2^{e_i} = (2-\xi^{e_i})\xi^{e_i}$	$w_2^{e_i} = \xi^{e_i}$

2.2.3 Determination of components of [A]

As shown in Equation (2.19), components of [A] involve integration of terms involving the shape function and the measured strain values within each element. Full field strain measurement techniques such as digital image correlation (2D-DIC, StereoDIC) provide strain values at a relatively dense set of discrete locations (Sutton, McNeill, Helm, and Chao 2000). Assuming that $\epsilon(\xi^{e_i})$ are available at discrete points within an element, the integration in Equation (2.19) can be performed numerically (e.g., a trapezoidal rule). If the measured strain values do not coincide with nodal locations, the strains at these locations are determined by an interpolation method. In this study, linear interpolation of the neighboring strain values, as shown schematically in Figure 2.5, is implemented. The trapezoidal numerical integration scheme used in this study is shown in Equation (2.20):

$$\int_0^1 g_j(\xi^{e_i})\epsilon(\xi^{e_i})d\xi^{e_i} = \sum_{p=1}^{m_{i-2}} \left[g\left(\frac{\left(\xi_p^{e_i} + \xi_{p+1}^{e_i}\right)}{2} \right) \frac{\epsilon_p^{e_i} + \epsilon_{p+1}^{e_i}}{2} \right] + g\left(\frac{\xi_1^{e_i}}{2}\right) \frac{\epsilon_0^{e_i} + \epsilon_1^{e_i}}{2} + g\left(\frac{\left(\xi_{m_{i-1}}^{e_i} + \xi_{m_i}^{e_i}\right)}{2} \right) \frac{\epsilon_{m_{i-1}}^{e_i} + \epsilon_{m_i}^{e_i}}{2}, \tag{2.20}$$

where $g_j(\xi^{e_i}) = N_j(\xi^{e_i})A(\xi^{e_i})$.

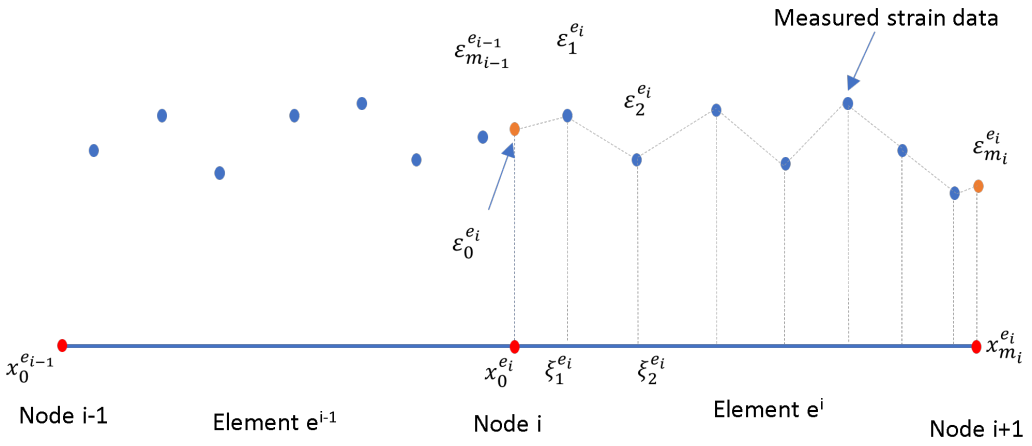

Figure 2.5 Schematic showing measured strain data locations with respect to node positions

2.3 ONE-DIMENSIONAL MATERIAL PROPERTY IDENTIFICATION WITH GAUSSIAN NOISE

The Young's moduli obtained in this section are based on synthetically generated strain data with randomly distributed, unbiased Gaussian noise. The strain data is generated using a known spatial distribution of Young's modulus. Computational predictions for the Young's modulus distribution using strain data with and without noise are obtained for two different Young's modulus spatial distributions including (a) linear and (b) step change (Heaviside step function).

For each case, varying levels of random noise in the generated strain data are added to understand the effect of noise on modulus predictions. Other variables considered in the parametric study include both (a) the number of elements and (b) the number of strain measurements within each element. Since cross-sectional area change has the same effect as a varying modulus for a one-dimensional bar, the examples considered in this section assume a constant cross-sectional area. The generated strain data with the added Gaussian noise is given in Equation (2.21):

$$\tilde{\epsilon} = \epsilon + \delta\epsilon, \tag{2.21}$$

where $\tilde{\epsilon}(x)$ is the input strain distribution with noise, ϵ is the theoretical strain data generated for a known elastic modulus distribution and $\delta\epsilon$ is the added Gaussian noise with zero mean and standard deviation of β_ϵ.

2.3.1 Linear distribution of Young's modulus

The linear distribution of Young's modulus considered in this work is given as

$$E = E_0(1 + x/L), \tag{2.22}$$

where L is the bar length and E_0 is Young's modulus at x = 0.

Defining normalized strain as $\epsilon_N = \epsilon/\epsilon_0$ where $\epsilon_0 = P/(AE_0)$, Figure 2.5 presents both Equation (2.22) and the predicted distribution of Young's modulus when solving Equation (2.19) using N_e =50 and N_d = 10 (ten strain data points per element) with (a) $\beta_\epsilon = 0$ (no noise), and (b) $\beta_\epsilon = 0.020$ (Gaussian noise in the normalized strain with standard deviation of 0.020). In order to show the robustness of Petrov-Galerkin method, results from Bubnov-Galerkin is compared in Figure 2.6. From Figure 2.6(a), it can be observed that the predicted modulus distribution coincides with the true modulus when there is no noise in the strain data for both Bubnov-Galerkin and Petrov Galerkin methods. As noise in the strain data increases, the predicted modulus begins to oscillate about the exact solution. However, as shown in Figure 2.6(b), oscillations in the modulus predictions using the Petrov-Galerkin method are significantly reduced when compared to the results using the Bubnov-Galerkin method.

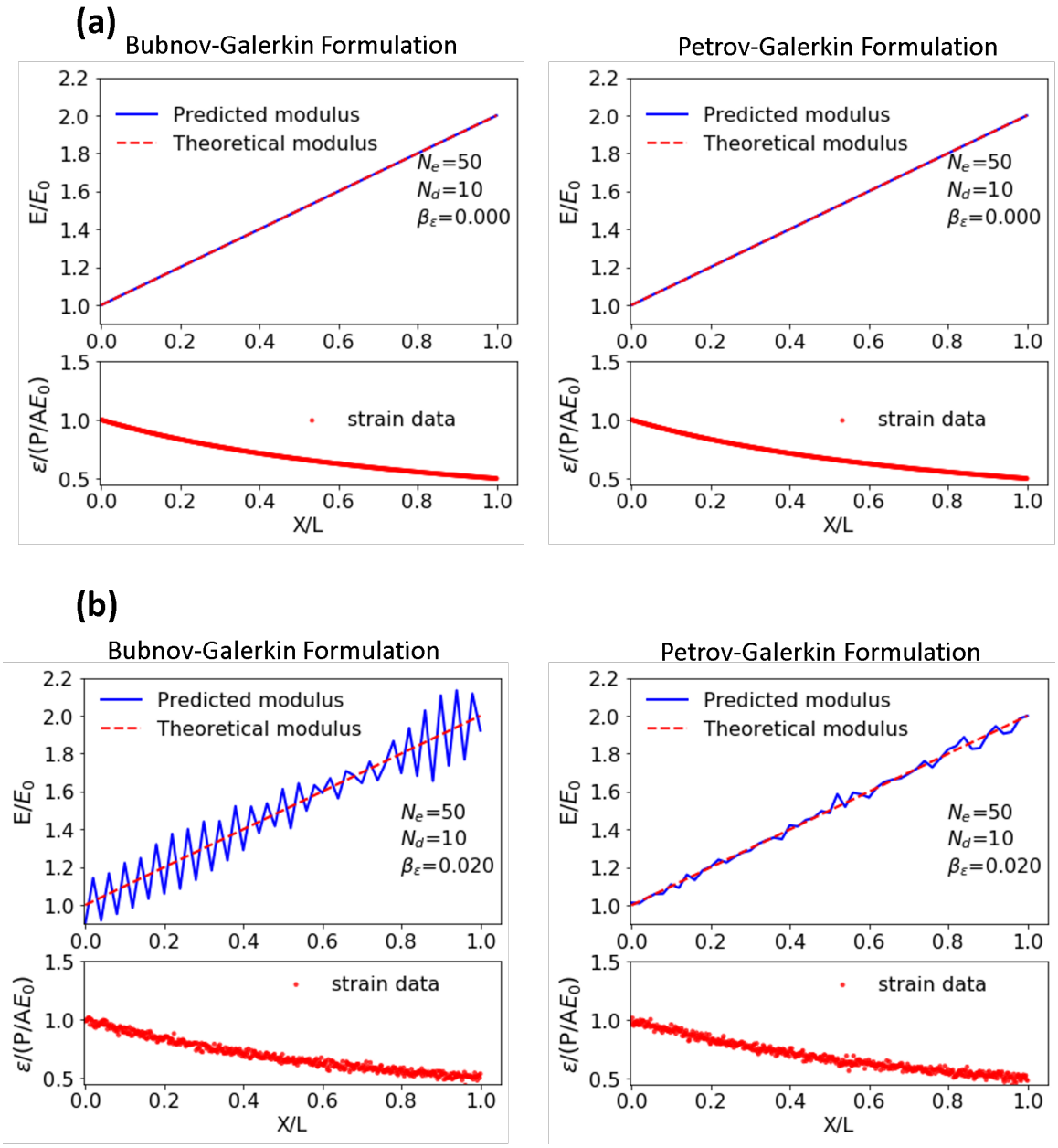

Figure 2.6 Comparison of the Predicted E(x)/E_0 using Bubnov-Galerkin and Perov-Galerkin method with respect to the exact solution for (a)$\beta_\epsilon = 0$, and (b) $\beta_\epsilon = 0.020$

2.3.2 Step change in Young's modulus (Heaviside distribution)

The most challenging situation involves step changes in the Young's modulus distribution, as given by Equation (2.23):

$$E(x) = E_0 \begin{cases} 2.00, & 0.00 \leq x/L < 0.25, \\ 1.75, & 0.25 \leq x/L < 0.50, \\ 1.50, & 0.50 \leq x/L < 0.75, \\ 1.25, & 0.75 \leq x/L \leq 1.00. \end{cases} \tag{2.23}$$

Situations such as given in Equation (2.23) are known to introduce spurious oscillations in the solution due to the presence of step changes that are inconsistent with the requirement for continuous derivatives in the domain. Even so, the authors performed 1D material property identification procedure to determine how sensitive the current formulation is to the discontinuous E(x) representation. For exact ϵ_N data in the continuous regions, Figure 2.7 compares the predicted Young's modulus using Bubnov-Galerkin method and Petrov-Galerkin method with the exact distribution for $N_e = 50$, $N_d = 10$ and $\beta_\epsilon = 0.020$. As shown in Figure 2.7, the discontinuities created oscillations that propagated throughout the domain for Bubnov-Galekin

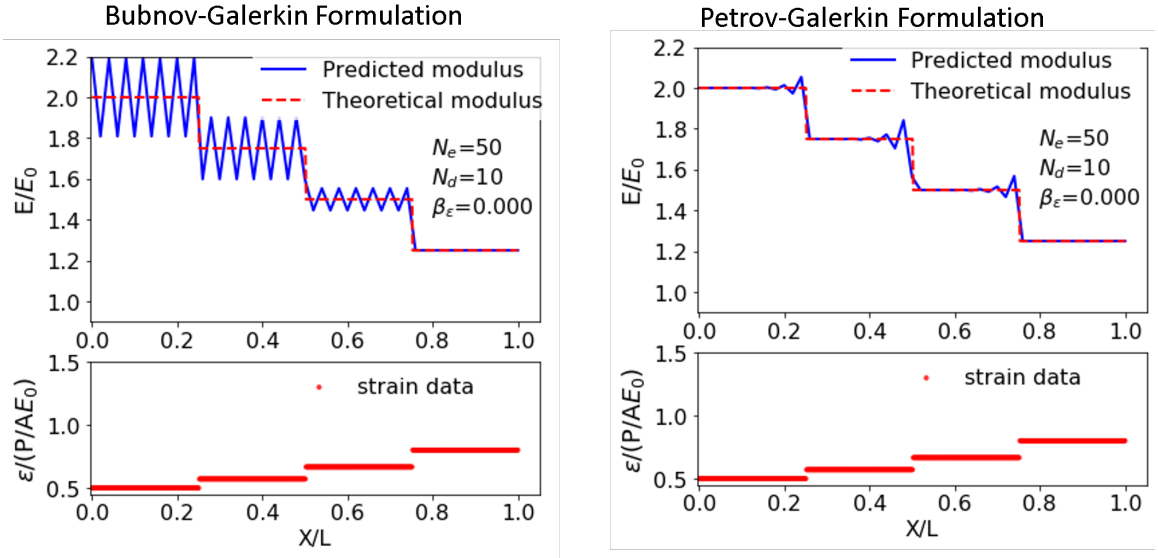

Figure 2.7 Comparison of the Predicted E(x)/E_0 using Bubnov-Galerkin and Petrov-Galerkin method with respect to the exact solution for N_e =50, N_d = 10 and $\beta_\epsilon = 0.000$

method. However, the oscillations dissipated away from the discontinuities for the Petrov-Galerkin method.

2.4 MODULUS PREDICTIONS WITH EXPERIMENTAL DATA

To assess the methodology using full field 2D-DIC experimental data, recent measurements by Alexander, Gunnarsson, Rafaels, and Weerasooriya (2020) are employed. In their work, authors performed axial compression experiments on the small bone sample shown in Figure 2.8(a). The specimen has a length of 9.18 mm, width of 7.3 mm and a cross sectional area of 70.95 mm^2; the experimental setup and DIC hardware details for the vision system used in their experiments are given in Alexander, Gunnarsson, Rafaels, and Weerasooriya (2020). As noted in Alexander, Gunnarsson, Rafaels, and Weerasooriya (2020), inspection of the micro-CT scan shown in Figure 2.8(a) indicates the specimen has a well-defined variation in bone structure along the vertical length that is nominally similar for vertical x-y and x-z cross-sections. Based on these observations, the authors in Alexander, Gunnarsson, Rafaels, and Weerasooriya (2020) assumed the specimen structure (i.e., bone volume fraction, V_f) is only a function of the position along the vertical direction (i.e., the x-direction in Figure 2.8(a)) and is independent of both transverse directions. Using a single camera vision system to obtain images of the bone specimen during compressive loading, the authors used commercial software, VIC-2D[1], to obtain full-field surface displacements and strains on a visible x-y surface. The full-field axial strain measurements for an axial stress, $\sigma = 4$ MPa, are shown in Figure 2.8(b) and the quasi-static average stress vs. average strain[2] results are shown in Figure 2.8(c).

In this work, the images obtained previously (Alexander, Gunnarsson, Rafaels,

[1]Correlated Solutions – VIC-2D v7, https://www.correlatedsolutions.com/vic-2d/

[2]The average stress, $\sigma_{avg} = P/A$ and average strain, $\epsilon_{avg} = (1/N)\sum_{i=1}^{N} \epsilon_{xx}^{i}$, where P is the compressive force, A is the area of cross section parallel to y-z plane and N is the number of DIC strain data points in the field of view.

and Weerasooriya 2020) are re-analyzed using VIC-2D with the analysis parameters given in Table 2.2 to obtain 1018 strain data points horizontally and 1415 strain data points vertically. Due to the relatively coarse nature of the natural speckle pattern in the specimen, a relatively large subset size is used, which has the effect of smoothing spatial gradients in the measured data (see Sutton, Orteu, and Schreier (2009) for speckle size and subset size requirements). As shown in Figure 2.8(a), variations in bone density within the specimen required the authors to use two different sets of DIC parameters within zones (A,B,C); the subset size in each zone is shown in Table 2.2, with each subset sufficiently large to span at least six intensity transitions in each direction (Sutton, Orteu, and Schreier 2009).

Inspection of Figure 2.8(b) confirms that the axial compressive strain field is heterogeneous, which is consistent with the CT scan image in Figure 2.8(a) that clearly shows the bone volume fraction is higher in Zones A and C. Detailed analysis of the CT images using a representative volume element (RVE) demonstrated that bone density is nominally uniform in the y and z directions, varying from top to bottom (x-direction) (Alexander, Gunnarsson, Rafaels, and Weerasooriya 2020). Based on these measurements, it is reasonable to assume specimen deformation in the axial

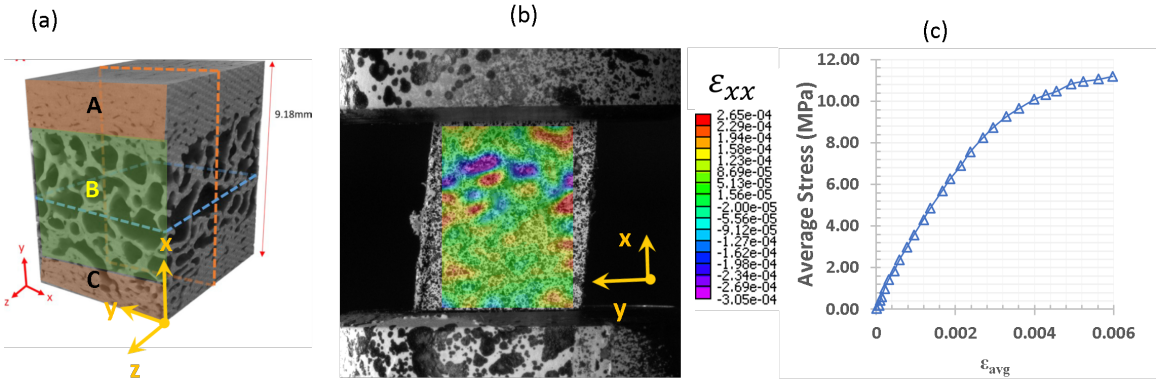

Figure 2.8 (a) Micro-CT scan image of bone specimen, (b) 2D-DIC measurements of axial strain field for $\sigma = 4$ MPa, (c) average axial stress vs strain data for the specimen

Table 2.2 DIC parameters selected for three zones in the area of interest shown in Figure 2.8(a)

DIC parameters	Zones A and C	Zone B
DIC software	VIC-2D, Version 7	VIC-2D, Version 7
Image filtering	Gaussian filter with a 3x3 pixel kernel	Gaussian filter with a 3x3 pixel kernel
Subset size	75 pixels (487 µm)	151 pixels (980 µm)
Step size	1 pixel (6.5 µm)	1 pixel (6.5 µm)
Subset shape function	Affine	Affine
Matching criterion	Zero-normalized sum of square differences (ZNSSD)	ZNSSD
Strain window	5 data points	5 data points
Virtual strain gauge size	79 pixels (513 µm)	155 pixels (1006 µm)
Strain formulation	Green-Lagrange	Green-Lagrange
Strain noise floor[3]	40 $\mu\epsilon$	30 $\mu\epsilon$

direction could be predicted using a one-dimensional model of an axially heterogeneous material, with the axial strain at each vertical position obtained by averaging the measured axial strains across the width of the specimen.

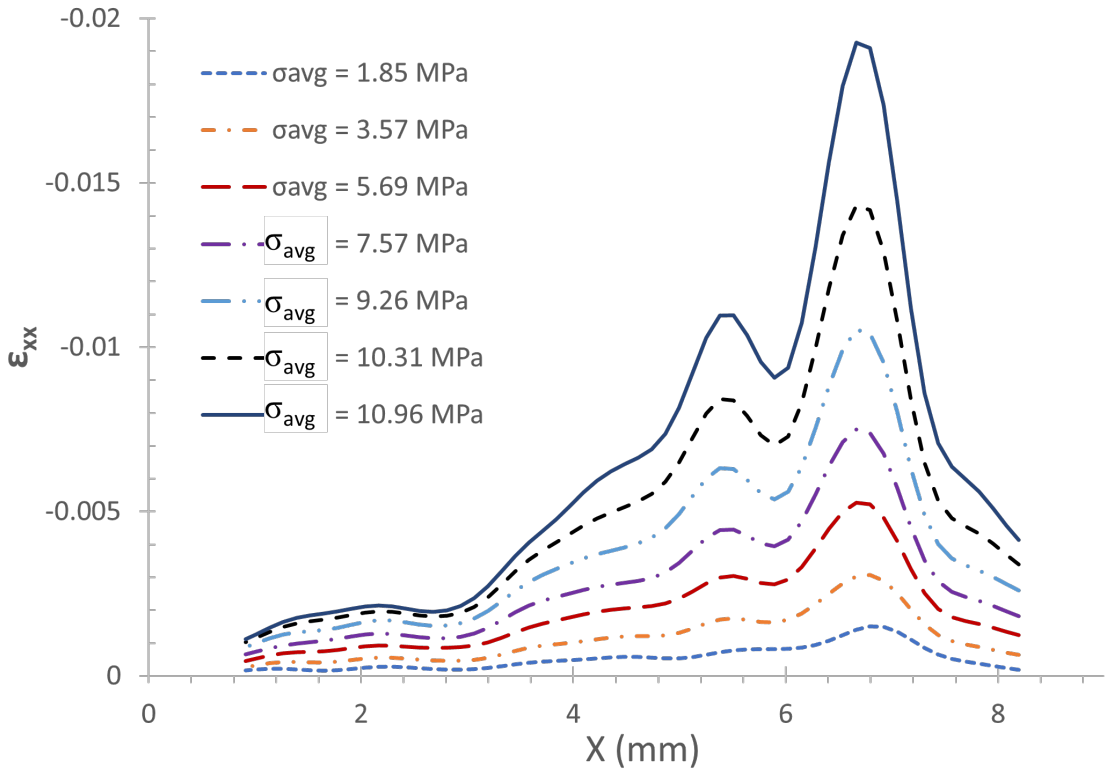

Figure 2.9 Average measured axial strain data (ϵ_{xx}) along length of specimen (x) for different axial stress values (σ_{avg})

The re-calculated average strains across the width of specimen in the central region using 2D-DIC data obtained during re-analysis of the images and the parameters in Table 2.2 for different load levels are shown in Figure 2.9. Though not shown in Figure 2.9, analysis of the strain data obtained along the entire length of the specimen demonstrates the measured strains near the top and bottom boundaries of the sample are nearly zero for all load levels, primarily due to frictional interaction of the loading platen surfaces, resulting in a complex localized stress state and constrained local deformations. Thus, only the strain data from the central 80% of the specimen is shown in Figure 2.9 and used in the one-dimensional material property identification procedure, with data from the upper 10% and lower 10% of the length excluded from the analysis.

2.4.1 Predictions of Young's Modulus for Elastic Range

Prior to presenting Young's modulus predictions using the measured full-field strain data, observations regarding the measured strain data are described. First, baseline analysis of specimen images using the parameters specified in Table 2.2 indicates variability range for the strain measurements is $\pm 40\mu\epsilon$. Secondly, since measured axial strains during the early stages of loading vary linearly and are on the order of $400\mu\epsilon$ or less, the signal to noise ratio is less than ten and β_ϵ is near 0.10. In such cases, to obtain accurate predictions for E(x), the required N_d for a given N_e will be quite high, even for a small number of elements. Since the maximum number of strain data is fixed by the vertical pixel dimensions of the camera (i.e., M < 1415 pixels), for $\sigma_{avg} < 0.50$ MPa, where average strain is less than $400\mu\epsilon$, variability in the predicted moduli is expected to be higher than at elevated stresses. To predict Young's modulus within the nominally elastic strain range, 1D material property identification procedure are performed for the range $1000\ \mu\epsilon \leq \delta/L = \epsilon_{engr} \leq 2000\mu\epsilon$, which corresponds the range 4 MPa $\leq \sigma_{avg} \leq$ 6 MPa.

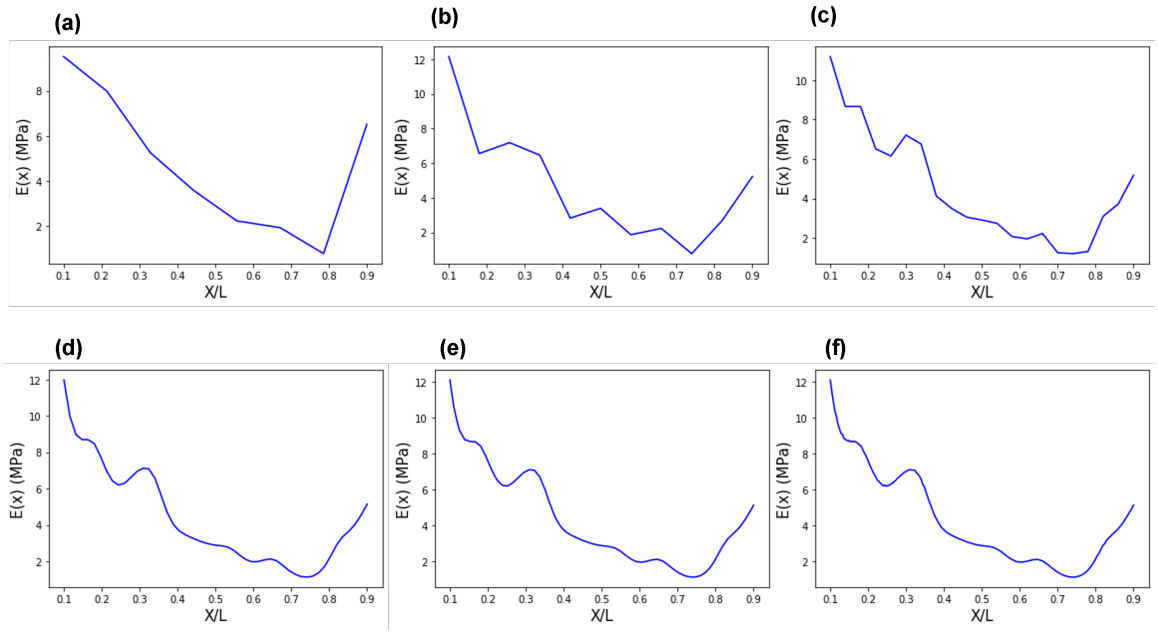

Figure 2.10 Distribution for predicted E(x) using Equation (2.19) with (a) $N_e = 7$, $N_d = 162$, (b) $N_e = 10$, $N_d = 114$, (c) $N_e = 20$, $N_d = 57$, (d) $N_e = 50$, $N_d = 23$ (e) $N_e = 200$, $N_d = 6$, and (f) N_e =400, $N_d = 3$ (specimen length, L = 9.18 mm)

Since higher discretization is preferred to reconstruct any variations in modulus, the material property identification is initiated with $N_e = 7$, $N_d = 162$, followed by increases in N_e while selecting the maximum N_d available. Progress towards convergence in the predicted moduli for the elastic range is shown in Figure 2.10. The predicted elastic moduli for three different load levels within the elastic range using 50 elements are shown in Figure 2.11, along with the independently estimated modulus distribution in Alexander, Gunnarsson, Rafaels, and Weerasooriya (2020). The material properties for the bone sample are obtained using only the Petrov-Galerkin method.[4]

As shown in Figure 2.11, the elastic modulus predicted using the three load levels are nearly the same, indicating the presence of elastic behavior within the load levels considered. In addition, the predictions in this study are in good agreement with

[4]Similar results are obtained using Bubnov-Galerkin method. The similarity in both methods is due to the data smoothing as a result of the averaging process explained in section 2.4.

previous estimates obtained by Alexander, Gunnarsson, Rafaels, and Weerasooriya (2020).

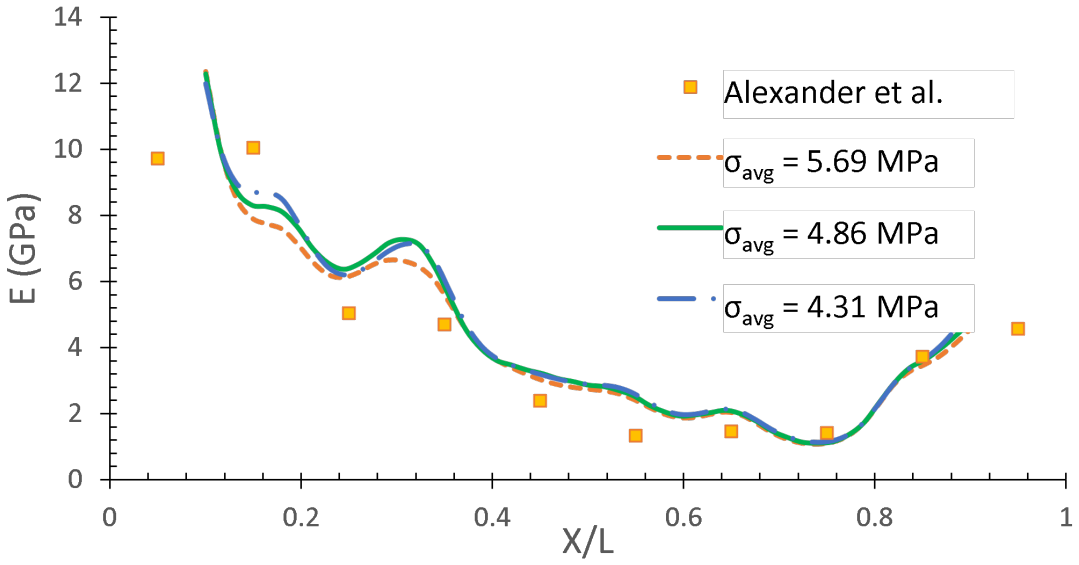

Figure 2.11 Elastic modulus predicted with using inverse method for three different load levels within elastic limit (50 elements were used in the inverse analysis) along with the result from Alexander, Gunnarsson, Rafaels, and Weerasooriya (2020)

2.4.2 Prediction of Secant Modulus Distributions

For monotonically increasing loading beyond the linear elastic region, Equation (2.19) is used incrementally to determine local secant modulus and its evolution with increasing stress. Following the procedures described previously, authors performed additional 1D material property identification procedure for higher loads to determine evolution of the local secant modulus. Figure 2.12 presents the modulus distributions obtained using Equation (2.19) for (a) a linear elastic case with $\sigma = 5.69$ MPa and (b) local secant modulus, E_S, through incremental analysis for stresses beyond the linear elastic range. Inspection of the results in Figure 2.12 highlights a reduction in E_s with increasing stress that is indicative of softening behavior in the bone material.

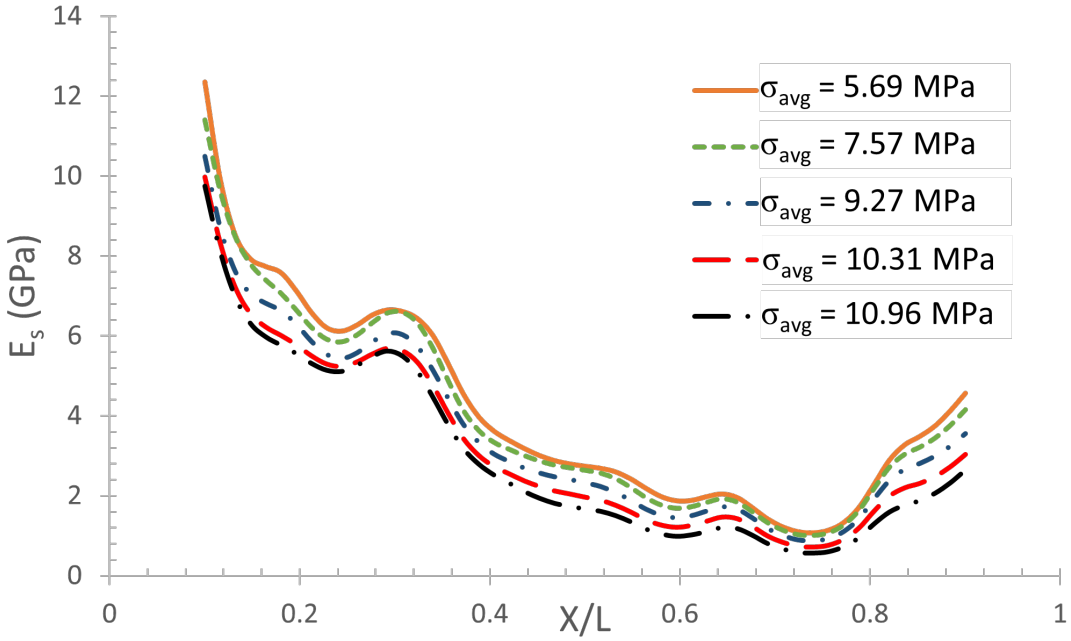

Figure 2.12 Predicted axial modulus distributions using Equation (2.19) for (a) E(x) in linear elastic case with $\sigma = 5.69$ MPa and (b) incremental analysis to obtain secant modulus, $E_S(x)$, for applied stresses beyond the linear elastic range

2.4.3 Reconstruction of local stress-strain response

The distributions E(x) and E_S(x) can be used to estimate local slopes of stress-strain data and then used to reconstruct σ_{avg} vs. ϵ_{avg} response of the bone material. Figure 2.13 shows the reconstructed σ_{avg} vs. ϵ_{avg} response of the bone material for four locations along the length of the specimen. The stress strain relationship shows difference in elastic modulus, yield point and hardening parameters at different sample locations. Model capability for calculating the constitutive relationship is illustrated in Figure 2.13.

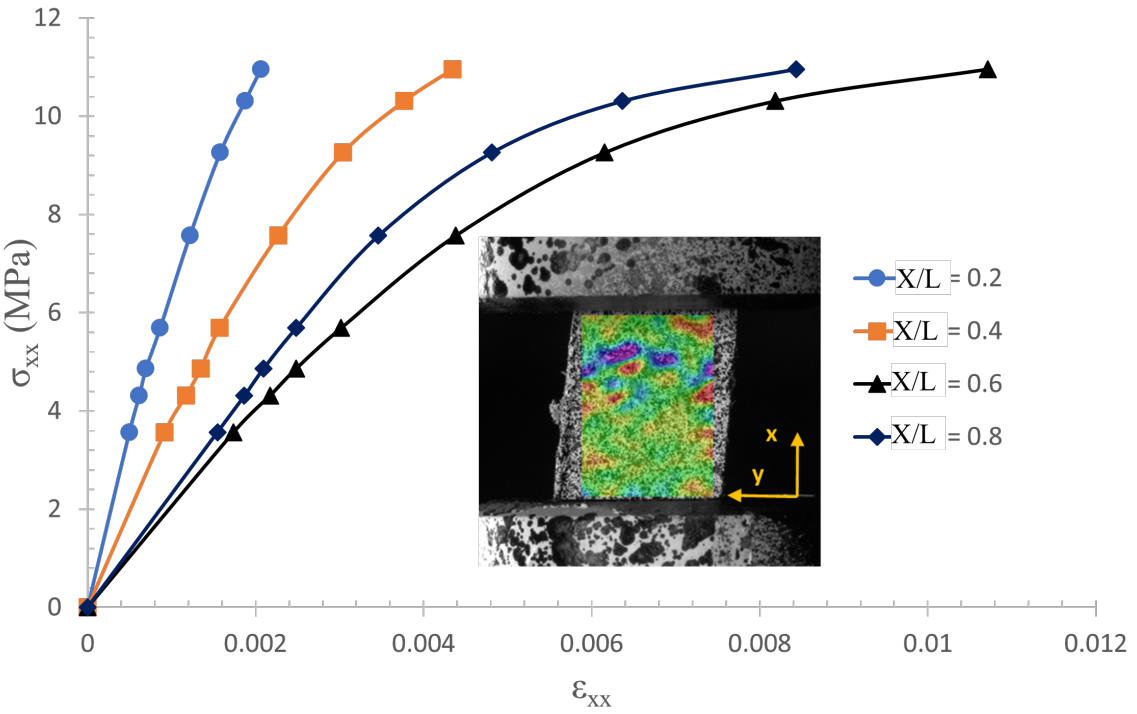

Figure 2.13 Reconstructed σ_{xx} vs. ϵ_{xx}(x) response of the bone material at (a) x= 1.84 mm, (b) x = 3.68 mm, (c) x = 5.52 mm and (d) x = 7.36 mm along vertical x-axis (L = 9.18 mm)

2.5 DISCUSSION OF RESULTS

The current finite element model uses small strain assumptions in the derivation (i.e., $\epsilon_{axial} \approx du/dx$). Thus, the approach is nominally limited to maximum strains on the order of 0.10, which is almost always the case when considering elastic response of a material. If this is a concern, the model could be modified to include the effects of larger strains. Another option would be to perform the analyses incrementally, with each increment of strain meeting the current model's strain requirements. To utilize the latter approach, the experiment should be performed in a way that provides sufficient strain data for each increment to ensure convergence in the 1D material property identification procedure. Using an incremental approach to extend the range of applicability of Equation (2.19) is reasonable for simple applications such as uniaxial compression or tension where the total strain vs. average stress are

the quantities of interest. For applications where (a) the stress state and boundary conditions are more complex (e.g., plane stress or plane strain) and (b) multiple material parameters are to be determined, the methodology will require extension, which is part of ongoing studies. When the small strain assumptions are valid, the method outlined in this work is readily extended for nonlinear stress stain relationship using the incremental approach, provided that loading is divided into multiple small increments where the strain increments beyond the elastic limit are selected to capture gradients in the stress strain curve (e.g., at the linear-non-linear transition). For the case of large strain, additional steps need to be performed to account for the change in geometry of the sample (area of cross section and node position). These approaches are directly related to the methods implemented in incremental plasticity and updated Lagrangian solutions.

2.6 CONCLUSIONS

A direct approach based on Petrov-Galerkin finite element principles is demonstrated to obtain the spatial distribution of Young's modulus, E(x), for 1D problems. Results using the 1D material property identification procedure with known spatial distributions of E(x) and axial strain measurements with additive Gaussian noise, β_ϵ, confirm that the methodology converges to the correct E(x) solution for various combinations of experimental data density(N_d) and levels of discretization (N_e). Application of the method to determine E(x) for a heterogeneous bone sample by using a dense set of experimentally obtained axial strain data using 2D-DIC or 3D-DIC measurements indicates the predicted distribution is in very good agreement with independently estimated measurements, providing additional confidence in the approach. Finally, an incremental approach is demonstrated to successfully extend the approach into the nonlinear regime and determine the secant modulus distribution, $E_S(x)$, at multiple load levels. The measured $E_S(x)$ is used to determine the local

stress strain response of the heterogeneous bone material at four distinct locations.

Chapter 3

EXPERIMENTAL INVESTIGATION OF PREPREG SLIT TAPE DEFECTS

An experimental investigation of out-of-plane wrinkle formation and in-plane deformations occurring in prepreg slit tape during automated fiber placement (AFP) and adherence of tows to a composite substrate is presented in this chapter. The AFP process is conducted on 6.35 mm wide individual tows that are placed along a straight path and steered along circular paths with radii of curvature, $R = 2540$ mm, 1270 mm, and 305 mm. Full-field shape, displacement and strain measurements are obtained using StereoDIC in three successive stages of the AFP process; (i) immediately after lay-up of the tow, (ii) one hour after lay-up and (iii) after reheating the specimen by traversing the AFP head close to the tow path and exposing the specimen to the same levels of IR radiation as employed during the initial lay-up (without compaction pressure). Measurements obtained after the initial tow layup show that (a) tows steered with $R = 2540$ mm and $R = 1270$ mm showed no evidence of significant out-of-plane wrinkling after placement, (b) tows steered with $R = 305$ mm incurred significant localized wrinkling along the compression side of the tow, with a consistent spacing between the localized wrinkles. Increases in wrinkle amplitude are observed for stages (ii) and (iii), indicating both time and temperature dependence of the deformations incurred in an as-placed tow.

3.1 INTRODUCTION

The common types of defects found in the steered tows are (a) out-of-plane wrinkling, (b) localized delamination from the substrate, (c) splitting of tows due to in-plane shear and (d) in-plane buckling (Abdi, Gürdal, and Huang 2017; Rajan et al. 2019b). Thus, identifying the ideal combination of heating and local pressure applied during AFP of tows steered along curvilinear paths is essential to increase adhesive strength and maximize quality of the as-placed tows so that the manufactured component will have optimal strength and fatigue life. Defining the "critical tow path" as curvilinear line along which a tow can be steered without incurring measurable localized out-of-plane wrinkling or related defects, it is essential that the minimum steering radius (R_c) for the critical tow path (Khani, Abdalla, and Gürdal 2015) be determined.

In this regard, various measurement and modeling techniques have been developed in recent years to identify the optimum process parameters and R_c for reducing the number of defects in the AFP steered laminates. Recently Oromiehie, Gangadhara Prusty, Compston, and Rajan (2017) used two fiber Bragg grating (FBG) sensors placed at an angle to each other (15°) between the 2^{nd} and 3^{rd} plies to measure in-situ temperature and strain during the AFP process. The FBG can also act as a structural health monitoring system (SHM) to detect the effect of flaws while providing strain and temperature measurements. The authors also show that acoustic emission due to the onset of local flaw growth can be detected by an FPG. The authors obtained temperature and strain data for a CF/PEEK composite (10 plies) during placement of fourth ply to tenth ply. However, validation of the accuracy of such measurements has yet to be completed. Furthermore placement of sensors can have an adverse effect on the adhesion of the tow to the surface.

Matveev, Schubel, Long, and Jones (2016) formulated a closed form solution to model wrinkle formation in steered tows with different R. The analytical expression

is based on elastic buckling of an orthotropic plate on an elastic foundation. An approximate solution to the wrinkle formation is obtained by using the Raleigh-Ritz method. The authors also obtained an expression for R_c. The tack stiffness is shown to have the largest effect on wrinkle formation and an increase in temperature during lay-up process can significantly increase tackiness. Beakou, Cano, Le Cam, and Verney (2011) published similar work in which the authors developed an approximate solution for the response of an orthotropic plate on an elastic foundation to determine the critical buckling load and R_c. The solution is obtained by assuming simply supported boundary conditions on three edges and a free boundary on the edge where wrinkling occurs. The authors also performed sensitivity analysis to show that the most important factors affecting critical buckling load are prepreg tack and tow width. The effect of delamination and viscoelasticity are not considered in either of these analytical models. Furthermore, neither model can predict in-plane wrinkling or other defects. Finally, neither the assumed in-plane load distributions nor the assumed out-of-plane wrinkle shape have been validated experimentally. Comparisons of these model predictions to experimental observations are typically performed through qualitative comparison of model predictions to photographs of the wrinkle shape/defects without direct comparison to quantitative metrics which is an indispensable part of model validation.

Regarding experimental characterization, recent work has been performed (Rajan et al. 2019a) using StereoDIC to quantify the full-field deformations and wrinkles that occur for thermoplastic tows that are steered along curvilinear paths, but not adhered to the substrate. Results from the study show that (a) uplift (wrinkling) occurs on the compressive side of the tow for circular paths with radius of curvature, R, in the range 305 mm $\leq R \leq$ 2540 mm, while the tensile side remains nominally flat on the surface of the planar substrate, (b) the wrinkle mode shape is the same for most specimen widths and various R (the lone exception is the narrowest tow width

(9.5 mm) and the smallest $R = 305$ mm, where the shape flattens near the centerline when the tape rotates by 90° and more), (c) the amplitude of wrinkling increases with increases in R in all but the exceptional case noted above and (d) increasing the temperature of the prepreg tape from 25 °C to 110 °C does not alter the wrinkle shape while increasing the amplitude of wrinkling by up to 10% .

With the exception of these recent studies, there is limited experimental data for the wrinkle shape, wrinkle spacing and full-field deformations in tows that are placed and adhered to a substrate along curvilinear paths. Taking advantage of the developments presented in (Rajan et al. 2019a), the enclosed work focuses on experimental characterization of the shape and deformation of AFP processed tows that are adhered to the substrate. StereoDIC (Helm, McNeill, and Sutton 1996; Sutton, McNeill, Helm, and Chao 2000; Sutton et al. 2017) is employed to obtain full field displacement data on the tow surface during AFP processing to improve our understanding of the mechanisms associated with wrinkling and other forms of defects. To this end, an experimental setup using StereoDIC is developed to investigate wrinkling modes and measure both the shape and deformation of as-placed and adhered tows as a function of tow path steering radii of curvature.

The remainder of this chapter is organized as follows. Section 3.2 describes the experimental process, including details regarding the AFP and the experimental setup employed to obtain deformation and shape measurements during processing. Section 3.3 presents the experimental findings and discussion of the results. Section 3.4 summarizes the findings.

3.2 EXPERIMENTAL SETUP AND PROCEDURES

3.2.1 Stereovision Measurement System

A typical StereoDIC setup consists of a stereo camera pair, mounting frame for the stereo cameras, a calibration grid, a dedicated computer with digital image correlation

software (VIC-3D[1]) and a suitable high contrast speckle pattern on the surface of the tow. Since many of the details regarding the stereovision system used in this study are similar to those described in Rajan et al. (2019a), a brief summary of the key camera and lens parameters used in this work is given in Table 3.1. As noted in Rajan et al. (2019a), linear polarizing filters for both the LED light and the camera lenses are required for these studies since it is not possible to coat the specimen surface and remove reflections; additional coatings applied to the tow (e.g. paint) altered the mechanical response of the flexible tow. The linear polarizers are adjusted to remove strong reflections from the images and provide a high contrast pattern with minimal reflectivity. Next, to obtain a white speckle pattern that could withstand the wear and elevated temperature conditions associated with the AFP process, two pattern application methods are evaluated. First, a fine spray of high temperature white flat paint (stable up to 700 °C) is applied to form a speckle pattern on the tow surface. The natural black background on the tow surface with the white dots of spray paint gave good contrast on the black tow surface. In the second approach, white airbrush paint is applied with an airbrush system to create a speckle pattern. Both speckle patterns are evaluated for resistance to abrasion due to friction between the compaction roller and other contact areas in the tow feed and guidance system inside the AFP head. Both the high temperature paint and the airbrush paint are observed to give similar abrasion and temperature resistance at the maximum temperature that occurs during the automated fiber placement process. Thus, both methods could be used effectively.

In this study, the maximum temperature of the tow during placement was in the range of 40 °C to 50 °C and airbrush paint was found be stable in this range. Since the authors found better control of the speckle pattern size using the airbrush process, all speckle patterns used in this work are applied using an airbrush. By

[1]Correlated Solutions – VIC-3D v8 http://correlatedsolutions.com/vic-3d/

Table 3.1 Camera and lens parameters of stereovision system for shape and deformation measurement of prepreg slit tape during AFP process

	Camera and lens parameters
Camera	5 MP CMOS PointGrey camera, 2448 x 2048 pixels^2 array, 3.45 µm pixel size
Calibration	12 x 9 dot grid, 5 mm dot diameter, 1.5 mm dot spacing
Lens	Nikon Micro-Nikkor with 25 mm focal length
Lens Filter	Linear polarizer
Light Source	LED with linear polarizing film
Lens Distortion	3rd Order Radial Distortion Correction

varying the size of the airbrush needle, the average speckle size is adjustable for a given application. The StereoDIC parameters selected for this work are shown in Table 3.2. An estimate for the accuracy of the strain measurements using StereoDIC is obtained by performing image correlation of multiple speckle images taken in the reference configuration. Results confirm that the standard deviation in the strain measurements for the parameters shown in Table 3.2 is about 150 $\mu\varepsilon$. Finally, the calibration process followed the general procedure outlined in Rajan et al. (2019a), though the calibration target used in these studies had different physical dimensions[2].

Table 3.2 StereoDIC parameters for AFP experiments

	StereoDIC parameters
Subset size	25 x 25 pixels^2
Step size	7 pixels
Strain filter type	Center-weighted Gaussian filter
Strain Filter size	5x5 data points (area of 35 x 35 pixels^2)
Strain measure	Lagrangian large strain tensor
Field of view	114 mm x 95 mm
Magnification	0.045 mm/pixel
Average speckle size	0.15 mm

[2]The calibration target dot size and spacing are given in Table 3.1

3.2.2 Data Stitching for AFP Experiments

In order to characterize the full-field behavior of a 6.35 mm wide by 610 mm long tow undergoing AFP processing, it is necessary to use relatively high magnification imaging to obtain accurate deformations across the width of the tow with available digital cameras, since the field of view is much smaller than the physical length of the tow to obtain the required measurement spatial resolution with available 5 MP digital cameras. Thus, multiple high magnification images are obtained along the length of the tow and used to extract deformation data spanning the entire tow width and length. To obtain the required spatial resolution over the complete length and width of the tow, one of two methods can be used; (a) use of several synchronized stereovision systems to obtain deformation measurements along the complete length of the tow or (b) employ a single stereovision system and capture overlapping images of regions along the entire length of the tow by rigidly translating and rotating the system.

For the second method using a single stereo camera pair, the tow remains stationary during the image acquisition process for both the reference (pre-AFP) and deformed (post-AFP) configurations. This is an important requirement for the single camera stereo system, as there is a time lapse between each successive image pairs from one end of the tow to the other end as the stereo camera pair is translated along the tow length. If the pre-AFP and post-AFP tow lengths continue to move and are not stationary, the first method (Multiview stereo system) should be used. In this work, it is observed that the tow remained stationary in the reference and deformed configurations for the duration of the image acquisition (30 seconds). Hence the second method (b) is implemented in this work.

As discussed in a recent book by Sutton, Orteu, and Schreier (2009) and demonstrated conclusively in the first known experiment on a commercial jet-liner (Sutton et al. 2017), once a stereovision system is calibrated, then the stereo camera pair can

be moved as a unit without affecting the calibration or measurement accuracy. For this to be true, the relative position of the two cameras in the stereo vision system should be fixed and the internal parameters in both cameras (e.g., focal lengths, distortion correction parameters) should remain the same. To meet these requirements, cameras typically are mounted on a rigid platform to ensure that no relative motion occurs between the two cameras. In order to check whether the cameras remain calibrated, the authors repeated the calibration process after each movement of the stereo system and compared the calibration parameters obtained before and after system movement. Results indicated negligible difference between the parameters for our studies, confirming that initial calibration parameters could be used to extract reliable measurements.

A schematic of the image acquisition method implemented in this work is shown in Figure 3.1. The stereo images are numbered 1 to N, with 1 on the left end and N for the right end of the tow. All the neighboring images are configured to have an overlap of about 20% of the field of view (FOV). The speckle images of the overlap region are used to obtain the rigid body coordinate transformation matrix between the two stereo camera systems and align neighboring image coordinates. Since the only difference between positions in the overlapped region obtained by the stereovision system before and after repositioning is a general rigid body motion, this observation can be used to "stitch together" common regions and extract shape and deformation data from different portions of the tow in a common coordinate system with relatively high spatial resolution. The process outlined above is used to obtain overlapping images for both the reference and deformed configurations of the tow. It is noted that the authors placed markers on the tow surface to assist in identifying the matching image sets in the reference and deformed positions. The white markers added to the tow to assist in identifying corresponding images in the reference and deformed configuration of the tow are larger than a physical camera pixel size and spaced at

an interval of 90 mm.

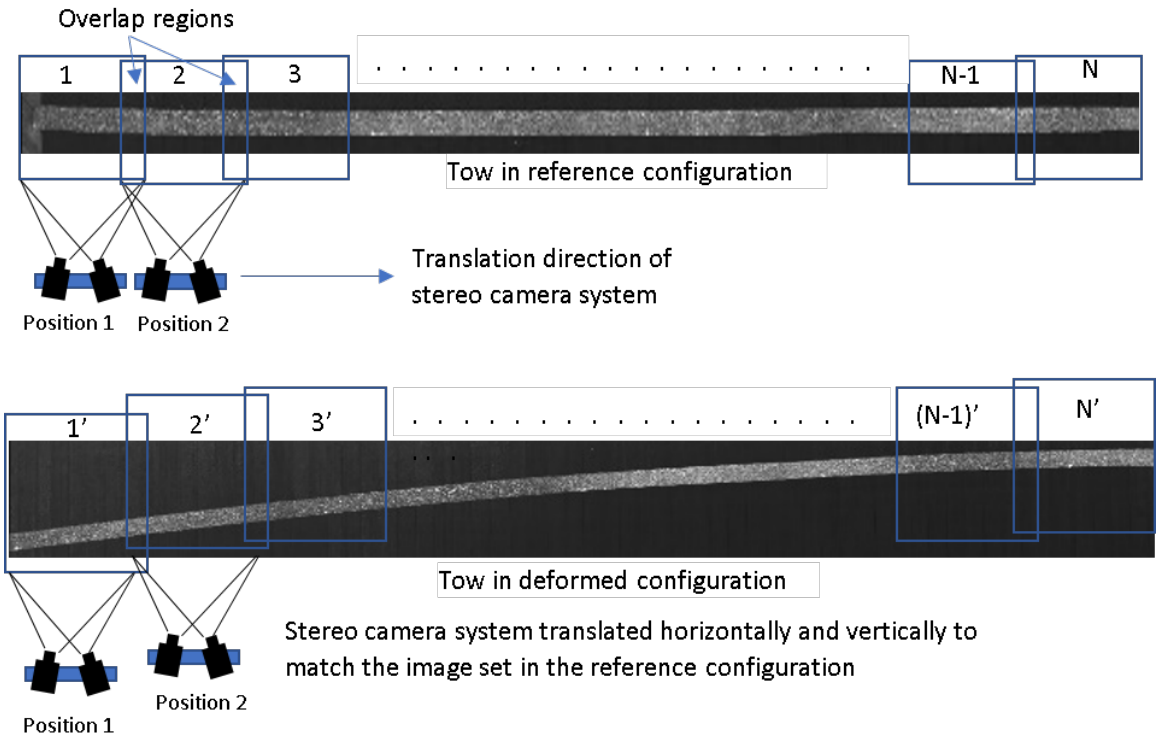

Figure 3.1 Schematic of the image acquisition process

The process outlined in the previous paragraph provides a direct way to obtain the required full-field displacement and strain data along the entire tow length. Straightforward analysis of the imaging process in our studies confirmed that the maximum length of tow that can be imaged while ensuring adequate spatial resolution across the width of the tow is about 114 mm. To obtain deformations along the entire length of the tow, the camera pair is moved as a rigid body approximately 90 mm a total of eight times and images are acquired of adjacent regions with 20% overlap. Post-processing using a stitching process to relate rotated and translated stereo camera coordinate systems is performed using a built-in multiview option in VIC-3D to combine full-field data along the entire length of the tow into a global coordinate system. The general procedure for data stitching is as follows.

- Correlate the speckle images in the matching images sets of reference and de-

formed coordinate system (for example image set 1 and 1' shown in Figure 3.1) to obtain displacement and strain data in the reference image set coordinate system.

- Using the translation vector between the coordinate system and transformation matrix obtained from the overlap region, transform the displacement and strain data from all image sets into the first image set coordinate system. For the 3rd to Nth image sets this involves multiple transformations ($A_{N1} = [A_{21}].[A_{32}]....[A_{N(N-1)}]$ where A_{ij} is the transformation from jth image set coordinate system to ith image set coordinate system).

3.2.3 AFP Lay-up Process and Stereovision Imaging

The prepreg slit tape used for AFP lay-up is a 6.35 mm wide Hexcel IM7G/8552-1 unidirectional prepreg slit tape. A commercial AFP system (Horizontal Lynx© AFP from Ingersoll Machine Tools) in the McNair Aerospace Center at the University of South Carolina is used to perform the fiber placement of tows along predefined paths using an offline program. Four different fiber paths are programmed for lay-up of tows including a straight path and three circular paths with $R = 2540$ mm, 1270 mm and 305 mm. All process variables including lay-up speed (2438 mm/min), temperature (40 °C) and compaction force (200 N) are maintained throughout the layup process. All the tows are placed on a substrate laminate of the same material [90/0/90].

To apply the speckle pattern and capture reference speckle images, tows are manually drawn from the machine head and straightened with light tension on a flat plate using masking tape (see Figure 3.2). After applying the speckle pattern to the whole length of the tow, slightly overlapping images with FOV of 114 mm x 90 mm spanning the length of the tow are obtained in the reference configuration. Once the entire length of the tow has been speckled and imaged, the tow is rewound onto the spool in preparation for AFP processing. For each tow path, speckle images spanning

the entire length of the tow are captured just after the tow is placed on the substrate. For investigating the influence of time and the effect of heating during the placement of neighboring tows on the already placed tow, the process is repeated to capture additional set of images (a) one hour after placement and (b) after re-heating of the as-placed tow by exposing the specimen to the same levels of heating as employed during the initial lay-up without mechanical loading. Reheating was performed immediately after measurement in (a) and DIC measurement on the reheated tow was completed within 30 seconds. Heating is performed using the IR heating element of the AFP system, which is brought very close to the steered tow (within 38 mm) as it is traversed along the length of the tow at 2438 mm/min.

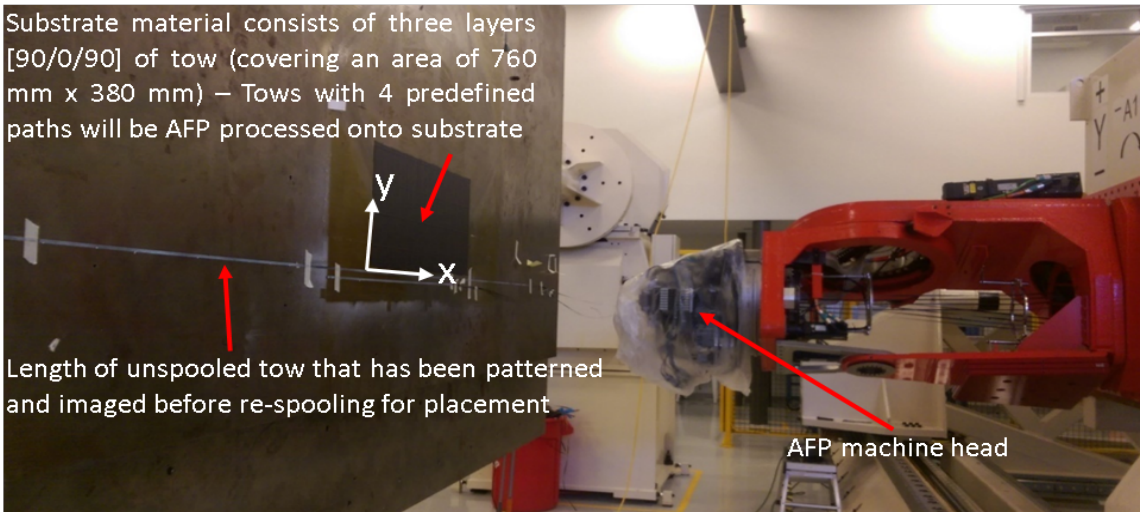

Figure 3.2 Photograph of the tool, substrate, AFP head and initial length of patterned, unspooled tow that is imaged before respooling

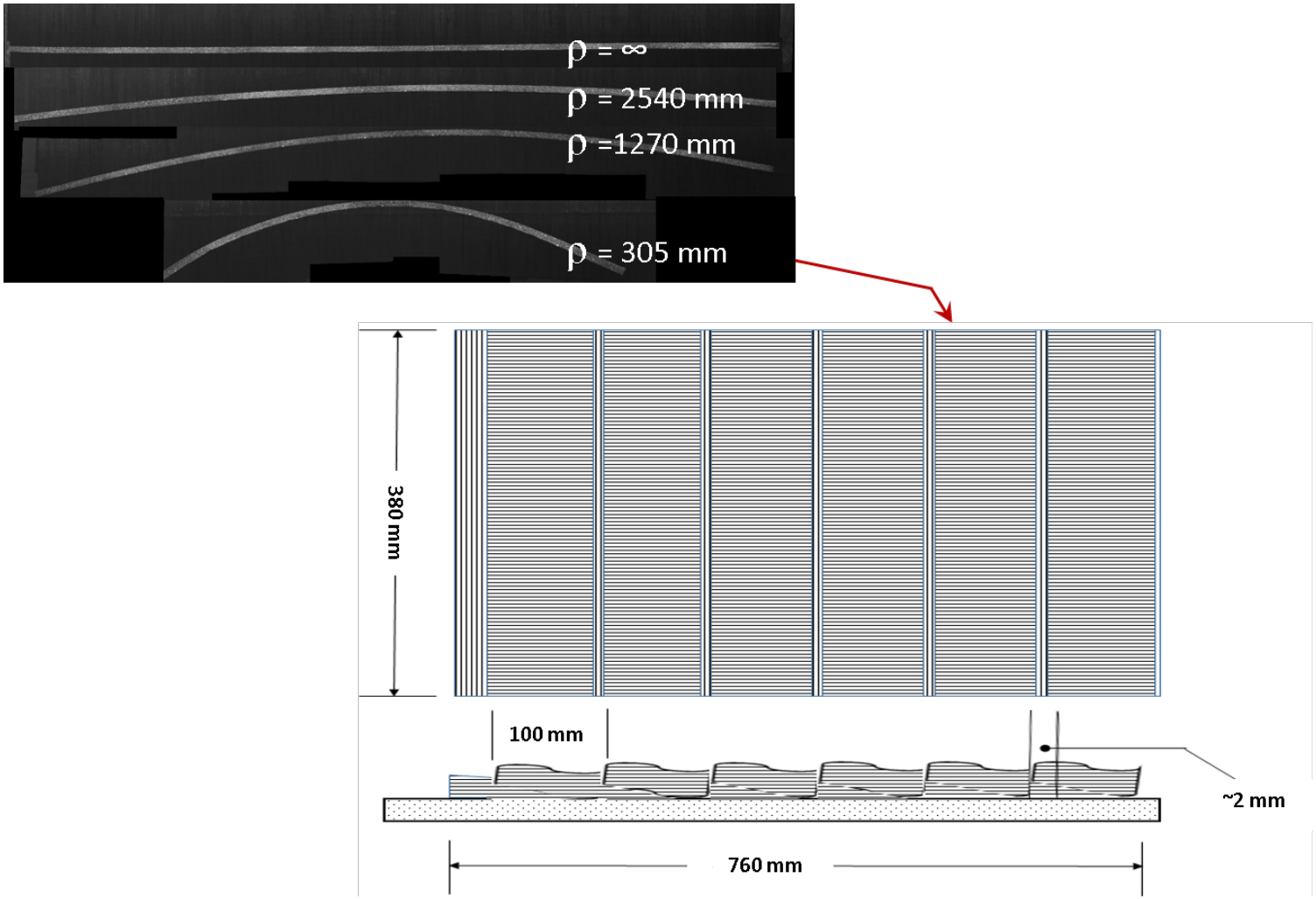

Figure 3.3 Speckle images of four different tow paths; INSET shows geometry of as-fabricated composite substrate for AFP of tows (Overlap of the substrate tows occurs every 100 mm in horizontal direction, resulting in periodic "defects" in tow substrate)

Figure 3.3 shows images of the four tows after undergoing AFP along a straight path and along circular arcs with $R = 2540$ mm, 1270 mm and 305 mm. To combine the data obtained from multiple images for each tow path and experimental condition, the stepwise shifting procedure outlined in Section 3.2.2 is performed. Each set of deformed images is compared with the reference (un-deformed) image set to obtain the shape and out-of-plane deformations of the tow. For all experimental results reported in the remainder of the article, analysis of the speckle images is performed using commercial DIC software, VIC-3D, with the StereoDIC parameters shown in Table 3.2.

3.3 EXPERIMENTAL RESULTS

3.3.1 Out-of-plane wrinkle shape after AFP lay-up along straight path

The deformed shape of the entire tow length along the straight path defined in Figure 3.3 is shown in Figure 3.4a, a magnified view of the deformed shape for 100 mm length of the tow is shown in Figure 3.4b and magnitude of the out-of-plane displacement for the entire length of the tow is shown in Figure 3.4c. As shown in Figure 3.4c, there is a clearly visible, regular, repeating pattern of out-of-plane wrinkling located every 100 mm along the length. Further investigation of this surface profile confirms that these local variations in the shape of the straight tow are due to the presence of gaps and overlaps in the as-manufactured laminate substrate[3] shown in Figure 3.3. Thus, the observed local out-of-plane wrinkle for the straight tow shown in Figure 3.4 reflect the structure of the substrate and are not indicative of wrinkling due solely to deformation of the tow during placement.

[3]The laminate substrate is fabricated by placing sixteen, 6.35 mm tows side-by-side in one pass using the AFP system and then repeating this process by moving the AFP head in a raster pattern

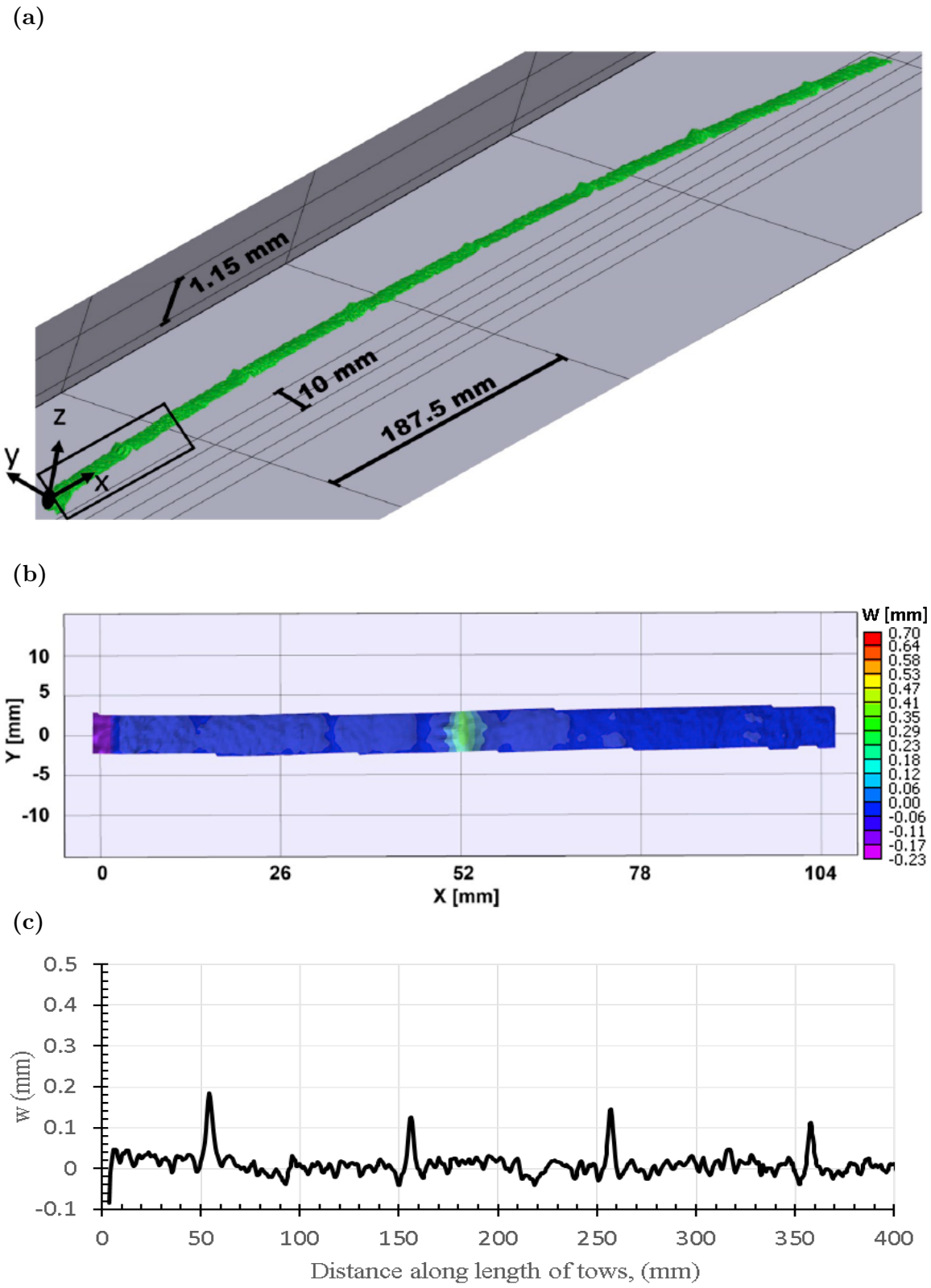

Figure 3.4 Tow placed along straight path showing (a) shape of the tow (b) out-of-plane displacement in the region highlighted by rectangular box and (c) displacements along a line 1 mm above the bottom edge

3.3.2 Out-of-plane wrinkle shape after AFP lay-up along three curved paths

Figures 3.5, 3.6 and 3.7 show the shape of the tows steered along circular paths with $R = 2540$ mm, 1270 mm and 305 mm, respectively. Comparison of the out-of-plane displacements along the length of tows for $R = \infty$, 2540 mm, 1270 mm and 305 mm are shown in Figure 3.8. As shown in Figure 3.8, all four tows experienced local wrinkling at the four locations where laminate substrate defects are present. Thus, the relatively small laminate substrate imperfections, on the order of the tow thickness of 0.100 mm, act as nucleation cites for local wrinkling in all cases.

Inspection of Figure 3.8 shows that for $R = 2540$ mm and 1270 mm, to a reasonable approximation, other than the wrinkles due to imperfections in the substrate, there are no large wrinkles in the tow after placement for either case. However for $R = 1270$ mm there are several small amplitude local wrinkle initiation sites (wrinkle height <0.080 mm). Since the amplitude is much larger than the StereoDIC measurement variability for w(x,y,z) of 0.006 mm, these smaller, separate wrinkles are not entirely noise in the data but appear to be due to a combination of substrate surface variations and initiation of tow wrinkling due to local conditions including tow deformation. For the smallest radius of curvature, $R = 305$ mm, there is a remarkable difference in the wrinkle amplitude and frequency. Here, the number and amplitude of new local wrinkles that are not due to substrate defects have increased significantly. Magnified views of the interaction of the local substrate imperfections and the deformation of the tow for $R = 305$ mm are shown in Figure 3.9.

Defining the measured distance between the peaks of adjacent wrinkles as the wavelength, λ, and the width of the wrinkle as l_w, Table 3.3 presents the average value and standard deviation of λ and l_w for $R = 2540$ mm, 1270 mm and 305 mm. Here, it is shown that as R decreases from 1270 mm to 305 mm, the mean value of wrinkle wavelength decreases by 1.5X. For wrinkles formed at substrate overlap

Table 3.3 Average wavelength (λ), width (l_w) and amplitude (w) of wrinkles for different radii of curvature

R (mm)	λ (mm)	l_w (mm)	w (mm)	Wrinkle location
∞	100.10 ± 0.63	6.62 ± 0.97	0.136 ± 0.033	Substrate overlaps only
2540	101.14 ± 0.66	6.02 ± 1.61	0.172 ± 0.045	Substrate overlaps only
1270	102.09 ± 0.61	7.80 ± 1.45	0.296 ± 0.145	Substrate overlaps only
305	21.30 ± 12.93	8.03 ± 1.77	0.488 ± 0.308	Distributed
305	15.55 ± 7.14	7.26 ± 2.32	0.504 ± 0.324	Distributed*

* Second set of data for tow lay-up on a substrate with reduced overlaps and gaps

locations, the amplitude increases by 2X and the wrinkle width increases by 1.16X. For wrinkles formed outside the substrate overlap regions, as R decreases from 1270 mm to 305 mm there is an order of magnitude increase in the amplitude and width of the wrinkles. With regard to λ, as shown in Table 3.3 there is relatively consistent l_w for $R = 1270$ mm, and much wider variability in l_w for $R = 305$ mm.

The experimental results indicate that high radii of curvature provide results that are nominally consistent with previous theoretical model predictions (Beakou, Cano, Le Cam, and Verney 2011; Matveev, Schubel, Long, and Jones 2016) whereas lower radii of curvature show much more standard deviation in l_w. The low standard deviation and consistency in the l_w for high values of R are nominally consistent with conditions that are used in typical plate/beam on elastic foundation models that are limited to relatively small deformations and displacements. The increased standard deviation in λ for smaller R indicates that additional nonlinearities are present in the mechanics of wrinkle formation that are not included in these models. Variability in the wavelength of wrinkles is also reported in Bakhshi and Hojjati (2018), where the authors placed 6.35 mm tows along curvilinear paths with R in the range of 558.8 mm to 2032 mm with wrinkles observed for $R = 558.8$ mm and 635 mm.

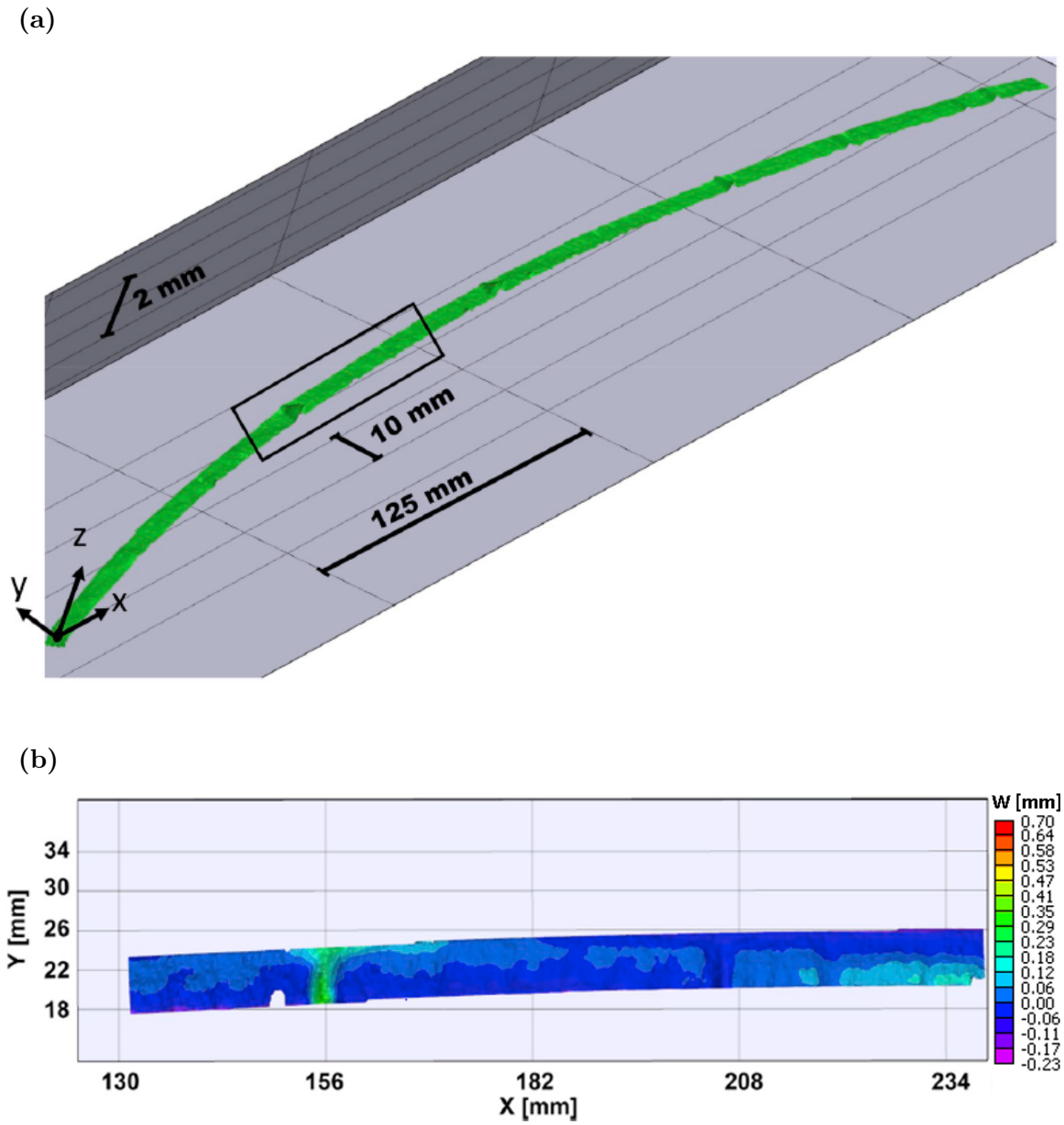

Figure 3.5 Tow placed along a circular path with $R = 2540$ mm showing (a) shape of the entire length of the tow and (b) deformation map in the region highlighted by rectangular box

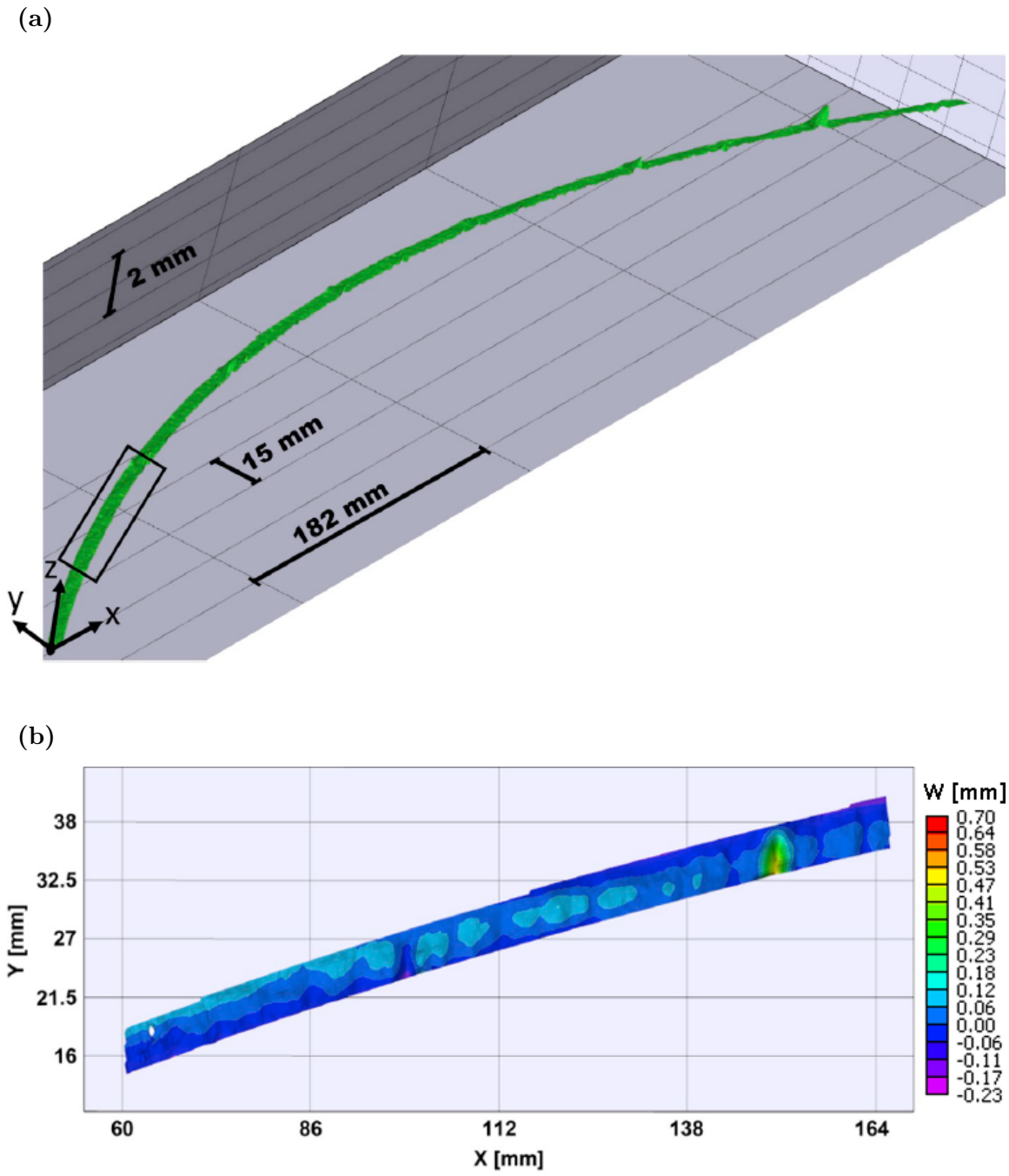

Figure 3.6 Tow placed along a circular path with $R = 1270$ mm showing (a) shape of the entire length of the tow and (b) deformation map in the region highlighted by rectangular box

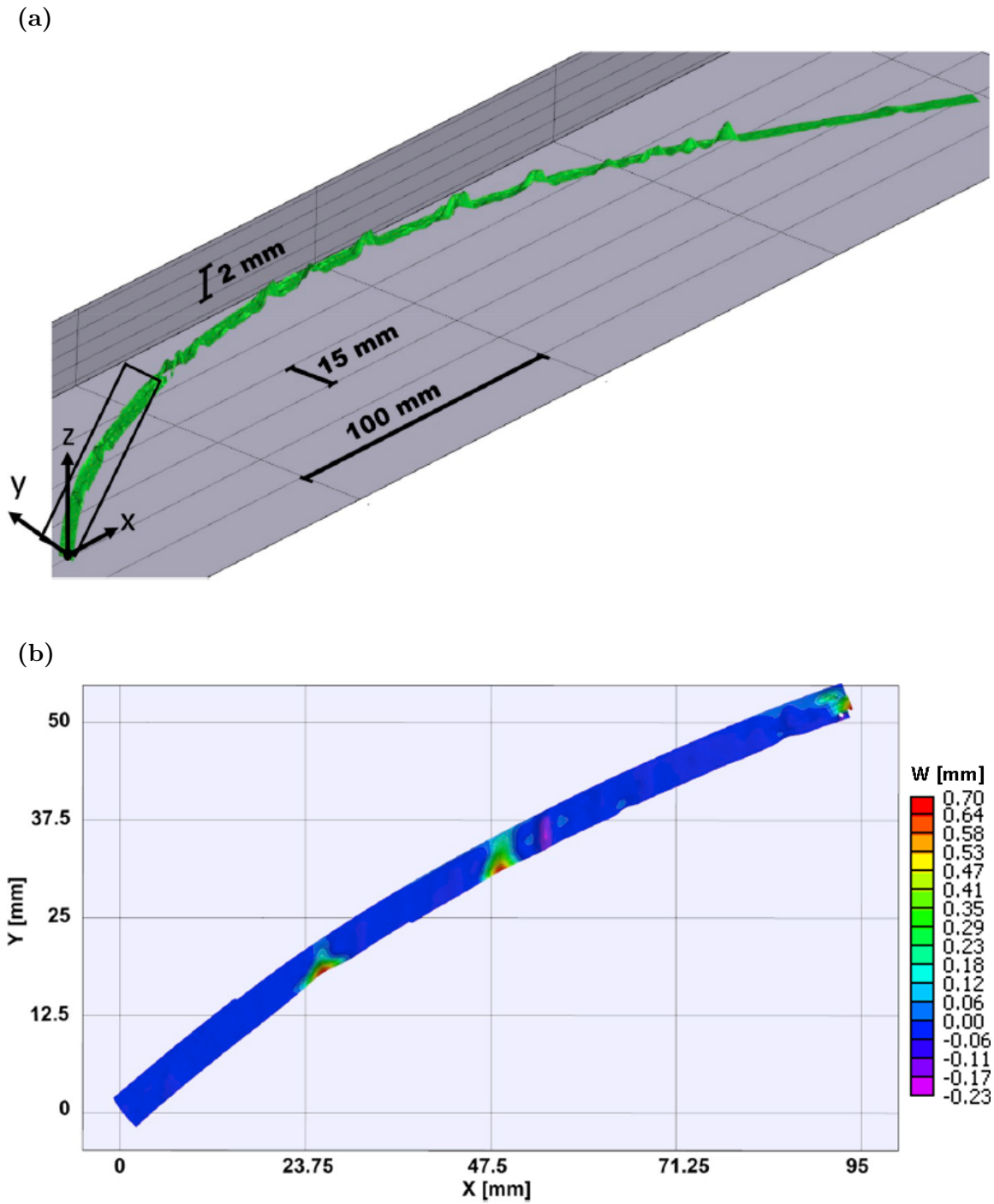

Figure 3.7 Tow placed along a circular path with $R = 305$ mm showing (a) shape of the entire length of the tow and (b) deformation map in the region highlighted by rectangular box

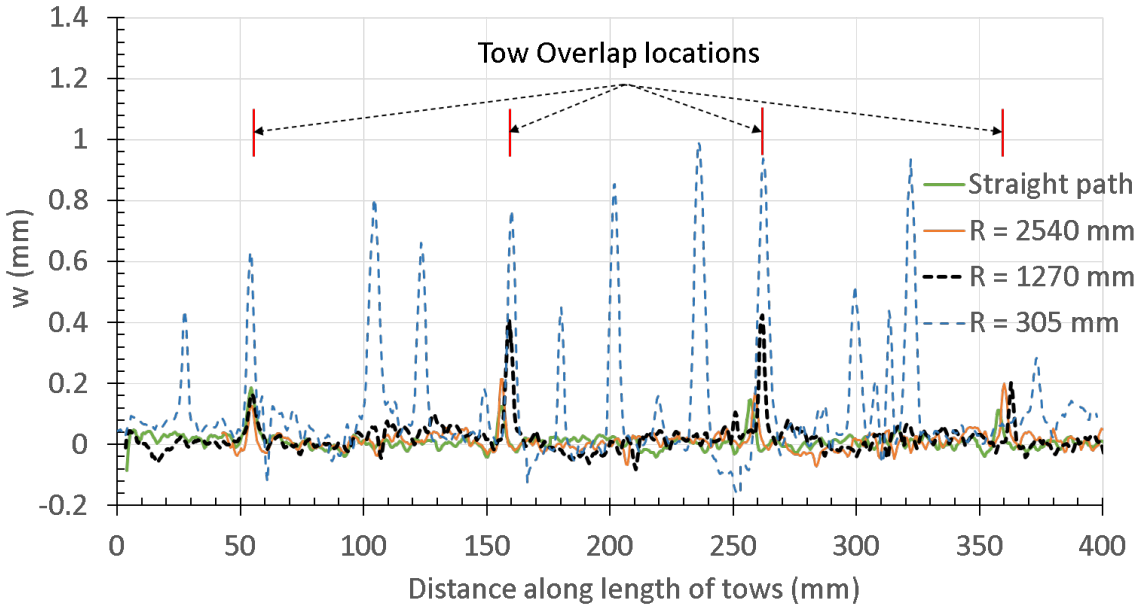

Figure 3.8 Comparison of out-of-plane deformation along the length of tows placed with $R = \infty$, 2540 mm, 1270 mm and 305 mm (plot corresponds to displacements along a line that is 1 mm above the bottom edge of the tow in the reference configuration)

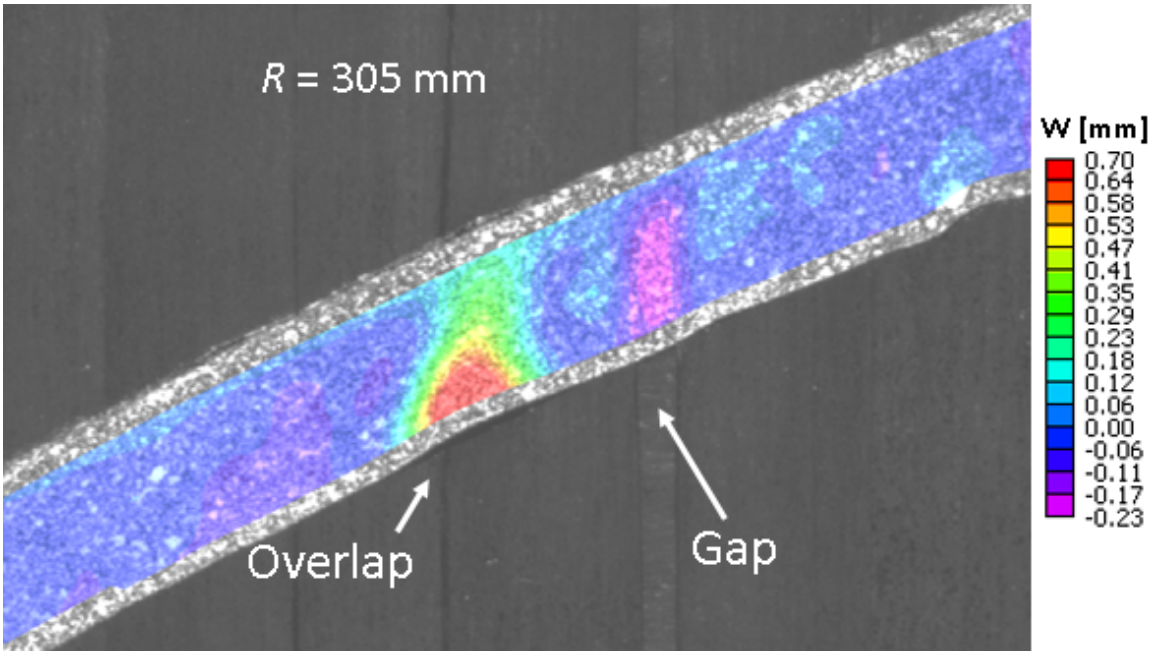

Figure 3.9 Effect of gap and overlap in the substrate on the deformation for tow placed with $R = 305$ mm

3.3.3 Time and temperature effect on the wrinkled shape

In order to investigate viscoelastic effects of the tow, a separate experiment is carried out for a tow that is placed at $R = 305$ mm. The substrate imperfections due to overlap and gaps are minimized in this lay-up process by improving the substrate quality. This reduced variability in the wrinkle wavelength compared to the previous experiment (see Table 3.3). Figure 3.10 shows the out-of-plane displacement field for a magnified region of the tow that has been steered with $R = 305$ mm at three specific stages. The in-plane coordinates shown in each figure correspond to the reference material directions for the tow prior to placement. Figure 3.10a shows the stage one conditions where the out-of-plane displacement data is obtained immediately after lay-up of the tow. Figure 3.10b shows the out-of-plane displacement data obtained one hour after lay-up. Measurements in Figure 3.10c are obtained just after re-heating of the tow occurred when the AFP heat source passed by close to the tow path. To simplify comparison of the data shown in Figure 3.10, results for the complete length of the tow along a horizontal line located 1 mm above the lower tow edge on the compressive side of the tow are shown in Figure 3.11.

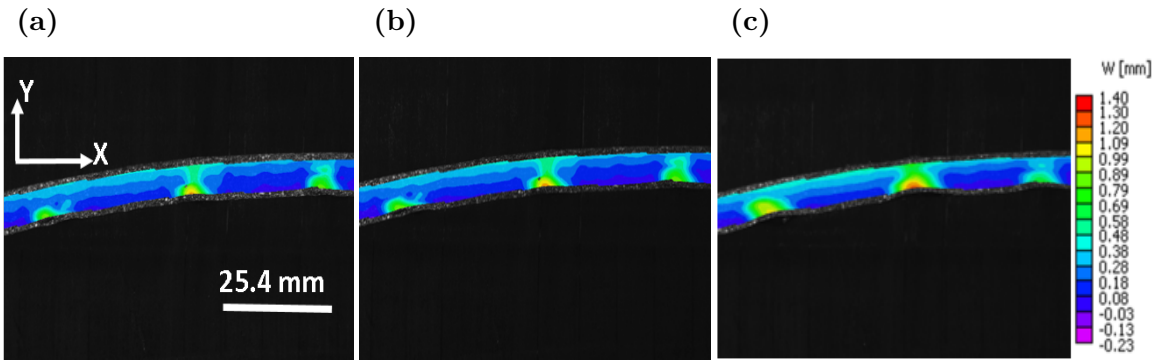

Figure 3.10 Out-of-plane deformation map of a portion of the tow with $R = 305$ mm (a)immediately after placement (b) one hour after placement and (c) after applying heating to the tow (the region shown is a subset of the whole length of the tow between 165 mm and 240 mm from the left end in the reference configuration)

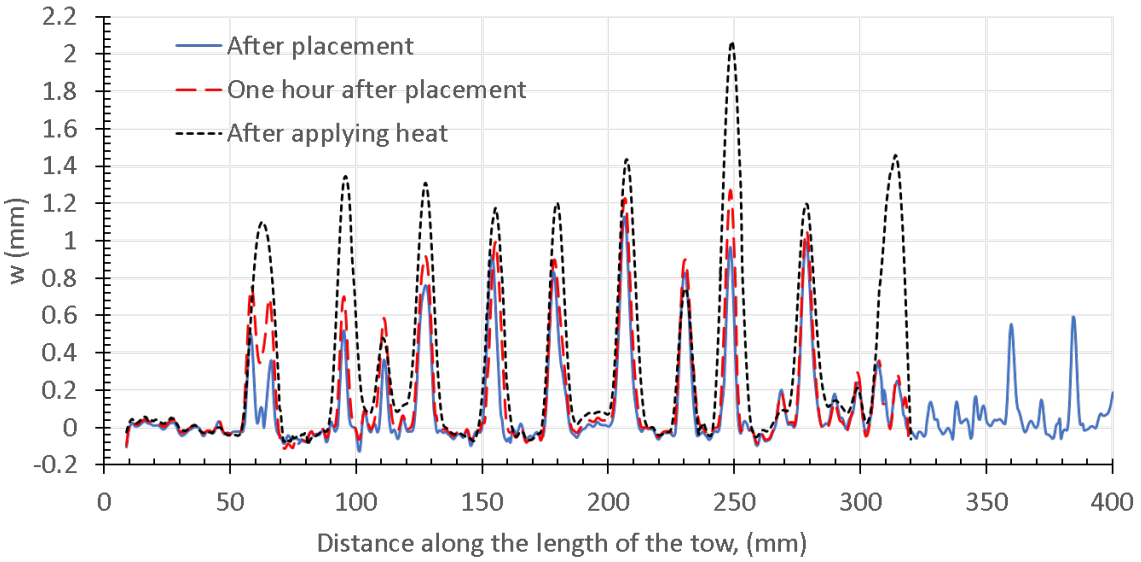

Figure 3.11 Out-of-plane deformation along a line 1 mm above the bottom edge of the reference configuration for $R = 305$ mm (region beyond 320 mm separated from substrate just before one hour so no additional measurements are available)

3.3.4 Deformation of tow after AFP lay-up

The out-of-plane wrinkle shapes for the AFP manufactured tow shows significant differences from the wrinkle shapes of tows when there is no adhesion (Rajan et al. 2019a). When there is no adhesion, it was shown that wrinkling occurs on the compressive side of the tow and only a single wrinkle occurs along the entire length of the tow. When adhesion is present, multiple wrinkles are formed on the compressive side.

If the adhesion is of sufficient strength to prevent uplift on the tensile side of the tow, the relatively inextensible carbon fibers on the tensile side are sufficiently restrained to remain in plane. In this case, the fibers tend to slide transversely towards the neutral surface, reducing the distance between them while minimizing the axial strain in the fibers. The "macroscopic" transverse Lagrangian strain associated with the observed sliding of fibers is shown in Figure 3.12 for $R = 305$ mm.

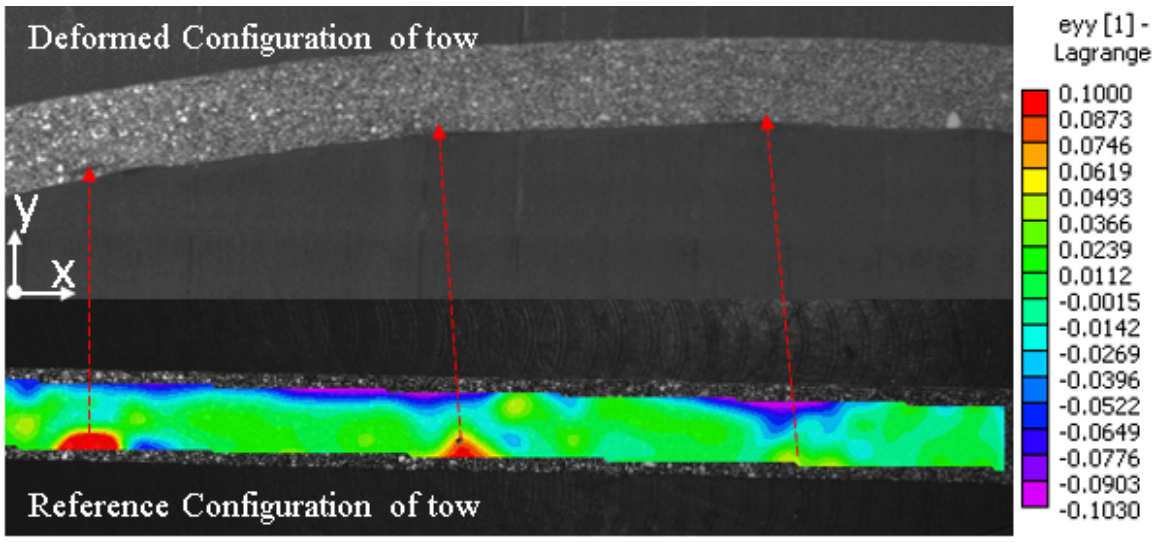

Figure 3.12 Transverse Lagrangian strain map on the surface of the tow immediately after placement with $R = 305$ mm for the region shown in Figure 3.10 (the arrows represent mapping of the material points from the reference to deformed configuration)

3.3.5 Effect of surface defects on wrinkle formation

As noted in section 3.3.2, the wrinkle shapes and wrinkle positions in tows with $R = 305$ mm during the AFP process are much more complex (see Figures 3.7 and 3.9) than the assumed shape used for analytical modeling in the published literature (Beakou, Cano, Le Cam, and Verney 2011; Matveev, Schubel, Long, and Jones 2016), with non-linearities such as the interaction of prepreg tow wrinkling deformation with highly nonlinear cohesive forces between the uncured tow and the laminate substrate contributing to the measured wrinkling response. As shown in the measurements in Figure 3.8, existing surface defects on the substrate act as nucleation sites for local wrinkling of the tow, most likely due to the lack of adhesion between the substrate and the tow at such locations. For smaller R, the substrate-induced wrinkles are supplemented by additional wrinkling sites. When the tow is steered with $R = 305$ mm, eighteen local wrinkle locations are observed over a length of 400 mm of the tow, with an average wavelength of 21.30 mm and a standard deviation in the wavelength of 12.93 mm. The average wavelength observed is nominally consis-

tent with results in (Matveev, Schubel, Long, and Jones 2016). Though quantitative data on the variability in the wavelength is not available in the published literature, photographs of the wrinkle pattern in (Matveev, Schubel, Long, and Jones 2016) indicate a non-uniform spacing of the wrinkles. The presence of variability in the frequency of occurrence of wrinkles also is reported in (Bakhshi and Hojjati 2018).

Results from a second lay-up experiment with reduced substrate overlaps and gaps (see Figure 3.11) show that the number of wrinkles increases (wavelength decreases) and variability in the wrinkle spacing decreases compared to the first lay-up experiment on a substrate with significant overlaps and gaps (see Figure 3.8). In addition, the average amplitude and width of the wrinkles decreases in the second lay-up experiment. A plausible reason for the lower number of wrinkles with increased amplitude and width at substrate overlap locations in the first experiment is that the measured larger l_w values result in additional energy release in these regions and less energy available to initiate new wrinkles.

As shown in Figure 3.11, during the first hour after placement, tow wrinkle amplitude increases as the temperature of the tow reaches ambient levels in the laboratory. After the tow is re-heated without additional mechanical loading, there can be marked changes in the out-of-plane wrinkle shape for the tow. For example two of the adjacent wrinkles between 50 mm and 75 mm from the left end merged into one large wrinkle. These experiments show that time and temperature-dependent properties of the binder material can influence the amplitude and coalescence of adjacent wrinkles, especially when fibers are steered at smaller radii of curvatures. Though the amplitude of the wrinkles increased with time, no new wrinkles are observed to form during the first one hour. In this regard, careful observation of the layup process showed that the wrinkles initiate immediately after the roller pressure is released. Hence, the experimental evidence strongly suggests that the initiation "toughness" for wrinkle formation will not be a function of time.

3.3.6 Additioanl defect types present in the AFP placed tows

Though the primary focus of this work is related to quantifying wrinkling as a function of radius of curvature during AFP, additional commonly observed defects during tow placement include (a) bunching of fibers, (b) folding over of tows during placement and (c) crack formation/matrix failure; Figure 3.13 shows photographs of these defects, with Figure 3.13a showing a severe case of fiber bunching combined with matrix failure. In our definition of fiber bunching, the results in Figure 3.12 for the transverse strain are an indicator that "fiber bunching" is occurring in our experiments. In addition, as shown in Figures 3.13b and 3.13c, tow fold-over and fiber-matrix cracking are also observed in this study. The defects shown in Figures 3.13a and 3.13b are mainly observed in regions of poor adhesion of the tow with the substrate. The separation and crack formation shown in Figure 3.13c are a function of the relatively weak uncured tow matrix and the presence of modest transverse tensile strains on the side closer to the inner radius. Another form of defect, in-plane wrinkling, is reported in Bakhshi and Hojjati (2018). However, for the selected radii of curvature, tow materials and process parameters, our experiments do not show any indication of in-plane wrinkling based on the measured strain or displacement data. One of the reasons for occurrence of in-plane wrinkles in Bakhshi and Hojjati (2018) could be due to the low adhesion of the tow with the aluminum tool, whereas in our layup experiments, the tows were placed on a substrate of the same material. The absence of indications of in-plane wrinkling suggests that this could be caused by higher energy being required to overcome the bonding stresses for inducing in-plane wrinkling (when compared to conditions for out-of-plane wrinkling and other forms of deformation seen in our experiments).

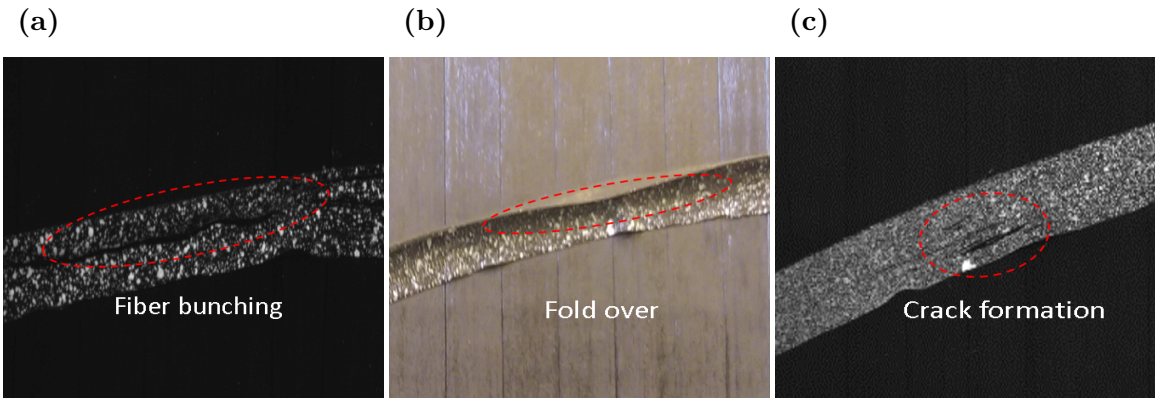

Figure 3.13 Commonly observed defect other than wrinkling in tows steered along curvilinear paths such (a)fiber bunching, (b) fold over and (c) as matrix failure

3.4 CONCLUSIONS

For the first time, an experimental investigation using StereoDIC to obtain in-situ measurements is presented quantifying out-of-plane wrinkle formation and in-plane deformations occurring in prepreg slit tape during automated fiber placement (AFP) and adherence of tows to a composite laminate substrate. The methodology is employed to obtain deformation of 6.35 mm in a thermoset prepreg tow after lay-up using AFP process to understand the effect of steering radius of curvature, R, time and temperature on wrinkle formation. The tow lay-up process is performed for a range of R using an industrial-scale AFP machine (Horizontal Lynx© AFP from Ingersoll Machine Tools), with full field three-dimensional tow shape and surface deformation measurements performed (a) immediately after lay-up of the tow, (b) one hour after lay-up and (c) shortly after applying heating to the already placed tow by traversing the AFP head with infrared heat source close to the tow path. Results from our experimental studies give the following observations.

- Tow wrinkling is observed in all tows at each location where the underlying laminate substrate showed surface defects such as tow overlaps and gaps.
- For straight paths and for a circular path with radius of curvature, $R = 2540$

mm, no additional out-of-plane wrinkles are observed away from the tow overlap locations.

- For circular paths with $R = 1270$ mm and 305 mm, additional wrinkles are observed with mean wavelengths of 30.25 mm and 21.3 mm with standard deviations of 8.89 mm and 12.93 mm, respectively. The amplitudes of the additional out-of-plane wrinkles for $R = 1270$ mm are on the order of the thickness of the tow. However, for $R = 305$ mm, the amplitudes of the wrinkles are an order of magnitude larger.

- For the shortest radius of curvature ($R = 305$ mm), the lay-up process was performed (a) on a substrate having defects (overlaps) at intervals of 100 mm and (b) on a substrate with no defects. For both lay-up trials, the spacing in trial (a) between the additional wrinkles that are not located at substrate defect locations showed large variability; 21.30 mm with a standard deviation of 12.93 mm. For trial (b) that had no surface defects, the mean wavelength is 15.55 mm with a standard deviation of 7.14 mm. The variability in the wavelength of wrinkles cannot be predicted by existing wrinkle models (Beakou, Cano, Le Cam, and Verney 2011; Matveev, Schubel, Long, and Jones 2016) that assumes a uniform spacing.

- During the first hour of lay-up, tow wrinkle amplitude increases to almost twice the amplitude of the wrinkle immediately after placement, apparently due to viscoelastic effects in the prepreg tack. However, the wrinkle mode shapes remain the same.

- After applying heating to the steered tow, wrinkles which are close to each other tend to merge into one large wrinkle, apparently due to considerable loss in stiffness of the cohesive layer between the tow and substrate.

Chapter 4

CHARACTERIZATION OF MODE I AND MODE II TRACTION-SEPARATION LAWS

As part of an effort to predict wrinkling of carbon-fiber tows during automated fiber placement, the cohesive zone traction-separation relations for two carbon fiber epoxy prepreg tows are quantified for Mode I and Mode II loading using a Rigid Double Cantilever Beam (RDCB) specimen. An explicit expression for normal traction versus normal separation (σ vs δ_n) and tangential traction versus tangential separation (τ vs δ_t) are derived using static equilibrium equations for an RDCB considering a compressive zone ahead of the process zone. The traction-separation relationships are in term of quantities that can be measured using a full field measurement technique (StereoDIC). The baseline traction-separation relationships obtained in this work are for conditions representative of those experienced by an uncured tow undergoing automated fiber placement (AFP) onto a substrate of a similar material with layup temperature T = 40 °C, pressure $p = 1$ MPa and contact time $t = 1$ sec. The RDCB is loaded in displacement control at a constant load line displacement rate of 0.3 mm/min. Speckle images for StereoDIC are captured using stereo vision systems equipped for capturing images of the RDCB specimen with a field of view of 100 mm x 75 mm. Analysis of the data obtained for Mode I and Mode II loading shows that the critical Mode I energy release rate $G_{Ic} = 120$ J/m^2 and critical Mode II energy release rate $G_{IIc} = 255$ J/m^2, with the maximum normal traction $\sigma_{max} = 0.50$ MPa and the maximum shear traction $\tau_{max} = 0.35$ MPa.

4.1 INTRODUCTION

In the previous AFP lay-up experiments conducted by Rajan et al. (2019b), it has been observed that "tackiness" of the tow, a term associated with the ability to bond the tow to a substrate, has a major influence on tow wrinkling. Tackiness is generally a function of the material and process parameters (e.g. roller pressure, lay-up temperature, contact time) for pressure sensitive adhesive materials. Delamination of a tow from a substrate to form a wrinkle can occur in three ways; (a) separation within the resin, designated as cohesive separation, (b) separation at the interface between the tow and the substrate, designated as adhesive separation and (c) mixed failure combining regions of cohesive and adhesive separation. Usually adhesive failure is characteristic of low tackiness due to lay-up process parameters such as pressure and temperature.

Of most relevance to the enclosed work are the cohesive zone models (CZMs). Originally introduced in the independent work of Dugdale (1960) and Barenblatt et al. (1962) as an effective way to perform finite element modeling of adhesive fracture, the pioneering work of Needleman (1987) and also Ungsuwarungsri and Knauss (1987) used CZM to describe the process of void nucleation and decohesion in an isotropically hardening, elastic-viscoplastic matrix. The success of CZMs is, in part, due to its effectiveness in modeling nonlinear effects when the process zone size is much larger than geometric dimensions, particularly when the process zone size is much larger than the transverse dimensions of the specimen (Ungsuwarungsri and Knauss 1987). An additional reason for its broad use is the relative ease of implementation in a finite element code, resulting in its inclusion in commercial codes such as ABAQUS.

To employ a CZM model in simulations, the constitutive properties of the adhesive in the form of a traction-separation relationship must be determined. In most of the literature, the nominal stress and separation in the adhesive during a probe-tack experiment (Mohammed, Charalambides, and Kinloch 2016) are related to the

traction-separation relationship for the adhesive layer. For example, in a recent publication Bakhshi and Hojjati (2018) used a CZM to predict the evolution of defects during AFP process with the opening mode cohesive traction-separation parameters determined experimentally using a probe tack test. The authors assumed the same traction-separation relationship for both the normal and in-plane shear directions, though it has been shown in the enclosed work that the shear traction-separation law is significantly different from the normal traction-separation law. Simulations performed by the authors indicated that out-of-plane wrinkling and localized delamination of the tow (blister) would occur, though no quantitative comparison with experimental data was presented.

In recently published experimental work (Rajan et al. 2019b), the authors performed AFP lay-up along circular paths with uncured carbon-epoxy tows manufactured with pressure-sensitive epoxy matrix and adhered to a substrate of the same material. Process parameters included heating the thermoset prepreg tows to 40 °C for several seconds to obtain improved contact and increased adhesion strength. The authors made several observations from their experimental studies, including visual evidence that tows not only separating vertically when a wrinkle occurs but also move horizontally (shear deformation in the tow matrix), especially for smaller radii of curvature. The complex nature of the tow wrinkling mechanism observed in previous work indicates that predicting the onset of out-of-plane wrinkling in an as-placed adherent tow will require quantitative measurement of "tow adherence" to the substrate.

4.1.1 Previous Experimental Methods for Measuring "Tack"

A common approach has been to determine the "tackinesss" of the tow using either a peel test or a probe-tack test. Recently, Crossley, Schubel, and Warrior (2012) developed a 90º peel test fixture to measure the steady-state peel force required to

separate prepreg tapes at different rates of peeling, temperatures and pressures representative of AFP processes. Based on temperature, compaction pressure and peel rate, the authors observed two distinct modes of failures; (a) adhesive failure at the tow-substrate interface, primarily due to poor contact and (b) cohesive failure within the tow resin. The peel resistance during adhesive failure was shown to increase with temperature, whereas an opposite trend was observed for cohesive failure. In their experiments, only a single parameter – the peel force - was used as a measure of "tackiness". Thouless and Yang (2008) showed that peel force is a complex function of the peel geometry, constitutive properties of the peel arm, substrate and interfacial properties. In related work, Wei and Hutchinson (1998) considered plastic dissipation in the peel arm of a rate independent elastic-plastic film bonded to an elastic substrate to derive a relationship connecting the steady-state peel force to cohesive zone traction-separation parameters (critical energy release rate and peak cohesive stress). The authors showed that plastic dissipation in the peel arm is a significant contributor to the macroscopic work of fracture. For the case of a prepreg tow, which is a rate dependent material, it is oftentimes necessary to consider viscoelastic and viscoplastic dissipation in the peel arm due to large deformation of the tow at the peel front. Further, Thouless and Jensen (1992) revealed that mixed mode conditions exist, even in 90^{o} peel tests where the mode mixity depends on the peel arm strain.

The probe-tack test involves bringing a flat-faced cylindrical or spherically shaped probe in contact with the adhesive, holding the compressive force for a short period of time (dwell time) and measuring the force as the probe separates from the adhesive at constant rate. Average stress in the contact area of the probe versus separation is considered to be the traction-separation law. Since deformation of the adhesive in a probe-tack test is not uniform throughout the contact area (Mohammed, Charalambides, and Kinloch 2016), correspondence of nominal stress and separation may not be accurate (Creton and Ciccotti 2016) to determine the traction-separation re-

lationship for CZM. Moreover, the shear traction-separation relationship cannot be obtained from a standard probe tack test.

Several other test geometries, such as scarf joint (Silva, Campilho, Silva, and Carvalho 2018), Brazilian disk (Freed and Banks-Sills 2008) and compact tension/shear specimens have been used for extracting mixed-mode traction-separation laws for different adhesive systems. For example, Liechti and Wu (2001) used a compact tension/shear specimen for extracting rate dependent traction-separation relationships for a rubber metal interface. The authors used a nonlinear viscoelastic model for the rubber. The cohesive layer was modeled using a nonlinear spring in parallel with a Kelvin element. Parameters for their traction-separation law were obtained from these geometries using an inverse method (Gowrishankar, Mei, Liechti, and Huang 2012). The inverse method is an iterative procedure which involves varying the parameters of a finite element (FE) model of the fracture specimen until a satisfactory match of the global response, such as load versus displacement, as well as local deformation response such as crack opening displacement, are consistent with experimental observations. Recently it has been shown for simple beam type geometries, where a closed form solution of the J integral exists, that the traction-separation law can be directly extracted by simultaneous measurement of the J integral and the crack opening displacement (Sørensen and Jacobsen 2003).

4.1.2 Rigid Double Cantilever Beam Experiment for Extracting Traction-Separation Law

The double cantilever beam geometry is a commonly used test method for obtaining traction-separation relationships, in part due to the existence of a closed form solution for the J integral in terms of measurable quantities such as far field load, crack root rotation and elastic properties of the adherends. For example, a simple method for direct extraction of the traction-separation relationship using double

cantilever beam geometry (DCB) is discussed in the pioneering paper by Sørensen and Jacobsen (2003). The direct extraction of the traction-separation relationship involves simultaneous measurement of the crack opening displacement and far field load. The opening displacement is usually measured using a non-contact measurement method such as StereoDIC (Sutton, McNeill, Helm, and Chao 2000; Sutton, Orteu, and Schreier 2009; Sutton 2013; Sutton et al. 2017). The traction-separation relationship can then be extracted by taking the first derivative of the J-integral with respect to the opening displacement (Högberg, Sørensen, and Stigh 2007; Zhu, Liechti, and Ravi-Chandar 2009; Wu, Gowrishankar, Huang, and Liechti 2016; Rajan, Sutton, Fuerte, and Kidane 2018; Gorman and Thouless 2019). The closed form expression for the J integral in these studies assumes that the far end of the beam is stress free. For most structural adhesives, it is relatively easy to satisfy the stress-free condition at the far end of DCB specimen by using a sufficiently long beam. However, when stiff adherends are used with soft adhesives, such as the uncured epoxy used in this work, the dimensions of the adherends (length and height) required for satisfying the far-field stress-free condition become impractical to manufacture for use in a conventional tensile test frame. One solution to this problem is presented in the work of Dastjerdi, Pagano, Kaartinen, McKee, and Barthelat (2012); Dastjerdi, Tan, and Barthelat (2013) where the authors have shown an alternate approach for extraction of normal traction vs separation ($\sigma - \delta_n$) relationship for soft biological adhesives using a rigid double cantilever beam assumption. In their work, the authors assumed the two adherends are rigid in comparison to the response of soft adhesives (i.e., the adherents). They have shown that, using the RDCB analysis, the $\sigma - \delta_n$ relationship can be obtained using simultaneous measurement of the load and load point displacement.

In this chapter, a modified version of the explicit expression for $\sigma - \delta_n$ relationship for an RDCB specimen is derived that includes the effect of a far-field compressive

zone ahead of the crack tip during Mode I loading. The rest of the chapter is structured as follows. Section 4.2 presents the theoretical background for use of an RDCB specimen along with a closed form expression for both $\sigma - \delta_n$ and $\tau - \delta_t$ relationships obtained for Mode I and Mode II loading conditions, respectively. Section 4.3 includes the experimental procedures for (a) manufacture of bonded, uncured carbon-epoxy tows, (b) Mode I and Mode II experiments using an RDCB specimen to quantify the traction-separation relationship for uncured, bonded carbon-epoxy tows when subjected to a constant displacement rate of 0.30 mm/min at room temperature (T = 25 °C) and (c) extraction of the mixed mode traction-separation relationships. Results and discussion are presented in section 4.4.

4.2 THEORETICAL BACKGROUND

4.2.1 Mode I traction-separation relationship

The RDCB analysis approach of Dastjerdi, Pagano, Kaartinen, McKee, and Barthelat (2012); Dastjerdi, Tan, and Barthelat (2013) for extracting $\sigma - \delta_n$ relationship is adopted in this work for Mode I loading. Dastjerdi, Pagano, Kaartinen, McKee, and Barthelat (2012) obtained explicit expressions for the $\sigma - \delta_n$ relationship of a soft biological adhesive considering static equilibrium and assuming the adherends are rigid. In their analysis, the authors did not include the effect of a compressive zone that exist at the end of the cohesive zone for a finite thickness adhesive. Since the adhesive in their work was very thin with negligible resistance to compression, excluding the effect of a compressive zone will not significantly affect the accuracy of their results. For the case of a prepreg tow, if the region ahead of the crack tip has a compressive zone propagating to the far boundary, the traction acting in the compressive zone can have a significant effect on the $\sigma - \delta_n$ relationship. For our studies, StereoDIC measurements of the full-field deformations along the length of the tow-to-tow bonded region confirmed the presence of a distinct compressive zone

in the adhesive (see Figure 4.8). The presence of the compressive zone was also reported in previous studies (Watson, Liao, Worswick, and Cronin 2018; Gorman and Thouless 2019).

In recently published work, Watson, Liao, Worswick, and Cronin (2018) derived an implicit expression for the $\sigma - \delta_n$ relationship by considering the effect of compression of the adhesive at the end of the beam. In their analysis of the RDCB specimen, the authors considered a point of rotation of the beam to define the tension to compression transition point and derived an implicit expression to obtain the $\sigma - \delta_n$ relationship. The derivation of $\sigma - \delta_n$ relationship using their analysis assumes the compressive stress to vary linearly with the closing displacement and requires knowledge of stiffness of the adhesive in the compressive region.

This chapter presents the derivation of an explicit form for the $\sigma - \delta_n$ relationship in terms of the opening displacements at the crack tip (δ_n), closing displacement at the far end of the beam (δ_{nc}) and far field load without prior knowledge of the $\sigma - \delta_{nc}$ relationship in the compressive region. Since fracture is observed to occur in the epoxy rich region in the middle of the adherent, the stress acting on the mid plane of the adherent in the deformed configuration as shown in Figure 4.1b is used to define the traction vector. Assuming that the $\sigma - \delta_n$ response of the material is continuous from compression to tension, the effect of large rotation of the beams is incorporated in the analysis. An expression for the $\sigma - \delta_n$ response for small rotations is deduced from the general form, giving a form that is similar to the expression in Dastjerdi, Pagano, Kaartinen, McKee, and Barthelat (2012), where it is shown that the presence of a compressive zone can be expressed as a correction term to the $\sigma - \delta_n$ expression.

As shown in Figure 4.1b the opening displacement ($v(x)$) at any point along the 'x' axis in the rigid adherend that is assumed to be well-bonded to the adherent can be expressed as shown in Equation (4.1).

(a)

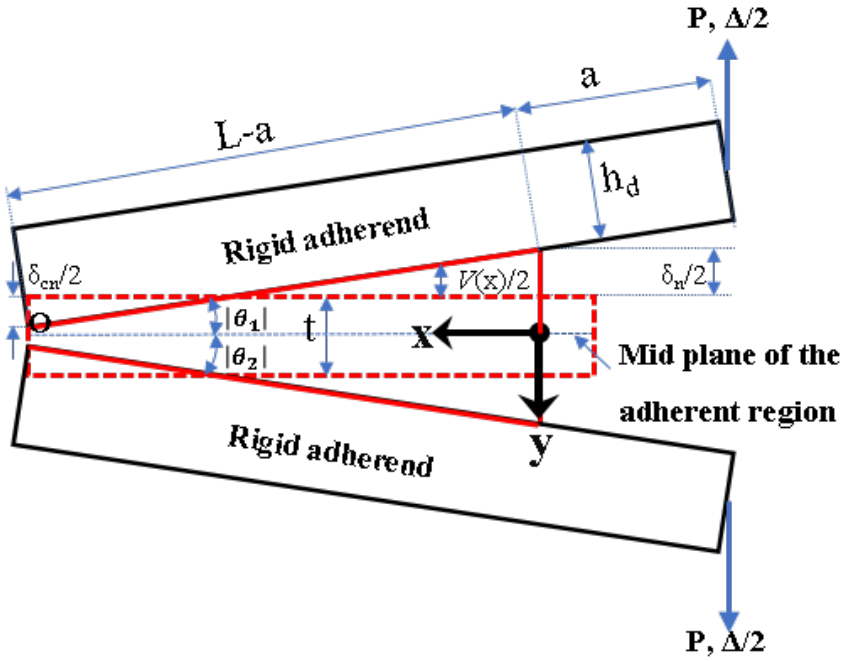

(b)

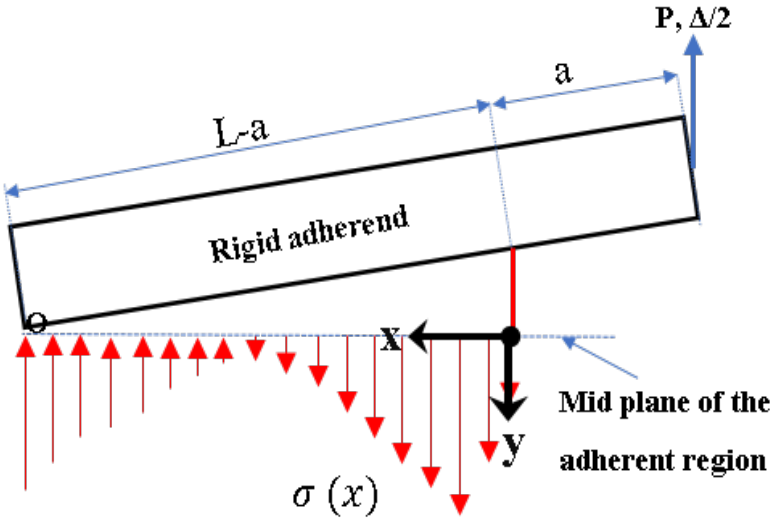

Figure 4.1 (a) Schematic of the RDCB specimen showing deformation of the adhesive adherent layer (the red dotted line represents reference position of the adhesive layer and solid line shows the deformed position of the adhesive layer), (b) free body diagram of the top portion of the traction RDCB sample showing traction ($\sigma(x)$) acting at the mid plane of the adherent. Though not shown, the z-axis is located at the x-y origin and perpendicular to the x-y directions.

$$v(x) = \delta_n - \frac{\delta_n + \delta_{nc}}{(L-a)cos(\theta)}x = \delta_n - 2x\,tan(\theta), \tag{4.1}$$

where δ_n is the vertical separation of the adherend interface at the crack tip, δ_{nc} is the relative displacement of the adherend interface in the negative 'y' direction at the far end of the beam, L is the length of the beam from left end to the load point; a is the initial crack length, $+\theta_1$ is the counter clockwise rotation of the top adherend, $+\theta_2$ is the counter clockwise rotation of the bottom adherend, and $\theta = \frac{1}{2}(\theta_1 - \theta_2)$ is 1/2 of the internal angle between the top and bottom adherends. Force balance in the 'x' direction is given in Equation (4.2).

$$\int_0^{(L-a)cos\theta} \sigma(x)dx = P, \tag{4.2}$$

where σ is the normal traction on the adhesive layer, and P is the vertical force per unit width. The balance of moments about the z-axis gives

$$\int_0^{(L-a)cos\theta} \sigma(x)xdx = -Pa\,cos(\theta). \tag{4.3}$$

In Equations (4.2) and (4.3), changing the variable from 'x' to v, the force and moment balance equations are given in Equations (4.4) and (4.5), respectively.

$$\int_{-\delta_{nc}}^{\delta_n} \sigma(v)dv = 2P\,tan(\theta), \tag{4.4}$$

$$\int_{-\delta_{nc}}^{\delta_n} \sigma(v)vdv = 2P\,tan(\theta)(\delta_n + 2a\,sin(\theta)) = 2P\Delta tan(\theta), \tag{4.5}$$

where $\Delta = \delta_n$ + 2a sin(θ) is the load line displacement.

Differentiating Equations (4.4) and (4.5) with respect to opening displacement, δ_n, the $\sigma - \delta_n$ relationships are obtained as

$$\sigma(\delta_n) = 2\,tan(\theta)\frac{dP}{d\delta_n} + \frac{2P}{cos^2(\theta)}\frac{d\theta}{d\delta_n} - \sigma(-\delta_{nc})\frac{d\delta_{nc}}{d\delta_n}, \tag{4.6}$$

$$\sigma(\delta_n) = \frac{\Delta}{\delta_n}\left(2\,tan(\theta)\frac{dP}{d\delta_n} + \frac{2P}{cos^2(\theta)}\frac{d\theta}{d\delta_n}\right) + \frac{P}{\delta_n}tan(\theta)\frac{d\Delta}{d\delta_n} + \frac{\delta_{nc}}{\delta_n}\sigma(-\delta_{nc})\frac{d\delta_{nc}}{d\delta_n}. \tag{4.7}$$

The two unknown quantities in Equations (4.6) and (4.7) are $\sigma(\delta_n)$ and $\sigma(-\delta_{nc})$, where $\sigma(\delta_{nc})$ is the traction versus closing displacement relation in the compressive zone. Using Equations (4.6) and (4.7), $\sigma(\delta_n)$ relationships for both the tensile and compressive regions can be extracted from a single experiment. The expression for $\sigma(\delta_n)$ obtained after substituting for $\sigma(-\delta_{nc})$ from Equation (4.6) into Equation (4.7) is given by

$$\sigma(\delta_n) = \frac{\Delta + \delta_{nc}}{\delta_n + \delta_{nc}}\left(2\,tan(\theta)\frac{dP}{d\delta_n} + \frac{2P}{cos^2(\theta)}\frac{d\theta}{d\delta_n}\right) + \frac{2P}{\delta_n + \delta_{nc}}tan(\theta)\frac{d\Delta}{d\delta_n}. \tag{4.8}$$

Substituting $\frac{\Delta+\delta_{nc}}{\delta_n+\delta_{nc}} = \frac{L}{L-a}$ in Equation (4.8):

$$\sigma(\delta_n) = \frac{L}{L-a}\left(2\,tan(\theta)\frac{dP}{d\delta_n} + \frac{2P}{cos^2(\theta)}\frac{d\theta}{d\delta_n}\right) + \frac{2P}{\delta_n + \delta_{nc}}tan(\theta)\frac{d\Delta}{d\delta_n}. \tag{4.9}$$

When rotation of the beam is small, the angle θ can be approximated by $\theta \approx \frac{\delta_n+\delta_{nc}}{2(L-a)}$. Hence, for small rotation of the beam, the $\sigma - \delta_n$ relationship in Equation (4.9) can be approximated as shown in Equations (4.10).

$$\sigma(\delta_n) = \frac{L}{(L-a)^2}\left[(\delta_n + \delta_{nc})\frac{dP}{d\delta_n} + P\left(1 + \frac{d\delta_{nc}}{d\delta_n}\right)\right] + \frac{P}{L-a}\left[\frac{L}{L-a}\left(1 + \frac{d\delta_{nc}}{d\delta_n}\right) - \frac{d\delta_{nc}}{d\delta_n}\right]. \tag{4.10}$$

Rearranging terms in Equation (4.10), the traction-separation relationship assuming small rotation of the beam is given in Equation (4.11).

$$\sigma(\delta_n) = \frac{L}{(L-a)^2}\left(\delta_n\frac{dP}{d\delta_n} + 2P\right) + \frac{L}{(L-a)^2}\left(\frac{d(P\delta_{nc})}{d\delta_n} + \frac{Pa}{L}\frac{d\delta_{nc}}{d\delta_n}\right). \tag{4.11}$$

The first term in the bracket on RHS of Equation (4.11) is the exact expression for $\sigma(\delta_n)$ as derived in Dastjerdi, Pagano, Kaartinen, McKee, and Barthelat (2012) assuming zero compressive zone length ahead of the cohesive zone. The second term in Equation (4.11) can be viewed as a correction term due to a finite compressive zone ahead of the cohesive zone. Equation (4.11) gives an explicit representation for the $\sigma - \delta_n$ relationship in the cohesive zone in term of geometric dimensions of the beam, load and displacement δ_n at the crack tip and displacement δ_{nc} at the far end

of the beam. An expression for the $\sigma - \delta_{nc}$ relationship in the compressive zone can be obtained from Equations (4.6) and (4.7), requiring no additional information of the material properties of the adhesive.

Both the in-plane rotations on the surface of the adherend, separation of the adherends at the crack tip and also compression of the adherent on the compressive end of the beams can be accurately measured using StereoDIC, providing an efficient way to extract the traction-separation relationships from the experimental measurements. Using synchronized load measurement with StereoDIC measurements, all parameters required to determine the traction-separation relationships in Equations (4.9) and (4.11) can be obtained. For reducing noise in the terms involving differentiation of load per unit width (P) and closing displacement (δ_{nc}) with opening displacement (δ_n), a moving average filter with a window size of five data points is used in all calculations.

4.2.2 Mode II traction-separation relationship

For pure shear loading with rigid adherends, the shear traction is assumed to be uniform along the length of the adherent. Thus, the shear traction for each load (and the corresponding tangential separation, δ_t) can be directly obtained from the load using Equation (4.12).

$$\tau(\delta_t) = \frac{P}{L - a}, \tag{4.12}$$

where τ is the shear traction vector, P is the load per unit width of the adherends (note that P is a function of δ_t for Mode II loading), and $L - a$ is the bonded length of the adhesive strip[1].

[1]Though the interface traction is expected to be different at the ends of the beam, variations in the traction due to edge effects are not included in the analysis due to the limited size of the edge effect zones relative to the length of the adherent.

4.3 MATERIALS AND EXPERIMENTAL METHODS

Figure 4.2 shows the RDCB fixture used in this work. The RDCB fixture is a modified version of the Mixed-Mode I/II MCB test fixture used by Högberg, Sørensen, and Stigh (2007). Only the Mode I (0°) and Mode II (90°) loading configurations are employed in this work. The RDCB adherends consist of two essentially rigid 6061-T6 aluminum beams of length L =100 mm, width W = 6 mm and thickness h_d = 12.7 mm. Thickness of the adherent region, $h_a \approx 0.32$ mm. In Figure 4.2, the holes on the top and bottom fixtures corresponding to Mode I and Mode II loading are marked with angles 0° and 90°, respectively.

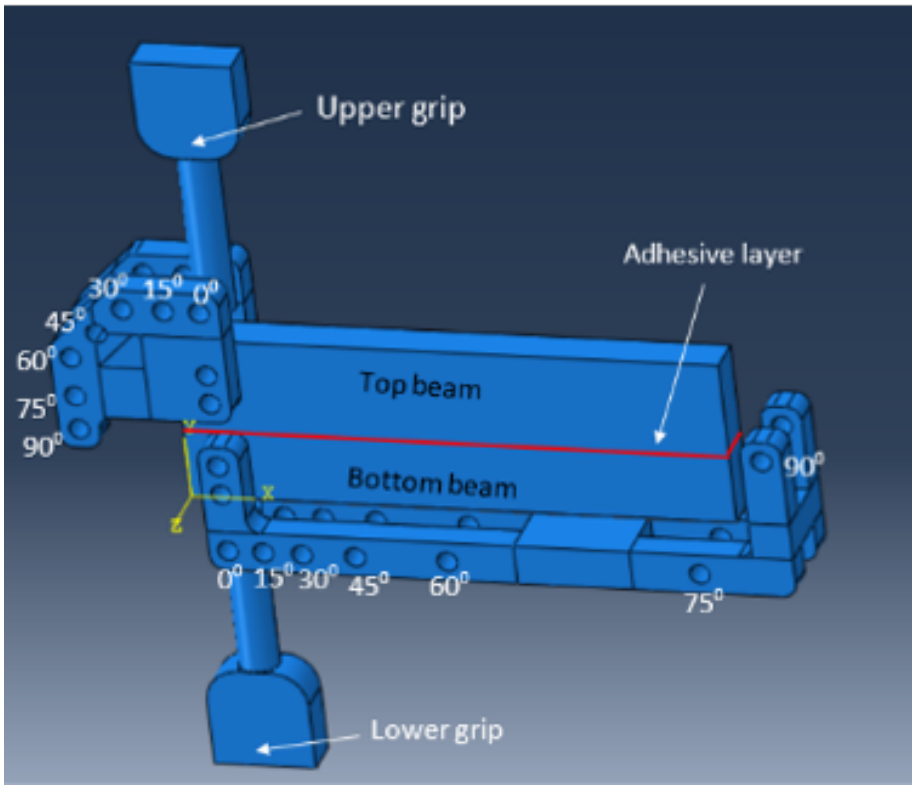

Figure 4.2 Schematic of the mixed mode RDCB test setup

4.3.1 Sample Preparation

The adherent region of the RDCB specimen consists of two uncured carbon fiber epoxy prepreg tows (IM7/8552-1 tow from Hexcel) that are bonded to each other. Figure 4.3 shows a schematic of the manufacturing process for the adherent region consisting of two bonded prepreg tows. In order to manufacture the RDCB specimen with adherents, two tows of approximately 100 mm in length, and 6.35 mm in width are extracted from a spool containing prepreg tow[2]. Since room temperature aging of thermoset prepreg is known to cause reductions in bonding tack and hence bond strength, all experiments were performed using prepreg that incurred short, consistent "out-time" prior to mechanical testing. Quantitative data regarding the effect of "out-time" on tow properties is provided in Appendix A. As shown in Figure 4.3, both the surface of the top silicone layer and the bottom aluminum plate are treated with a release agent. One prepreg tow is placed on the lower rigid plate and the second prepreg tow is placed on a flat silicone rubber surface; the silicone rubber surface is the same material used in a typical AFP compaction roller. Next, a Teflon layer is placed at one end of the bottom tow (see Figure 4.3) to form a pre-crack. At this point, both tows are heated using a heat gun until the optically measured surface temperature of the tows reaches the required temperature (40 °C). The infrared thermometer used for measurement of the tow surface temperature has a measurement accuracy of ±2 °C. Once the temperature is reached, the top tow is immediately pressed together with the bottom tow using a pneumatic press[3], while maintaining an average contact pressure of 1 MPa for 1 sec. After processing, the bonded tows are allowed to equilibrate at room temperature (25 °C), which takes approximately 60 seconds. The adherend

[2]The spool is stored at −20 °C inside vacuum sealed bags and it is thawed until the temperature of the tow reached ambient temperature.

[3]The pneumatic loading system is calibrated to obtain the required pressure and the contact time using a pressure transducer mounted directly below the silicon rubber plate where the two tows contact each other.

faying surfaces are prepared by using a coarse grit sandpaper (P50) to create a rough surface on both the adherends, followed by cleaning the surfaces using water and acetone. The prepreg tow laminate having [0/0] orientation is strongly adhered to the aluminum adherends, using Loctite® 426TM adhesive with the fiber direction aligned along the length of the beam. Once the RDCB specimen is fabricated, it is immediately placed in the loading fixtures and the Mode 1 or Mode II loading process is performed at room temperature with a constant load line displacement rate of 0.3 mm/min. It is important to note that the selected process variables are intended to ensure that the adhesive strength is optimized so that cohesive separation within the bond region of the laminate is the most likely failure process.

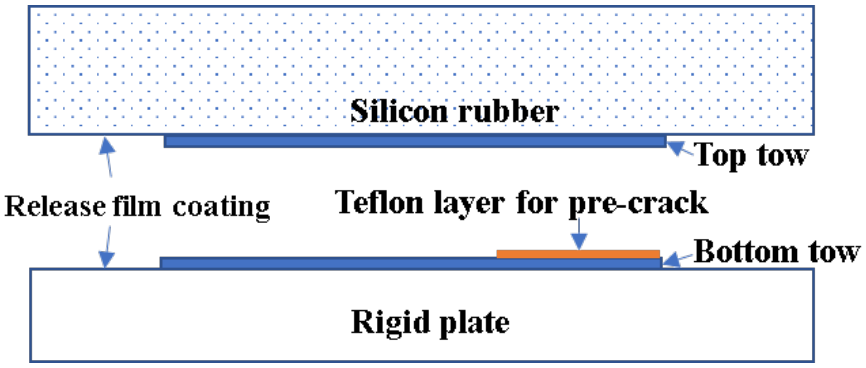

Figure 4.3 Schematics of preparing the tow sample

4.3.2 StereoDIC Measurement System

The stereovision system setup used in this work is shown in Figure 4.4. The system consists of a pair of Point Grey 12 MP CMOS stereo cameras, 35 mm lenses and linear polarizing filters. The linear polarizers are adjusted to remove specular reflections from the images. A high contrast speckle pattern, required for DIC analysis, is produced by applying a thin coat of white paint, followed by sprinkling black paint using an airbrush system. The resulting speckle pattern has nominally an isotropic distribution throughout the field of view with an average speckle size of 80 µm. For the magnification used in the work, each pixel corresponds to 25 µm on the object.

Hence each speckle is sufficiently sampled by the camera sensors (at least 3 x 3 pixel^2) for accurate displacement measurement. The speckle pattern and grey scale intensity distribution are shown in Figure 4.5.

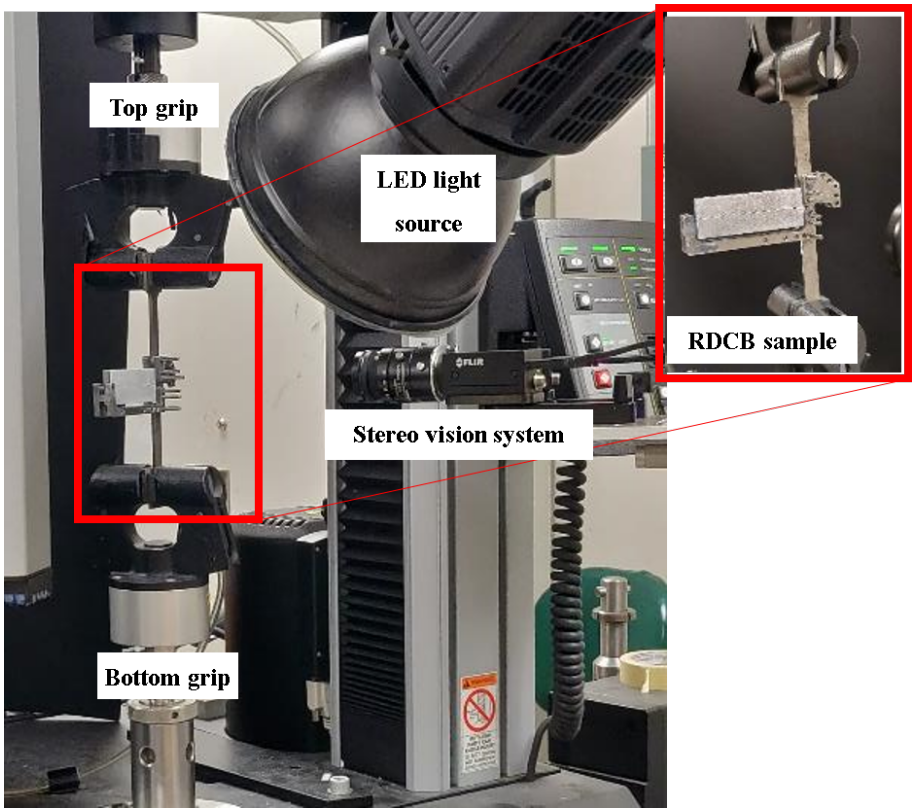

Figure 4.4 Photograph of the Mode I RDCB experimental set up

The calibration process for the stereo vision system followed the general procedure outlined in Rajan et al. (2019a) using a standard calibration target. The calibration target dimensions and a summary of the key camera and lens parameters used in this work are given in Table 4.1. The size of the calibration grid is chosen such that it covers more than two-thirds of the fields of view for both cameras in the stereo vision system. A total of 50 image pairs are obtained and used to provide an over-determined data set for system calibration. All StereoDIC analyses are performed using Correlated Solutions' VIC-3D software. The StereoDIC parameters selected for this work are shown in Table 4.2. The 25 x 25 pixel^2 subset size corresponds to a 0.6 x 0.6 mm^2 area on the object and a 5 x 5 central Gaussian weighted strain filter is

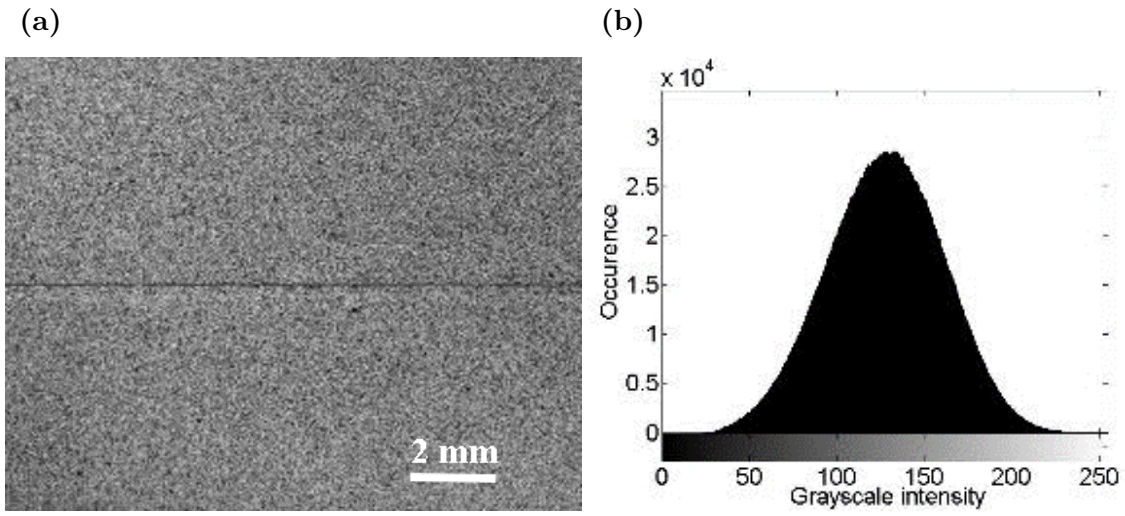

Figure 4.5 (a) Random speckle pattern for stereoDIC, (b) gray-scale intensity pattern of the random pattern

used for strain measurements, corresponds to ≈ 0.88 x 0.88 mm^2 area on the object. The displacement resolution achieved in the current system is ≈ 40 nm.

Table 4.1 Camera and lens parameters of stereo vision system for RDCB experiments

	Camera and lens parameters
Camera	12 MP CMOS PointGrey camera, 4096 x 3000 pixels^2 array, 3.45 µm pixel size
Calibration	9 x 9 dot grid, 1 mm dot size, 4 mm dot spacing
Lens	Nikon Micro-Nikkor with 35 mm focal length
Lens Filter	Linear polarizer
Light Source	LED with linear polarizing film
Lens Distortion	3rd Order Radial Distortion Correction

4.3.3 Experimental setup

Each RDCB specimen is loaded in displacement control at a far-field displacement rate of 0.3 mm/min using an Instron 5566 test frame with a 5 kN load cell. A photograph of the complete experimental configuration is shown in Figure 4.4. The RDCB specimen is attached to the upper and lower pin grips using 3 mm diameter pins. Synchronized recording of both the stereo image pairs and the load cell signal

Table 4.2 StereoDIC parameters for RDCB experiments

	StereoDIC parameters
Subset size	25 x 25 pixels^2
Step size	7 pixels
Strain filter type	Center-weighted Gaussian filter
Strain Filter size	5x5 data points (area of 35 x 35 pixels^2)
Strain measure	Lagrangian large strain tensor
Field of view	100 mm x 75 mm
Magnification	25 µm/pixel
Average speckle size	80 µm

is performed using a National Instrument data acquisition system and VIC-Snap software. Image and load acquisition are performed at 2 Hz.

4.4 RESULTS AND DISCUSSION

Computed tomography (CT) image of a tow specimen with four layers of tow ($[90/0]_s$) bonded under the conditions described in Section 4.3.1 is shown in Figure 4.6. A relatively small number of air gaps are visible in the epoxy rich interface region between the two middle tows having the same fiber orientation ([0/0]) compared to the interface region between tows with orthogonal fiber orientation ([0/90]). This observation indicates that intimate contact is achieved at the interface between two tows having the same fiber orientation compared to the interface between two tows having orthogonal fiber directions. Hence, the strength of the interface between two bonded tows is likely to be a function of fiber orientation. It is noted that the four-layer tow specimen was specifically used for CT imaging to understand the effect of tow orientation on interface formation; all specimens used in this work are formed by bonding two tows which have the same [0/0] fiber orientation[4]. The central interfacial thickness of the epoxy layer is of the same order as the distance between fiber bundles in the bulk material (≈ 8 µm). In addition, the CT image shows that there

[4]For tow specimens with different fiber orientation a lower energy release rate is expected due to higher number of airgaps at the epoxy rich interface; variation of the fracture properties with fiber orientation will be subject of our future publication.

is very good contact along the entire interface length, with the exception of a few air gaps. Since the air gap defects are away from the crack tip region, experimental evidence indicates that the room-temperature baseline cohesive traction-separation relationships obtained in this work are nominally consistent with well-bonded regions obtained during AFP manufacturing.

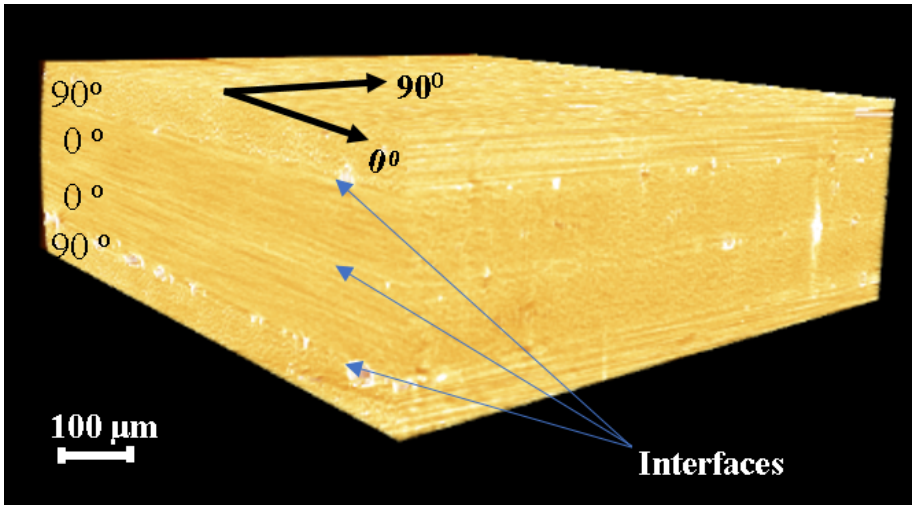

Figure 4.6 CT image of the tow sample showing the interfaces

A total of six samples are randomly selected from a batch of 20 samples prepared for Mode I and Mode II experiments. Out of the six samples, three samples were subjected to Mode I loading and the remaining three were subjected to Mode II loading. Results for all Mode I and Mode II samples are included to show sample to sample variations. Load versus load-line displacement (F-Δ) results for both Mode I and Mode II cases are shown in Figure 4.7. Figures 4.8 and 4.9 show the experimental estimates for the Mode I opening strain and Mode II shear strain, respectively, along the entire adherent length for an applied load of 30 N. The strain fields shown in Figures 4.8 and 4.9 correspond to points 1 and 2, marked on the F-Δ curve in Figure 4.7 (30 N load), respectively. Full-field data for the tensile strain, e_{yy}, and shear strain, e_{xy}, shown in Figures 4.8 and 4.9 are underestimates of the actual tow strains. The underestimates are due to the fact that the StereoDIC imaging system

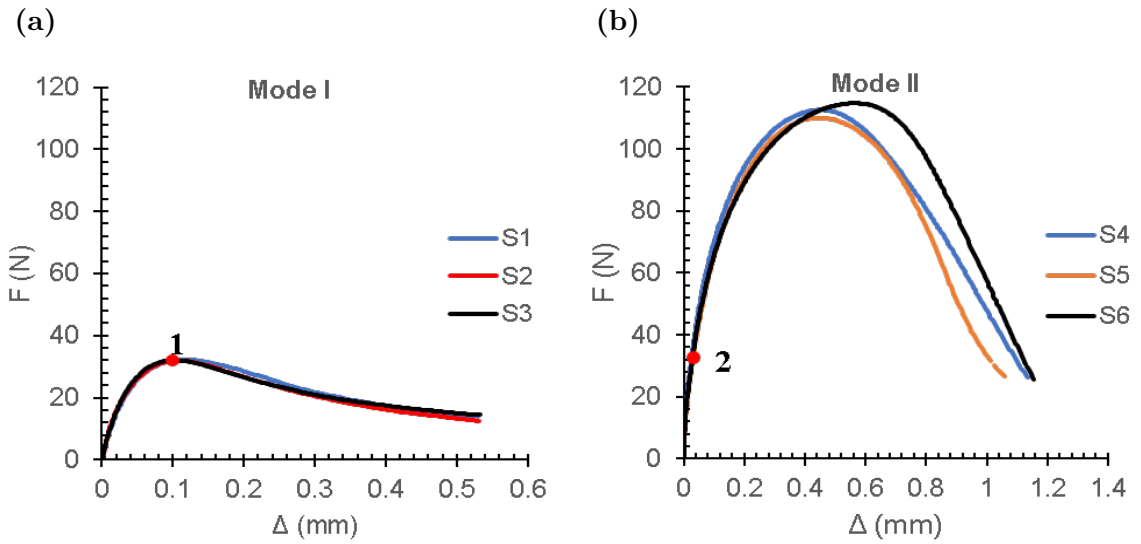

Figure 4.7 Load vs load line displacement for (a) Mode I and (b) Mode II loading

has a virtual strain gage size of $\approx 880\,\mu m$ whereas the entire adherent thickness is $320\,\mu m$. Thus, the virtual strain gage data includes a majority of information from the rigid adherends which have negligible strain during the loading process.

Inspection of Figure 4.7 shows that the Mode I results for all specimens have essentially no scatter, with a steady and progressive decrease in adhesive stiffness as a primary characteristic of the Mode I data. The Mode II data also is quite consistent, with all specimens having the same trends and a maximum difference in the energy release rate (area under the load versus load-line displacement) that is less than 5%. Observation of the vertical strain field data in Figure 4.8 for the Mode I sample reveals a compressive zone in the tow, extending from the end of the cohesive zone to the far end of the beam. Since the compressive zone size is significant compared to the bond length, it is necessary to consider the effect of the compressive zone in the derivation of the $\sigma - \delta_n$ relationship (Equation (4.11)) for Mode I. For Mode II, the experimental results shown in Figure 4.9 indicate that whole length of the tow interface is undergoing extensive deformation and thus damage during the loading process.

Figures 4.10a and 4.10b show variation of δ_{nc} with δ_n and average in-plane rotation

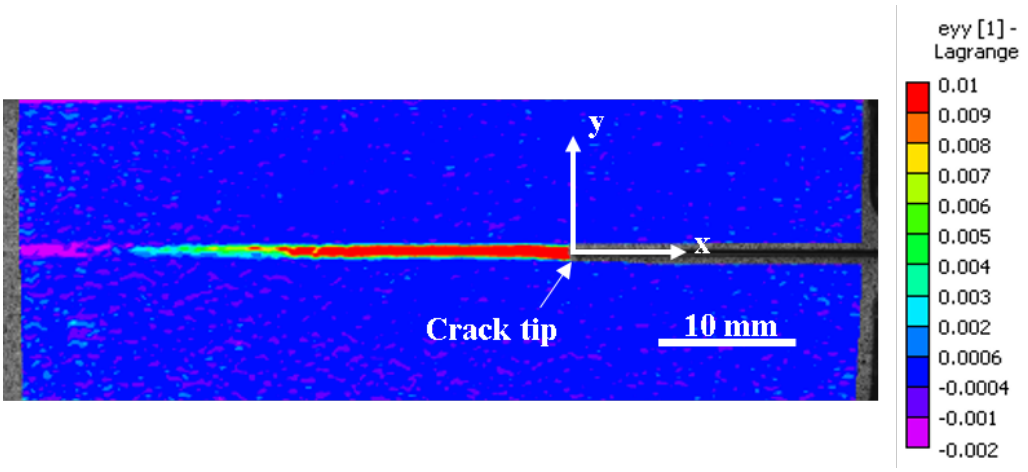

Figure 4.8 Green Lagrange strain field in the y direction (e_{yy}) for Mode 1 loading case; the strain field shown corresponds to a load of 30 N (point 1 in the Mode I F-Δ curve of Figure 4.7)

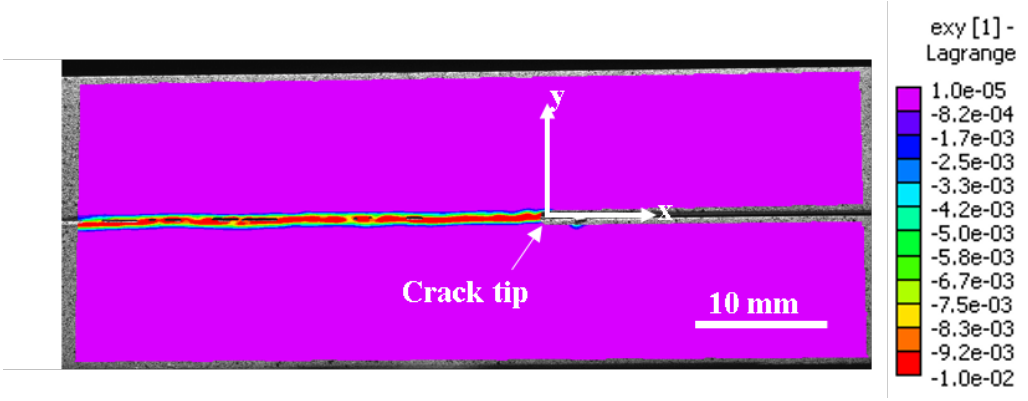

Figure 4.9 Green Lagrange in plane shear strain field (e_{xy}) for Mode 1 loading case; the strain field shown corresponds to a load of 30 N (point 2 in the Mode II F-Δ curve of Figure 4.7)

of the top and bottom adherends (θ) versus δ_n. The derivative of these variables with δ_n is also plotted in Figure 4.10. From Figure 4.10a, it is observed that $\frac{d\delta_{nc}}{d\delta_n}$ decreases with δ_n indicating that the cohesive zone size is increasing with δ_n. Also, the point of rotation of the beam moves towards the far end of the beam. Figure 4.10b shows that the maximum angle of rotation of the beam is less than 0.008 rad. Hence the traction-separation expression shown in Equation (4.11) is consistent with a small angle approximation. Thus, Equation (4.9) has negligible difference with respect to the predictions using Equation (4.11). The normal and tangential traction–separation

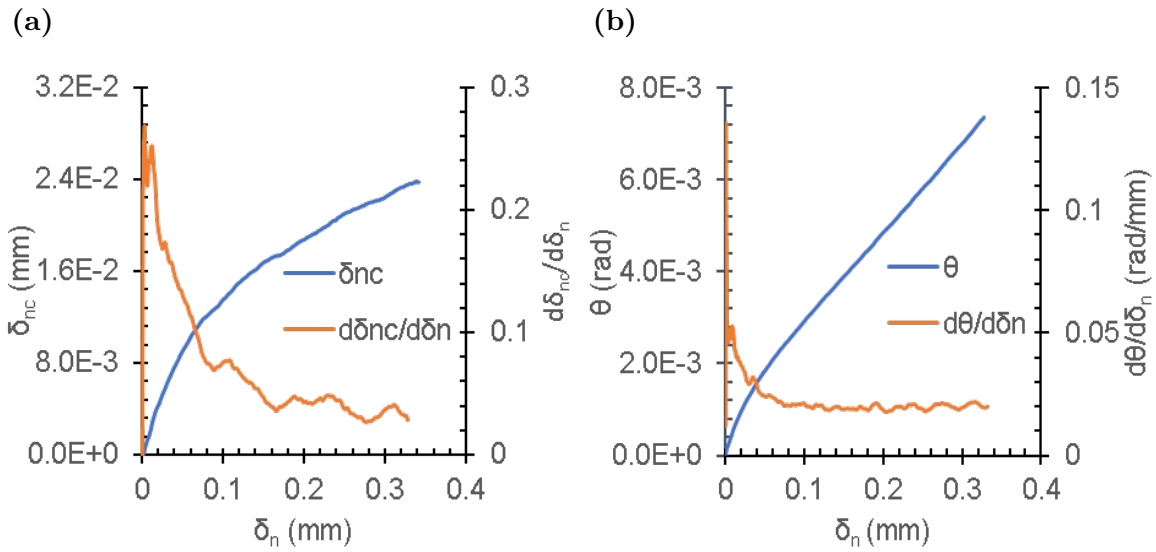

Figure 4.10 (a) Variation of δ_{nc} and $\frac{\delta_{nc}}{d\delta_n}$ vs δ_n, (b) θ and $\frac{d\theta}{d\delta_n}$ vs δ_n for Mode I loading

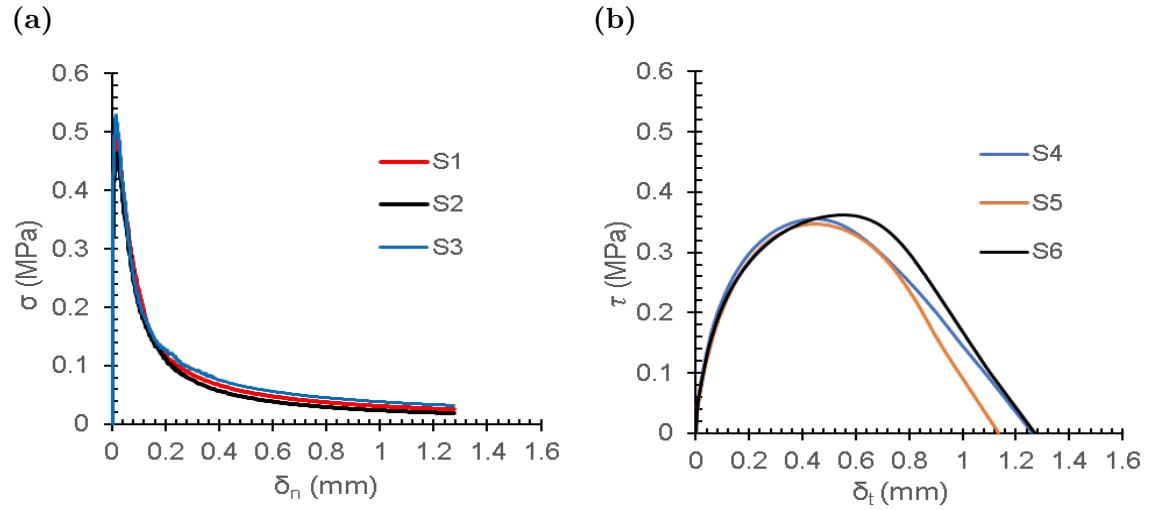

Figure 4.11 Traction-separation relationships for (a) Mode I and (b) Mode II

laws thus obtained are shown in Figures 4.11a and 4.11b, respectively. Since the traction-separation laws are directly related to the load histories shown in Figure 4.7, a similar sample to sample variation is observed in the traction-separation laws for Mode I and Mode II.

The average values of maximum tangential traction (τ_{max}) and maximum normal traction (σ_{max}) are 0.35 MPa and 0.5 MPa, respectively. The maximum separation at crack initiation for Mode I and Mode II loading has almost the same magnitude

Table 4.3 Summary of traction – separation parameters for Mode I & II

Failure mode	Maximum traction (σ_{max}, τ_{max}) [MPa]	Critical separation# ($\delta_n^\star$ $\delta_t^\star$) [mm]	Separation at failure (δ_{nmax}, δ_{tmax}) [mm]	Energy release rate (G_{Ic}, G_{IIc}) [Jm^{-2}]
Mode I	0.50	0.02	1.3	120
Mode II	0.35	0.50	1.2	255

Critical separation is defined as the separation at maximum traction

(1.2 mm). The large value of maximum separation indicates that the uncured epoxy separation initiates in a ductile manner at the experimental loading rate used in the experiments. The normal traction-separation law shows that maximum traction occurs when the separation is less than 0.02 mm, and the traction decreases sharply with further increase in separation. The normal traction-separation law has a characteristic long tail, indicating that strain at failure of the uncured epoxy is more than 500%. Beyond a separation of 1.2 mm, the uncured epoxy was observed to form fibrils bridging the tow surfaces. The epoxy fibrils have negligible resistance to stretching, hence the traction is essentially zero at a separation of 1.2 mm. The average energy release rate (area under the traction-separation law) for Mode II (255 J/m^2) is 2.1 times larger than Mode I energy release rate (120 J/m^2). Table 4.3 presents a summary of the average values of key traction-separation parameters, including the maximum traction, critical separation displacement, maximum separation at failure and energy release rate for Mode I and Mode II loading cases.

Another difference between the σ-δ_n and τ-δ_t relationship shown in Figures 4.11a and 4.11b is in the initial slope of the elastic portion of the traction-separation curves. The σ-δ_n corresponding to Mode I loading has a higher slope when compared to Mode II loading. The lower slope in the case of the τ-δ_t relationship indicates that the uncured epoxy within the prepreg tow has lower shear stiffness compared to its stiffness in the normal direction. As noted by Chai (1992), when the thickness of the adhesive is on the order of a few microns, a triaxial stress state may exist in

the process zone, contributing to the observed increase in stiffness in the normal direction. Since the measured thickness of the epoxy layer between the two tows using CT images is $\approx 10\,\mu m$ (See Figure 4.6), the presence of triaxial stresses in the region is consistent with results obtained by Chai (1992).

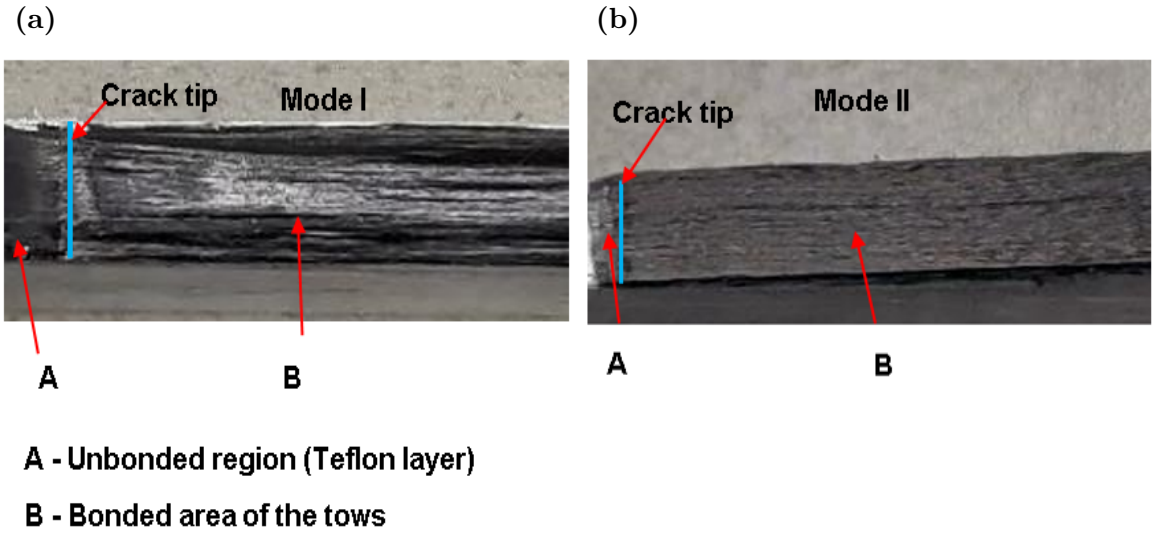

Figure 4.12 Typical low magnification images of fracture surfaces for (a) Mode I and (b) Mode II

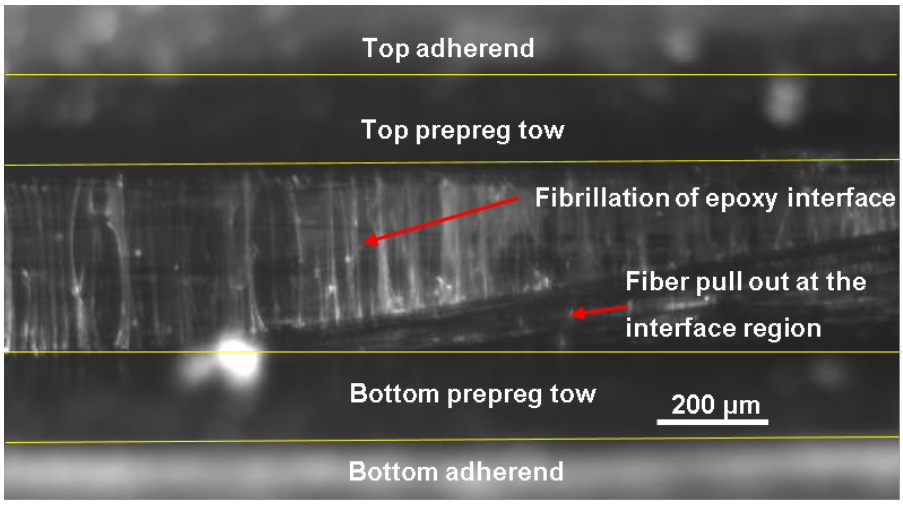

Figure 4.13 Fibrillation of uncured epoxy in the cohesive zone

To provide a physical connection for the measured traction-separation relationships, Figure 4.12 shows the fracture surfaces for Mode I and Mode II loading. For Mode II loading, the photo in Figure 4.12b shows that the fracture surface is relatively smooth, without carbon fiber pullout or bridging/fibrillation between tows. Conversely, though Figure 4.12a is relatively unremarkable, as shown in Figure 4.13 the fracture surfaces for Mode I loading show considerable epoxy fibrillation across the surface with no observable carbon fiber interaction. Cavitation of the soft interface in the presence of hydrostatic stresses has been identified as the main source for formation of fibrils (Lakrout, Sergot, and Creton 1999; Vossen, Schreurs, Sluis, and Geers 2014). As the loading progresses beyond the point of maximum traction in the σ-δ_n curve, the fibrils are highly stretched, resulting in a reduction in the cross-sectional area of each fibril with further loading inducing breakage of some of the fibrils. For Mode I loading, fibrils are the main source of resistance to crack growth beyond the point of maximum traction (Lakrout, Sergot, and Creton 1999). Hence the stiffness reduction in the cohesive zone due to damage accumulation can be related to reduction in the number of fibrils per unit area. Formation of fibrils was also observed by Liechti and Wu (2001) during debonding of a rubber-metal interface. Recognizing the rate dependent deformation response of the fibrils, the effect of loading rate on the traction-separation relation for the uncured tow interface will be the subject of future studies.

4.5 CONCLUSION

Mode I and Mode II fracture experiments are conducted using an RDCB specimen for direct extraction of traction-separation relationships for two uncured carbon epoxy prepreg tows bonded using a manufacturing process similar to a standard AFP lay-up process. The Mode I σ-δ_n relationship is obtained using an explicit expression for σ-δ_n derived for the RDCB specimen considering the effect of large rotation of the

adherends and the presence of a compressive zone ahead of the cohesive zone region. For Mode II loading, the traction-separation relationship is obtained by considering uniform shear stress along the length of the specimen, a condition that is consistent with experimental observation of indicating a nominally uniform shear strain along the entire length of the bond region.

The measured value of critical energy release rate in Mode II fracture (G_{IIc}) is $\approx$ 2.1X higher than the Mode I energy release rate (G_{Ic}). The maximum separation in the normal direction (σ_{max}) and tangential direction (τ_{max}) have almost the same magnitude ($\approx$ 1.3 – 1.2 mm). The maximum tractions in the tangential and normal directions are 0.35 MPa and 0.5 MPa respectively. For Mode I loading, significant fibrillation of the uncured epoxy is observed, indicating the presence of hydrostatic stresses. In the case of Mode II loading, the fracture surface is smooth and epoxy fibrillation is not observed.

Finally, this chapter focuses on cohesive failure of the bond region between two tows at 25 °C. The effect of variations in process parameters, including pressure, temperature, contact time and rate of loading on the traction separation relationships will be the subject of future work.

Chapter 5

FINITE ELEMENT MODELING OF WRINKLE FORMATION DURING AUTOMATED FIBER PLACEMENT OF PREPREG SLIT TAPE

Simulations and experiments for automated fiber placement (AFP) of prepreg slit tape (tow) on a flat surface with different radii of curvature are presented, with emphasis on characterization of wrinkle formation. Bonding of the slit tape to the substrate surface is modeled through a sticky contact definition in Abaqus. Subsequent delamination and wrinkling are predicted through incorporation of mixed mode cohesive traction-separation laws (TSLs) for contact and bonding of slit tape and substrate. Comparisons of predicted wrinkle shape, amplitude and wavelength to experimental measurements show excellent agreement for a 6.35 mm wide IM7/8552-1 prepreg tow placed on a flat surface using four different radii of curvature. In addition, simulations are demonstrated to be capable of capturing the mechanisms of wrinkle formation using a generally accepted damage model. Careful inspection of the stress and deformation conditions at the tow-substrate interface under the compaction roller reveals a combination of Mode II and Mode III fracture, with significant damage predicted under the roller due to the Mixed Mode II/ III traction conditions. After passage of the roller, nearly instantaneous initiation and growth of wrinkles occurs with relatively consistent spacing under predominantly Mode I conditions at the interface.

5.1 INTRODUCTION

Composite manufacturing technologies such as automated fiber placement (AFP) and automated tape laying (ATL) are the choice of manufacturing of advanced aircraft composite structures. The composite structural components of new generation of military aircraft and for space applications are almost entirely manufactured using AFP process. One of the remarkable advancements in the AFP manufacturing compared to the conventional composite manufacturing techniques is the introduction of a programmable computer controlled robotic arm for placement of bands of tows precisely along programmed paths at controlled layup speed, temperature, and compaction pressure. The flexibility in controlling the layup process parameters for a specific composite material system and for a given tow path allows manufacturing of high-quality composite parts consistently at much faster production rates. Programmability of the AFP placement arm to steer tows at preferred orientation opens a wide range of design options for tailoring properties of composite laminates that would otherwise not be possible with conventional manufacturing. For example, orienting fibers within each lamina along optimal paths can result in favorable stress distributions and improved performance of a laminate for specific applications (Lopes, Gürdal, and Camanho 2008; Abdi, Gürdal, and Huang 2017). Variable stiffness composite parts manufactured using AFP process have been shown to exhibit improved buckling resistance. The advantages of the AFP process make it a preferred manufacturing technique for major aircraft manufactures.

The maximum possible curvature of the tow path for an AFP layup process is limited by the acceptance level of defects that occur in the steered tows. One of the major defects observed in an AFP placed tow is out-of-plane wrinkling. The primary parameters controlling the out-of-plane wrinkle defect are (a) radius of curvature of the tow path, (b) width of the tow and (c) tackiness of the tow, which is a complex function of process parameters such as layup speed, temperature and compaction

pressure. Using narrow width slit tapes/tows in the AFP layup process expands the range of accessible tow path curvature by minimizing the out-of-plane buckling load and tendency for wrinkle formation. New generations of AFP machines incorporate sophisticated placement heads having capability for placing multiple tows up to 32 bands having widths ranging from 3 mm to 12 mm, providing flexibility to cut and restart individual tows, and the capability to independently control feed rate for individual tows, thus reducing defects and wastage of materials without compromising production rate (Dirk, Ward, and Potter 2012; Qureshi, Swait, Scaife, and El-Dessouky 2014). Further reduction in defects is possible by optimizing process parameters for a specific composite system, which improves tow bonding to the substrate. Understanding wrinkle formation and its relationship to tow bond strength ("tackiness") and process parameters is crucial for the success of AFP processing and the production of high quality composite parts. Though trial and error can be implemented for finding optimum process parameters, it is a time-consuming process, and the entire process must be repeated for a different material system. To this end, several AFP process models were developed. Some of the recently developed AFP process models are discussed in the following paragraph.

Beakou, Cano, Le Cam, and Verney (2011); Matveev, Schubel, Long, and Jones (2016) implemented an orthotropic plate-on-elastic-foundation model to predict tow wrinkling. Beakou, Cano, Le Cam, and Verney (2011) developed an approximate theoretical solution assuming simply supported boundary conditions on three edges and a free boundary on the edge where wrinkling occurs to determine the critical buckling load and minimum steering radius. Matveev, Schubel, Long, and Jones (2016) modified the boundary conditions of Beakou, Cano, Le Cam, and Verney (2011) and derived a closed form solution to model out-of-plane wrinkle formation in steered tows with different radii of curvature. Neither model included the effect of compaction pressure on tackiness or the initiation and growth of damage during the

placement process. Bakhshi and Hojjati (2019) incorporated viscoelastic properties of the interface region in a plate-on-foundation model for predicting time dependent growth of wrinkles after initiation.

Bakhshi and Hojjati (2018) used a finite element model along with a cohesive tow-substrate interface to predict the evolution of defects during the AFP process, with the opening mode cohesive traction-separation law (TSL) parameters determined experimentally using a probe-tack test; the authors assumed the same TSL for both the normal and in-plane shear directions. Simulations performed by the authors indicated that out-of-plane wrinkling and localized delamination of the tow (blister) would occur, though there was no quantitative comparison with experimental data. In our previous work (Rajan et al. 2020a), experiments clearly showed that the Mode II TSL is significantly different from the Mode I TSL. There are only a few published work focused on understanding the deformation mechanisms and subsequent occurrence of wrinkle formation during AFP placement of uncured thermoset tows. This chapter presents developemnt of a finite element-based tow placement and adhesion model to simulate the AFP process along curvilinear paths for thermoset tows. The rest of the chapter is organized as follows, Section 5.2 of the manuscript includes material properties and the experimental AFP set-up modeled. The finite element model is discussed in Section 5.3. Results and discussion are presented in Section 5.4.

5.2 MATERIAL AND METHODS

The IM7/8552-1 prepreg tows used in a series of AFP experiments are selected for FE simulations. Material properties of the tows required for the simulations include (a) metrics for tackiness of the tow during processing and (b) the elastic properties of the orthotropic tow. The tackiness metrics used in the simulations are the measured TSL for the tows. Details of the experimental program to determine the Mode I and Mode II TSL are described in chapter 4. The RDCB experiments consists of a rigid

double cantilever beam specimen with prepreg tows bonded using conditions similar to those present during AFP placement of the tow (Rajan et al. 2020a).

5.2.1 Traction-separation relations for cohesive interaction

The tackiness of a tow when adhered to a substrate is modeled in our simulations using cohesive surface interaction of the contacting surfaces. The cohesive interaction is quantified by defining a TSL relating the relative opening/sliding of the contacting surfaces to the associated surface traction.

Mode I response

The Mode I TSL extracted from rigid cantilever beam experiments by the authors is shown in Figure 5.1a[1]. The softening part of the TSL is nonlinear, indicating ductile behavior. In the finite element model for tow placement, the Mode I TSL can be mathematically represented by Equations (5.1) and (5.2).

$$\sigma_n = K_n \delta_n, \tag{5.1}$$

$$K_n = \begin{cases} K_{n0}, & \text{if } \delta_n \leq \delta_{n0}, \\ K_{n0}(1 - D_n), & \text{if } \delta_n > \delta_{n0}, \\ 0, & \text{if } \delta_n \geq \delta_{nc}, \end{cases} \tag{5.2}$$

where K_n is the stiffness of the Mode I TSL, which is a function of a damage variable (D_n) and the opening displacement δ_n, δ_{n0} is the maximum separation up to which elastic behavior exists, with damage accumulating when separation exceeds δ_{n0}, and δ_{nc} is the separation at which the cohesive element is completely damaged and no longer able to resist tensile traction. The TSL parameters K_{n0}, δ_{n0} and δ_{nc} have

[1]The Mode I and Mode II TSL obtained in previous work and used in these simulations represent the tackiness of well-adhered IM7/8552-1 tows that are bonded with contact pressure of 1 MPa, layup temperature of 40 °C and bonding contact time of 1 sec.

single values. The damage variable (D_n) is a function of the effective separation (δ_n-δ_{n0}) which is valid for $\delta_n > \delta_{n0}$. These parameters are directly obtained from the experimentally obtained TSL (σ_n-δ_n). Parameters of the TSL are shown in Table 5.1. The damage variable is also calculated from the experimentally obtained TSL using Equation (5.3).

$$D_n = 1 - \frac{\sigma_n}{\sigma_{n0}}\left[1 + \frac{1}{\delta_{n0}}(\delta_n - \delta_{n0})\right]^{-1}, \tag{5.3}$$

where σ_{n0} is the traction at separation of δ_{n0}.

In order to show the importance of modeling the complete shape of the TSL in the finite element model, the experimental load versus displacement response of the RDCB specimen is compared with finite element result incorporating TSL with (a) a linear softening part and (b) nonlinear softening that matches the experimentally determined shape. As shown in Figure 5.1a, the elastic part of the TSL is the same for both models. The maximum separation in the linear softening model is estimated from the experimentally measured critical energy release rate ($\delta_{nc} = 2G_{IC}/\sigma_{n0}$ where G_{IC} is the Mode I critical energy release rate). For the non-linear softening model, the shape of the softening curve is defined using a tabular representation of D_n as a function of effective separation (δ_n-δ_{n0}) calculated from Equation (5.3) (Camanho and Dávila 2002). Figure 5.1b presents load versus displacement results for the RDCB specimen as predicted by each model. As shown in Figure 5.1b, the shape of the TSL strongly affects the ability to match the global load-displacement data. As such, the shape of the TSL is important when modeling separation processes in soft adhesives with cohesive zone sizes that are oftentimes much larger than characteristic dimensions of the specimen.

Mode II response

The Mode II TSL extracted from a rigid cantilever beam experiment (Rajan et al. 2020a) is shown in Figure 5.2a. The Mode II TSL is represented in the FE model

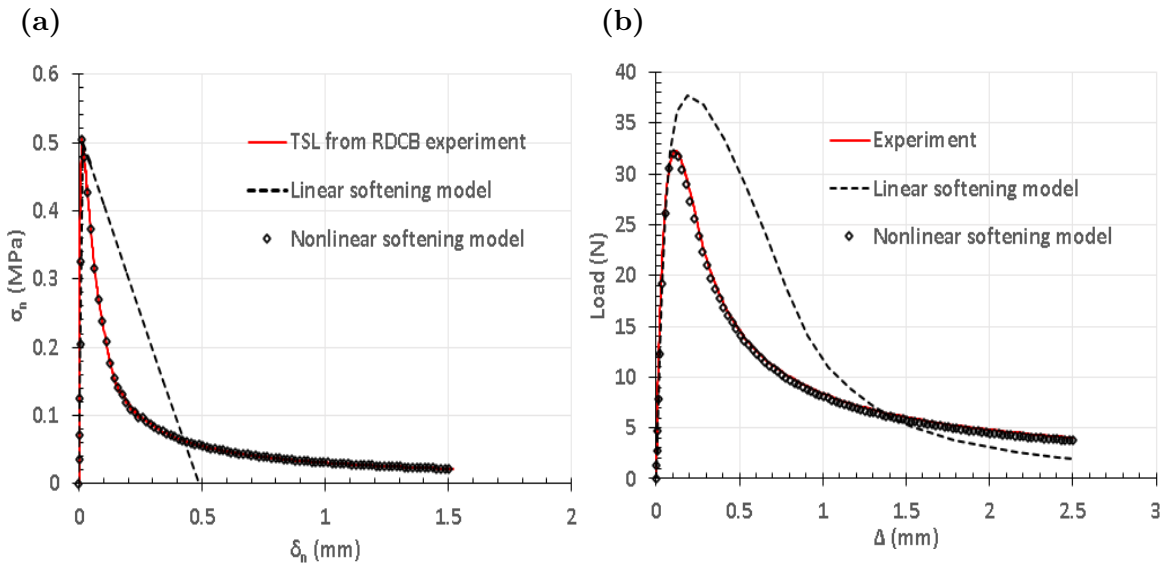

Figure 5.1 (a) Mode I traction-separation data obtained using RDCB experiment and two independent models of CZM traction-separation response, (b) load versus displacement data from Mode I RDCB experiment with predictions based on linear softening and non-linear softening CZM

using Equations (5.4) and (5.5).

$$\sigma_t = K_t \delta_t, \tag{5.4}$$

$$K_t = \begin{cases} K_{t0}, & \text{if } |\delta_t| \leq |\delta_{t0}|, \\ K_{t0}(1 - D_t), & \text{if } |\delta_t| > |\delta_{t0}|, \\ 0, & \text{if } |\delta_t| \geq |\delta_{tc}|, \end{cases} \tag{5.5}$$

where K_t is the stiffness of the Mode II TSL, which is a function of damage variable (D_t) and tangential separation δ_t, δ_{t0} is the separation up to which elastic behavior exists and damage accumulates when the separation exceeds δ_{t0}, and δ_{tc} is the separation at which the cohesive element is completely damaged. Parameters of the TSL are shown in Table 5.1. The magnitude of the Mode II traction is assumed to be same in the positive and negative shear directions. The shear damage variable is calculated from the experimental TSL (σ_t-δ_t) relationship using Equation (5.6).

$$D_t = 1 - \frac{\sigma_t}{\sigma_{t0}} \left[1 + \frac{1}{\delta_{t0}} (\delta_n - \delta_{t0}) \right]^{-1}, \tag{5.6}$$

where σ_{t0} is the traction at separation of δ_{t0}.

Figure 5.2b shows the FE predicted load versus displacement results incorporating the shape of the experimentally obtained Mode II TSL using the shear damage variable (Equation (5.6)) expressed as a function of effective shear displacement $(\delta_t - \delta_{t0})$ in tabular form. The nonlinear softening law for Mode II TSL provides load versus displacement predictions that are in excellent agreement with experimental results. In addition, when the cohesive zone size is small compared to the characteristic dimensions of the sample, the maximum traction and energy release are the only important parameters necessary to accurately predict the global load-displacement data. Due to the expected large size of the active CZM for the soft adhesive used in this work, the shape of the softening part of the TSL is exactly replicated in the CZM of the tow-substrate interaction to ensure accurate modeling of the separation processes. The cohesive zone size effects on global response were similarly observed in previous studies (Shet and Chandra 2004).

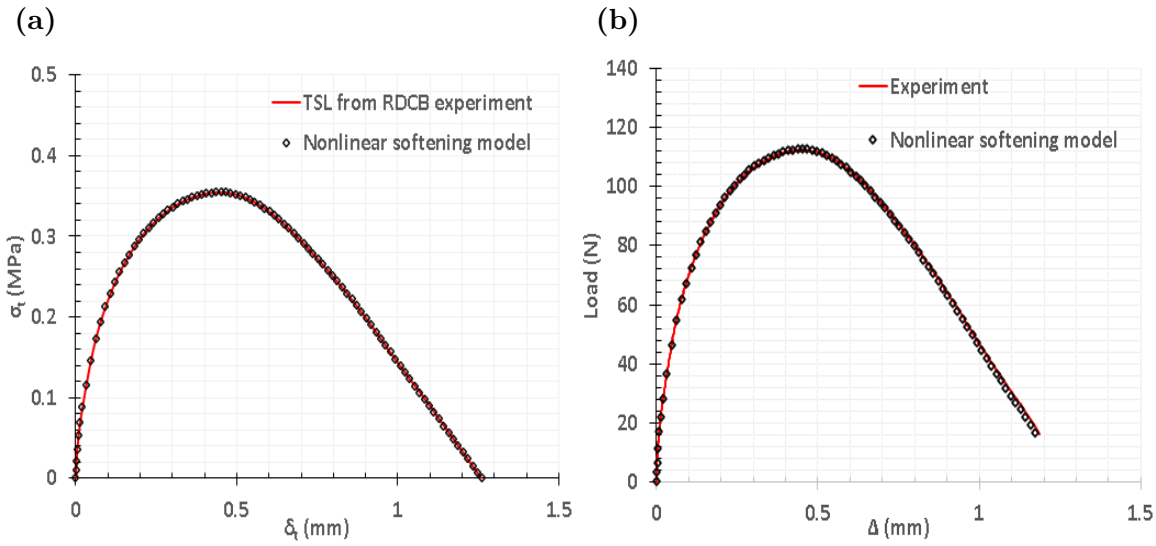

Figure 5.2 (a) Mode II traction-separation data obtained using RDCB experiment and CZM traction-separation model response using non-linear softening law, (b) load versus displacement data from Mode II RDCB experiment and model predictions using non-linear softening law

Table 5.1 Parameters of the TSL for Mode I and Mode II

Fracture mode	Elastic stiffness(N/mm^3)	Separation at damage initiation (mm)	Maximum separation (mm)	Traction at damage initiation (MPa)
Mode I	$K_{n0} = 36.86$	$\delta_{n0} = 0.0137$	$\delta_{nc} = 2.833$	$\sigma_{n0} = K_{n0}\delta_{n0} = 0.506$
Mode II	$K_{t0} = 6.98$	$\delta_{t0} = 0.0067$	$\delta_{tc} = 1.253$	$\sigma_{t0} = K_{t0}\delta_{t0} = 0.047$

Mixed mode response

For calculating the mixed mode TSL, the pure Mode III and Mode II TSL are assumed to be the same. The TSL employed in this work to model mixed mode loading is expressed in Equation (5.7).

$$\begin{bmatrix} \sigma_n \\ \sigma_t \\ \sigma_s \end{bmatrix} = \begin{bmatrix} K_n & 0 & 0 \\ 0 & K_t & 0 \\ 0 & 0 & K_s \end{bmatrix}, \tag{5.7}$$

where K_s, σ_s and δ_s are the elastic stiffness ($K_s = K_t$), traction and separation in the second shear direction (Mode III), respectively. The coupling terns in the stiffness matrix in Equation (5.7) are assumed to be zero.

Damage initiation

In this study, a quadratic traction criterion as expressed in Equation (5.8) is employed in the FE model for predicting initiation of damage.

$$\left(\frac{\langle \sigma_n \rangle}{\sigma_{n0}}\right)^2 + \left(\frac{\tau}{\sigma_{t0}}\right)^2 = 1, \tag{5.8}$$

where $\tau = \sqrt{(\sigma_t)^2 + (\sigma_s)^2}$ is the resultant shear traction, and $\langle \sigma_n \rangle$ is nonzero only for positive values of σ_n.

Damage evolution

The TSL for a mixed mode case is described using the resultant traction, $\sigma = \sqrt{(\sigma_n)^2 + (\tau)^2}$ and resultant separation, $\delta = \sqrt{(\delta_n)^2 + (\delta_t)^2 + (\delta_s)^2}$. Damage evolution for the mixed mode case is described based on the damage variable shown in

Equation (5.9), which is a generalization of the Mode I and Mode II formulae given in Equations (5.3) and (5.6).

$$D = 1 - \frac{\sigma}{\sigma_0}\left[1 + \frac{1}{\delta_0}(\delta - \delta_0)\right]^{-1}, \tag{5.9}$$

where σ_0 is the traction at initiation of damage (based on Equation (5.8)), and δ_0 is the separation at initiation. The softening part is determined by assuming a mixed mode energy criterion shown in Equation (5.10).

$$\frac{G_I}{G_{Ic}} + \frac{G_{II}}{G_{IIc}} + \frac{G_{III}}{G_{IIIc}} = 1. \tag{5.10}$$

In Equation (5.10), G_{Ic}, G_{IIc}, G_{IIIc} are the critical energy release rates for the local Mode I, Mode II and Mode III loading conditions ($G_{IIc} = G_{IIIc}$), respectively, and G_I, G_{II}, G_{III} are the local applied energy release rates at any time for the three modes, respectively. The T-S relationship satisfying Equation (5.10) for different Mixed Mode I and II ratios is shown in Figure 5.3.

Rate dependency

With regard to wrinkle initiation and growth, experimental studies and preliminary simulation results indicate that wrinkle initiation occurs immediately after initial bonding under the AFP roller. Based upon recent viscoelastic measurements for the IM7/8552-1 slit tape (Rajan et al. 2021), the separation process is expected to occur at much faster rate than the viscoelastic characteristic time of the material. For this reason, viscoelastic effects are not modeled in this work. However, for predicting the longer-term time-history of wrinkle growth, a fully time dependent TSL and viscoelastic modulus of the tow material should be considered.

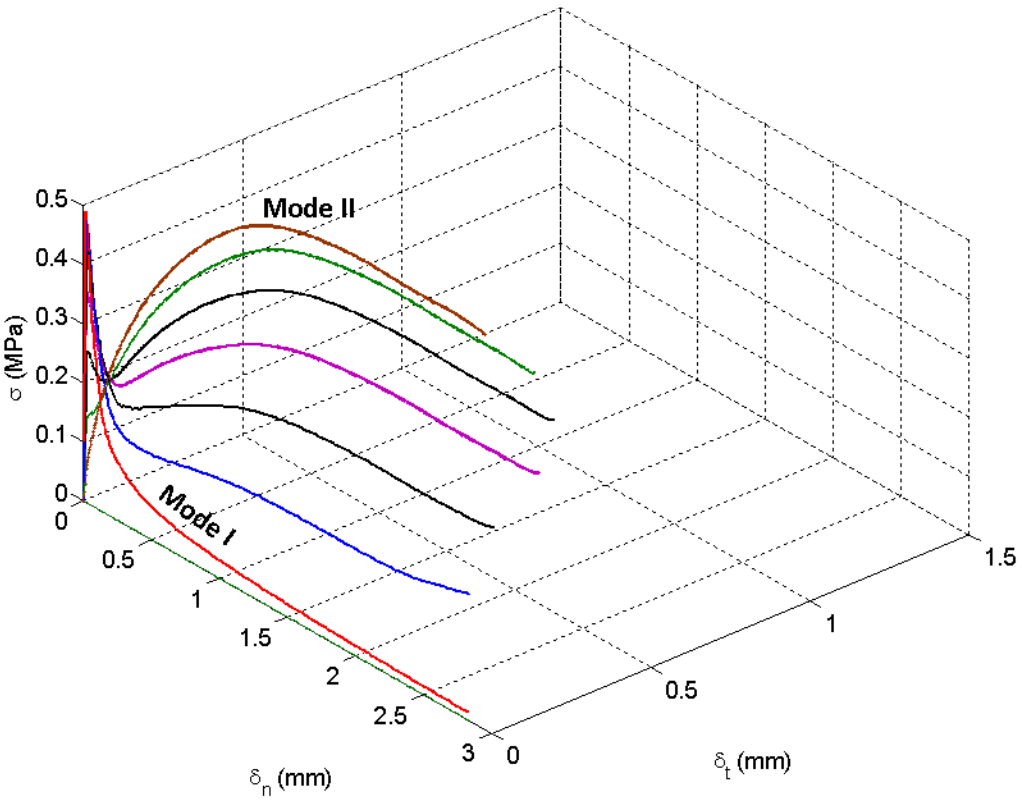

Figure 5.3 Traction separation relationship for different mode mixity ratios satisfying the energy ratio criterion given in Equation (5.10)

5.2.2 Elastic Properties of Tow: Baseline Experiments and Simulation Parameter Values

The elastic constitutive properties of uncured IM7/8552-1 tow material are assumed to be orthotropic. Due to the extremely soft matrix material in the uncured tow and limited literature data for this material system, the authors performed a number of experiments to estimate several of the elastic properties.

The elastic property in the fiber direction(E_1) is obtained by tensile experiments. The tensile test samples are shown in Figure 5.4, and Figure 5.5 shows the complete test setup. A Tinius Olsen 5000 uniaxial test frame with a load cell capacity of 22.2 KN (5000 pounds) is used in the experiments. The strain fields on the tow surface are measured using a StereoDIC system. The StereoDIC system consists of

two 5 MP Point Grey cameras with CMOS image sensors. The stereo camera images are synchronized with the load-displacement data acquisition system to capture both strain and load data during the deformation process. A LED light source with light intensity of 5000 lumens is used for illuminating the sample. The sample used in this experiment is a 6.35 mm wide slit tape (IM7/8552-1) with a gauge length of 165 mm. Glass fiber woven composite tabs with a thickness of 1 mm are bonded on both ends of the slit tape to allow it to be placed inside the grips of the tensile test machine without causing damages to the fibers from gripping pressure. A speckle pattern is applied on the surface using an airbrush with an average speckle size is 0.2 mm. The StereoDIC baseline displacement variability is $\approx$ 40 nm. Three uniaxial test samples are evaluated to obtain an average stress-strain response at a displacement-controlled loading rate of 2.5 mm per minute[2]. All three samples gave consistent results, with sample-to-sample variation less than 5%. The average stress versus strain data and a linear fit to the data are shown in Figure 5.6. Lateral compressive strains in the tensile specimens were observed to induce transverse buckling of the tow, introducing deformations that were not solely due to Poisson effect. Thus, the measured lateral strains during tensile loading were not used to extract Poisson's ratio.

Figure 5.4 Sample for uniaxial testing of tows in fiber direction

[2]The tow modulus in the fiber direction measured from a tensile experiment is independent of loading rates for the range of strain rates experienced during the AFP process

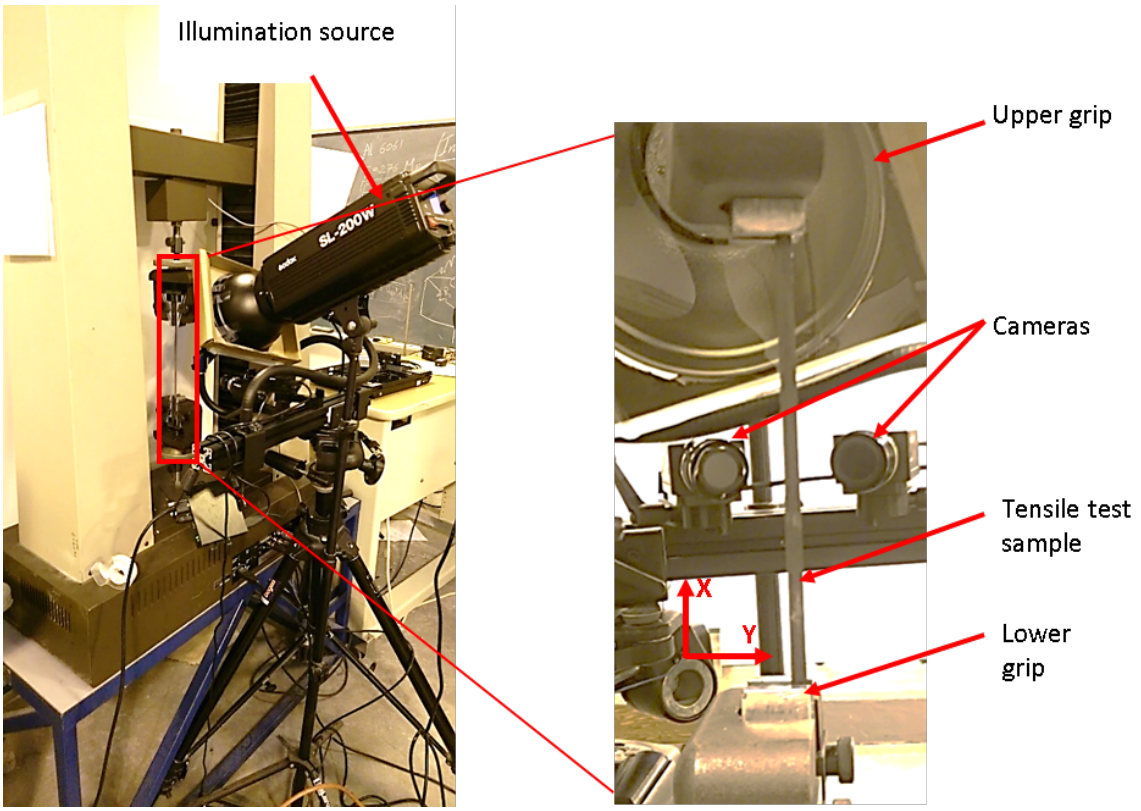

Figure 5.5 Experimental setup of uniaxial tensile test in the fiber direction

In order to obtain an estimate of the modulus in the matrix direction and the corresponding Poisson's ratio, a separate set of carefully controlled experiments were performed using a Bose ElectroForce 3200 Series test frame using a 2N (200-gram force) load cell with load variations of ±0.001 N. The transverse tensile samples are manufactured by extracting a 25.4 mm long strip from the spool of 6.35 mm wide tow. Glass fiber woven composite tabs are attached to the sides of the specimen; the tabs are then placed within the grips of the test frame, as shown in Figure 5.7. Since out-of-plane motion of the specimen is minimal due to low thickness and high compliance of the specimen, a single camera was employed with 2D DIC image analysis to analyze deformed speckle images of the tensile specimen and calculate strains. The camera used is the same type employed for the axial tensile experiments, with a Nikon 85 mm lens having a working distance of 30 mm for acquiring high magnification images. The tow surface is again speckled using an airbrush, with an average speckle size of

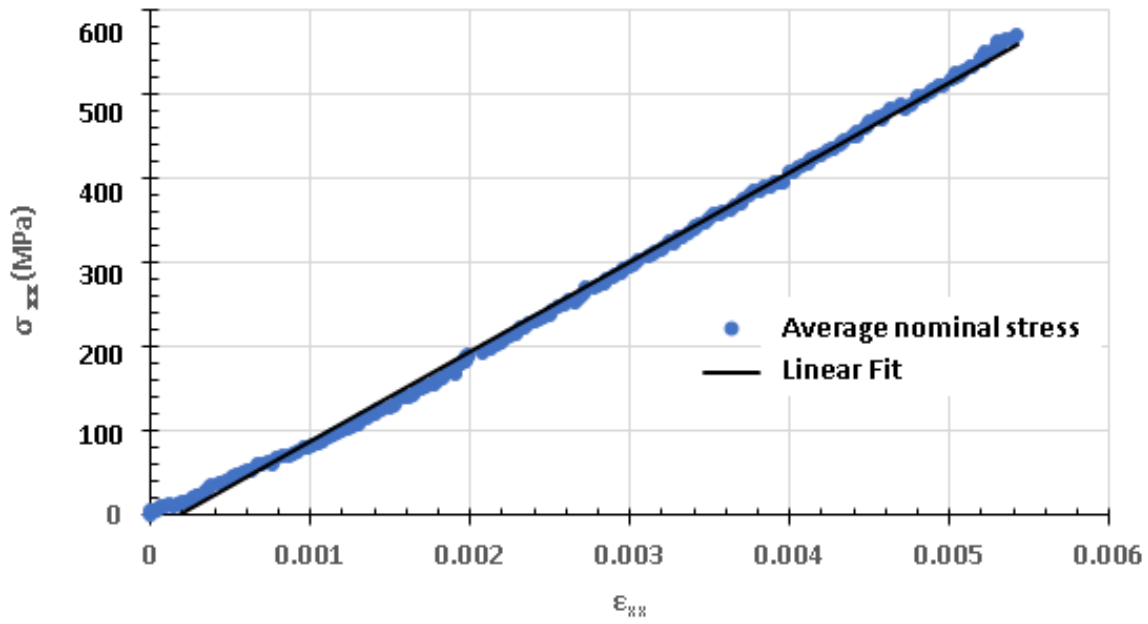

Figure 5.6 Linear fit to the average stress versus strain data obtained from 3 tensile samples

50 µm. The complete experimental setup for tensile testing in the transverse direction is shown in Figure 5.7.

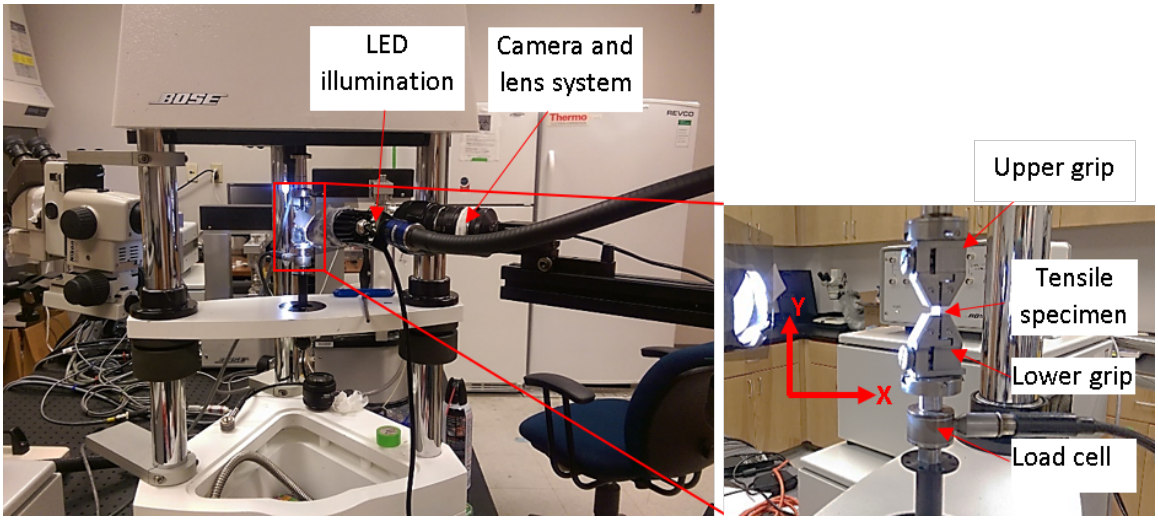

Figure 5.7 Experimental set up for transverse direction tensile loading showing camera and light system; INSET: enlarged view of the specimen in the tensile grips

The average stress versus average strain in the matrix direction for loading rate of 25 mm per minute is shown in Figure 5.8. The transverse stress-strain data exhibited substantial variability due to (a) low strength of the matrix in the uncured state, increasing the difficulties in sample preparation and mechanical loading without initial damage to the specimen and (b) viscoelastic effects in the matrix epoxy during the specimen preparation and tensile experiment. The modulus in the matrix direction is determined by measuring slope of the initial part of the stress strain curve where strain is lower than 0.01%. The average modulus in the matrix direction is 345 MPa. Due to high stiffness of the carbon fibers, strain in the fiber direction is negligible (much lower than the measurement accuracy). Regarding the remaining elastic parameters, a computational parametric study showed the following;

- wrinkle formation mechanism is unaffected for values of Poisson's ratio, ν_{12}, in the range $0.1 \leq \nu_{12} \leq 1$,
- values of the in-plane and out-of-plane shear moduli, G_{12} and G_{13}, in the range 500 MPa $\leq (G_{12}, G_{13}) \leq$ 5000 MPa gave similar wrinkle formation.

Thus, it is assumed in this work, $\nu_{12} = 0.24$ and all shear moduli[3] $G_{12} = G_{13} = G_{23}$ = 5000MPa. All relevant material properties and geometric dimensions of the tow model are shown in Table 5.2. Only the short-term response of the tow is modeled, as wrinkles initiate almost instantaneously after passage of the compaction roller.

As a final note regarding material characterization for the AFP simulations, bending stiffness of the tow has been shown to be a major parameter influencing wrinkle formation during the AFP process (Liang, Hamila, Peillon, and Boisse 2014). Due to a lack of experimental data for bending stiffness of uncured IM7/8552-1 slit tape at the process temperature of 40 °C, a series of three-point bend creep experiments were

[3]A miniature picture frame experiment could be performed for accurate measurement of the in-plane shear modulus, G_{12}, though the authors did not do so since the wrinkling process was shown to be similar for any quantitative value in the range noted above.

performed by using a TA dynamic mechanical analysis system (Rajan, Sutton, Oseli, Emri, and Matta 2017; Rajan et al. 2021). The creep-compliance master curve shown in Figure 5.9 summarizes the experimental effort and provides the relevant viscoelastic response of an uncured IM7/8552-1 tow at 40 °C (see Appendix B for details of the creep experiment). A brief development describing how the DMA measurements of compliance vs time are used to ensure that the continuum shell elements used to model the tow have the same bending stiffness is discusses in Rajan et al. (2020b).

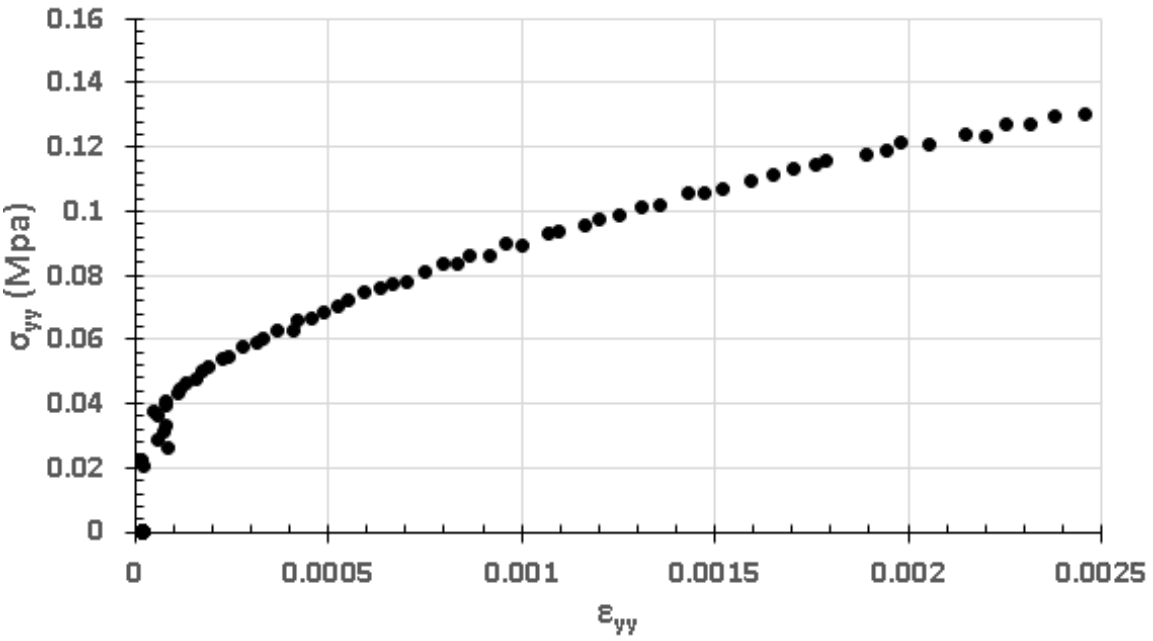

Figure 5.8 Average stress versus strain data in the matrix direction obtained from 3 tensile samples

Table 5.2 Material properties and thickness of the prepreg tow model

E_x	E_y	ν_{xy}	G_{xy}	G_{xz}	G_{yz}	Thickness (d)
106 GPa	0.35 GPa	0.24	5 GPa	5 GPa	5 GPa	0.107 mm

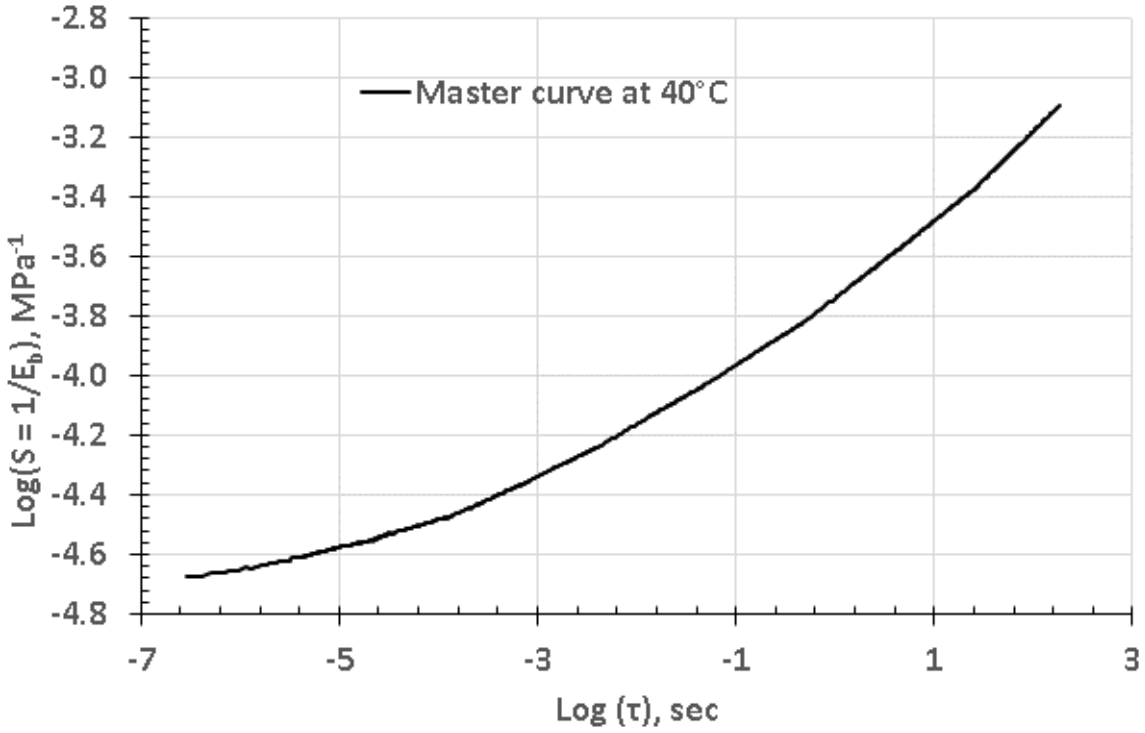

Figure 5.9 Creep compliance master curve for IM7/8552-1 tow at 40 °C

5.3 AFP SIMULATIONS

Simulation of the AFP process requires that several components involved in the AFP process. including the tool, compaction roller, tow and tow guidance mechanism, are modeled. In this work, all simulations are performed using Abaqus Explicit. The complete model of the AFP process is shown in Figure 5.10. As shown in Table 5.3, from a computational standpoint the stable simulation time increment for the AFP process is controlled by the size of the tow element. The AFP simulations in this work identified an optimum tow element size of 0.5 mm x 0.5 mm, which is the largest element size for which wrinkle spacing and amplitude are consistently repeated. Further decreases in the size of the element significantly increase the computational time. For the optimal tow element size, 5.2 x 10^6 iterations are required to complete each simulation. In addition to defining an optimal tow element size, mass

scaling of each tow element is employed to increase the stable time increment to 1 x 10^{-7} seconds without significantly affecting the computational results. Here, mass scaling of only the tow by a factor of 6.75 was employed. With the selected mass scaling, computational time for a 12 node 1.4 GHz cluster is about 4 hours which can be reduced to less than an hour by using a 32 node 2.5 GHz cluster. In the following sections, models of the individual parts of the AFP process are described.

Table 5.3 Summary of the element type, minimum size of the element, number of elements and stable time increment for different components of the FE model

Component	Element type	Minimum element size (mm)	Total number of elements	Stable time increment (µs)
Tow	Four node doubly curved shell element with reduced integration (S4R) and hourglass control	0.5 x 0.5	11128	0.0385
Compaction roller rubber	Eight node linear brick element with incompatible modes (C3D8I)	1.88 x 1.93 x 3.07	16218	2.96
Tool	Four node 3-D bilinear rigid quadrilateral element (R3D4)	2 x 2	62500	
Tow guide	Four node 3-D bilinear rigid quadrilateral element (R3D4)	0.25 x 1	8646	
Pin	Four node 3-D bilinear rigid quadrilateral element (R3D4)	2 x 2	2576	
Hub	Four node 3-D bilinear rigid quadrilateral element (R3D4)	2 x 2	2444	

5.3.1 AFP substrate (Tool)

Since the author's previous experimental measurements of wrinkle shape and size using StereoDIC were performed on a flat tool where the tow was placed along different radii of curvature (R = 305 mm, 1270 mm and 2540 mm), all simulations in this study included a rigid flat panel model for the substrate where the tow layup process is performed. Figure 5.10 shows the tool model along with a model of the roller and

tow placement path. Since the tool is a thick steel plate, finite element discretization of the tool/substrate is performed using rigid shell elements (R3D4 elements in Abaqus). The size of the tool is 500 mm x 500 mm and the size of each element is 2 mm x 2 mm. Also shown in Figure 5.10 is a cylindrical datum coordinate system defined on the axis of the roller at a radial distance, R, from the global system, where R is equal to the required radius of the curved tow paths. All boundary conditions are defined based on this coordinate system. The translational and rotational degrees of freedom of the tool are constrained at the rigid body reference point (O) of the tool. For defining the deformations and stresses on the deformed shape of the tow, a local orthonormal coordinate system (t, b, n) is defined and shown in Figure 5.10. The direction t is tangent to the tow path, b is in the transverse or width direction of the tow and n is normal to the surface of the tow facing the tool surface. The origin of the local coordinate axes t and b is located at the intersection of the mid-planes through the thickness and width direction of the tow. The material properties of the tow are defined based on local coordinates.

5.3.2 Compaction Roller

The compaction roller in the AFP system consists of a rigid inner cylinder with a compliant material on the outer layer (usually a silicone rubber layer in an AFP system). The soft outer layer of the compaction roller maintains a more uniform pressure distribution across the tow to reduce damage in the tow when it is placed on the substrate. The roller FE mesh along with inner cylinder and pin are shown in Fig. 12. The outer rubber material is discretized using three-dimensional, linear hexahedral elements with incompatibility mode (C3D8I element in Abaqus). The

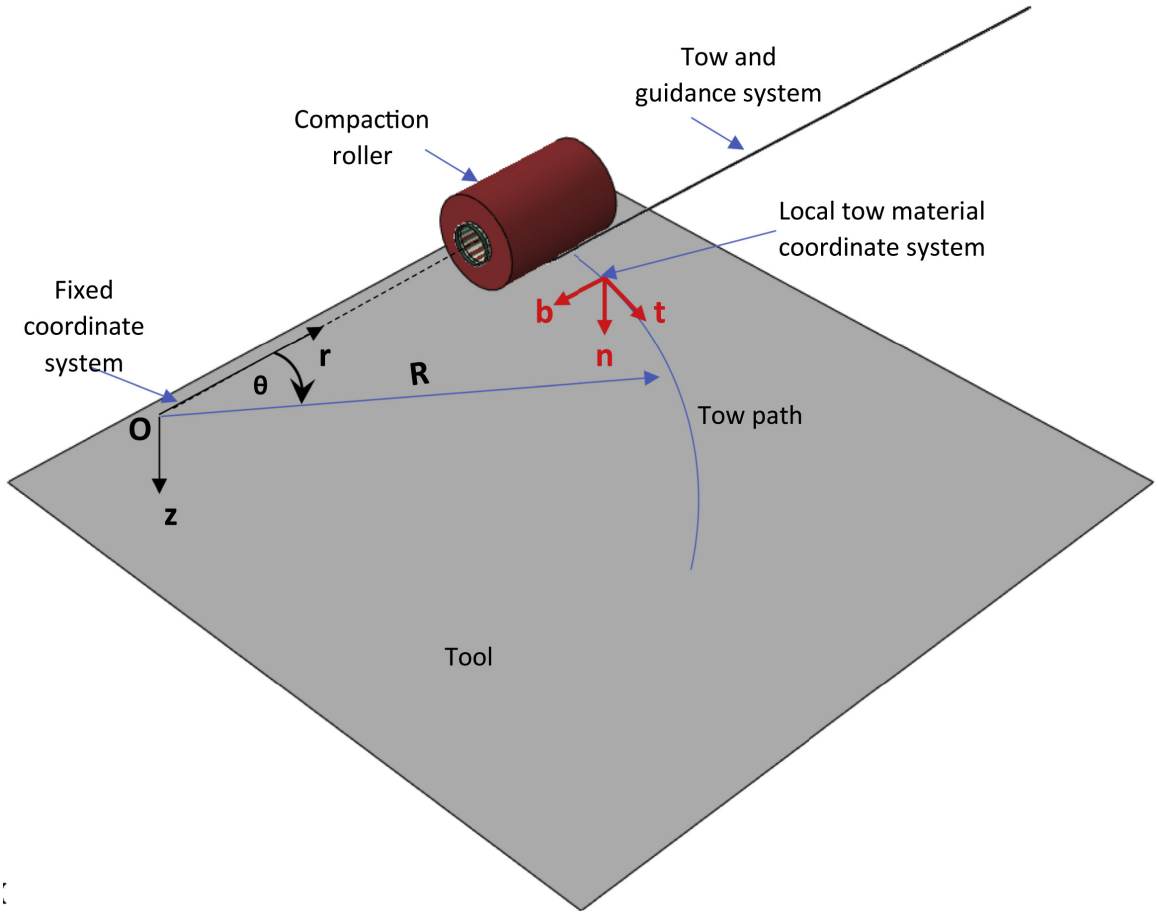

Figure 5.10 Finite element model of the AFP process showing individual components, roller path and coordinate system

outer layer of material is modeled as an isotropic linear elastic material[4] with Young's modulus of 50 MPa and Poisson's ratio of 0.45. The roller has an outer diameter of 70 mm, inner diameter of 30 mm and width of 100 mm. All degrees of freedom of the inner surface of the roller are tied to a rigid hub that is modeled using rigid shell elements. A rigid pin in the center of the roller also is modeled using rigid shell elements (see Figure 5.11). Frictionless contact interaction is defined between the hub and the pin to allow the hub to rotate freely about the pin axis. Motion of the hub along the radial coordinate direction is constrained so that there is no relative

[4]The authors also used a nonlinear hyperplastic constitutive relationship for the outer roller layer for comparison to the results when using a linear elastic material. The results were essentially the same for wrinkle prediction for both mode when using the experimental estimate for roller pressure of 1 MPa.

slip between the hub and the pin along the pin axis. Motion of the compaction roller is controlled by specifying boundary conditions for the rigid body reference point of the pin defined at the origin of the coordinate system shown in Figure 5.10.

Simulations are performed in two steps. In the first step, a downward displacement (z direction) of 2 mm is specified for the pin, constraining all other degrees of freedom. The first step simulates application of compaction pressure to the tow. The downward displacement is incremented from zero to 2 mm in 0.02 sec along a smooth curve such that downward velocity of the roller at the end of the first step is zero with rebounding of the roller from the tool eliminated. The deformed shape of the compaction roller after the first step is shown in Figure 5.12. The 2 mm downward displacement results in the same contact length (12 mm) as in the validation AFP experiment. Recently, Bakhshi and Hojjati (2020) identified deformation of the roller as a contributing parameter influencing wrinkle formation. This led investigators to suggest the need for improved roller designs to enhance the distribution of compaction pressure (Denkena, Schmidt, and Weber 2016) for AFP layup on doubly curved surfaces.

In the second step, the pin is rotated about the z-axis while constraining all other degrees of freedom of the pin. The distance of the center of the pin axis from the axis of rotation is set to be equal to the required radius of curvature of the tow path, as shown in Figure 5.10. The angle of rotation (θ) of the pin about the z-axis for a specified radius is calculated by requiring the total length of the path of the roller about the center of the axis to be equal for all radii of curvature (1.2 radians for R = 305 mm). The angle θ is increased from zero to 1.2 radians at a constant angular velocity which corresponds to a layup speed of 1.83 m/sec.

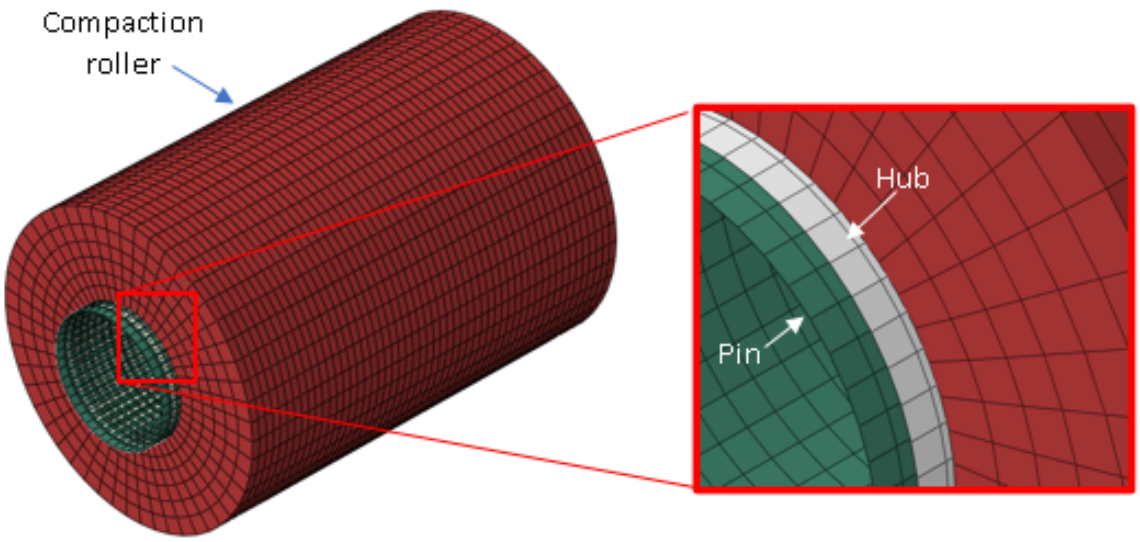

Figure 5.11 Finite element model of the roller showing outer rubber layer, hub and pin

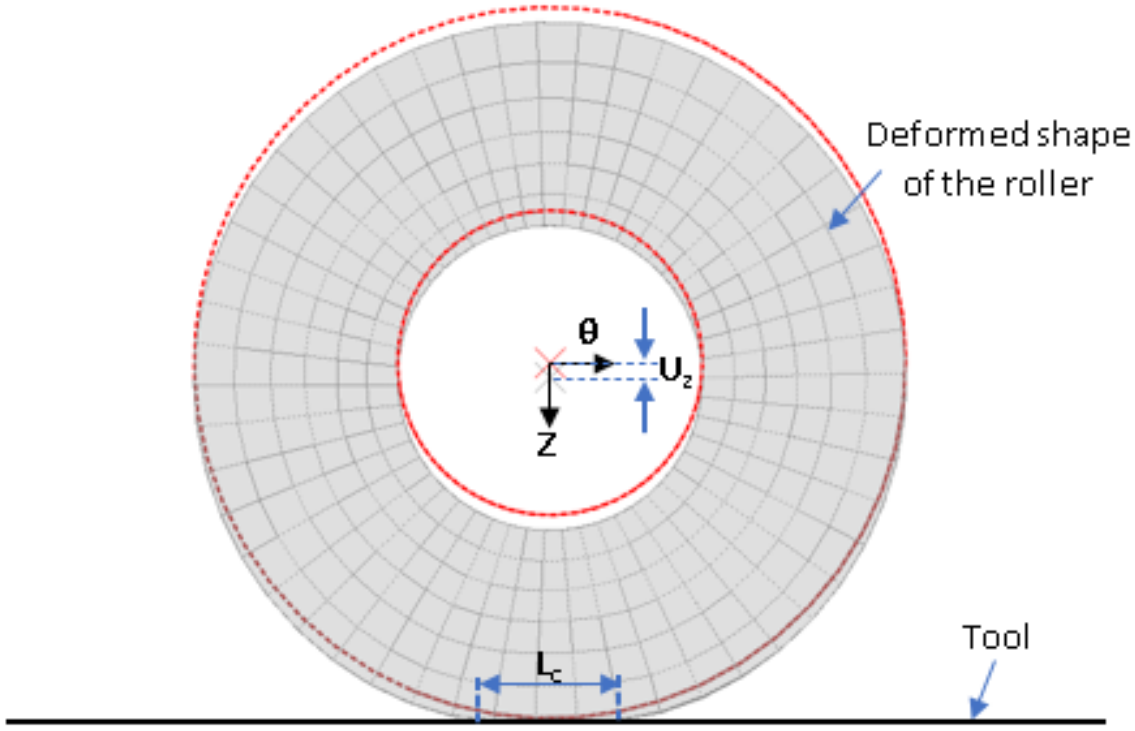

Figure 5.12 Deformed shape of the roller superimposed on the undeformed shape (dotted line); contact length, L_c is 12 mm for a downward displacement, $U_z = 2$ mm (θ is defined in Figure 5.10)

5.3.3 Tow Guidance System

Since the uncured tow is held together in the transverse direction by a weak matrix and is susceptible to buckling of the stiff carbon fibers under compressive load, the AFP head consists of a series of rollers for controlling the feed rate and slots for controlling the path of the tow. One of the roles of the guidance system is to eliminate unwanted deformation of the tow before it enters the compaction roller. Since any form of buckling of the tow during tow feeding can have a detrimental effect on the quality on the tow placement, slight pretension (19 N) is applied to the tow to prevent compressive stresses in the tow and possible buckling within the tow feeding mechanism. In this regard, the authors have observed defects such as overlaps, gaps and twist in the as-placed tow for low values of tow tension. Another potential buckling concern is shown in Figure 5.13. Here, bucking of the tow immediately ahead of the roller is observed in the simulations when the tow is not properly guided ahead of the roller, resulting in deviation of the tow from the specified path that induces local wrinkles just ahead of the roller. The tow guidance system shown in Figure 5.13 consists of a rigid slot for the tow passage and constrains the tow only up to the point of contact of the tow with the roller. Compressive stress at the inner radius of the tow ahead of the roller induces buckling of the tow, resulting in unwanted contact of the tow with the substrate before application of roller compaction pressure; early contact can lead to deviations from the as-specified path.

The photograph in Figure 5.14a shows the compaction roller and tow guidance system in our previous AFP experimental work (Rajan et al. 2019b). The tow guidance system maintains a small clearance between the tow-guide and tool to prevent possible interference between the two. Simulation results including the modified tow guidance system are presented in Figure 5.15a, showing no sign of buckling or unintended contact of the tow with the tool. Hence the tow-guide shown in Figure 5.14a is shown to be effective in preventing pre-compaction buckling of the tow, while main-

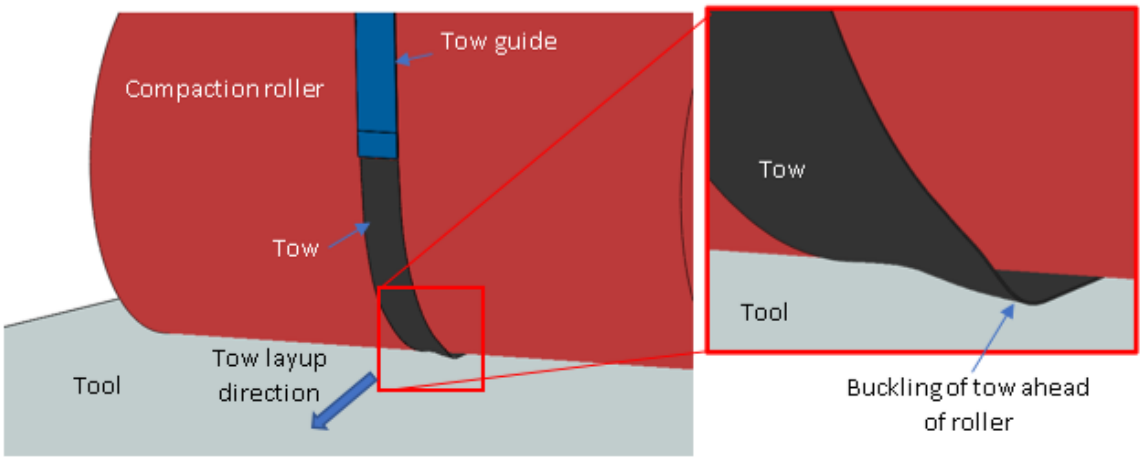

Figure 5.13 Buckling of the tow ahead of the roller due to the absence of tow guidance ahead of the roller; inset showing magnified view of the tow bucking and contact of the tow with the tool before application of compaction pressure

taining the tow path along the predefined radius. In these simulations, the FE model of the tow-guide is discretized using rigid shell elements and motion of the tow-guide is kinematically coupled to the roller pin so that the compaction roller, pin and the tow-guide moves as a rigid body. The current model didn't include complex mechanism used for tow feeding, which involves multiple rollers within an actual AFP head, as their presence was not judged to be important for accurate prediction of wrinkle formation.

In summary, the tow-guide has two parts, one representing tow guidance close to the roller and a second one for simulating tow constraint in the tow feeding mechanism. The latter consists of a rigid slot for tow passage where the tow is constrained to translate longitudinally (fiber direction). Pretension is applied to the tow model by specifying a distributed shell edge load of 3 N/mm to the far end of the tow. The tow guide system close to the roller described previously allows the tow to be in contact with the roller, providing better representation of the real-world AFP process shown in Figure 5.14a. Furthermore, the tow-guide constrains out-of-plane buckling of the tow towards the tool so that unintended contact with the tool is prevented. In this work, tangential contact of the tow with the roller is modeled with a penalty friction

coefficient of 0.2. Possible stickiness of the tow with the roller can be included using a cohesive surface interaction criterion; this effect was not included in the AFP model considered in this work.

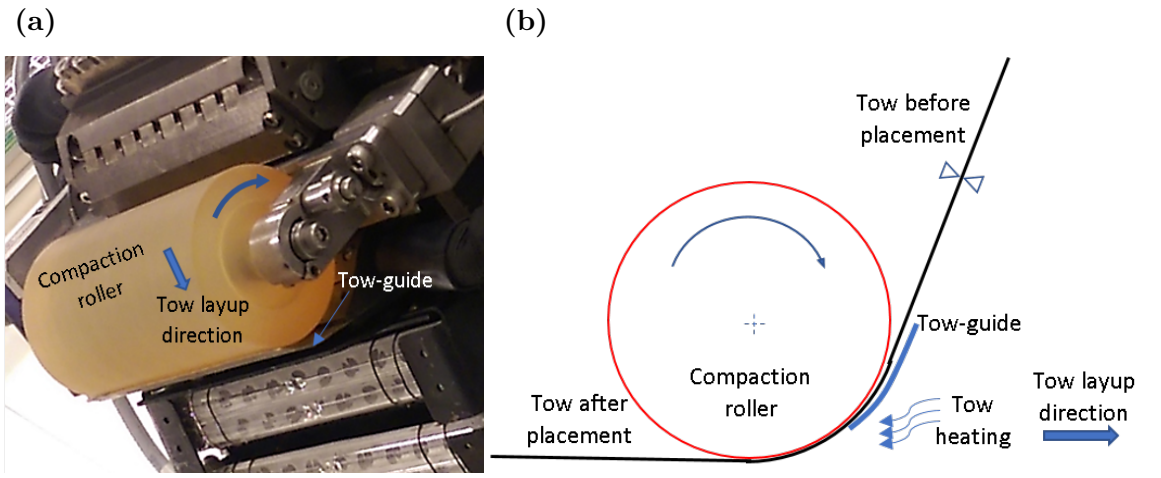

Figure 5.14 (a) Photograph of the roller showing the position of the tow guidance system ahead of the roller and (b) schematic of the tow placement process

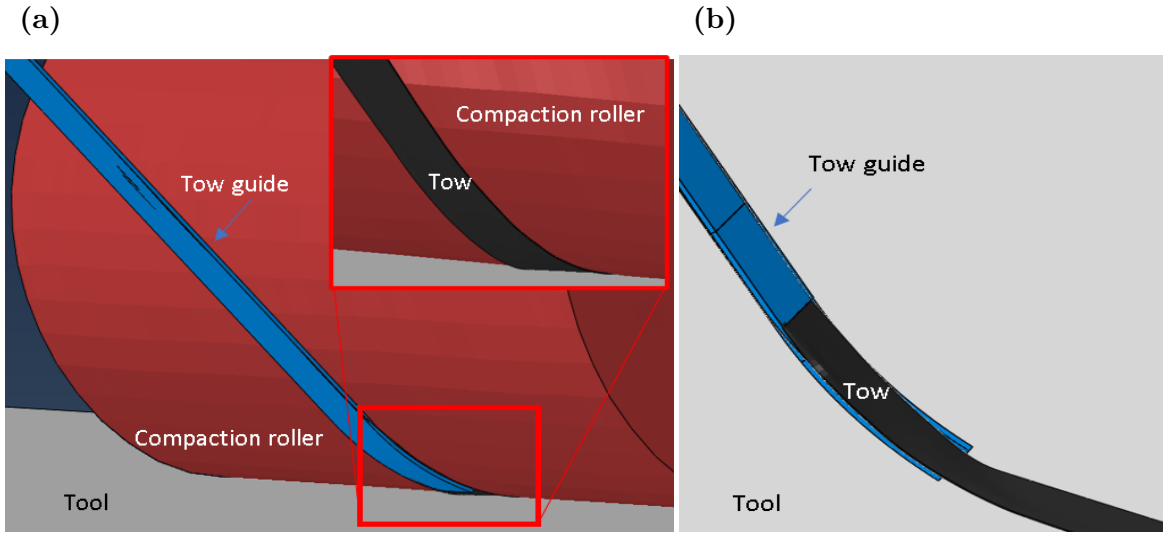

Figure 5.15 (a) Finite element modeling of tow guidance system, INSET: magnified view of the tow ahead of the roller; for better visibility the tow, the guidance system is removed from the view and (b) magnified view of the tow guidance system close to the roller; the roller is removed from the view for better visibility of the tow guidance system and tow interaction ahead of the roller

5.3.4 Prepreg Tow Model

The tow is modeled using quadratic shell elements with orthotropic lamina properties. The experimental program for measurement of constitutive properties of the lamina is described in Section 5.2.2. Tow adhesion to the substrate is modeled using the cohesive contact interaction criteria available in the Abaqus framework. The constitutive behavior of the cohesive contact is fully defined using the mixed mode TSL in Section 5.2.1. Cohesive contact interaction is found to be more efficient than using cohesive elements for modeling tow adhesion. The sticky contact condition is invoked when any of the nodes of the tow experience contact with the tool surface.

5.4 RESULTS AND DISCUSSION

Simulations of the AFP process, including incorporation of the measured TSL for tow-to-tow bonding during placement, are performed for four different circular paths, with radii of curvature R = 305 mm, R = 635 mm. R = 1270 mm and R = 2540 mm. Results for all four simulations are reported in this section. For mixed mode TSL, the damage parameter D is determined based on the change in slope of the traction-separation response with increasing δ (Camanho and Dávila 2002). It is noted that experimental data for wrinkle formation during AFP placement of the tows is available in Rajan et al. (2019b) for three of the selected radii of curvature. Simulation predictions are compared to the experimental results for R = 305 mm, R = 1270 mm and R = 2540 mm, the three radii of curvature where data exists. Consistent with experimental observations, our simulations (a) show no evidence of wrinkles for radii of curvature of 1270 mm and 2540 mm and (b) predict wrinkle formation occurs for R = 305 mm. Simulations also predict wrinkle formation for R = 635 mm, but with lower frequency than for R = 305 mm.

Figures 5.16a and 5.16b present the predicted wrinkle shape and wrinkle amplitude for R = 305 mm and R = 635 mm, respectively. Inspection of Figures 5.16a and

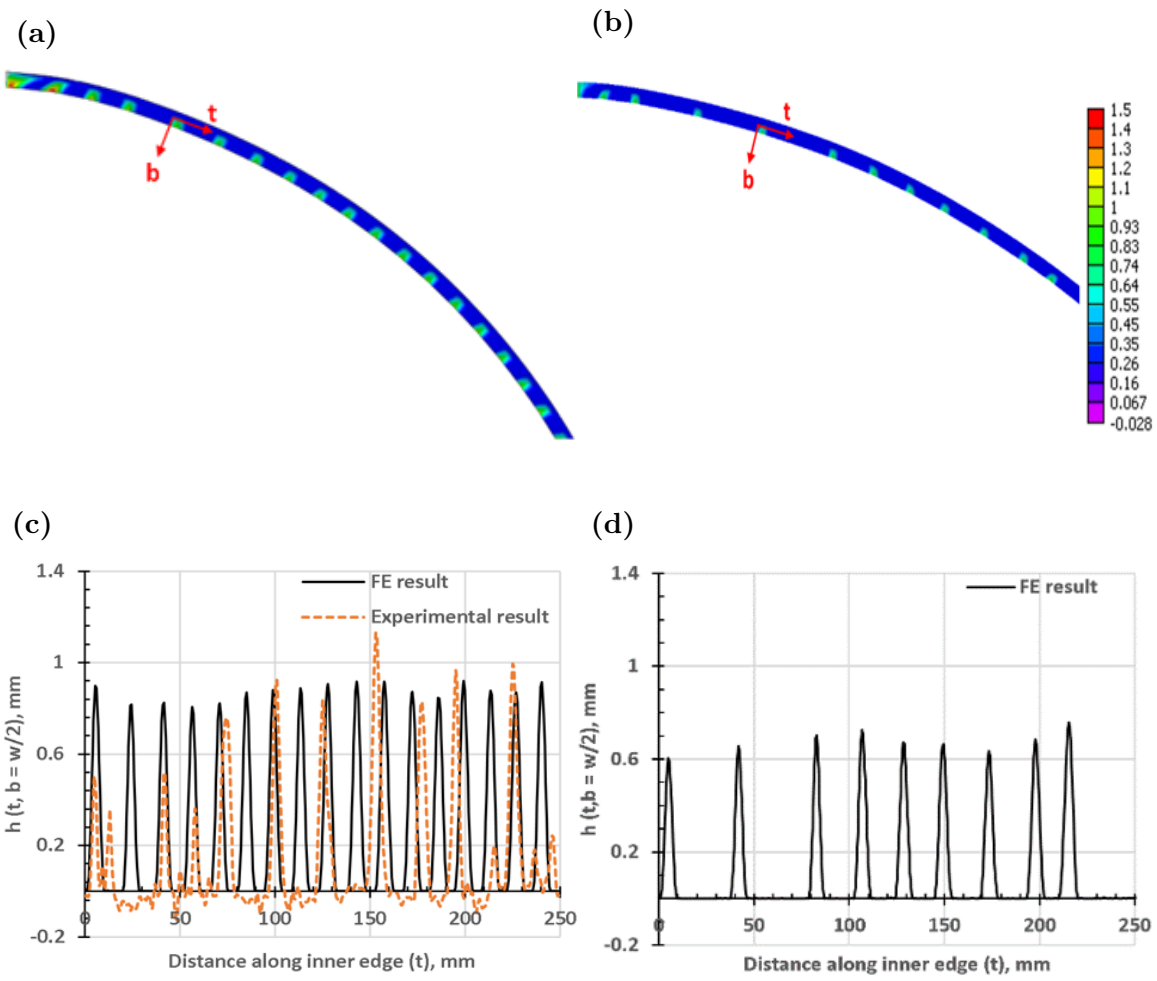

Figure 5.16 (a) Simulation predictions of wrinkle shape, wrinkle amplitude and wrinkle spacing for $R = 305$ mm, (b) $R = 635$ mm, (c) FE and experimental result of the spatial distribution of the wrinkle height along inner edge of the tow for R = 305 mm and (d) FE results for $R = 635$ mm

5.16b shows that free edge conditions near the start and end of the tow path cause deviations in wrinkle characteristics; these wrinkles are not included in Figures 5.16c and 5.16d. The horizontal coordinate of the graphs in Figures 5.16c and 5.16d is the arc length along the inner edge and is offset to zero at the beginning of the 5^{th} wrinkle along the tow path. Figure 5.16c directly compares the simulation and experimental measurements for wrinkle spacing and height along the inner edge of the tow for $R =$ 305 mm. As shown in Figure 5.16c, simulations predict that wrinkles form at quite regular intervals with a consistent amplitude.

Table 5.4 summarizes and compares FEA predictions and experimental measurements of wrinkle spacing and amplitude for all path radii of curvature. As shown in Table 5.4, the simulation results for $R = 2540$ mm, 1270 mm and 305 mm are in very good agreement with experimental results. Table 5.4 confirms that the predicted mean values for amplitude and spacing/wavelength are in very good agreement with experimental measurements. Consistent with expectations, the experimental measurements have much larger variability in the wrinkle amplitude and wavelength. One of the reasons for larger variability in the experimental measurements is the presence of substrate surface defects, such as roughness, overlaps and gaps on the tow layup substrate, as reported in recently published work (Rajan et al. 2019b). For example, the negative values in the amplitude of wrinkles seen in experimental data are due to the presence of gaps in the substrate. Substrate surface imperfections are not modeled in the FE model presented in this chapter.

Table 5.4 Comparison of finite element and experimental results of wrinkle wavelength and amplitude for different radii of curvature

R	Wrinkle wavelength, λ (mm)		Wrinkle amplitude, h (mm)	
(mm)	Finite element	Experimental	Finite element	Experimental
305	14.65 ± 1.35	15.55 ± 7.14	0.86 ± 0.04	0.50 ± 0.32
635	26.29 ± 8.26	Not available	0.67 ± 0.05	Not available
1270	No wrinkles	No wrinkles	0	0
2540	No wrinkles	No wrinkles	0	0

The spacing and amplitude of the predicted wrinkles along the inner edge of the tow for a radius of curvature of 635 mm are shown in Figure 5.16d. Consistent with the discussion for $R = 305$ mm, four wrinkles near the start and end of the tow path are not included in Figure 5.16d. As expected, the predicted number of wrinkles per unit length is found to be less (higher wavelength) than for $R = 305$ mm. In addition, the maximum predicted amplitude of wrinkles decreases relative to the predictions for $R = 305$ mm. For the larger radii of curvature ($R = 1270$ mm and 2540 mm), no wrinkles were observed experimentally and are not predicted to occur

in the simulations.

Taken together, the agreement between the experimental measurements and simulation predictions indicate that the simulation process developed in this work is an accurate model for predicting wrinkling or similar defects that occur during the AFP process. Thus, for a given tow material system (e.g. for mixed mode TSL defining the cohesive behavior of the tow), the simulation platform can be used to determine the range of path curvatures that can be accommodated without incurring wrinkle defects during the process. Furthermore, the effect of other parameters (e.g. roller composition, roller pressure, process temperature, lay-down speed) can be assessed using the AFP model and the appropriate TSL for the tow material, temperature and pressure. In addition to this important application of the author's simulation platform for robust AFP processing with minimal wrinkling, an equally important and interesting aspect of the simulations is to improve understanding of the fundamental mechanistic aspects that are present and govern the initiation and evolution of wrinkles in tows during placement. This aspect is the focus of the remainder of the discussion.

5.4.1 Steady state stresses on the tow in the wrinkle region

Considering the "steady-state" longitudinal stress distribution on the top surface of a tow over a representative length (including at least three wrinkles) for the two shortest radii of curvature where wrinkles formed, the predicted stress distributions for $R = 305$ mm and $R = 635$ mm are shown in Figures 5.17a and 5.17b, respectively. The maximum tensile stresses due to out-of-plane buckling occurs at the location of each wrinkle. On both sides of the uplifted wrinkle are two clearly visible compressive regions. Thus, each wrinkle affects a finite-sized region surrounding the delaminated, uplifted tow wrinkle location. Between these regions, the tow is predicted to have low, nearly constant, longitudinal stress.

Since physically observable wrinkling is initiated by stresses and deformations within the tow, further investigation is focused on the conditions that are predicted to be present at the mid-thickness of the tow along the inner edge of the tow where the maximum compressive conditions are expected to occur. Noting that conditions between wrinkles are essentially the same (see Figures 5.17a and 5.17b), focus will be on the longitudinal stress between two specific wrinkles.

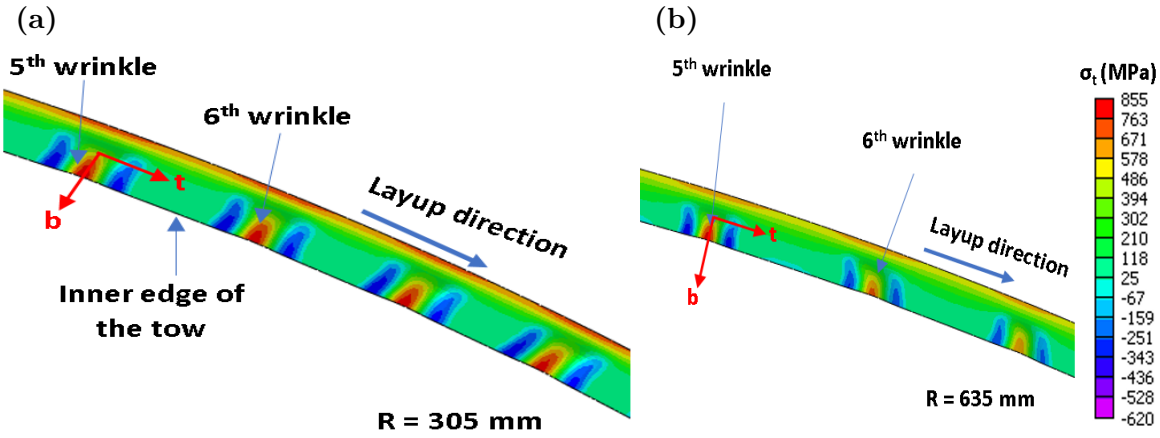

Figure 5.17 (a) Steady-state longitudinal stress map on the top of the tow surface for $R = 305$ mm and (b) $R = 635$ mm

Figure 5.18 presents the compressive longitudinal stress at mid-thickness along the inner edge[5] between the 5th and 6th wrinkle for all four radii of curvature. For R = 2540 mm, the compressive stress along the length is constant at 100 MPa. As R decreases to 1270 mm, the compressive stress remains constant but has increased to 230 MPa without wrinkle formation. The rapid increase in longitudinal compression indicates that stresses are approaching values that can initiate wrinkling. For the two smaller radii of curvature, wrinkling has occurred, and the stress distributions are much different. In both cases, the minimum compressive stress of 20 MPa at mid-thickness is at the wrinkle location, with the stress rising to a maximum midway between the wrinkles. The maximum compressive stress for $R = 635$ mm is 2X larger

[5]The origin of the coordinate system is selected at the point of maximum wrinkle amplitude of the 5th wrinkle and normalization is with respect to the distance between the peaks of 5th and 6th wrinkle (λ)

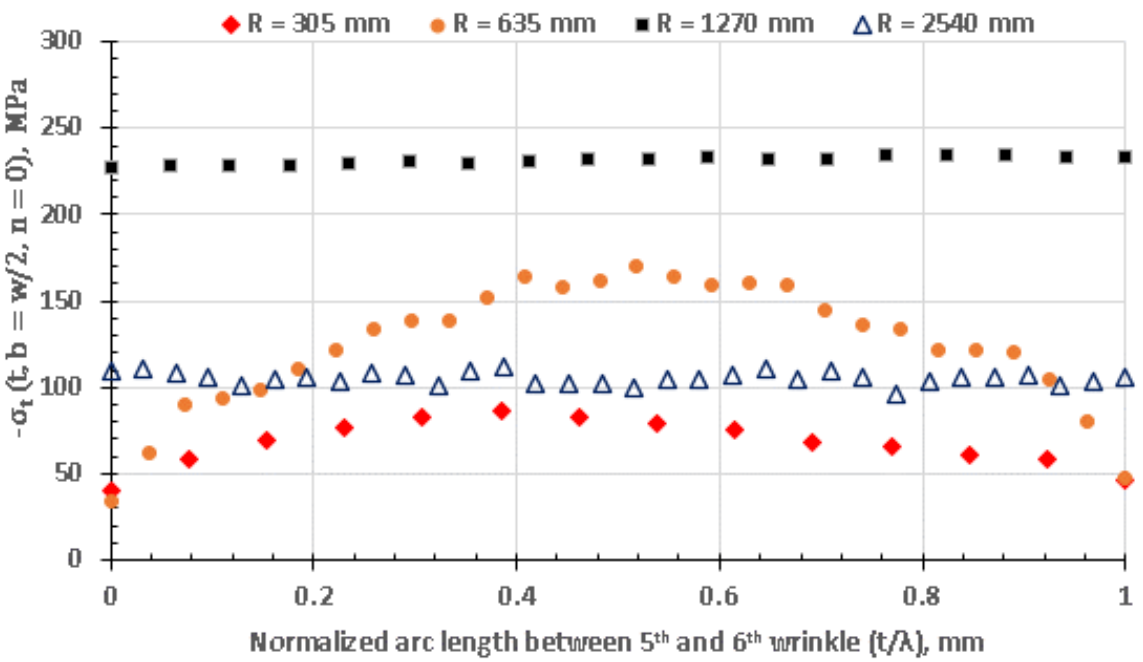

Figure 5.18 Steady state longitudinal stress along normalized inner edge distance (t/λ) of the tow about neutral plane (for $R = 305$ mm and 635 mm the stress distribution is of the region between the peaks of 5^{th} and 6^{th} wrinkle)

than the maximum stress for $R = 305$ mm. Taken together, these findings indicate that as the number of wrinkles per unit length of the tow increases (wavelength decreases), there is increased relaxation of the compressive stress along the inner edge between wrinkles due to separation of the tow in the wrinkle region altering the local boundary conditions. These results are in contrast with the nearly constant compressive stress distribution predicted for higher radii of curvature ($R = 1270$ mm and 2540 mm). Precisely how these "steady-state" conditions are developed requires close investigation of the conditions within the tow and on the tow adhesion surface as the roller passes over the tow and moves away. This process is described in some detail in the next section.

5.4.2 Mechanisms for initiation and spacing of wrinkles

The mechanism of wrinkle formation can be studied by examining the evolution of stresses and deformations of the tow during the AFP placement process. The longitudinal stress distributions on the top surface of the tow (σ_t at $n = -d/2$) at different times, from initiation of tow separation to complete separation and formation of wrinkles, are shown in Figure 5.19 for the two shortest radii of curvature ($R = 305$ mm and $R = 635$ mm). The section of the tow shown in Figure 5.19 is a fixed length of the tow for a given radius of curvature between 5^{th} wrinkle under the roller and 6^{th} wrinkle. The reference time (τ) is based on the initiation time for the 6^{th} wrinkle. The dotted red lines in each figure indicate the roller contact area during and immediately after initiation of the 6^{th} wrinkle. Inspection of the compressive longitudinal stress along the inner edge of the tow immediately before initiation of the 6^{th} wrinkle in Figure 5.19 shows similar stress magnitude for $R = 305$ mm and 635 mm. Line plots showing the temporal evolution of σ_t along the inner edge are shown as solid lines in Figures 5.20a 5.20b for $R = 305$ mm and 635 mm, respectively. For both $R = 305$ mm and 635 mm, the magnitude of σ_t along the inner edge increases as distance from 5^{th} wrinkle increases, rapidly reaching a maximum just before initiation of the 6^{th} wrinkle, with an elapsed time that is less than 1 ms after passage of the roller. As the wrinkle forms, compressive stresses along the inner surface rapidly decrease. Within 3 ms after wrinkle formation, the stresses are approaching the "steady-state" levels shown in Figures 5.17 and 5.18.

Also shown in Figures 5.20a and 5.20b are the evolutions of uplift displacement of the tow along the inner edge for $R = 305$ mm and 635 mm, respectively. The wrinkle uplift occurs just as separation initiates at the tow-substrate surface. Additional insight regarding uplift displacement at the initiation of 6^{th} wrinkle is provided in Figure 5.21, which presents a higher resolution view of tow uplift displacement, showing the presence of micro-buckles along the inner edge for both radii of curva-

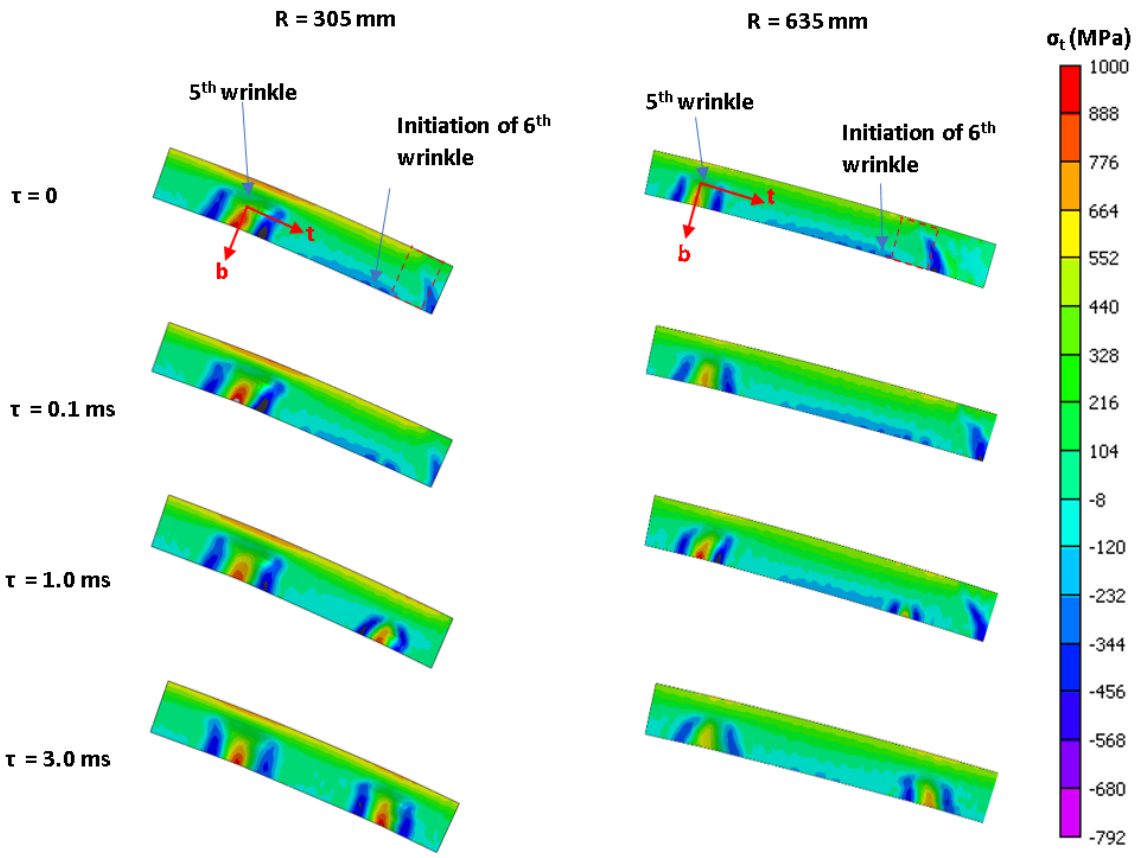

Figure 5.19 Longitudinal stress map on the top surface of the tow for $R = 305$ mm and $R = 635$ mm, between 5^{th} and 6^{th} wrinkle, at different times starting from initiation to complete formation of the next wrinkle

ture. The micro buckles are present during the placement process before initiation of large wrinkles. Based on the stress distributions in the tow up to wrinkle initiation shown in Figures 5.20a and 5.20b, the micro-buckles allow partial relaxation of the compressive stresses on the inner edge, so that σ_t is only slightly different for $R = 305$ mm and $R = 635$ mm. The peaks in compressive stress of Figures 5.20a and 5.20b occur just behind the roller. Static analysis shows that the peak is due to transverse gradients in shear traction at the roller-tow boundary contributing to corresponding increases in compressive stress up to the roller location.

Inspection of the trends in σ_t for $\tau = 0$ in Figures 5.20a and 5.20b shows that σ_t reaches a plateau after a certain distance from the neighboring wrinkle (e.g., for R = 635 mm). This indicates that, for the AFP tow placement process, a "transition

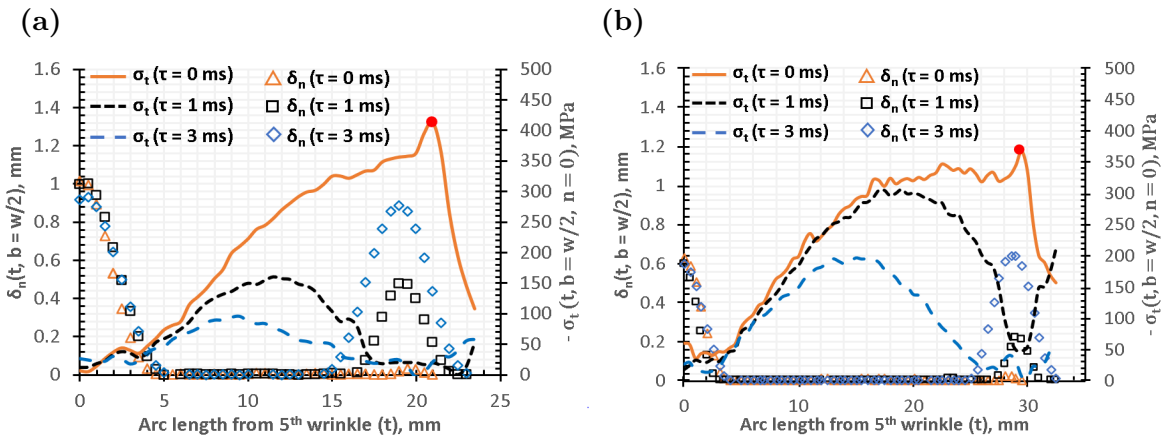

Figure 5.20 Longitudinal compressive stress in the mid plane ($n = 0$) and opening displacement along inner edge between 5$^{\text{th}}$ and 6$^{\text{th}}$ wrinkles at different times starting from initiation to complete formation of the 6$^{\text{th}}$ wrinkle for (a) $R = 305$ mm and (b) $R = 635$ mm (the instant when the 6$^{\text{th}}$ wrinkle initiates is defined to be $\tau = 0$)

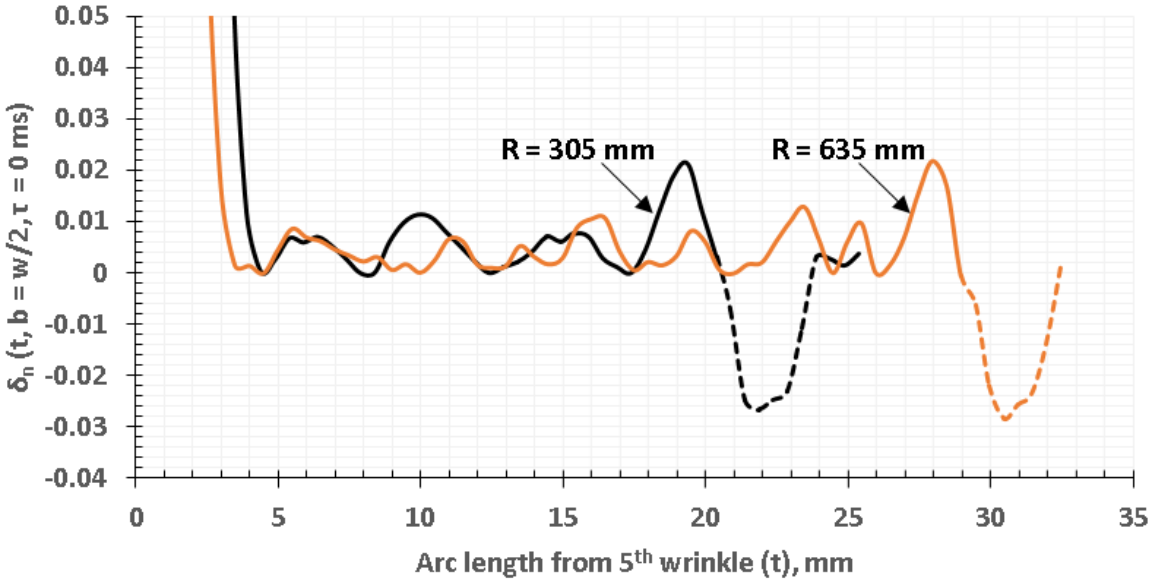

Figure 5.21 Presence of micro buckles along inner edge between 5$^{\text{th}}$ and 6$^{\text{th}}$ wrinkles at the initiation of the 6$^{\text{th}}$ wrinkle for $R = 305$ mm and 635 mm the dotted line shows the region of roller contact (negative opening displacement)

length" exists beyond which the compressive stress distribution on the inner edge is constant up to the initiation of a new wrinkle. In this case, transition length is defined as the minimum distance between wrinkles for which the effect of a neighboring wrinkle does not influence the stress distribution between wrinkles prior to formation of the next wrinkle. The transition distance is ≈ 14 mm for the AFP process and tow

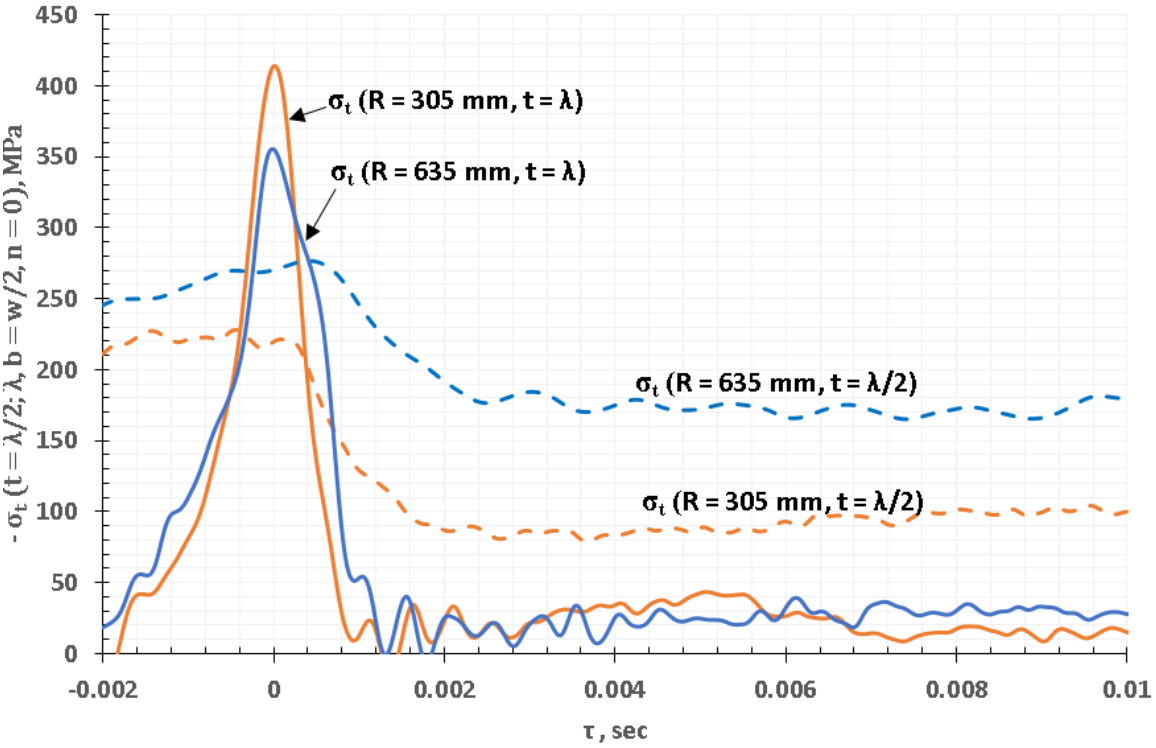

Figure 5.22 Evolution of longitudinal compressive stress at two points on the inner edge of the tow at mid-thickness, one at the location of the initiation of 6$^{\text{th}}$ wrinkle and other at mid-point between 5$^{\text{th}}$ and 6$^{\text{th}}$ wrinkle for $R = 305$ mm and 635 mm

material used in this study. The lower stress relaxation at the midpoint between the wrinkles for $R = 635$ mm than that for $R = 305$ mm, as shown in Figure 5.18, can be explained based on the wrinkle wavelength relative to the transition length. Since the midpoint between the 5$^{\text{th}}$ and 6$^{\text{th}}$ wrinkle for a tow path with $R = 305$ mm is much closer (5 mm) to the neighboring 5$^{\text{th}}$ wrinkle than for $R = 635$ mm (10.5 mm), σ_t is lower for $R = 305$ mm at the midpoint. As expected, at the same distance from the 5$^{\text{th}}$ wrinkle, the tow path with $R = 305$ mm has higher σ_t than that of $R = 635$ mm. The effect of the transition length is also evident in Figure 5.22, which shows the history of σ_t at the point of initiation of the 6$^{\text{th}}$ wrinkle and at the mid-point between the 5$^{\text{th}}$ and 6$^{\text{th}}$ wrinkle along the inner edge, with distances normalized by the wrinkle wavelength for consistency in the comparisons.

The processes occurring under the roller during tow placement are fundamental

to the initiation and growth of wrinkles. The surface shear forces under the roller at positions where wrinkles form for $R = 305$ mm and 635 mm are shown in Figures 5.23a and 5.23b, respectively. The compressive side of the tow experiences high shear forces (Mode II mostly, and some Mode III) during placement along curvilinear paths due to roller rotation. These upper surface forces induce damage in the tow at the tow-substrate interface. Near mid-width of the tow, the shear forces are mostly Mode III but are much smaller than the Mode II forces at the outer edges of the tow. The temporal evolution of damage, the longitudinal compressive normal stress, and the opening displacement at the point of initiation of the 6^{th} wrinkle for $R = 305$ mm are shown in Figure 5.24. In addition, the contact pressure induced by the roller is shown in Figure 5.25.

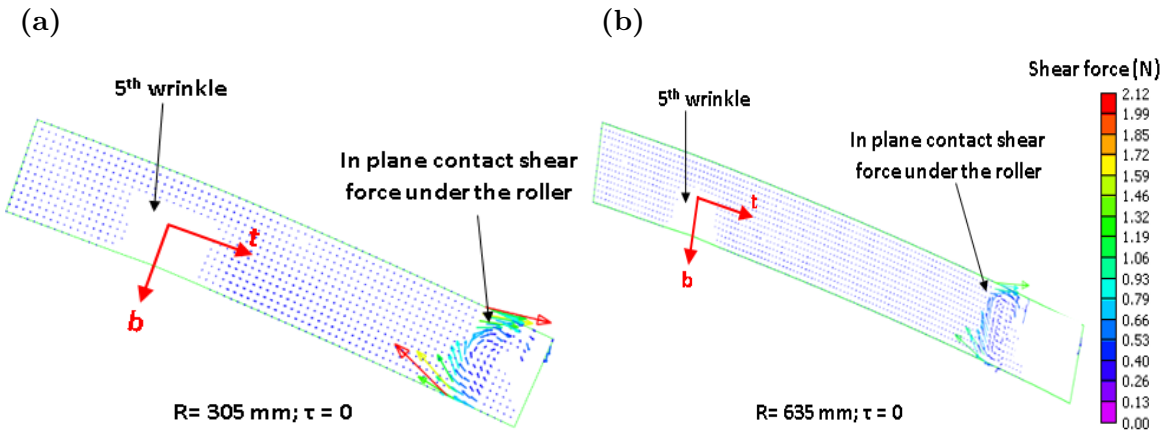

Figure 5.23 (a) Local shear forces on top surface of tow due to traction from roller for $R = 635$ mm and (b) $R = 635$ mm

To improve understanding of how wrinkles form, there are four time intervals in Figure 5.24,

- Region I: Immediately before contact with the roller (between τ^b and τ^a),
- Region II: Roller compaction zone (between τ^c and τ^b),
- Region III: After roller compaction and before initiation of wrinkle (between τ^d and τ^c),

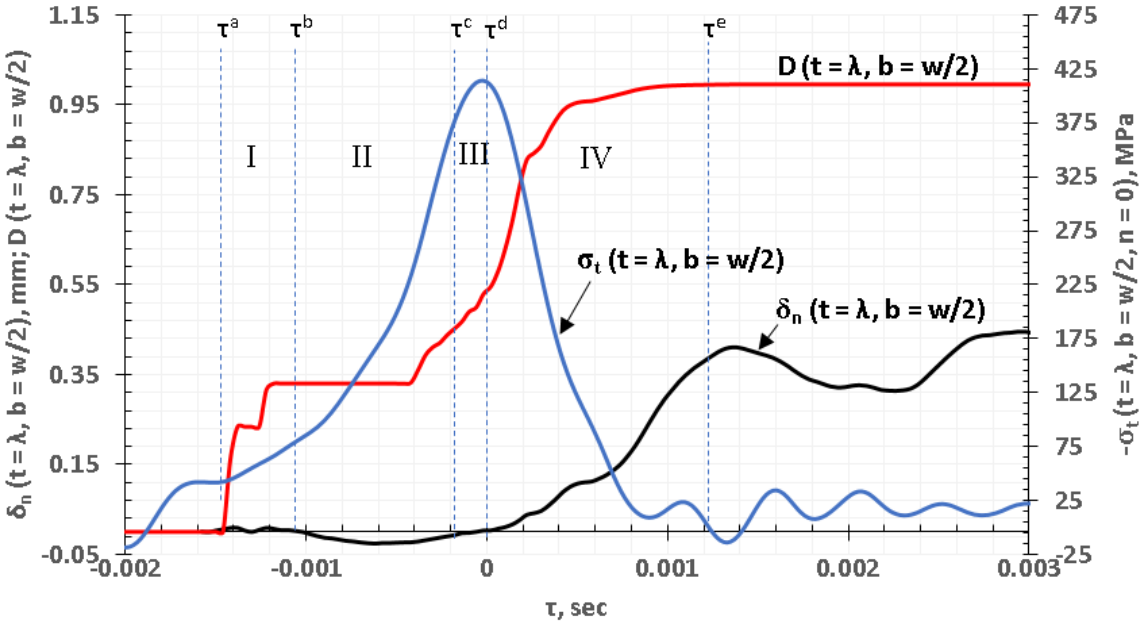

Figure 5.24 Evolution of longitudinal compressive stress (σ_t), damage variable (D), and opening displacement (δ_n) at the point of initiation of the wrinkle on the compression edge of the tow for $R = 305$ mm

Region I correspond to conditions immediately ahead of the roller as it approaches the location where the 6th wrinkle forms. This region incurs relative slip (shear) between the tow and substrate, and small tensile opening stresses that are less than the maximum value. These conditions result in pre-compression damage before entering the compaction zone in Region II. As shown in Figsures 5.24 and 5.25, pre-compression damage can be up to 35% of the total damage required for separation. During the early stages of the Region II compaction zone, higher compressive stresses, up to 8 MPa, are present and no additional damage is predicted during the roller compaction process.

Towards the end of region II and beginning of region III, damage continues due to higher shear forces. In this region, the compressive longitudinal stresses reach a peak and begin to decline in concert with the presence of small tensile opening stresses on the interface. The higher shear forces shown in Figure 5.23a induce tangential Mode II and Mode III slip displacements between tow and substrate, increasing damage.

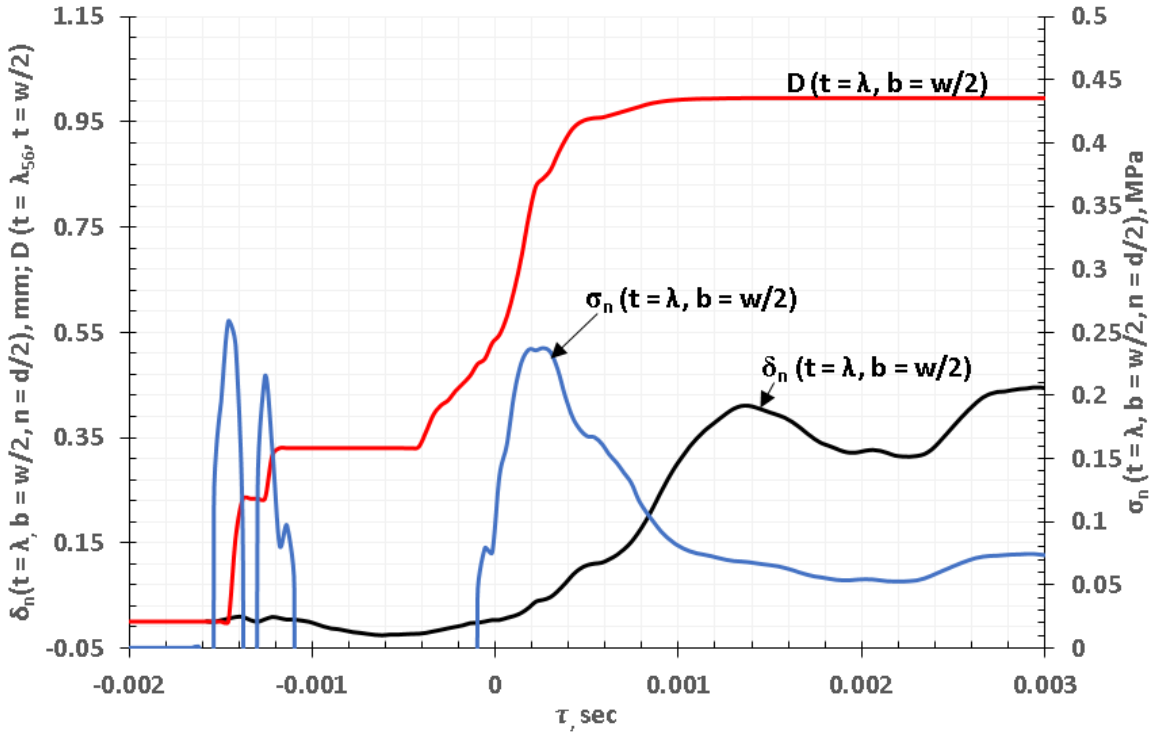

Figure 5.25 Evolution of normal traction (σ_n), damage variable (D) and opening displacement (δ_n) on the tow-substrate surface at the point of initiation of the wrinkle for $R = 305$ mm (compressive stress due to roller pressure is not shown here)

During this time, the compaction pressure has dissipated, and small tensile opening stresses occur. The combined set of tensile stresses and shear result in satisfaction of the mixed mode failure criterion and set the stage for opening of the separated interface. In Region IV, the longitudinal compressive stress decreases rapidly as the interface separates and wrinkle amplitude increases.

As shown in Figure 5.24, the time from initial damage at the location of the 6$^{\text{th}}$ wrinkle to the beginning of wrinkle uplift is less than 1.5 ms, demonstrating that the predicted evolution of a wrinkle is remarkably fast. Finally, it is noted that the maximum wrinkle amplitude occurs towards the left side of the point of initiation of the 6$^{\text{th}}$ wrinkle, consistent with the evolution of the constraining effect of the roller as it moves along the tow path.

As noted earlier, the distribution of longitudinal compressive stress along the

inner edge of the tow reveals that a "transition length" exists for a given tow and interface properties. In these simulations, shorter radii of curvature are predicted to have smaller wrinkle wavelength. For the smaller radii of curvature, $R = 305$ mm and 635 mm, simulations show that the resulting wrinkle wavelength is less than the "transition length" so that the region between the wrinkles has lower maximum residual compressive stress. Since simulations and experiments both show that for $R \geq 1270$ mm, no wrinkles are formed, these results can be used to provide an estimate for the critical radius of curvature where the wrinkle wavelength is larger than the "transition length". For this material and AFP process, $R_{transition} \approx 1000$ mm.

As discussed in the previous section and shown in Figures 5.24 and 5.25, damage growth is predicted to occur immediately ahead of the roller due to relative slip between the tow and substrate and small tensile stresses. In addition, once an element of the tow approaches the maximum longitudinal compressive stress, significant damage is also predicted to occur primarily due to slip (Mode II & III) and the presence of small tensile stresses on the interface. As shown in Figures 5.23a and 5.23b, deformation of the tow under the roller causes sliding motion in the longitudinal (t) and transverse (b) directions, with the Mode II component much larger on the edges and lower at mid-width of the tow. As the roller moves away from the region, relatively small tensile opening stresses are predicted to occur in the interface region, setting the stage for separation of the tow from the substrate.

The discussion given above regarding damage accumulation for various local modes of loading is provided for the specific TSL measured by the authors for the temperatures and pressures applied in their previous RDCB experiments. As the tow material changes, or the temperatures and pressures vary during tow layup, the TSL will necessarily change and thus the damage introduced by each local mode of loading may change. In fact, preliminary simulation studies by the authors for different TSL have shown that softer interface material with reduced maximum traction and increased

maximum separation can result in (a) tow separation due to shear and tow sliding along surface, (b) separation of tow on tension side of tow and rollover of delaminated tow region and (c) transverse wrinkling of tow that would result in fiber separation and fiber bunching in transverse direction. Details regarding these observations will be subject of future study.

Finally, previous work by Harvey and Cebon (2005) for bitumen fracture indicated that fracture toughness and the measured nominally Mode I TSL are a function of the rate of separation for slow rates of loading. Thus, additional experiments may be needed to assess the importance of rate effects during tow placement.

5.5 CONCLUSIONS

A simulation platform has been developed and used successfully to model the AFP process and tow wrinkling during placement along curvilinear paths. Using measured and estimated tow material properties of IM7/8552-1 and the measured TSL for Mode I and Mode II loading, no wrinkles were predicted to form for tow paths with radii of curvature $\geq$ 1270 mm. These predictions for wrinkling, including wavelength and amplitude, are in very good agreement with experimental measurements for paths with three radii of curvature. For a roller speed of 1.83 m/s, simulation studies focusing on the mechanics and mechanisms of wrinkle formation have elucidated critical aspects of the process that result in initial wrinkle formation within 1.5 ms, with the wrinkle predicted to grow to full size within 2 ms. Summarizing the discussion in the previous section, the process in the adhesive zone resulting in wrinkle formation during AFP of a tow is as follows;

- roller approach, with initial damage up to 35% due to local deformations and stresses,
- compaction under roller, pressures up to 8 MPa, with no predicted additional

damage,

- high shear forces along tow edges during latter stages of compaction, with additional 20% damage,
- passage of roller inducing small tensile stresses at tow-substrate interface resulting in fully damaged region, tow-substrate separation, wrinkle formation and uplift,
- wrinkle growth to full size occurring at high rate after roller passage.

Given the high rate of wrinkle formation during the AFP process, viscoelastic effects are not significant, as is evident from the early stage creep master curve for the tow (Figure 5.9) showing minimal creep at high rate for the process temperature, $T = 40\,^{\circ}C$.

Results from these simulations confirm that the AFP model is capable of predicting wrinkling of tows during processing. The simulation platform currently is being extended to study a variety of issues including (a) how changes in tow material properties and process parameters (e.g. placement speed, temperature, roller pressure) affect the types of damage and tow defects that can occur, (b) how the presence of gaps and overlaps on the substrate surface affect tow wrinkling, (c) the effect of multi-ply curved surfaces on tow processing and tow defect formation, and (d) how the wrinkle formation process occurs when placing tows on top of recently placed tows.

Chapter 6

SUMMARY AND FUTURE WORK

6.1 DIRECT MATERIAL PROPERTY IDENTIFICATION USING FINITE ELEMENT METHOD AND DIC STRAIN DATA

The robustness of a Petrov-Galerkin method to obtain the spatial distribution of Young's modulus for a heterogeneous material with properties varying along a single direction (e.g. a nominally one-dimensional configuration) is shown in this work. The success of this method motivates future extension of the approach to higher dimensions. Some of the challenges for extension to two-dimensional predictions of heterogeneous property distributions are as follows. First, in order to solve the PDE, traction boundary conditions are required on the surface of the sample. Secondly, a process must be implement to select appropriate test functions that ensure stability of the solution(s). Third, there should be consideration for developing the methodology to predict properties in anisotropic materials. Finally, the methodology should be validated by comparing predictions to existing known solutions, if they are available.

The traction boundary conditions could be defined by incorporating a known material between the specimen boundary and loading fixture. The analyst should make sure that the calibrated material has similar range of modulus as the specimen in order to ensure there is a good signal to noise ratio. Moreover, a large mismatch in modulus at the interface can cause the stress states to be different from the 2D stress state assumption potentially introducing error in the estimated boundary traction. For the case of anisotropic behavior, the PDEs cannot be solved using experimental

measurements obtained for one type of loading. For anisotropic materials, the matrix equations resulting from distinct loading responses need to be solved using a least square method.

For a 2D case, it is difficult to obtain a closed form solution for the strain distribution in a heterogeneous material system. In such cases, validation of the algorithm typically is performed using experimental data generated from a known heterogeneous material system, with StereoDIC measurement uncertainty determined through baseline imaging studies. Since the PDEs for a 2D problem are coupled equations under general loading conditions, it is necessary to check if the optimum test function space is dependent on the type of loading. The parametric study performed for the 1D case can be repeated for the 2D case by generating data for various DIC parameters such as subset size, filter size and speckle size. For three-dimensional applications, the additional challenge is measurement of three dimensional strain distribution inside the material with sufficient resolution and accuracy. Finally the approach can be implemented in a machine learning framework and the model can be trained with large set of DIC data available for known heterogeneous material systems.

6.2 EXPERIMENTAL MEASUREMENT AND MODELING OF TOW-WRINKLING DEFECTS GENERATED DURING AUTOMATED FIBER PLACEMENT PROCESS

The experimental method developed in this work for extracting traction-separation relationship of tow-tow interface and finite element model for simulating AFP process and predicting formation of wrinkles lays a foundation for understanding the different mechanisms involved in wrinkle defect formation. Refinements in the model are still possible for expanding the predictive capability of the model. Some of the important areas for improvement in the finite element (FE) model of automated fiber placement (AFP) process are discussed in the following paragraph.

The current model can predict several defects such as longitudinal and transverse wrinkles and tow fold-over. For predicting defects due to damage within the tow such as transverse matrix cracking, splitting of the tow though the thickness, and in plane waviness, damage mechanisms within the tow should be modeled. Transverse matrix crack and tow splitting in the thickness direction are some of the defects observed in the independent experiments but are not predicted by the model. There are two different ways damage within a tow can be implemented in the FE model. In the first approach, a prepreg tow can be modeled as multiple bundles which are joined at the sides by cohesive elements. The optimum thickness and width of each bundles can be determined by a sensitivity study so that the FE model results are not affected by bundle size. Transverse matrix cracking will appear as damage at the interface of individual bundles of the FE model. Each bundle can also have different layers through the thickness with a cohesive interface between the layers, which will make the model capable of predicting tow splitting in the thickness direction. In the second approach, matrix damage can be modeled by incorporating a composite damage initiation and evolution criterion, such as Hashin or Puck (Wang and Duong 2016). Tows analyzed with a damage model allow discretization using 2D conventional shell elements which may reduce the computational time required to solve the model.

Bibliography

Abdi, F., Gürdal, Z., and Huang, D. (2017). "Certification Modeling of Composites Fuselage, Considering Effect of Defects from Fiber Placement Manufacturing Processes". In: *55th AIAA Aerospace Sciences Meeting*.

AERO-Boeing 787 from the ground up (2016). URL: `http://www.boeing.com/commercial/aeromagazine/articles/qtr_4_06/article_04_2.html` (visited on 09/26/2020).

Ahn, K., Peterson, L., Seferis, J., Nowacki, D., and Zachmann, H. (1992). "Prepreg aging in relation to tack". In: *Journal of applied polymer science* 45.3, pp. 399–406.

Ajdari, A., Nayeb-Hashemi, H., and Vaziri, A. (2011). "Dynamic crushing and energy absorption of regular, irregular and functionally graded cellular structures". In: *International Journal of Solids and Structures* 48.3-4, pp. 506–516.

Alexander, S. L., Gunnarsson, C. A., Rafaels, K., and Weerasooriya, T. (2020). "Multiscale response of the human skull to quasi-static compression". In: *Journal of the Mechanical Behavior of Biomedical Materials* 102, p. 103492.

Alshahrani, H. and Hojjati, M. (2017). "A new test method for the characterization of the bending behavior of textile prepregs Part A Applied science and manufacturing". In.

ASTM (2013). "Standard test method for assignment of the glass transition temperature by dynamic mechanical analysis". In.

Avril, S., Bonnet, M., Bretelle, A.-S., Grédiac, M., Hild, F., Ienny, P., Latourte, F., Lemosse, D., Pagano, S., Pagnacco, E., et al. (2008). "Overview of identification methods of mechanical parameters based on full-field measurements". In: *Experimental Mechanics* 48.4, pp. 381–402.

Bakhshi, N. and Hojjati, M. (2018). "An experimental and simulative study on the defects appeared during tow steering in automated fiber placement". In: *Composites Part A: Applied Science and Manufacturing* 113, pp. 122–131.

Bakhshi, N. and Hojjati, M. (2019). "Time-dependent wrinkle formation during tow steering in automated fiber placement". In: *Composites Part B: Engineering* 165, pp. 586–593.

Bakhshi, N. and Hojjati, M. (2020). "Effect of compaction roller on layup quality and defects formation in automated fiber placement". In: *Journal of Reinforced Plastics and Composites* 39.1-2, pp. 3–20.

Barenblatt, G. I. et al. (1962). "The mathematical theory of equilibrium cracks in brittle fracture". In: *Advances in applied mechanics* 7.1, pp. 55–129.

Barton, J. M. (1985). "The application of differential scanning calorimetry (DSC) to the study of epoxy resin curing reactions". In: *Epoxy resins and composites I.* Springer, pp. 111–154.

Beakou, A., Cano, M., Le Cam, J.-B., and Verney, V. (2011). "Modelling slit tape buckling during automated prepreg manufacturing: A local approach". In: *Composite structures* 93.10, pp. 2628–2635.

Bertin, M., Hild, F., Roux, S., Mathieu, F., Leclerc, H., and Aimedieu, P. (2016). "Integrated digital image correlation applied to elastoplastic identification in a biaxial experiment". In: *The Journal of Strain Analysis for Engineering Design* 51.2, pp. 118–131.

Boisse, P., Hamila, N., and Madeo, A. (2016). "Modelling the development of defects during composite reinforcements and prepreg forming". In: *Philosophical Transactions of the Royal Society A: Mathematical, Physical and Engineering Sciences* 374.2071, p. 20150269.

Camanho, P. P. and Dávila, C. G. (2002). "Mixed-mode decohesion finite elements for the simulation of delamination in composite materials". In.

Cengel, Y. A. and Boles, M. A. (2007). *Thermodynamics: An Engineering Approach 6th Editon (SI Units)*. The McGraw-Hill Companies, Inc., New York.

Chai, H. (1992). "Experimental evaluation of mixed-mode fracture in adhesive bonds". In: *Experimental Mechanics* 32.4, pp. 296–303.

Chasiotis, I. and Knauss, W. G. (2002). "A new microtensile tester for the study of MEMS materials with the aid of atomic force microscopy". In: *Experimental Mechanics* 42.1, pp. 51–57.

Chen, X., Wu, Z., Nie, G., and Weaver, P. (2018). "Buckling analysis of variable angle tow composite plates with a through-the-width or an embedded rectangular

delamination". In: *International Journal of Solids and Structures* 138, pp. 166–180.

Chu, T., Ranson, W., and Sutton, M. A. (1985). "Applications of digital-image-correlation techniques to experimental mechanics". In: *Experimental mechanics* 25.3, pp. 232–244.

Creton, C. and Ciccotti, M. (2016). "Fracture and adhesion of soft materials: a review". In: *Reports on Progress in Physics* 79.4, p. 046601.

Crossley, R., Schubel, P., and Warrior, N. (2012). "The experimental determination of prepreg tack and dynamic stiffness". In: *Composites Part A: Applied Science and Manufacturing* 43.3, pp. 423–434.

Dastjerdi, A. K., Pagano, M., Kaartinen, M., McKee, M., and Barthelat, F. (2012). "Cohesive behavior of soft biological adhesives: experiments and modeling". In: *Acta Biomaterialia* 8.9, pp. 3349–3359.

Dastjerdi, A. K., Tan, E., and Barthelat, F. (2013). "Direct measurement of the cohesive law of adhesives using a rigid double cantilever beam technique". In: *Experimental Mechanics* 53.9, pp. 1763–1772.

Denkena, B., Schmidt, C., and Weber, P. (2016). "Automated fiber placement head for manufacturing of innovative aerospace stiffening structures". In: *Procedia Manufacturing* 6.Supplement C, pp. 96–104.

Dirk, H.-J. L., Ward, C., and Potter, K. D. (2012). "The engineering aspects of automated prepreg layup: History, present and future". In: *Composites Part B: Engineering* 43.3, pp. 997–1009.

Dodwell, T., Butler, R., and Hunt, G. (2014). "Out-of-plane ply wrinkling defects during consolidation over an external radius". In: *Composites Science and Technology* 105, pp. 151–159.

Dörr, D., Schirmaier, F. J., Henning, F., and Kärger, L. (2017). "A viscoelastic approach for modeling bending behavior in finite element forming simulation of continuously fiber reinforced composites". In: *Composites Part A: Applied Science and Manufacturing* 94, pp. 113–123.

Dugdale, D. (1960). "Yielding of steel sheets containing slits. J. Me& Phys". In: *Solids 8* 100404.

Emri, I. and Gergesova, M. (2010). "Time-dependent behavior of solid polymers". In: *Rheology: Encyclopedia of Life Support Systems (EOLSS)* 1, pp. 247–330.

Emri, I. and Tschoegl, N. (1993). "Generating line spectra from experimental responses. Part I: Relaxation modulus and creep compliance". In: *Rheologica Acta* 32.3, pp. 311–322.

Erland, S., Dodwell, T., and Butler, R. (2017). "Characterisation of bending mechanics in uncured laminated materials using a modified Dynamic Mechanical Analysis". In: *arXiv preprint arXiv:1709.07940*.

Ferry, J. D. (1980). *Viscoelastic properties of polymers*. John Wiley & Sons.

Freed, Y. and Banks-Sills, L. (2008). "A new cohesive zone model for mixed mode interface fracture in bimaterials". In: *Engineering Fracture Mechanics* 75.15, pp. 4583–4593.

Frigione, M. and Kenny, J. (2002). "Thermokinetic effect of the aging of epoxy matrix prepregs for high performance composites". In: *Polymer composites* 23.4, pp. 530–537.

Gergesova, M., Zupančič, B., Saprunov, I., and Emri, I. (2011). "The closed form tTP shifting (CFS) algorithm". In: *Journal of Rheology* 55.1, pp. 1–16.

Gergesova, M., Saprunov, I., and Emri, I. (2016). "Closed-form solution for horizontal and vertical shiftings of viscoelastic material functions in frequency domain". In: *Rheologica Acta* 55.5, pp. 351–364.

Gorman, J. and Thouless, M. (2019). "The use of digital-image correlation to investigate the cohesive zone in a double-cantilever beam, with comparisons to numerical and analytical models". In: *Journal of the Mechanics and Physics of Solids* 123, pp. 315–331.

Gowrishankar, S., Mei, H., Liechti, K. M., and Huang, R. (2012). "A comparison of direct and iterative methods for determining traction-separation relations". In: *International journal of fracture* 177.2, pp. 109–128.

Grunenfelder, L. K. and Nutt, S. R. (2012). "Prepreg age monitoring via differential scanning calorimetry". In: *Journal of Reinforced Plastics and Composites* 31.5, pp. 295–302.

Harvey, J. and Cebon, D. (2005). "Fracture tests on bitumen films". In: *Journal of materials in civil engineering* 17.1, pp. 99–106.

Helm, J. D., McNeill, S. R., and Sutton, M. A. (1996). "Improved three-dimensional image correlation for surface displacement measurement". In: *Optical Engineering* 35.7, pp. 1911–1921.

Helm, J. D., Sutton, M. A., and McNeill, S. R. (2003a). "Deformations in wide, center-notched, thin panels, part I: three-dimensional shape and deformation measurements by computer vision". In: *Optical Engineering* 42.5, pp. 1293–1305.

Helm, J. D., Sutton, M. A., and McNeill, S. R. (2003b). "Deformations in wide, center-notched, thin panels, part II: finite element analysis and comparison to experimental measurements". In: *Optical Engineering* 42.5, pp. 1306–1320.

Hild, F. and Roux, S. (2006). "Digital image correlation: from displacement measurement to identification of elastic properties–a review". In: *Strain* 42.2, pp. 69–80.

Hoefnagels, J., Bertin, M., Du, C., and Hild, F. (2018). "Crystal plasticity parameter identification by integrated DIC on microscopic topographies". In: *Residual Stress, Thermomechanics & Infrared Imaging, Hybrid Techniques and Inverse Problems, Volume 8*. Springer, pp. 47–49.

Högberg, J. L., Sørensen, B. F., and Stigh, U. (2007). "Constitutive behaviour of mixed mode loaded adhesive layer". In: *International Journal of Solids and Structures* 44.25-26, pp. 8335–8354.

Hubert, P., Johnston, A., Poursartip, A., and Nelson, K. (2001). "Cure kinetics and viscosity models for Hexcel 8552 epoxy resin". In: *International SAMPE symposium and exhibition*. SAMPE; 1999, pp. 2341–2354.

Kallel, F. and Bertrand, M. (1996). "Tissue elasticity reconstruction using linear perturbation method". In: *IEEE Transactions on Medical Imaging* 15.3, pp. 299–313.

Kawabata, S. and Niwa, M. (1989). "Fabric performance in clothing and clothing manufacture". In: *Journal of the Textile Institute* 80.1, pp. 19–50.

Khani, A., Abdalla, M., and Gürdal, Z. (2015). "Optimum tailoring of fibre-steered longitudinally stiffened cylinders". In: *Composite Structures* 122, pp. 343–351.

Knauss, W. G., Emri, I., and Lu, H. (2008). "Mechanics of polymers: viscoelasticity". In: *Handbook of experimental solid mechanics*, pp. 49–95.

Lakrout, H., Sergot, P., and Creton, C. (1999). "Direct observation of cavitation and fibrillation in a probe tack experiment on model acrylic pressure-sensitive-adhesives". In: *The Journal of Adhesion* 69.3-4, pp. 307–359.

Li, Y., Feng, Z., Hao, L., Huang, L., Xin, C., Wang, Y., Bilotti, E., Essa, K., Zhang, H., Li, Z., et al. (2020). "A review on functionally graded materials and structures via

additive manufacturing: from multi-scale design to versatile functional properties". In: *Advanced Materials Technologies* 5.6, p. 1900981.

Liang, B., Hamila, N., Peillon, M., and Boisse, P. (2014). "Analysis of thermoplastic prepreg bending stiffness during manufacturing and of its influence on wrinkling simulations Part A Applied science and manufacturing". In.

Liechti, K. M. and Wu, J.-D. (2001). "Mixed-mode, time-dependent rubber/metal debonding". In: *Journal of the Mechanics and Physics of Solids* 49.5, pp. 1039–1072.

Lopes, C. S., Gürdal, Z., and Camanho, P. P. (2008). "Variable-stiffness composite panels: Buckling and first-ply failure improvements over straight-fibre laminates". In: *Computers & Structures* 86.9, pp. 897–907.

Luo, P., Chao, Y., Sutton, M., and Peters, W.-H. (1993). "Accurate measurement of three-dimensional deformations in deformable and rigid bodies using computer vision". In: *Experimental mechanics* 33.2, pp. 123–132.

Margossian, A., Bel, S., and Hinterhoelzl, R. (2015). "Bending characterisation of a molten unidirectional carbon fibre reinforced thermoplastic composite using a Dynamic Mechanical Analysis system". In: *Composites Part A: Applied Science and Manufacturing* 77, pp. 154–163.

Martin, M. C. (1986). *Elements of thermodynamics*. Prentice Hall.

Matveev, M. Y., Schubel, P. J., Long, A. C., and Jones, I. (2016). "Understanding the buckling behaviour of steered tows in Automated Dry Fibre Placement (ADFP)". In: *Composites Part A: Applied Science and Manufacturing* 90, pp. 451–456.

Mohammed, I., Charalambides, M., and Kinloch, A. (2016). "Modeling the effect of rate and geometry on peeling and tack of pressure-sensitive adhesives". In: *Journal of Non-Newtonian Fluid Mechanics* 233, pp. 85–94.

Needleman, A. (1987). "A continuum model for void nucleation by inclusion debonding". In.

Neggers, J., Hoefnagels, J. P., Geers, M., Hild, F., and Roux, S. (2015). "Time-resolved integrated digital image correlation". In: *International Journal for Numerical Methods in Engineering* 103.3, pp. 157–182.

Oromiehie, E., Gangadhara Prusty, B., Compston, P., and Rajan, G. (2017). "In-situ simultaneous measurement of strain and temperature in automated fiber placement (AFP) using optical fiber Bragg grating (FBG) sensors". In: *Advanced Manufacturing: Polymer & Composites Science* 3.2, pp. 52–61.

Qureshi, Z., Swait, T., Scaife, R., and El-Dessouky, H. M. (2014). "In situ consolidation of thermoplastic prepreg tape using automated tape placement technology: Potential and possibilities". In: *Composites Part B: Engineering* 66, pp. 255–267.

Raghavan, K. and Yagle, A. E. (1994). "Forward and inverse problems in elasticity imaging of soft tissues". In: *IEEE Transactions on nuclear science* 41.4, pp. 1639–1648.

Rajan, S., Sutton, M. A., Wehbe, R., Tatting, B., Gurdal, Z., and Kidane, A. (2019a). "Measured surface deformation and strains in thin thermoplastic prepreg tapes steered along curved paths without adhesion using StereoDIC". In: *Experimental Mechanics* 59.4, pp. 531–547.

Rajan, S., Sutton, M. A., Fuerte, R., and Emri, I. (2018). "Time Temperature Superposition and Prony Series Coefficients of Asphalt Roof Shingle Material from Viscoelastic Creep Testing". In: *Challenges in Mechanics of Time Dependent Materials, Volume 2*. Springer, pp. 33–38.

Rajan, S., Sutton, M. A., Fuerte, R., and Kidane, A. (2018). "Traction-separation relationship for polymer-modified bitumen under Mode I loading: Double cantilever beam experiment with stereo digital image correlation". In: *Engineering Fracture Mechanics* 187, pp. 404–421.

Rajan, S., Sutton, M. A., McMakin, W., Compton, E., Kidane, A., Gurdal, Z., Wehbe, R., and Farzana, Y. (2020a). "Characterization of Mode I and Mode II traction–separation laws for cohesive separation of uncured thermoset tows". In: *International Journal of Fracture* 221.1, pp. 25–38.

Rajan, S., Sutton, M. A., Oseli, A., Emri, I., and Matta, F. (2017). "Linear viscoelastic creep compliance and retardation spectra of bitumen impregnated fiberglass mat and polymer modified bitumen". In: *Construction and Building Materials* 155, pp. 664–679.

Rajan, S., Sutton, M. A., Sockalingam, S., McMakin, W., Gurdal, Z., and Kidane, A. (2020b). "Simulations and experiments for automated fiber placement of prepreg slit tape: Wrinkle formation and fundamental observations". In: *Composites Part B: Engineering*, p. 108287.

Rajan, S., Sutton, M. A., Wehbe, R., Gurdal, Z., Kidane, A., and Emri, I. (2021). "Characterization of viscoelastic bending stiffness of uncured carbon-epoxy prepreg slit tape". In: *Composite Structures* 275, p. 114295.

Rajan, S., Sutton, M. A., Wehbe, R., Tatting, B., Gürdal, Z., Kidane, A., and Harik, R. (2019b). "Experimental investigation of prepreg slit tape wrinkling during au-

tomated fiber placement process using StereoDIC". In: *Composites Part B: Engineering* 160, pp. 546–557.

Réthoré, J., Roux, S., and Hild, F. (2008). "Noise-robust stress intensity factor determination from kinematic field measurements". In: *Engineering Fracture Mechanics* 75.13, pp. 3763–3781.

Ropers, S., Sachs, U., Kardos, M., and Osswald, T. A. (2017). "A thermo-viscoelastic approach for the characterization and modeling of the bending behavior of thermoplastic composites–Part II Part A Applied science and manufacturing". In.

Sargent, J., Chen, J., Sherwood, J., Cao, J., Boisse, P., Willem, A., Vanclooster, K., Lomov, S. V., Khan, M., Mabrouki, T., et al. (2010). "Benchmark study of finite element models for simulating the thermostamping of woven-fabric reinforced composites". In: *International Journal of Material Forming* 3.1, pp. 683–686.

Schreier, H. W., Braasch, J. R., and Sutton, M. A. (2000). "Systematic errors in digital image correlation caused by intensity interpolation". In: *Optical engineering* 39.11, pp. 2915–2921.

Shahkarami, A., Van Ee, D., and Poursartip, A. (2009). "Material characterization for processing: Hexcel 8552". In: *National Center for Advanced Materials Performance, Wichita, KS*.

Sherwood, J., Fetfatsidis, K., Winchester, D., Jauffrès, D., Avitabile, P., and Chen, J. (2010). "Using modal analysis to investigate the validity of finite element models for simulating the thermostamping of woven-fabric reinforced composites". In: *International Journal of Material Forming* 3.1, pp. 687–690.

Shet, C. and Chandra, N. (2004). "Effect of the shape of T–δ cohesive zone curves on the fracture response". In: *Mechanics of Advanced Materials and Structures* 11.3, pp. 249–275.

Silva, D., Campilho, R., Silva, F., and Carvalho, U. (2018). "Application a direct/cohesive zone method for the evaluation of scarf adhesive joints". In: *Applied Adhesion Science* 6.1, p. 13.

Sørensen, B. F. and Jacobsen, T. K. (2003). "Determination of cohesive laws by the J integral approach". In: *Engineering fracture mechanics* 70.14, pp. 1841–1858.

Soulat, D., Allaoui, S., and Chatel, S. (2009). "Experimental device for the preforming step of the RTM process". In: *International Journal of Material Forming* 2.1, p. 181.

Stenger, F. (1974). "On the convergence and error of the bubnov-galerkin method". In: *Proceedings of the Conference on the Numerical Solution of Ordinary Differential Equations*. Springer, pp. 434–450.

Sutton, M., Matta, F., Rizos, D., Ghorbani, R., Rajan, S., Mollenhauer, D., Schreier, H., and Lasprilla, A. (2017). "Recent progress in digital image correlation: background and developments since the 2013 WM Murray Lecture". In: *Experimental Mechanics* 57.1, pp. 1–30.

Sutton, M. A. (2013). "Computer vision-based, noncontacting deformation measurements in mechanics: a generational transformation". In: *Applied Mechanics Reviews* 65.5.

Sutton, M. A., McNeill, S. R., Helm, J. D., and Chao, Y. J. (2000). "Advances in two-dimensional and three-dimensional computer vision". In: *Photomechanics*. Springer, pp. 323–372.

Sutton, M. A., Orteu, J. J., and Schreier, H. (2009). *Image correlation for shape, motion and deformation measurements: basic concepts, theory and applications*. Springer Science & Business Media.

Thomas, L. (2003). "Making accurate DSC and MDSC® specific heat capacity measurements with the Q1000 Tzero™ DSC". In: *TA Bulletin TA310. TA Instruments, New Castle. http://www. tainstruments. com/main. aspx* 2&id.

Thouless, M. and Jensen, H. (1992). "Elastic fracture mechanics of the peel-test geometry". In: *The Journal of Adhesion* 38.3-4, pp. 185–197.

Thouless, M. and Yang, Q. (2008). "A parametric study of the peel test". In: *International Journal of Adhesion and Adhesives* 28.4-5, pp. 176–184.

Ungsuwarungsri, T. and Knauss, W. G. (1987). "The role of damage-softened material behavior in the fracture of composites and adhesives". In: *International Journal of Fracture* 35.3, pp. 221–241.

Vossen, B. G., Schreurs, P. J., Sluis, O. van der, and Geers, M. (2014). "Multi-scale modeling of delamination through fibrillation". In: *Journal of the Mechanics and Physics of Solids* 66, pp. 117–132.

Wang, C. H. and Duong, C. N. (2016). "Chapter 2 - Failure criteria". In: *Bonded Joints and Repairs to Composite Airframe Structures*. Ed. by C. H. Wang and C. N. Duong. Oxford: Academic Press, pp. 21–45.

Wang, J., Long, A. C., and Clifford, M. J. (2010). "Experimental measurement and predictive modelling of bending behaviour for viscous unidirectional composite materials". In: *International journal of material forming* 3.2, pp. 1253–1266.

Watson, B., Liao, C.-H., Worswick, M. J., and Cronin, D. S. (2018). "Mode I traction-separation measured using rigid double cantilever beam applied to structural adhesive". In: *The Journal of Adhesion*, pp. 1–21.

Wei, Y. and Hutchinson, J. W. (1998). "Interface strength, work of adhesion and plasticity in the peel test". In: *Recent Advances in Fracture Mechanics*. Springer, pp. 315–333.

Williams, M. L., Landel, R. F., and Ferry, J. D. (1955). "The temperature dependence of relaxation mechanisms in amorphous polymers and other glass-forming liquids". In: *Journal of the American Chemical society* 77.14, pp. 3701–3707.

Wu, C., Gowrishankar, S., Huang, R., and Liechti, K. M. (2016). "On determining mixed-mode traction–separation relations for interfaces". In: *International Journal of Fracture* 202.1, pp. 1–19.

Wu, Z., Raju, G., and Weaver, P. M. (2018). "Optimization of postbuckling behaviour of variable thickness composite panels with variable angle tows: Towards "Buckle-Free" design concept". In: *International Journal of Solids and Structures* 132-133, pp. 66–79.

Zhu, Y., Liechti, K. M., and Ravi-Chandar, K. (2009). "Direct extraction of rate-dependent traction–separation laws for polyurea/steel interfaces". In: *International Journal of Solids and Structures* 46.1, pp. 31–51.

Appendix A

EFFECT OF OUT-TIME ON UNCURED THERMOSET PREPREG SLIT TAPE

Layup preparation time for automated fiber placement (AFP) process may last for days or even weeks. During which the thermoset prepreg slit tape outside the refrigerated "creel house" can undergo room temperature aging. The room temperature aging of thermoset prepreg is observed to cause significant reduction in the tack, resulting in insufficient bonding of the tow to the substrate. The prepreg out-time is regularly monitored during its life span and a quantitative metric for determining the fitness of a prepreg for AFP process is critical. The glass transition temperature is one of the properties of the prepreg which can be easily measured and has a direct relationship with tackiness. In this chapter, a differential scanning calorimetry (DSC) was used to quantify changes in glass transition temperature (T_g), and degree of cure of Hexcel 8552-1 epoxy prepreg having out-time ranging from 1 hr to 336 hrs. It was observed that, as the aging progresses, the glass transition temperature of the epoxy resin increases from its initial value of $T_g = 0.7\,^{\circ}\mathrm{C}$ to $11.7\,^{\circ}\mathrm{C}$ after 336 hrs of curing. The glass transition temperature as a function of room temperature aging was tabulated. The increase in T_g is more rapid after 48 hrs of out-time. Rate of increase in the degree of cure was observed to reduce significantly beyond out-time of 168 hrs. The effect of aging process on the storage modulus ($E^{'}$) and T_g of prepreg slit tapes having out-time from 8 days to 90 days was investigated using dynamic mechanical analyzer (DMA). The DMA experiments were conducted for test temperatures in the

range of $-20\,^{\circ}\mathrm{C}$ to $80\,^{\circ}\mathrm{C}$ and at loading frequency of 1 Hz. The T_g of the material increased to $44.8\,^{\circ}\mathrm{C}$ after an out-time of 90 days.

A.1 INTRODUCTION

Thermoset prepreg slit tapes used in AFP placement process consists of reinforcing fibers impregnated with uncured or partially cured (B-staged) (Ahn, Peterson, Seferis, Nowacki, and Zachmann 1992) themosetting resin. The uncured state of the matrix material improves the processability of the prepregs by being tacky at room temperature. For the autoclave prepregs, curing process usually takes place inside an autoclave after placement on tool surface[1]. The glass transition temperature (T_g) of the uncured epoxy is much lower than room temperature which makes it tacky at room temperature. One of the advantages of working with thermoset prepreg is the lower operating temperature during placement process. One the other hand, the thermoplastic prepregs require much higher temperature and sophisticated ventilation system to remove volatiles during placement process. However, the lower processing temperature of thermoset prepregs comes at a price, demanding stricter storage requirements such as keeping inside vacuum bags at subzero temperatures and constant monitoring of out-time of the material.

Thermoset prepreg tows usually are stored in a vacuum bag at temperatures well below its T_g. Each tow usually is thawed to room temperature, a process that can take more than one hour. If there is a considerable out-time for the prepreg material, partial curing of the epoxy can take place that will raise the T_g of the material, so that a higher processing temperature might be required to obtain the same level of "tack" as for an uncured tow. A guideline for deciding the out-time limits for a specific material system and determining aging based on measurable

[1]A different type of prepreg which cures at room temperature, known as out of autoclave prepregs (OOA), is increasingly being used in the AFP manufacture of large scale composite parts.

thermomechanical properties is crucial for improving the product quality and reducing material cost. One such property is the T_g of the prepreg, which also determines tack level of the material. In this chapter it is shown how degree of cure and T_g of IM7/8552-1 tow changes with out-time. Only a few published data on the degree of cure and increase in glass transition for a Hexcel 8552 epoxy resin system exist, and these are for temperatures above 100 °C (Hubert, Johnston, Poursartip, and Nelson 2001; Shahkarami, Van Ee, and Poursartip 2009). The previous DSC experiments on Hexcel 8552 epoxy were conducted at the Boeing Material Technology Laboratory in Seattle, WA using a Perkin-Elmer DSC-7, following an isothermal temperature program for each experimental temperature where T > 100 °C. In their work, it was demonstrated that cure rates (reaction rates) decrease significantly when the resin undergoes vitrification (glass transition) (Hubert, Johnston, Poursartip, and Nelson 2001). The reaction rate reduction is the result of the corresponding reduction in resin free-volume and molecular mobility that accompanies vitrification, causing a shift in the cure rate controlling mechanism from kinetics to molecular diffusion. Once this change in mechanism is obtained at a given cure temperature, a limited degree of cure is reached soon after glass transition occurs.

For most prepreg materials (including the IM7/8552-1 tow) there is only a limited data on the effect aging or cure time (at ambient temperature or during AFP processing with elevated temperature) on T_g. From the previous studies, it is evident that the relationship of both the viscoelastic modulus of the prepreg material at different temperatures and T_g with the aging are important parameters determining the optimum process parameters for tow lay-up process. This chapter presents the measured degree of cure of IM7/8522-1 prepreg material pre-cured for different periods of time in the range of 1 hr to 336 hrs, changes in glass transition temperature with degree of cure using a differential scanning calorimetry, and storage modulus of the tow via experiments in a three-point bend configuration using a dynamic mechanical ana-

lyzer. This chapter has two parts, the first part includes the measurement of degree of cure and glass transition temperature of 8552-1 epoxy using differential scanning calorimetry and the second part consists of storage and loss modulus measurement of the IM7/8552-1 tow using dynamic mechanical analyzer.

A.2 DIFFERENTIAL SCANNING CALORIMETRY (DSC) – BACKGROUND

The DSC measurement involves measurement of difference in energy inputs to a sample material and an inert reference material (aluminum) as a function of temperature whilst the sample and reference material are subjected to a controlled temperature program (Barton 1985), such as constant rate heating, cooling, isothermal conditions, et cetera. The DSC is widely used in the analysis of polymers for finding the critical transition temperatures such as T_g, crystallization and melting temperatures and quantitative measurement of enthalpy of fusion during melting, heat of reaction during curing of a thermoset material. The extensive use of DSC is in part due the convenience and the relative ease for monitoring the course of exothermic reactions involved in the curing of epoxy resins, requiring relatively small quantities of the sample material, with masses of a few milligrams. Another advantage of the DSC is simultaneous measurement of thermal transitions (e.g., T_g) associated with the degree of crosslinking or state of cure of a resin using the heat flow data from DSC.

Two type of DSC systems are currently used; power compensation DSC and heat flux DSC. The power compensation DSC has separate sample and reference holders with individual heaters and platinum resistance thermometers (PRT). Temperatures of the sample and reference are controlled independently using separate, identical furnaces. The temperatures of the sample and reference are equilibrated by varying the power input to the two furnaces; the energy required to do this is a measure of the

enthalpy or heat capacity changes in the sample relative to the reference. An example is the Perkin-Elmer DSC 8000 (Perkin-Elmer Corporation). On the other hand, the heat flux DSC utilizes a single external heater; the sample and reference are connected by a low–resistance heat–flow path (constantan disc). Changes in either enthalpy or heat capacity induce a difference in its temperature relative to the reference. The temperature difference is recorded. Then, the temperature difference is related to enthalpy change in the sample using calibration experiments. An example is the DuPont DSC.

A.2.1 DSC heat flow measurement - Theory

First law of thermodynamics can be used to explain the theory involved in the relation of DSC heat flow rate measurement with the heat of reaction during curing of the epoxy resin. Consider the thermal equilibrium of an epoxy sample of mass M_s and an inert reference sample (empty aluminum pan) of mass M_r in the reference pan of the DSC cell shown in Figure A.1.

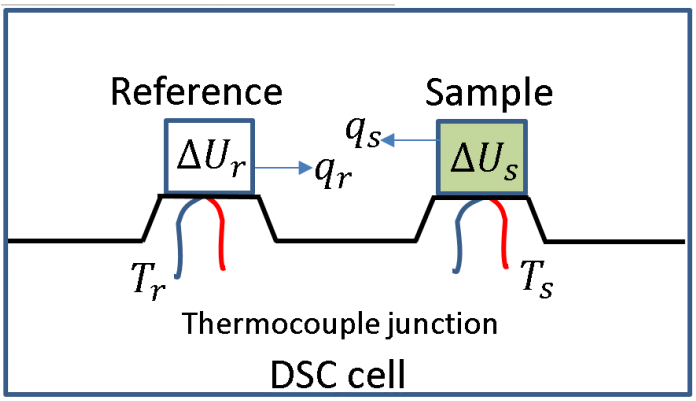

Figure A.1 Schematic of the heat flow in a heat flux DSC cell containing a sample material and an inert reference material

The DSC control system adjust the flow of heat into the sample and reference in order equilibrate the temperatures of the sample and reference material. The difference in the heat flow rate between the sample and reference $(d(q_s - q_r)/dt)$ is

the output from the DSC. Applying the first law of thermodynamics (Cengel and Boles 2007) to the reference and sample material we can write

$$\frac{dU_r}{dt} = -\frac{dq_r}{dt}; \frac{dU_s}{dt} = -\frac{dq_s}{dt}, \tag{A.1}$$

where U is the internal energy, and q is the heat flow out of the control (subscripts r and s corresponds to reference and sample material respectively). In this work, exothermic or outward heat flow is considered positive. Since the reference material is an inert material and the reference material is at a constant pressure,

$$\frac{dU_r}{dt} = -\frac{dq_r}{dt} = M_r C_r^p \frac{dt}{dt}, \tag{A.2}$$

where C_r^p is the heat capacity at constant pressure of the reference material and T is the temperature of the sample and reference material. For a positive temperature ramp, the heat is flowing into the material, hence q_r is endothermic (or it has negative sign).

For the epoxy material sample, heat capacity changes with increase in temperature due to reversible (glass transition) and irreversible (curing) changes occurring in the material. The change in the heat capacity occurs mainly at the glass transition temperature (presence of a jump in the heat flow rate versus time curve) and from the start of curing reaction (which is about 60 °C for Hexcel 8552-1 epoxy at a heating rate of 10 °C per minute) to the completion of the curing (275 °C). After completion of cure, the heat capacity will be different from the original uncured material, but it will remain constant for further increase in the temperature until thermal degradation of the material occurs at even higher temperature (400 °C). The heat flow from the sample can be expressed in terms of apparent heat capacity and enthalpy of curing reaction as follows:

$$q_s = -\int_0^t \frac{d(M_s C_s^p T)}{d\tau} d\tau + \int_0^t \frac{d(M_s H_s^{cure})}{d\tau} d\tau, \tag{A.3}$$

where C_s^p and H_s^{cure} are the heat capacity at constant pressure and specific enthalpy of cure (exothermic reaction) respectively of the sample material represented as a

function of time or temperature. For a dynamic ramp experiment with a constant increase in temperature, time and temperature are related by the rate of increase of temperature given by, $T = Ct$, where C is the rate of temperature increase in °C/sec. Assuming that the mass of the sample does not change with time (it is observed by weighing the sample before and after the experiment that the change is mass is less than 0.1%) heat flow rate from the sample can be expressed as

$$\frac{dq_s}{dt} = -M_s\left[C_s^p\frac{dT}{dt} + T\frac{dC_s^p}{dt} - \frac{dH_s^{cure}}{dt}\right]. \tag{A.4}$$

The difference in the heat flow rate between the sample and reference is given by

$$\frac{dq}{dt} = \frac{dq_s}{dt} - \frac{dq_r}{dt} = \left[\frac{dT}{dt}(M_rC_r^p - MC_s^p) - M_sT\frac{dC_s^p}{dt}\right] + M_s\frac{dH_s^{cure}}{dt}. \tag{A.5}$$

The heat flow rate represented by terms in the square bracket on the right-hand side of Equation (A.5) is called baseline heat flow rate (dq_b/dt). The baseline heat flow rate has two parts, one is due to the difference in the heat capacity and mass of the sample and reference material ($dT/dt(M_rC_r^p - MC_s^p)$) and the second term is due to the rate of change of the heat capacity of the sample material which occurs mainly during the irreversible curing reaction. Figure A.2 shows schematically the baseline and the total heat flow rate during a typical DSC dynamic temperature ramp experiment of an epoxy resin material. For finding the heat of reaction of the sample, the baseline is subtracted from the total heat flow and the resulting data is integrated from the start to finish of the curing reaction (see Equation (A.6)). The specific heat of reaction is

$$H_s^{cure} = \frac{1}{M_s}\int_{t_1} t_2\frac{d(q - q_b)}{dt}dt, \tag{A.6}$$

where the baseline heat flow is given by, $q_b = dT/dt(M_rC_r^p - MC_s^p) - M_sT(dC_s^p)/dt$.

The heat flow rate due to curing reaction can now be related to the reduction in the number of reacting molecules of the epoxy sample as follows. If there are m_0 total reactant molecules and there are m molecules reacting with a constant heat of

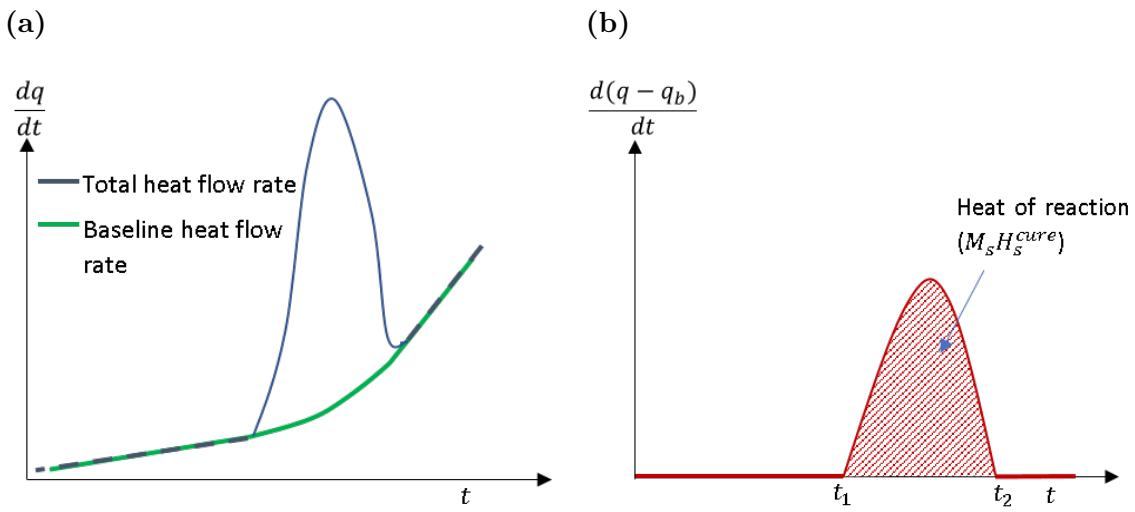

Figure A.2 (a) Schematic of the baseline and total heat flow output from DSC during temperature ramp experiment of a typical epoxy sample, and (b) heat of reaction

reaction per molecule (Barton 1985), then the heat flow rate is proportional to the reduction in the number of reactants given by

$$\frac{d(q-q_b)}{dt} \propto -\frac{dm}{dt}. \tag{A.7}$$

The constant of proportionality is given by Q_0/m_0, where Q_0 is the overall heat of reaction (i.e., total heat emitted until completion of the reaction, $Q_0 = M_s H_s^{cure}$). Hence, Equation (A.7) can be written as

$$\frac{d(q-q_b)}{dt} = -\frac{Q_0}{m_0}\frac{dm}{dt}. \tag{A.8}$$

The degree of cure (α) is defined as the ratio of the total number of reacted molecules to the initial number of molecules available for reaction (m_0), given by

$$\alpha = -\frac{1}{m_0}\int_0 t - \frac{dm}{dt}. \tag{A.9}$$

The total number of remaining molecules capable of reacting is $m_0 - m$. Thus $d(m_0 - m)/dt = -dm/dt$ is the rate of reduction of the remaining reacting molecules leading to exothermic heat flow. As $(m_0 - m)$ decreases, then the level of cure is clearly increasing, so that $d(m_0 - m)/dt$ is proportional to the rate of cure, i.e., $d\alpha/dt =$

$-(1/m_0)dm/dt$. Using Equations (A.8) and (A.9), α and $d\alpha/dt$ can be expressed in term of the heat flow rate as follows:

$$\alpha = \frac{1}{Q_0}\int_0^t \frac{d(q-q_b)}{dt}, \tag{A.10}$$

$$\frac{d\alpha}{dt} = \frac{1}{Q_0}\frac{d(q-q_b)}{dt}. \tag{A.11}$$

Thus, $d\alpha/dt$ can be directly obtained from heat flow rate output from DSC by first subtracting the baseline then multiplying by $1/Q_0$. The degree of cure (α) takes values between 0 and 1, where $\alpha = 0$ corresponds to an uncured material and $\alpha = 1$ implies a fully cured material.

A.2.2 DSC Heating Programs

There are two types of heating experiments performed to extract α for the material. One is the isothermal heating program where the temperature of the sample and reference material are maintained at a predetermined value and heat flow rate is measured during the isothermal hold time. The second heating program is known as a dynamic temperature ramp experiment in which the temperature of the sample and reference are increases at a predetermined rate.

Isothermal Experiment

If the temperature (T) is high enough (more than 100 °C for 8552-1 epoxy), the time necessary to obtain various degree of cure, including complete cure, are relatively short, on the order of hours or even minutes. In such a case, one can perform a single isothermal DSC experiment as shown schematically in Figure A.3a to find α for various hold times. During the isothermal experiment at a temperature, the DSC system records heat flow rate away from the material as a function of time (exothermic reactions), shown in Figure A.3b. Using the heat flow rate data ($d(q-q_b)/dt$) the cure rate, $d\alpha/dt = (1/Q_0)d(q-q_b)/dt$. Integration of the cure rate from 0 to time t,

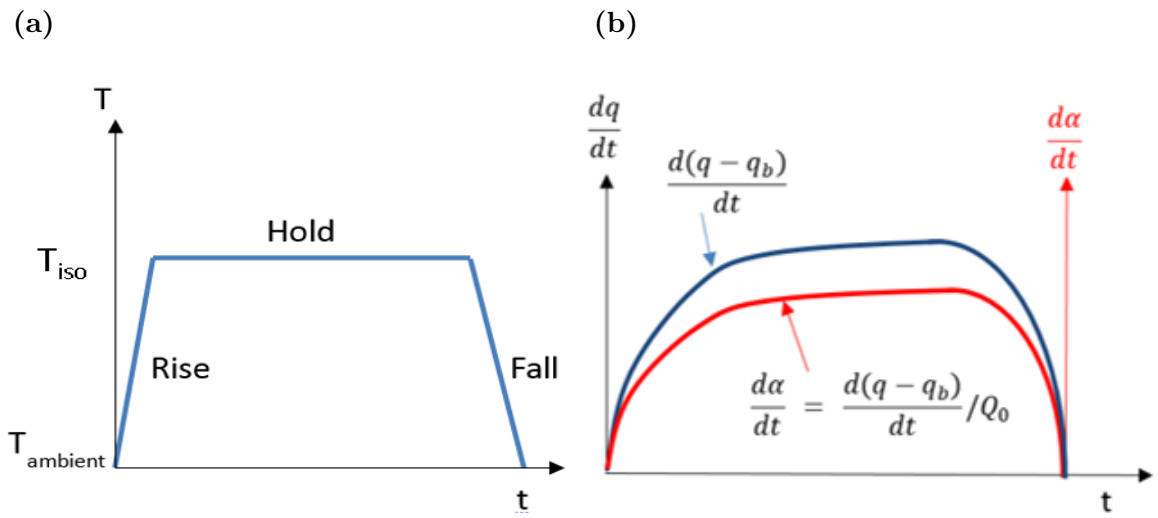

Figure A.3 Schematic of (a) the temperature history during an isothermal experiment, (b) heat flow rate and cure rate of the sample during a typical isothermal experiment

give the degree of cure at time t for the material when subjected to a temperature T. For example, Shahkarami, Van Ee, and Poursartip (2009) obtained degree of cure of Hexcel 8552 uncured polymer using isothermal experiments for T $\geq$ 100 °C.

Dynamic Temperature Ramp DSC Experiment

For relatively low temperatures, the time necessary to obtain various levels of cure can be months or even years. In such cases, running an isothermal DSC for an extended period is not practical. Under such conditions, a dynamic temperature ramp DSC experiment becomes necessary to quantify the degree of cure. In this work, the following procedure was adopted for finding α at low temperatures.

- The uncured prepreg is taken out of the refrigerator and allowed to thaw inside vacuum bag until the temperature reaches room temperature (25 °C). It is them taken out of the vacuum bag and stored in a controlled temperature (25 °C) and humidity conditions (65% RH) typically existing in AFP room for an extended period (from 1 hr to several weeks). A number of samples are thus formed which are stored under isothermal conditions for different durations (t_1,

$t_2 \ldots$). During this un-monitored external storage period (since storage take place outside the DSC chamber), the samples will begin the curing process through an exothermic reaction. Since heat flow during this storage period is not monitored, the history of cure is not available. However, the final degree of cure of the samples at the end of the storage can be obtained by measuring the residual heat of reaction (Q_r) using DSC dynamic temperature ramp test, as shown schematically in Figure A.4.

- In the dynamic temperature ramp experiment, each sample with a specified external storage period is placed inside the DSC cell and the temperature of the sample increased at a constant rate (dynamic ramp) until cure is completed. The area under the heat flow rate versus time graph from start to end of the dynamic temperature ramp experiment gives the residual heat of reaction (Q_r). A reference sample corresponding to storage time of $t_0 = 0$ hr is used to obtain the total heat of reaction ($Q_0 = Q_{r,t=0}$).

Degree of cure for different samples (S_1 to S_N) can be obtained using Equation (A.12):

$$\alpha_{t=t_i} = (Q_0 - Q_{r,t=t_i})/Q_0. \tag{A.12}$$

Here, $\alpha_{t=t_i} = (Q_0 - Q_{r,t=t_i})/Q_0$ is interpreted as the amount of cure of the material after being held at temperature T_{iso} for the hold time ($t = t_i$) shown in Figure A.4. From the above procedure, N discrete (α, t) data points can be obtained for N samples held at isothermal conditions.

A.3 EXPERIMENTAL METHOD AND MATERIAL

A.3.1 DSC EXPERIMENTAL SET UP AND SAMPLE PREPARATION

TA instruments' DSC Q2000 is used to obtain the heat flow rate from the sample subjected to dynamic temperature ramp experiments described in section A.2.2. All

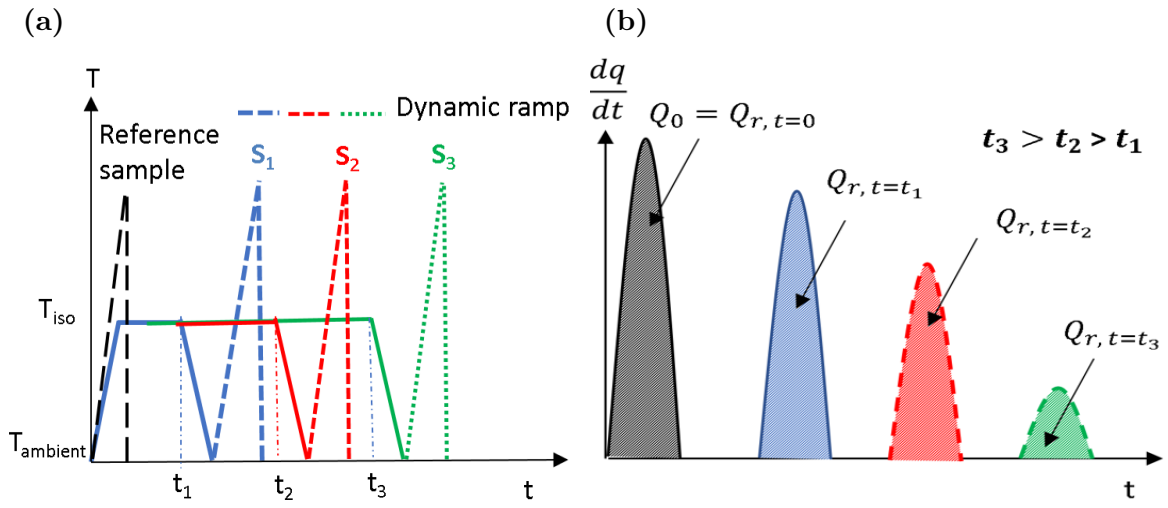

Figure A.4 Schematic of (a) temperature history during a dynamic ramp experiment and (b) residual heat of reaction for samples pre-cured for different periods at room temperature

the heat flow rate results are obtained with a temperature ramp rate of 10 °C/min. A photo of the DSC and a magnified view of the DSC cell are shown in Figure A.5.

Material and Sample Preparation

All experiments were carried out using samples extracted from IM7/8552-1 tow. The samples were aged in ambient conditions (temperature of 25 °C and relative humidity of 50 ± 10 %). Samples having an approximate dimensions of of 3 mm x 3 mm were extracted from the 6.35 mm wide Hexcel IM7/8552-1 tow using scissors. The samples weighed approximately 5 to 6 mg, measured using a scale (microbalance) having a standard deviation of ±0.03 mg. Since only a small quantity of the sample is used in the DSC analysis, accurate measurement of the mass of the sample is essential for accurate determination of specific heat of reaction. The sample was placed inside TA Instrument's standard aluminum pans as shown in Figure A.6. After placing a standard aluminum lid on the pan, it is crimped using TA instruments' TZero™ press (Thomas 2003) as shown in Figure A.7. The reference material is fabricated starting with an empty pan and crimping the empty pan and lid using the TZero™

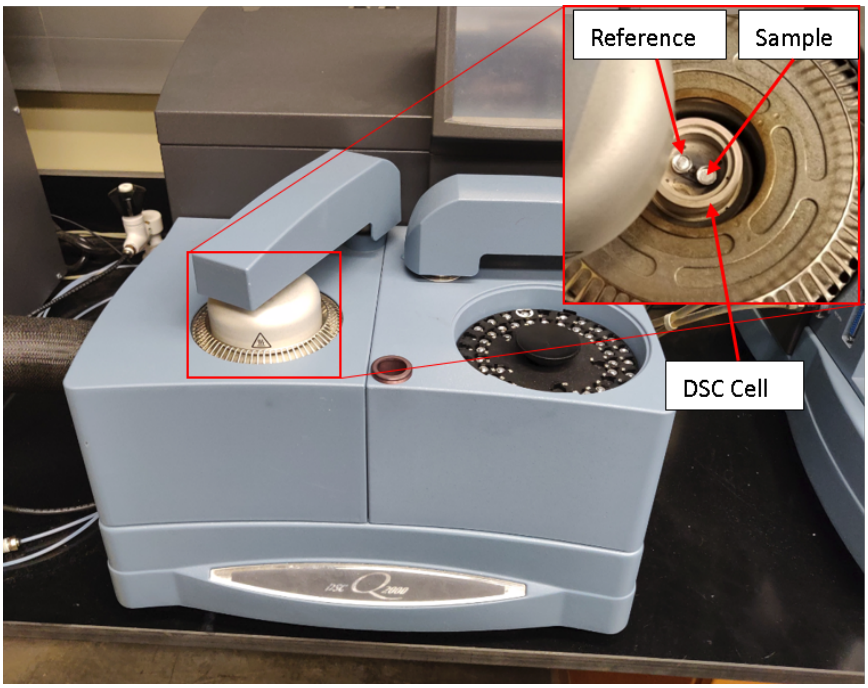

Figure A.5 TA instruments' DSC Q2000, INSET: Magnified view of the DSC cell with reference and sample material

press. Weight of the sample, sample pan and reference pan (standard deviation of ±0.03 mg) are entered in the TA instruments DSC control software for calculation of T4P heat flow. The manufacturer's specification of the resin weight fraction in the Hexcel IM7/8552-1 prepreg slit tape is 35%. In calculation of sample mass and specific heat of reaction, it is assumed that the resin weight fraction remains the same throughout the tow and variations in the resin weight fraction, if any, are neglected[2].

[2]In the calculation of degree of cure, it is assumed that the resin weight fraction of the IM7/8552-1 tow is as specified by the manufacturer (0.35). With the availability of a neat resin, estimation of α should be verified in future studies.

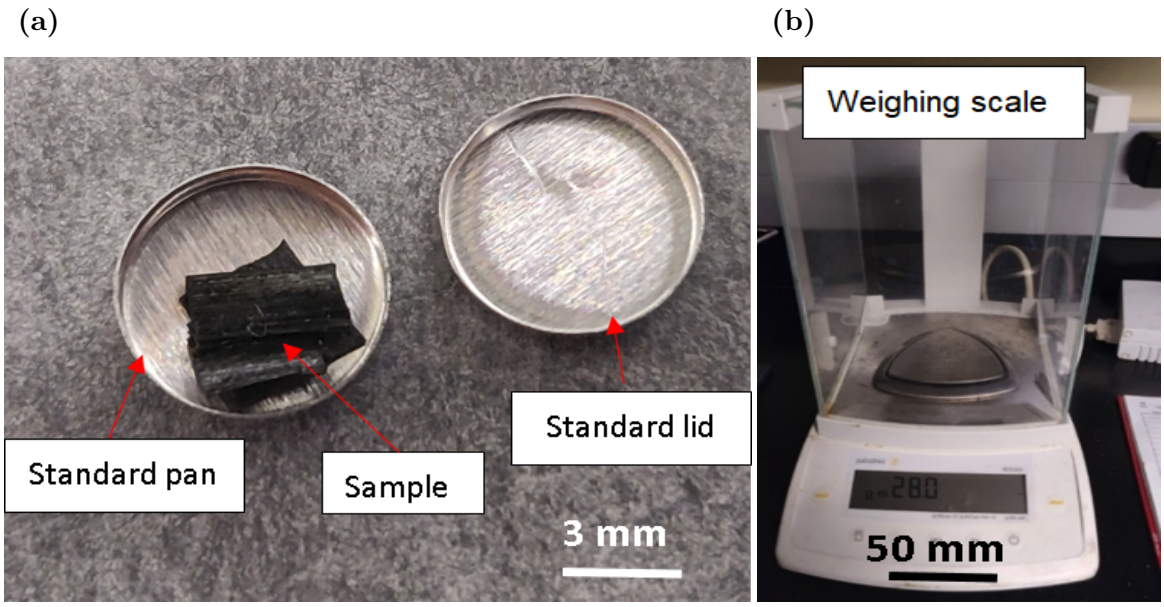

Figure A.6 (a) Prepreg sample inside standard aluminum pan and (b) weighing scale (microbalance) used to measure weight of the sample with a standard deviation of ±0.03 mg

Time Temperature History of Specimen

In general, the thermal history of the material is divided into three stages (see Figure A.8).

- Stage A: Corresponds to the time before DSC analysis of the sample. The sample might undergo a number of thermal changes during transportation and storage. The complete pre-test history of the sample is unknown. It is assumed that $Q_{pre-test}$ is negligible and was neglected in our previous calculations.

- Stage B: Corresponds to time when the sample is exposed to the ambient conditions (e.g., T = 25 °C and RH = 65%). The time period a sample stays in stage B is between 1 hr and 336 hrs. During stage B, the sample will undergo partial curing, the level of curing depends on the exposure time. Also, if the atmosphere is humid, moisture accumulates in the sample and its presence can be measured by taking the difference in the weight of the sample at the start and end of the exposure time. The heat emitted by the sample during stage B

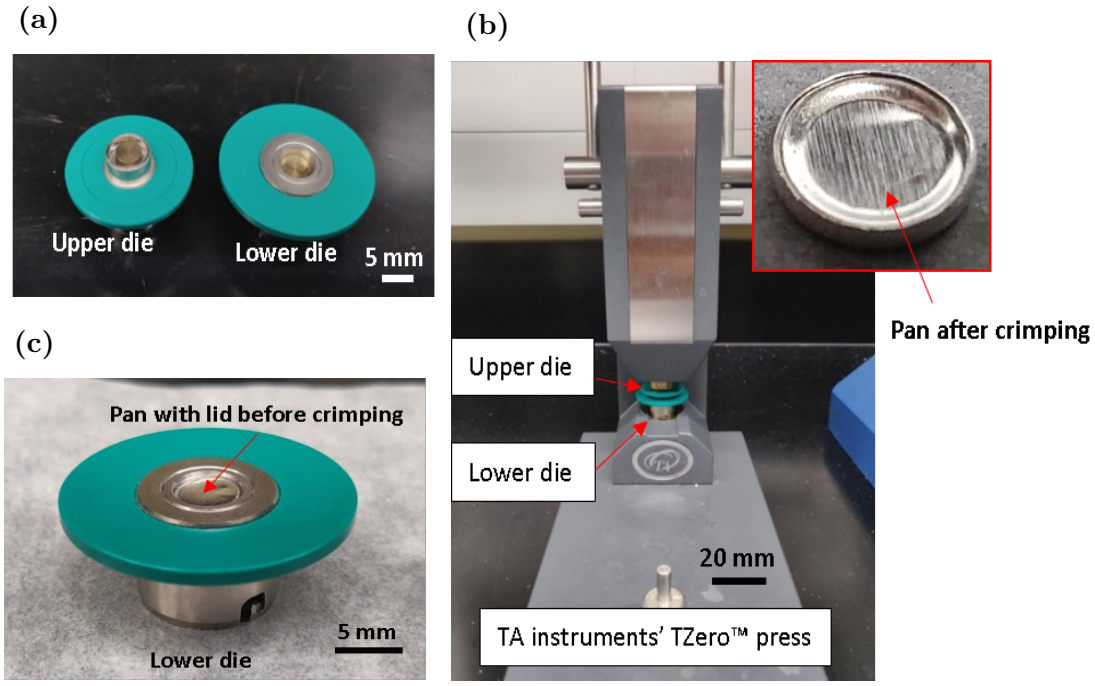

Figure A.7 (a) Upper and lower die used for preparing the standard aluminum pan with prepreg sample inside, (b) TA instruments' TZero^{TM} press for crimping the pan and lid, INSET: standard pan after crimping and (c) lower die with pan and lid before crimping

is denoted by Q_{iso}, and this quantity is indicative of the degree of cure of the sample after exposure (Q_{iso} is not measured directly using DSC; it is calculated from residual heat of reaction measured in stage C).

- Stage C: At the end of Stage B, the sample is place inside DSC and is cooled to $-40\,^{\circ}\mathrm{C}$. The sample is then heated at a constant rate until temperature reaches $320\,^{\circ}\mathrm{C}$. The maximum temperature is chosen such that the curing reaction is complete, and no significant thermal degradation of the sample occurs. The residual heat of reaction for stage C (Q_r) is measured using the heat flow rate output from DSC as discussed in section A.2.2.

- Degree of cure, α, is given by $\alpha(t = t_i) = Q_{iso}/Q_0 = (Q_0 - Q_r)/Q_0$, where Q_0 is the total heat of reaction and $Q_0 = Q_r + Q_{iso}$.

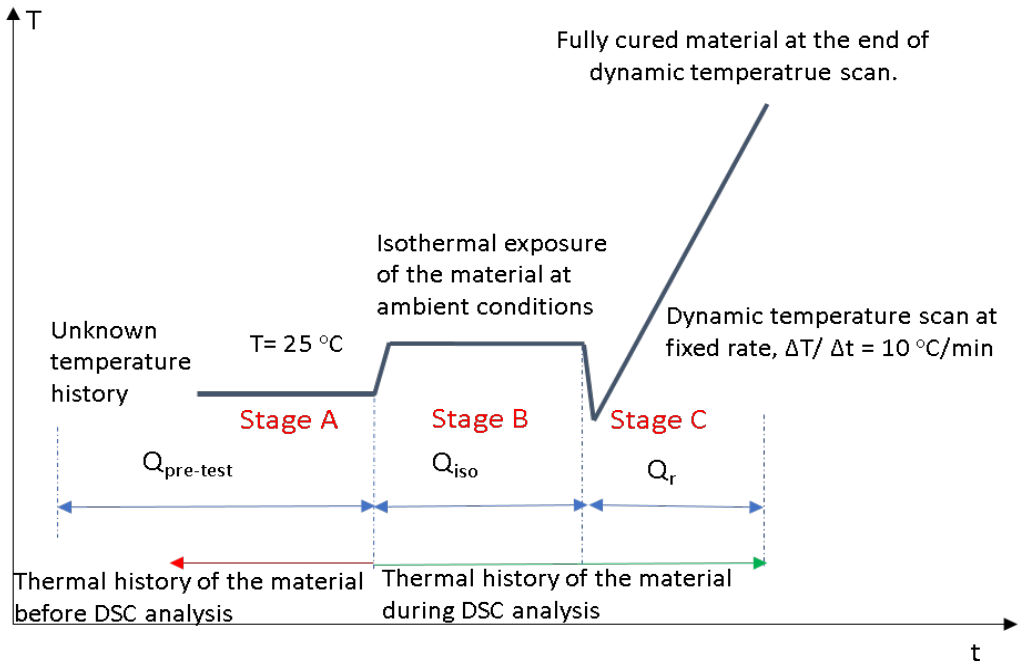

Figure A.8 Thermal history of the material before and during DSC experiment

A.3.2 DMA EXPERIMENTAL SET UP AND SAMPLE PREPARATION

The DMA used in performing the dynamic experiments is a TA instruments RSA III DMA equipped with liquid nitrogen cooling in the State Center for Mechanics, Materials and NDE located at the University of South Carolina. Minimum temperature achievable is $-150\,^{\circ}\mathrm{C}$ (using liquid nitrogen cooling) and maximum temperature is $650\,^{\circ}\mathrm{C}$. The specimen geometry selected for creep compliance experiments is a 3-point bend geometry. The 3-point bend specimen is chosen due to its higher compliance compared to the DMA load train so that displacements measured by the transducers will be least affected by system compliance. The experimental setup is same as shown in Appendix B, Figure B.1.

Procedures for sample preparation are the same as for the creep compliance experiment described in section B.2.1. The temperature and loading cycle are as follows. The storage modulus and T_g are determined using the DMA by conducting an os-

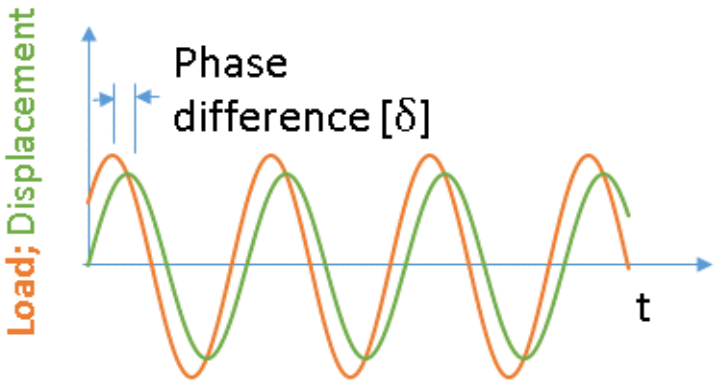

Figure A.9 Schematic of the load and displacement history of the specimen during oscillatory strain experiment

cillatory strain experiment on a 3-point bend specimen with a frequency of 1 Hz. The temperature is swept over the range $-20\,^{\circ}\mathrm{C}$ to $80\,^{\circ}\mathrm{C}$ with an increment of $2\,^{\circ}\mathrm{C}$. Schematic of the load-displacement history of the specimen during the oscillatory strain experiment (dynamic) is shown in Figure A.9. The expressions for complex modulus (E^*), storage modulus ($E^{'}$), loss modulus ($E^{''}$) and tan (δ) are shown in Equations (A.14) to (A.17).

$$\epsilon = \epsilon_0(\omega t); \sigma = \sigma_0(\omega t + \delta), \tag{A.13}$$

$$E^* = E^{'} + iE^{''}, \tag{A.14}$$

$$E^{'} = \frac{\sigma_0}{\epsilon_0} cos(\delta), \tag{A.15}$$

$$E^{''} = \frac{\sigma_0}{\epsilon_0} sin(\delta), \tag{A.16}$$

$$tan(\delta) = \frac{E^{''}}{E^{'}}, \tag{A.17}$$

where ω is the frequency of oscillatory strain, ϵ_0 and σ_0 are the maximum amplitude of strain and stress respectively.

A.4 RESULTS AND DISCUSSION

The DSC heat flow results for 8552-1 resin with different pre-cure time periods are shown in Figures A.10 to A.17. The total specific heat of reaction obtained from an uncured sample is $Q_0 = 564.6$ KJ/Kg. The measured total heat of reaction measured is close to the resin heat of reaction of 8552 resin given in previous studies; Q_0, 564 KJ/Kg in Shahkarami, Van Ee, and Poursartip (2009), and 531 kJ/kg in Hubert, Johnston, Poursartip, and Nelson (2001). Using residual specific heat of reaction for samples with different pre-cure time periods at room temperature, α is calculated using Equation (A.12). The values for α for different pre-cure periods is tabulated in Table A.1. It can be observed that increase in degree of cure is much faster in the early stages, eventually stabilizing at its maximum value, $\alpha = 7.9\%$.

Table A.1 Degree of cure (α) for different cure periods at 25 °C

Cure temperature(°C)	Cure time (Hrs)	Residual heat of reaction, Q_r (KJ/Kg)	Degree of cure, α	T_g(°C)
25	1	557.8	0.012	1.33
25	2	551.7	0.023	1.89
25	6	540.5	0.043	2.24
25	24	532.6	0.057	3.65
25	48	529.9	0.062	5.62
25	168	524.4	0.071	11.61
25	336	519.8	0.079	11.70

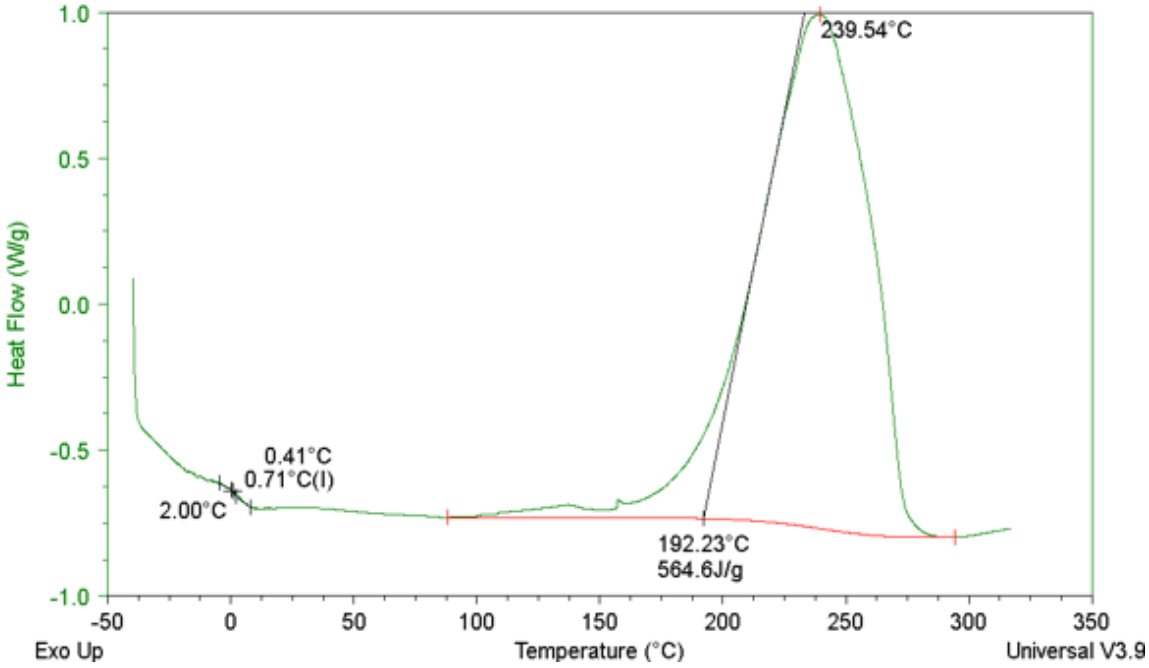

Figure A.10 Specific heat flow rate data for uncured 8552-1 epoxy

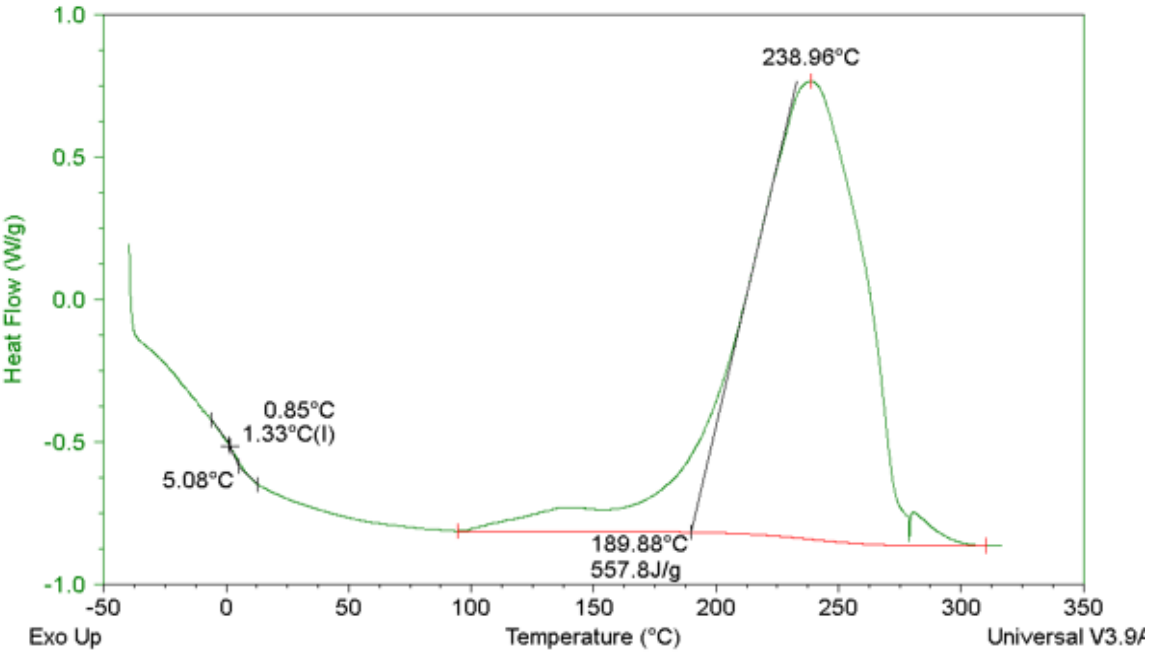

Figure A.11 Specific heat flow rate data for 8552-1 sample pre-cured for 1 hr at 25 °C

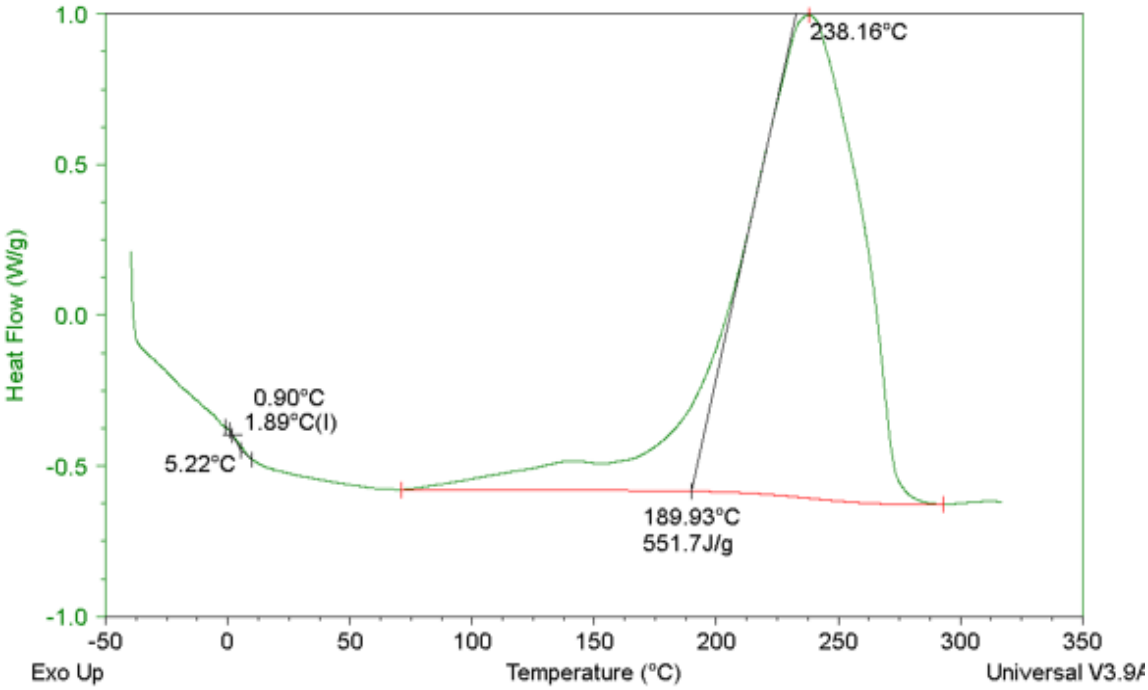

Figure A.12 Specific heat flow rate data for 8552-1 sample pre-cured for 2 hrs at 25 °C

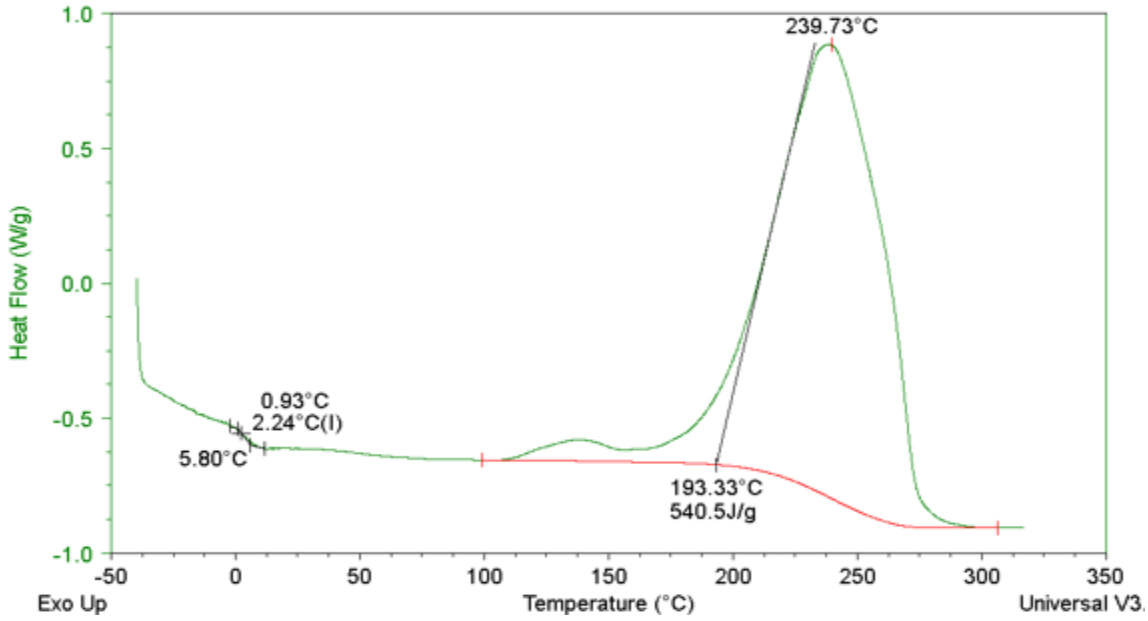

Figure A.13 Specific heat flow rate data for 8552-1 sample pre-cured for 6 hrs at 25 °C

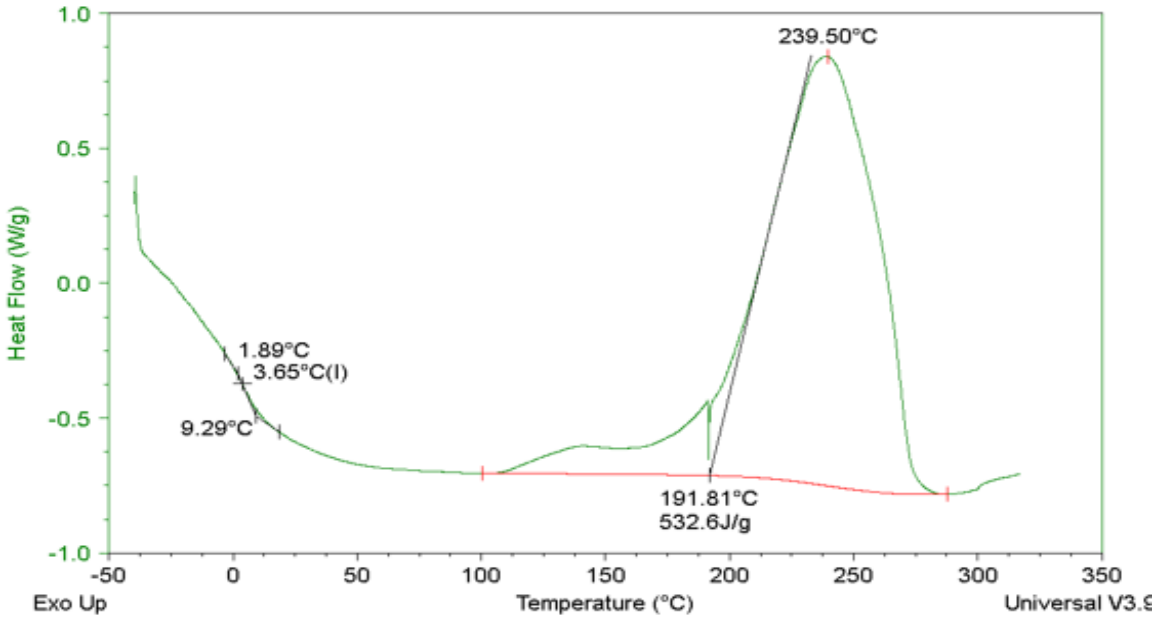

Figure A.14 Specific heat flow rate data for 8552-1 sample pre-cured for 24 hrs at 25 °C

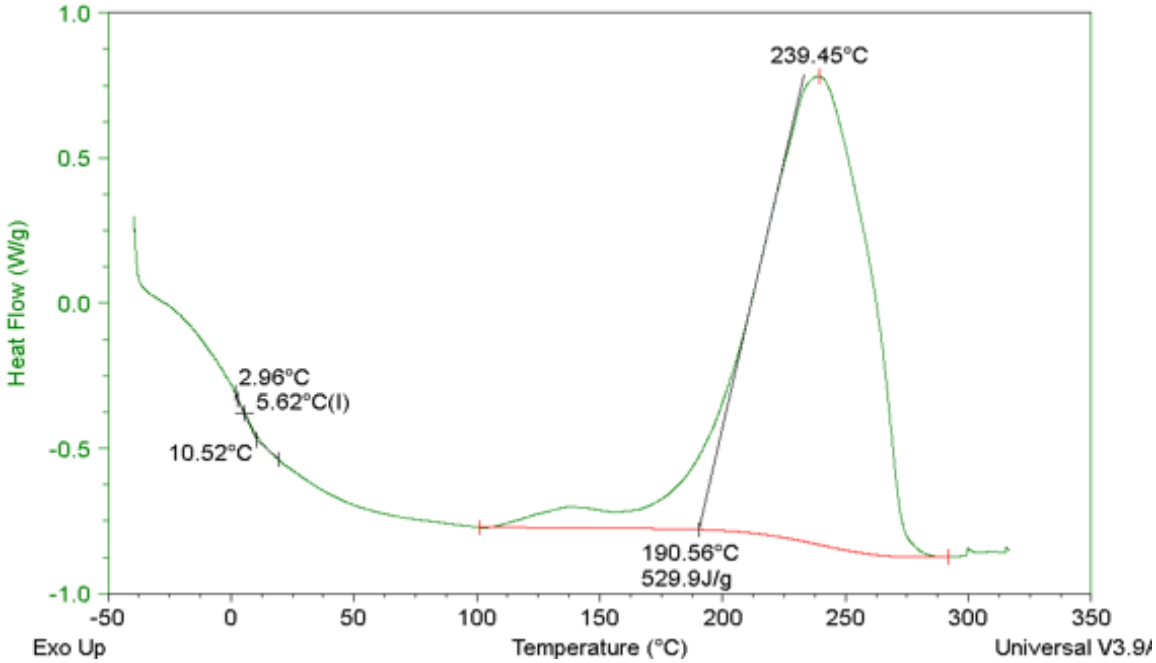

Figure A.15 Specific heat flow rate data for 8552-1 sample pre-cured for 48 hrs at 25 °C

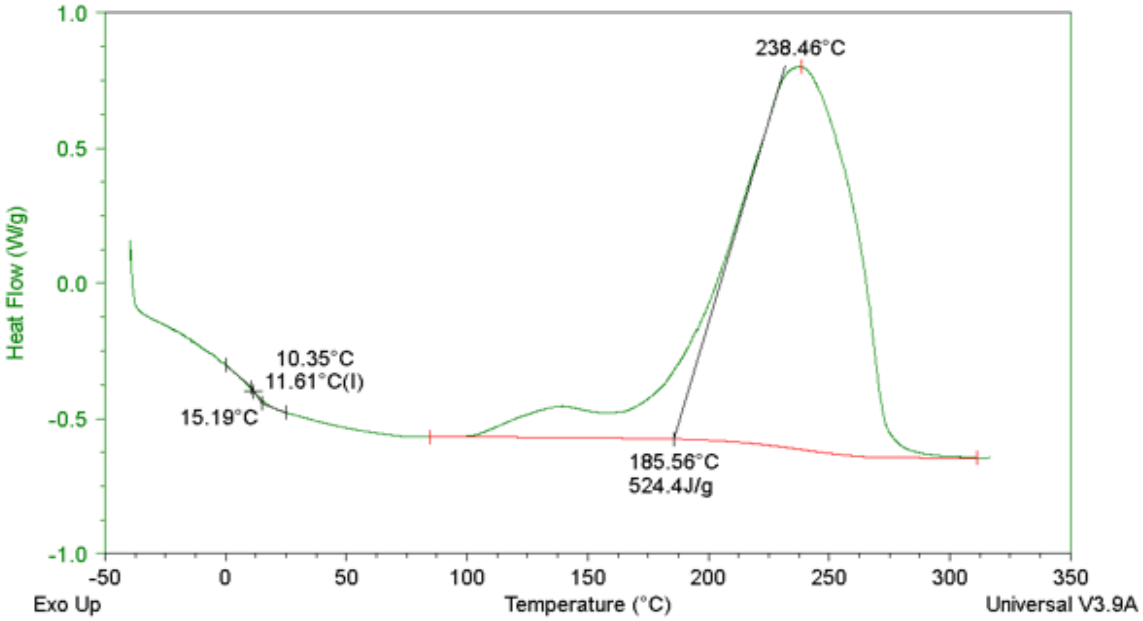

Figure A.16 Specific heat flow rate data for 8552-1 sample pre-cured for 169 hrs at 25 °C

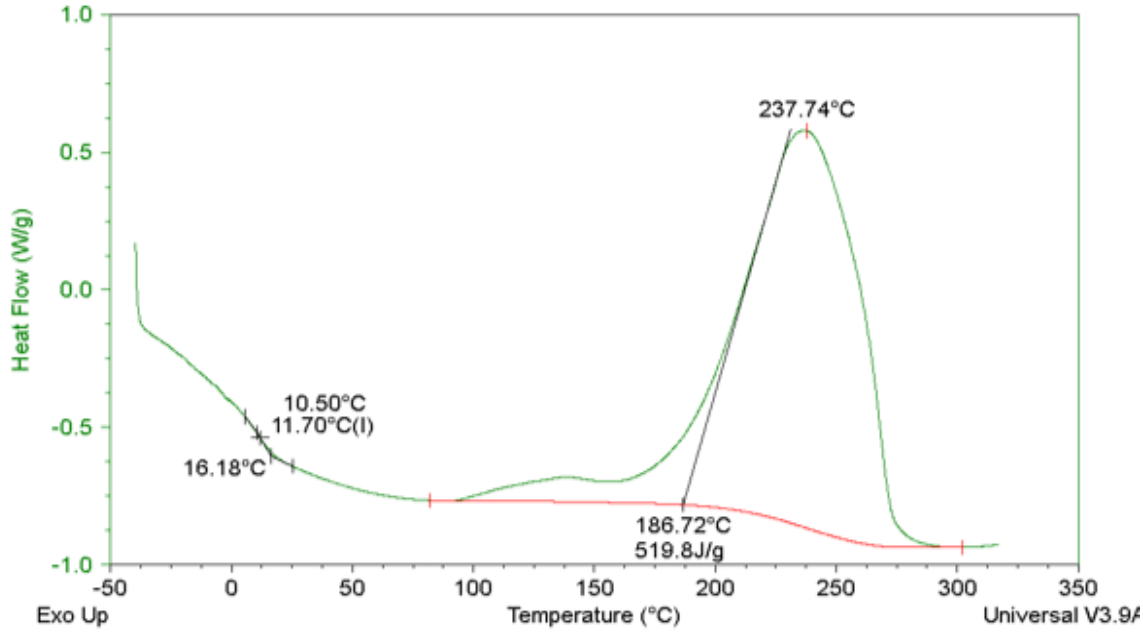

Figure A.17 Specific heat flow rate data for 8552-1 sample pre-cured for 336 hrs at 25 °C

A.4.1 Change in glass transition temperature and degree of cure

Careful examination of the DSC heat flow data shows an increase in glass transition temperature when the exposure time increases from 1 hr to 336 hrs. The T_g of uncured material is close to 0 °C. As T_g increases, the specific heat capacity of the material changes, and is manifest as a change in slope of the heat flow output from DSC. The increase in T_g along with degree of cure of IM7/8552-1 material pre-cured for different periods at room temperature are shown in Table A.1. It is observed that as the cure state progresses, T_g of the epoxy resin also increases from its uncured value of $T_g = 0\,°C$, to a maximum value of $T_g = 11.7\,°C$ after 336 hrs of curing at room temperature.

Increase in T_g with degree of cure is shown in Figure A.18. The increase in T_g is more rapid for degree of cure between 0.04 and 0.07 and the rate of increase in T_g drops significantly beyond degree of cure of 0.07 (out-time of 168 hrs and more). Investigation of the effect of room temperature aging on T_g of an out of autoclave (OOA) prepreg system in Grunenfelder and Nutt (2012) revealed a linear increase in T_g with aging up to 60 days. Three types of OOA prepreg materials investigated in their study were (a) five harness satin (5HS) carbon fiber fabric with a toughened epoxy resin (CYCOM 5320, Cytec Engineered Materials, USA), (b) eight harness satin fabric (8HS) with a toughened epoxy resin formulated for long out-life (CYCOM 5320-1, Cytec Engineered Materials, USA) and (c) 2 x 2 twill carbon fiber fabric and a toughened epoxy matrix (MTM44-l/CF5804A, Advanced Composites Group, UK). The change in T_g of all the three samples from no aging (uncured state) to 60 days of aging at ambient conditions is as follows; (a) T_g increased from 0 °C to 50 °C, (b) T_g increased from 0 °C to 25 °C, and (c) T_g increased from 0 °C to 20 °C. Differences in the trends in T_g with out-time of the Hexcel 8552-1 epoxy used in our study and the OOA epoxy system are due to the type of curing agent used. In contrast to the Hexcel 8552-1 epoxy system, the OOA epoxy fully cures at room temperature.

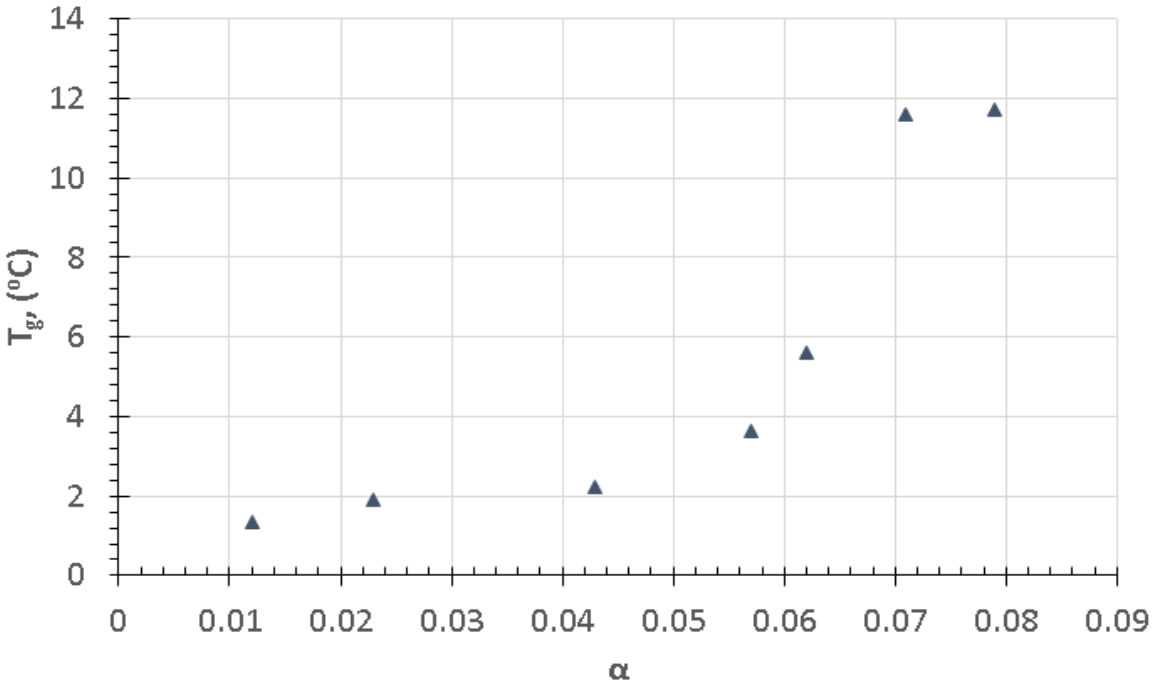

Figure A.18 Increase in glass transition temperature of 8552-1 epoxy resin with increase in degree of curing (aging) at 25 °C

In another study using an epoxy matrix composite (tetraglycidyl diamino diphenyl methane-diamino diphenyl sulfone), reinforced with standard carbon fibers (Frigione and Kenny 2002), the T_g of the material is observed to increase from 0 °C in the uncured state to 57 °C after 175 days of aging at ambient conditions. The authors observed a rapid increase in T_g beyond 60 days of aging. A similar trend in T_g with aging is observed for the Hexcel 8552-1 epoxy system used in our study, where the increase in T_g was rapid after 2 days of out-time[3]. Changes in degree of cure (α) with aging of the epoxy system used in their study showed a rapid increase in aging up to 7 days, before decreasing to steady rate. The Hexcel 8552-1 epoxy used in our study showed similar trends with a rapid increase in α up to 48 hrs. The increasing α for both epoxy systems is consistent with the kinetic model shown in Equation (A.18) (Frigione and Kenny 2002). The cure kinetic model fit to the Hexcel

[3]The degree of cure and T_g of the Hexcel 8552-1 epoxy system up to an out-time of 14 days measured using DSC is presented here; for prepreg aging up to 60 days see section A.4.2.

8552-1 epoxy system is shown in Figure A.19, and the model parameters are n = 1.087, $\alpha_m = 0.079$, and k = 4.23 x 10^{-4}/sec at 25 °C.

$$\frac{d\alpha}{dt} = k(\alpha_m - \alpha)^n, \tag{A.18}$$
$$k = k_0 e^{-E/RT},$$

where α_m, and α, are the maximum and actual degrees of reaction, respectively, k is the temperature-dependent rate constant at temperature T, k_0 is the rate constant at reference temperature, E is the Arrhenius activation energy, and n is the reaction order.

The maximum degree of cure (α_m) in the low temperature curing process of thermoset prepregs increases with temperature, with a linear relationship between (α_m) and cure temperature observed in Frigione and Kenny (2002). The effect of prepreg aging on tack was investigated in Ahn, Peterson, Seferis, Nowacki, and Zachmann

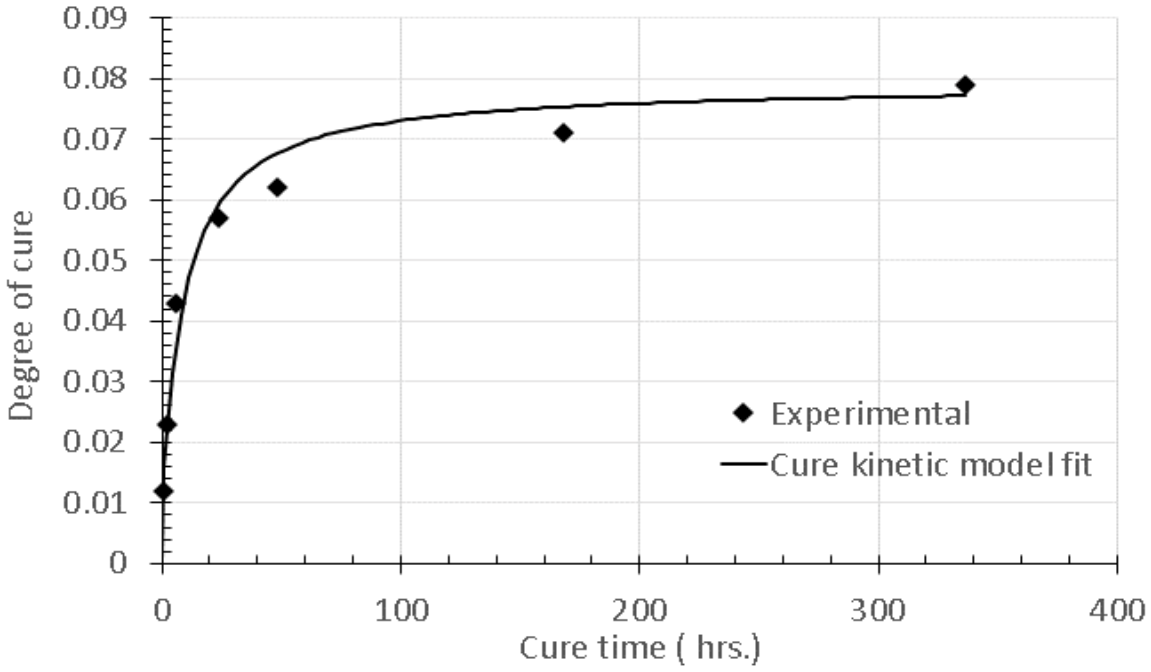

Figure A.19 Degree of cure versus aging time for 8552-1 epoxy resin for cure temperature of 25 °C

(1992) for carbon fiber/epoxy prepreg system (Hercules 3501-6). The authors measured prepreg tack as a function of prepreg aging at ambient and elevated temperatures. In their study, the prepreg tack was found to be a strong function of T_g, which decreased noticeably with room temperature aging time. The authors also measured change in degree of cure and T_g with time for storage temperatures of 25 °C and 75 °C. The degree of cure was observed to rapidly increase in the early periods of aging (up to 48 hrs), reaching maximum cure when cure time exceeds 300 hrs. The maximum degree of cure for a storage temperature of 75 °C was 0.55 and the corresponding degree of cure for storage temperature of 55 °C was 0.2. In their work, T_g was observed to increase linearly with degree of cure for both the storage temperatures and the maximum value of T_g at equilibrium cure was 20 to 25 °C higher than the storage temperature. These observations are comparable to the trends in the degree of cure and T_g observed for the Hexcel 8552-1 epoxy used in our work and for other epoxy systems reported in Frigione and Kenny (2002); Grunenfelder and Nutt (2012).

A.4.2 Storage and loss modulus of IM7/8552-1 tow

DMA is commonly used by polymer and soft-material scientists for conducting (a) transient creep experiments to obtain creep compliance and (b) dynamic oscillatory experiments to obtain loss modulus and storage modulus at different temperature and oscillatory frequencies (Rajan, Sutton, Oseli, Emri, and Matta 2017; Rajan, Sutton, Fuerte, and Emri 2018). In this work, storage and loss moduli of the IM7/8552-1 tow for a range of temperature from −20 °C to 80 °C are obtained using a DMA by applying an oscillatory loading with a frequency of 1 Hz[4]. Typically there is orders of magnitude decrease in the storage modulus from glassy to rubbery state, with changes in storage modulus at T_g being more pronounced than changes in heat flow measured by DSC.

[4]see Appendix B for viscoelastic creep compliance and retardation spectra.

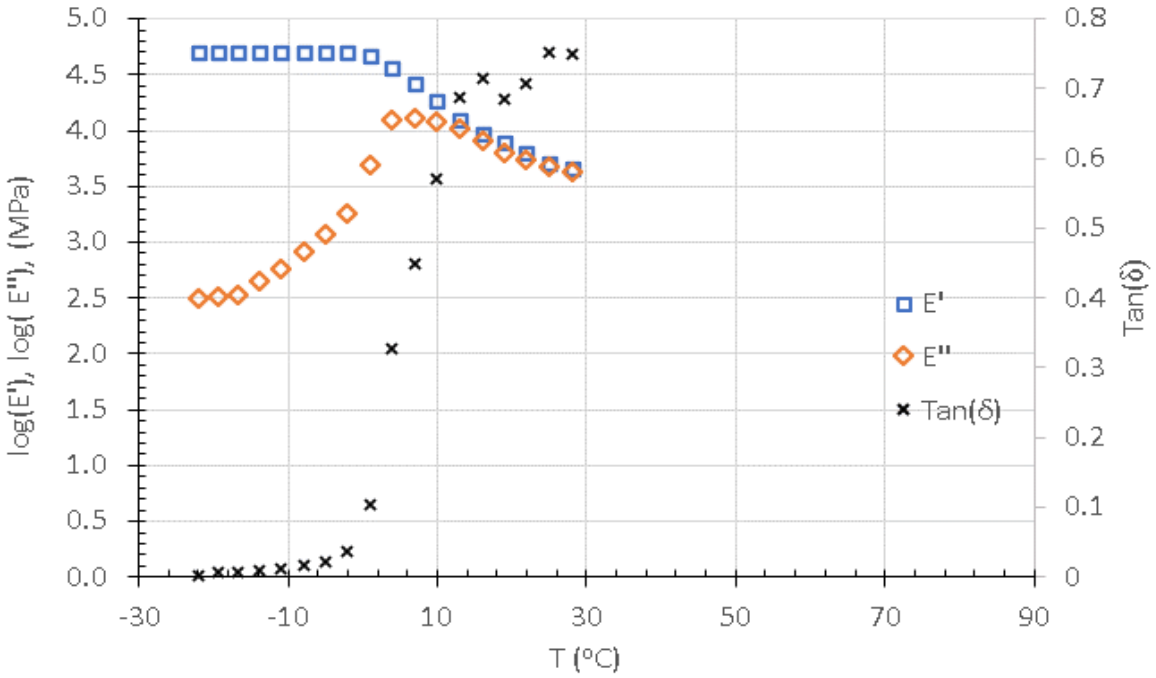

Figure A.20 Storage modulus, loss modulus and tan(δ) of uncured prepreg

Variations in the storage modulus ($E^{'}$), loss modulus ($E^{''}$) and tan(δ) (tan($E^{''}/E^{'}$)) with temperature during the dynamic experiments of the uncured prepreg tow are shown in Figure A.20. As shown in the figure, storage modulus incurs significant reductions as the temperature increases above $-2\,^{\circ}$C. The loss modulus and tan(δ) reach peak values at $4\,^{\circ}$C and $28\,^{\circ}$C, respectively. Based on these results and the ASTM E1640-13 standard procedure (ASTM 2013) using the intersection of two tangent lines to the storage modulus curve, with one below the sigmoidal transition and the other at the inflection point, T_g of the uncured prepreg is estimated to be $0\,^{\circ}$C, which is slightly lower than that observed from DSC analysis ($0.7\,^{\circ}$C). The variations in $E^{'}$, $E^{''}$ and tan(δ) for the prepregs with aging times of 8 days and 90 days are shown in Figures A.21 and A.22 respectively. The T_g of the prerpeg material increased to $19.6\,^{\circ}$C after an out-time of 8 days and $44.8\,^{\circ}$C after 90 days of aging at ambient conditions. The T_g of the material after 90 days of aging was $19.6\,^{\circ}$C higher than the ambient temperature. Similar finding are also reported in Ahn, Peterson, Seferis, Nowacki, and Zachmann (1992); Frigione and Kenny (2002).

The small difference in measured T_g values from DMA experiments compared

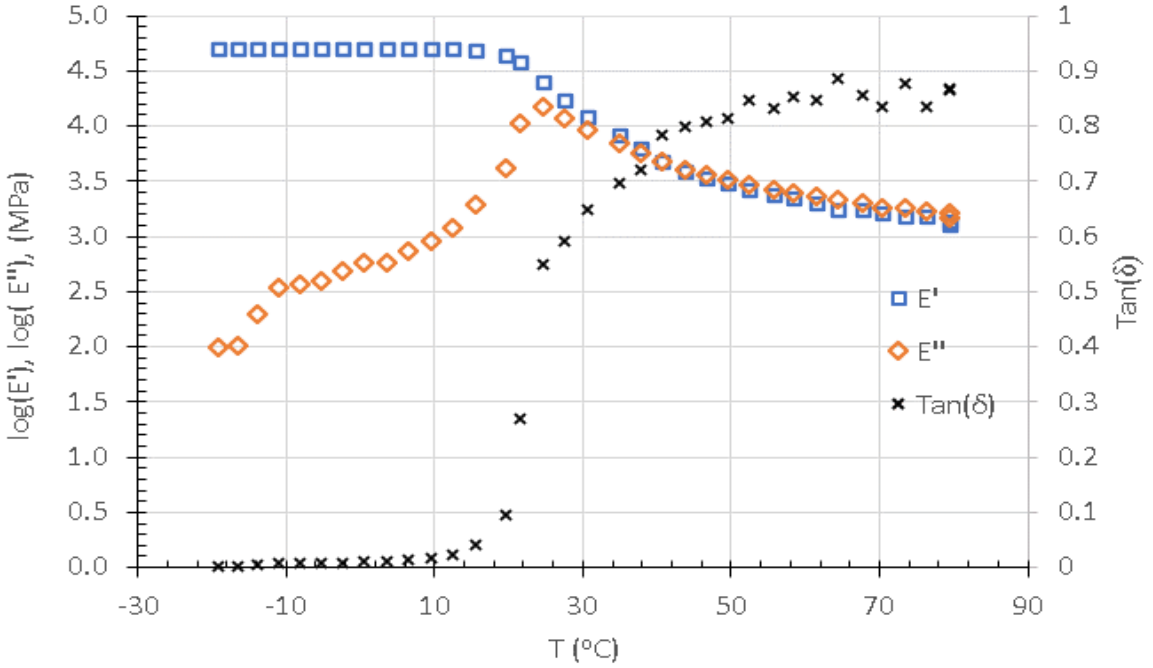

Figure A.21 Storage modulus, loss modulus and tan(δ) of prepreg with aging time of 8 days

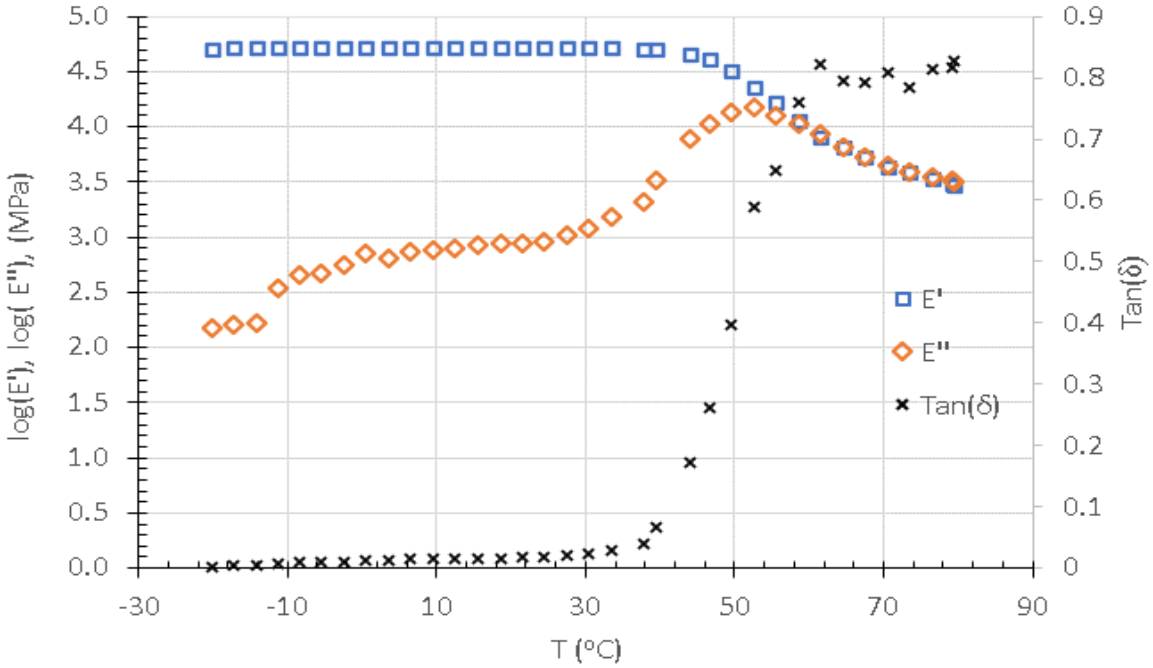

Figure A.22 Storage modulus, loss modulus and tan(δ) of prepreg with aging time of 90 days

to DSC measurement is due to the difference in the method used for estimating T_g[5]. Changes in the modulus and heat flow rate gradually affect T_g of the polymer, which is in sharp contrast to changes observed for crystalline materials. Thus estimation of T_g may vary slightly depending on the type of procedure implemented. It is to be noted that modulus of the material has higher sensitivity to temperature at the T_g than heat capacity changes, so that T_g measured using DMA is more accurate. The change in T_g measured using DSC and DMA experiments are combined in Figure A.23, showing results for aging time from uncured state to 90 days. Increases in T_g were significant beyond an out-time of 48 hrs, indicating that processability of the prepreg could be severely impaired with aging time beyond 48 hrs.

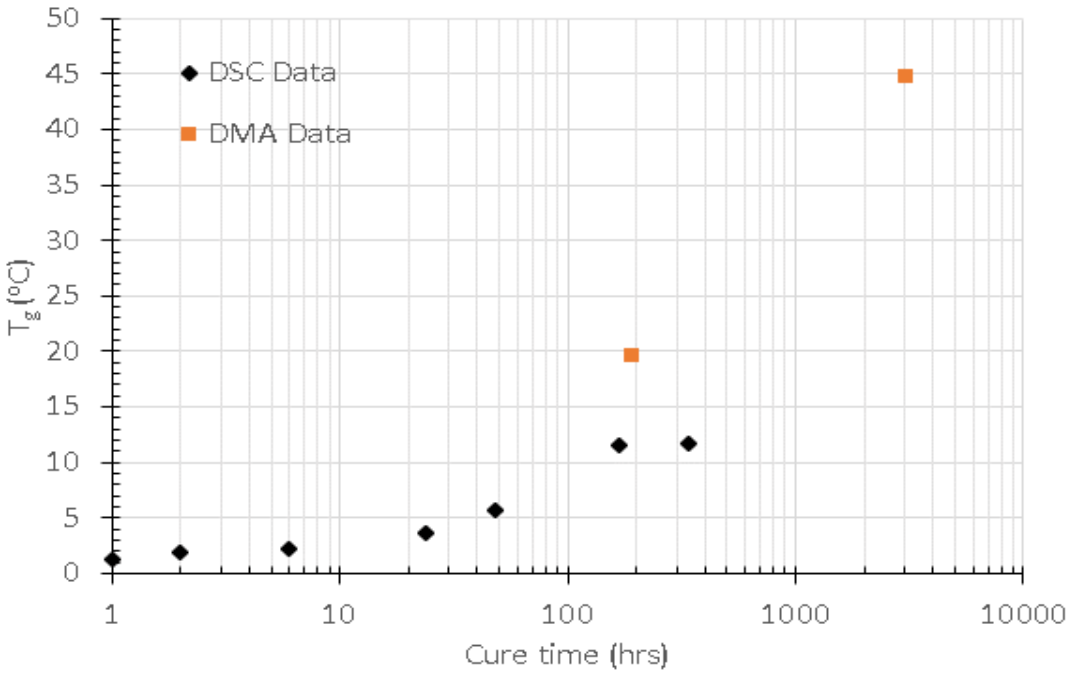

Figure A.23 Change in T_g of prepreg with aging time up to 90 days measured using DSC and DMA

[5]In some of the literature, peak in loss modulus is used for estimating T_g.

A.5 CONCLUSION

The heat flow rate for Hexcel IM7/8552-1 prepreg tow pre-cured for periods ranging from 1 hr to 336 hrs at room temperature (25 °C) are obtained using TA Instruments' Q2000 DSC. A dynamic temperature ramp program is chosen to obtain the residual heat of reaction and degree of cure of the epoxy samples pre-cured at relatively low temperatures. The measured specific heat of reaction of an uncured sample was measured to be 564.6 KJ/Kg, which is close to the specific heat of reaction of 8552 resin reported in Shahkarami, Van Ee, and Poursartip (2009); Barton (1985). The degree of cure of the epoxy increases with cure time at a higher rate in the initial stages of cure and the rate of curing decreases significantly after an out-time of 168 hrs. The reduction in rate of cure of the epoxy is associated with vitrification of the molecules occurring as a result of T_g of the material approaching storage temperature of the sample during the curing period (25 °C). The cure kinetic model was observed to fit well with the degree of cure measured using DSC experiemnts. Storage modulus, loss modulus, $\tan(\delta)$, and T_g of the tow, in the uncured state and with room temperature out-times of 8 days and 90 days, are obtained using three-point bend specimen using a RSA III DMA. The T_g of the prepreg is observed to increase to 44.8 °C after 90 days of out-time.

Appendix B

VISCOELASTIC CHARACTERIZATION OF PREPREG SLIT TAPE

The creep response of uncured thermoset prepreg slit tape during 3-point bend testing at different temperatures measured using RSA III dynamic mechanical analyzer is presented in this chapter. Short term creep experiments were conducted for a duration of 1000 seconds at ten different temperatures ranging from $-5\,^{\circ}\mathrm{C}$ (below T_g of $0\,^{\circ}\mathrm{C}$) and to $40\,^{\circ}\mathrm{C}$ (nominal processing temperature). The material is found to obey the time temperature superposition principle (TTSP) in the temperature range selected for creep experiments. Using TTSP, the creep compliance master curve spanning more than eight logarithmic decades is obtained for a reference temperature of $40\,^{\circ}\mathrm{C}$. The time-temperature shift factor is observed to follow closely to William-Landel-Ferry (WLF) model and WLF parameters are obtained by least square fitting of the experimentally determined shift factors with WLF model. The WLF model for the material can be used to extend the master curve for different temperatures above T_g of the material. The creep compliance data is further used to obtain retardation spectra of the material using an algorithm based on the work of Emri and Tschoegl (1993). The steps required for extraction of the retardation spectra from creep compliance are explained in detail. Finally, it is shown that, the creep compliance reconstructed from retardation spectra accurately represents the experimental results.

B.1 INTRODUCTION

In a recent study, Liang, Hamila, Peillon, and Boisse (2014) identified the out-of-plane bending stiffness of the prepreg tow as a critical factor influencing the size and number of wrinkles. In order to determine AFP process parameters for minimal wrinkling, accurate prediction of wrinkle formation during the placement process is necessary. A recently successful tow placement simulation methodology (Rajan et al. 2020b) employed the finite element (FE) method with continuum material parameters. The simulations require measurement of an "effective" bending stiffness of the tow material for the range of temperatures relevant to the AFP process. In the remainder of the introduction, a review of previous research regarding FE modeling and experimental characterization of effective tow bending stiffness is discussed.

Modeling of bending of prepreg material has been a focus of many studies related to thermoforming processes. Conventional plate theory assuming zero through-thickness shear deformation is observed to over-predict the bending stiffness of the prepreg, especially at higher temperatures (Liang, Hamila, Peillon, and Boisse 2014; Alshahrani and Hojjati 2017). Processing temperature of thermoplastic prepreg is above its melting temperature and the matrix material behave like a viscous fluid resulting in large shear deformation. For a prepreg fabric material with a weak matrix material (uncured thermoset tow or thermoplastic prepreg near matrix melting temperature), significant though-thickness shear may be present during bending. In order to account for the significant difference in the in-plane tensile modulus and out-of-plane bending modulus, a common method adopted by many investigators is through decoupling of bending and membrane behavior in the FE formulation. For example, Dörr, Schirmaier, Henning, and Kärger (2017) modeled the bending response of thermoplastic prepreg using conventional shell elements with decoupled bending and membrane behavior. The bending moment and membrane forces are calculated independently using the curvature tensor and membrane strains, respec-

tively. Authors have also included the viscoelastic effects in the bending response using Maxwell and Kelvin-Voigt model in an effort to improve the simulations. In a related paper, Soulat, Allaoui, and Chatel (2009) used standard shell finite elements in the thermoforming simulation of unidirectional thermoplastics tows. The authors included an additional degree of freedom to model thickness changes during consolidation of the prepreg. The primary focus of their FE model was the prediction of removal of porosity during reconsolidation. In both models, the effect of intra-ply shear during bending is ignored.

An alternate approach to FE modeling of bending of prepreg is employed in Rajan et al. (2020b) where the geometric thickness of the tow is adjusted so that a single modulus in the fiber direction (E_1) can be used to predict both the bending and membrane tensile stiffness. This approach allows one to use a continuum shell element finite element formulation in the AFP simulation for predicting wrinkles. The authors used a reduced tow thickness with shell elements to model tow response, confirming that the model predictions of wrinkle shape and frequency are consistent with experimental observations and measurements.

Previous work characterizing bending stiffness, such as employed in ASTM D1388 cantilever beam tests and Kawbata bending tests (Kawabata and Niwa 1989), were primarily focused on the response of woven textile fabrics. Liang, Hamila, Peillon, and Boisse (2014) measured the bending stiffness of a thermoplastic prepreg material using a cantilever beam bending experiment performed at temperatures relevant for their thermoforming process. The bending moment curvature relation was obtained by measuring deformation of the prepreg sample using images of the side edge at each temperature. The authors have shown that bending stiffness influences the size of wrinkle formation during a thermoforming process. Alshahrani and Hojjati (2017) employed a vertical cantilever beam test method for characterization of bending stiffness of out-of-autoclave woven prepreg. For modeling bending behavior, the authors used

Euler-Bernoulli beam theory assumptions. The vertical cantilever test set up has the advantage of removing the effect of gravity load on the bending response. Short-term stress relaxation experiments (300 sec) using the cantilever test method were used to quantify the viscoelastic response. The bending experiment relaxation modulus was fitted with a three parameter Prony series to obtain the viscoelastic parameters. However, the model fit to the moment-curvature relation for small values of curvature was shown to be inaccurate, possibly due to large relative error in the measurement of the small specimen curvature. In addition, the authors also observed that prediction of the specimen response at higher temperature using time-temperature superposition did not agree with independent experimental measurements. In their relaxation studies, the authors applied relatively large deformations; however, for many polymeric materials, linear viscoelastic theory is valid for a range of small strain and deformation (Ferry 1980).

In another study, bending stiffness measurements for unidirectional thermoset prepregs was performed by Wang, Long, and Clifford (2010) by performing a buckling experiment. The authors identified three distinct responses, such as elastic buckling for small deformation of the prepreg, a transition region and plastic buckling associated with large deformation, and fiber slipping and intra-lamina shear deformation. It was assumed that elastic buckling response can be modeled using simple beam bending theory, whereas in the transition and plastic buckling regions the response is much more complex. A comprehensive review on different types of bending tests performed for characterizing bending behavior of uncured slit tape and woven fabrics is given in Alshahrani and Hojjati (2017).

Though the cantilever beam test method is commonly used for characterizing the bending behavior of woven fabric and prepreg material, some of the drawback of the cantilever bending experiment identified in various studies are (a) difficulty in measuring accurate moment-curvature data near the clamped edge (data corre-

sponding to small curvatures), (b) viscoelastic or rate effects are difficult to quantify due to imprecise load/displacement measurements, and (c) requirements for accurate temperature control using a custom-built testing frame.

An alternative, widely accepted approach for characterizing the bending behavior and viscoelastic properties of polymeric materials over a broad range of temperatures is to employ a Dynamic Mechanical Analyzer (DMA). Interestingly, there are relative few authors who have published DMA-based data for characterizing the viscoelastic bending stiffness of uncured thermoset prepreg. Erland, Dodwell, and Butler (2017) modified simple beam theory to include the effect of intra-ply shear by allowing plane sections of the beam to be non-orthogonal to the neutral plane. The resulting equation for bending deflection has an additional term that is a function of beam length. In their studies, the authors found that the oscillatory intra-ply shear modulus is a strong function of temperature. However, viscoelastic effects were not obtained by the authors. Dodwell, Butler, and Hunt (2014) employed a simplified one-dimensional analytical model for predicting out-of-plane wrinkling during compaction of multilayer plies over an external radius in thermoforming process. For predicting the wrinkling behavior of uncured AS4/8552 prepreg, the authors performed DMA experiments to determine the bending stiffness of the prepreg. Margossian, Bel, and Hinterhoelzl (2015) used DMA experiments to quantify the bending stiffness of a thermoplastic prepreg laminate in the molten state. The bending stiffness was calculated for constant strain rates using Euler-Bernoulli beam assumptions for small deformation of the beam. The time-temperature dependent viscoelastic parameters normally calculated from standard viscoelastic experiments such as creep, relaxation or oscillatory tests were not reported in their work. In a related study, Ropers, Sachs, Kardos, and Osswald (2017) determined the viscoelastic properties of a thermoplastic prepreg using DMA at different frequencies and temperature range. Time temperature superposition was used to obtain the master curve for frequencies ranging from 10^{-9}/sec to

10^{11}/sec. The authors also compared results from a finite element simulation based on a 20-term Prony series model fit to the experimental data (the method used to obtain the Prony series terms was not reported). Their simulation predictions deviated substantially from the experimental measurements with increasing temperature.

Since most published literature for viscoelastic characterization is for fiber-reinforced woven or unidirectional composites with thermoplastic matrix material, research focused on characterizing the viscoelastic behavior of uncured thermoset tow materials continues to be of long-term interest. This is especially relevant in advanced manufacturing applications. For example, AFP processing occurs at speeds up to 2m/s in aerospace applications, resulting in highly transient thermomechanical conditions in each tow. In such cases, characterization of the linear viscoelastic response of tows is important to quantify the significance of time-dependent effects in wrinkle formation and for robust FE modeling of the AFP process. In this work, a Dynamic Mechanical Analyzer is employed for performing tow bending experiments over a range of temperatures relevant to AFP processes to determine both the creep compliance and the retardation spectra for an uncured thermoset prepreg material (IM7/8552-1). Since it was shown in the previous study (Rajan et al. 2020b) that tow deformation during the early stages of wrinkle formation is small, the work of Liang, Hamila, Peillon, and Boisse (2014) is relevant. As shown in their previous experimental studies, a linear relationship between the bending moment and curvature of the tow exists for small curvatures. Thus, for relatively thin thermoset tows undergoing small deformations, the bending deflection can be approximated using Euler-Bernoulli beam theory[1]. Using the linear moment-curvature relationship, short-term creep experiments for eight different temperatures in the range of $-5\,^{\circ}$C to $40\,^{\circ}$C are performed. Using time temperature superposition, a master curve extending over nine logarithmic decades

[1]The linear moment-curvature relationship is written $M = EI\kappa$, where κ is the curvature and EI is the bending stiffness.

is obtained. Rest of this chapter is organized as follows. Section B.2 presents the experimental set up and materials used for bending stiffness characterization. Consistent with observed tow processing conditions, linear viscoelastic theory is used to model the material response and briefly explained in Section B.3. Experimental results and their relevance in assessing the importance of viscoelasticity in wrinkle formationare presented in Sections B.4. Conclusions are given in Section B.5.

B.2 EXPERIMENTAL SETUP

The Dynamic Mechanical Analyzer (DMA) from TA Instruments is used for measurement of creep compliance of the uncured prepreg material, IM7/8552-1. The specimen is subject to three-point bending using the fixture shown in Figure B.1a. The tow secimen dimensions and coordinate system are shown in Figure B.1b. Since the DMA is designed for testing soft materials and has high compliance compared to the tow along the fiber direction, a three-point bend geometry is the most suitable test configuration for measuring viscoelastic properties (Rajan, Sutton, Oseli, Emri, and Matta 2017). Short term creep experiments (1000 sec) are performed within the environmental chamber every 5 °C increment in the range of −5 °C to 40 °C. At the highest temperature (40 °C), the time period for creep experiment is reduced to 200 sec in order to reduce the effect of aging of the material on the creep data. Experiments were not conducted above 40 °C, as significant changes in creep compliance are observed, indicating occurrence of cross-linking of the thermoset resin within a short time (200 secs), making the use of linear viscoelastic theory inappropriate. For each temperature, twenty experiments were conducted using different samples to record sample-to-sample variations and obtain a consistent average response.

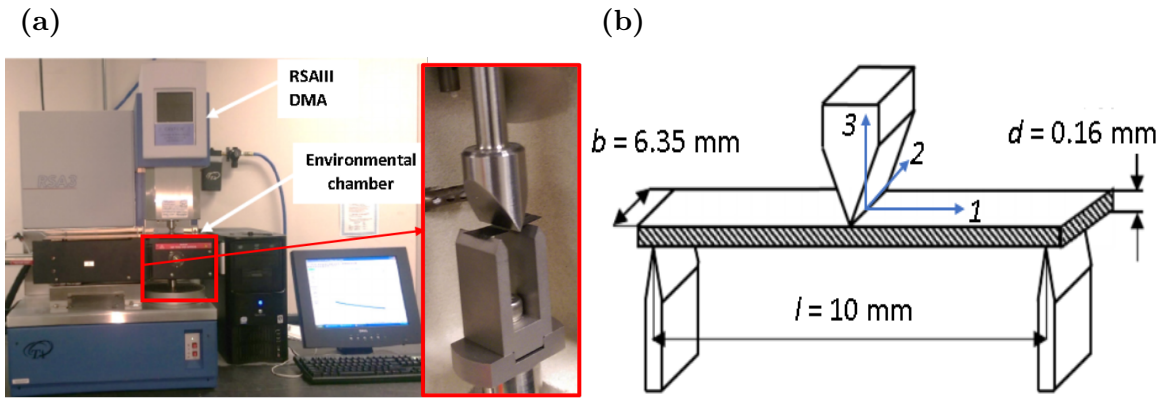

Figure B.1 Dynamic mechanical analyzer setup showing (a) close-up view of the three-point bend fixture and (b) schematic of the specimen geometry with orthogonal coordinate system

B.2.1 Material and sample preparation

The material used for all creep experiments is IM7/8552-1 prepreg tow in the uncured state. Each creep sample consists of one layer of tow having a width of 6.35 mm after it is excised from the spool to the required length (12 mm). In total, 180 samples were prepared from one batch of spool supplied by Hexcel. Experiments utilize separate samples since the material ages with time and significant changes in viscoelastic properties can occur depending on the temperature and exposure time. Sample preparation is as follows. Spool containing the prepreg tow is removed from freezer and thawed inside a vacuum sealed bag at room temperature to prevent contamination with moisture during thawing, then, samples of required length are cut from the spool. Initial curvature in the tow is straightened by placing it on a flat Teflon coated surface and slightly pressing with silicone rubber. The sample is then removed from the Teflon coated surface and immediately placed on the three-point bend fixture inside the DMA environmental chamber, where temperature is maintained at the required level by flow of dry nitrogen gas.

B.2.2 Experimental procedure

The experimental procedure is as follows. First, the sample is placed inside the environmental chamber on bending fixture. Once the sample is inside the chamber, heating or cooling system is activated and the sample is soaked at test temperature for 200 seconds to thermally equilibrate with surroundings. Then, sample is immediately subjected to a constant load, with load-line displacement recorded at 0.5 Hz for duration of creep experiment. Cooling below room temperature is achieved by controlled evaporation of liquid nitrogen (LN2). Since dry nitrogen is used to cool the specimen, moisture contamination is eliminated. For higher temperatures, heating uses a heating coil with nitrogen gas as the medium to minimize oxidation of the material at higher temperature. Each creep experiment is performed by controlling the applied load history to closely approximate a step function, which is ideal for our creep experiment. Due to inertia of the loading system, oscillation in the load is inevitable during the very early stages of the experiment. These oscillations are observed to dissipate within a few seconds (3 secs). To simplify creep compliance calculations and eliminate the effect of transient loading conditions, creep data obtained during the first 10 seconds of loading is excluded. The creep load for each temperature is determined by ensuring that material response is within the linear range. For the tow material system, data has shown that the specimen is linear viscoelastic when the maximum strain in the material is less than 0.5%.

The DMA system has a load resolution of 1 mN and a displacement resolution of 1 µm. The temperature inside the environmental chamber is measured at 3 different locations, with all measurements within 0.5 °C from the programmed test temperature. A thermocouple sensor close to the specimen is used in feedback control of the test temperature, and the DMA temperature controller maintain the test temperature within ±0.1 °C throughout the test period.

B.3 LINEAR VISCOELASTIC THEORY

Linear viscoelastic constitutive relation for creep experiment oftentimes is expressed using the hereditary integral (Knauss, Emri, and Lu 2008) shown in Equation (B.1):

$$\epsilon_{ij}(x_k, t) = \int_0^t S_{ijkl}(t-\tau)\frac{d\sigma_{ij}(x_k,\tau)}{d\tau}d\tau, \tag{B.1}$$

where S_{ijkl} are components of the compliance tensor, ϵ_{ij} are the creep strain components, σ_{ij} are the applied stress, and τ is an integration variable. For three-point bend creep loading shown in Figure B.1b, Equation (B.1) can be written as

$$\epsilon_{ij}(x_1, x_3, t) = \int_0^t S_{1111}(t-\tau)\frac{d\sigma_{11}(x_1,x_3,\tau)}{d\tau}d\tau, \tag{B.2}$$

$$d\sigma_{11}(x_1, x_3, \tau) = d\sigma_{11}(x_1, x_3)\delta(\tau), \tag{B.3}$$

where $\delta(\tau)$ is the Kronecker delta function. Hence, the creep strain-stress relation simplifies to

$$\epsilon_{11}(x_1, x_3, t) = S_{1111}(t-\tau)\sigma_{11}(x_1, x_3). \tag{B.4}$$

Using Euler-Bernoulli beam theory, the strain in the x_1 direction (along the fiber direction) at mid-span of the sample ($x_1 = 0$) can be expressed as

$$\epsilon_{11}(x_1 = 0, x_3, t) = -\frac{48\Delta(t)Mx_3}{Pl_3}, \tag{B.5}$$

where t is the time of application of the load, $\Delta(t)$ is the mid-span deflection of the beam, P is the applied load, and M is the moment at mid-span ($M(x_1 = 0) = Pl/4$). The mid span stress $\sigma_{11}(x_1 = 0, x_3)$ is

$$\sigma_{11}(x_1 = 0, x_3, t) = -\frac{12Mx_3}{bd^3}. \tag{B.6}$$

Using Equations (B.4) to (B.6), the creep compliance can be written as

$$S_{1111}(t) = \frac{4\Delta(t)bd^3}{Pl^3}. \tag{B.7}$$

For simplification, S_{1111} is expressed as S in the remainder of this work. Equation (B.7) shows that the creep compliance can be obtained by simultaneous measurement of both load and load line displacement. The load applied during the creep experiment (0.25 N), is three orders of magnitude higher than the load due to weight of the sample. Thus, the effect of sample weight is neglected in all calculations.

B.3.1 Viscoelastic model

One of the common ways to model linear viscoelastic response is though mechanical analogs that consist of a series of springs and dashpots. Two commonly used models are Maxwell and Kelvin-Voigt. Typically, more than 5 elements are required for capturing the response accurately (Knauss, Emri, and Lu 2008). In this work, the Kelvin–Voigt model with more than 10 elements represents the viscoelastic creep compliance of the tow material. The Kelvin-Voigt model for creep compliance model is given in Equation (B.8). The model parameters, including S_i and τ_i, are obtained using a nonlinear curve fitting procedure described in Emri and Tschoegl (1993).

$$S(t) = S_\infty - \sum_{i=1}^{N} S_i e^{(-\frac{t}{\tau_i})} + \psi_f t. \tag{B.8}$$

Here, S_∞ is the long-term compliance, ψ_f is the fluidity, N is the number of Kelvin-Voigt elements, S_i and τ_i are the creep compliance and characteristic time for the i$^{\text{th}}$ individual element, respectively.

B.3.2 Time temperature superposition principle (TTSP)

Time-temperature equivalence has been observed to be valid for most amorphous polymers that are considered thermo-rheological simple materials (Knauss, Emri, and Lu 2008). For such materials, the viscoelastic response at a longer time can be obtained using the short-time viscoelastic response of the same material at a higher temperature. The TTSP principle is mathematically expressed in Equation (B.9).

$$S(t,T) = S(a_T t, T_{ref}), \tag{B.9}$$

$$a_T < 1 \text{ if } T > T_{ref},$$

$$a_T > 1 \text{ if } T < T_{ref},$$

$$a_T = 0 \text{ if } T = T_{ref},$$

where a_T is the shift factor and $a_T t$ is termed the "reduced time". Equation (B.9) shows that creep compliance of a material at a test temperature T is equivalent to creep compliance at a reference temperature on the reduced time axis. The shift factor, $a_T < 1$ for $T > T_{ref}$, indicates decrease in characteristic time with increase in temperature and vice versa.

The shifting is the "weakest" step of time-temperature superposition procedure. In the past, shifting was performed manually. This problem has been resolved by Gergesova, Zupančič, Saprunov, and Emri (2011); Gergesova, Saprunov, and Emri (2016) using a closed form mathematical methodology for performing the time-temperature and/or time-pressure superposition, called CFS-algorithm. This algorithm completely removes issues related to manual shifting procedure. CFS methodology recently became the new ISO 18437-6:2017 standard[2]. The proposed mathematical formulation of the shifting procedure takes into account that material functions measured at two different temperatures represent the material behavior at two different thermodynamic states, which differ in the corresponding Gibbs free energy (Martin 1986) by

$$\Delta W = \int_{T_0}^{T_k} \tilde{S} dT, \tag{B.10}$$

where W denotes Gibbs free energy, $\tilde{S}$ is the internal entropy of the material, while T_0 and T_k represent two selected equilibrium thermodynamic states at which the corresponding segments of the material function have been measured. The rate at

[2]https://www.iso.org/obp/ui/#iso:std:iso:18437:-6:ed-1:v1:en

which mechanical energy is absorbed per unit volume of a viscoelastic material at a given boundary condition T_k is equal to the stress power, i.e., the rate at which work is performed. The stress power at time t is defined as

$$dW(t,T_k)dt = \sigma(t,T_k)\frac{d\epsilon(t)}{dt}. \tag{B.11}$$

The absorbed mechanical energy causes material inherent structural (molecular) rearrangements during the relaxation or creep process. Thus, any two segments of the material function, measured at the reference state T_0, and any other selected state T_k, that need to be superimposed (shifted) into a master curve should have the same energy release rate at all points of the superimposing interval. This criterion may be expressed as

$$\frac{dW(t,T_0)}{d\log t}\Big|_{t=t_j} = \frac{dW(t,T_k)}{d\log t}\Big|_{t=t_k}. \tag{B.12}$$

Equation (B.12) is fulfilled when the overlapping area H between two segments is equal to zero, as shown in Figure B.2.

This yields a closed form equation for the shift factor

$$\log a_{T_k} = \frac{\sum_{i=1}^{U-1}\left[\frac{\log t_{k,i+1}+\log t_{k,i}}{2}(\log G_{k,i+1} - \log G_{k,i})\right] - A_0}{\log G_{0,N_1} - \log G_{0,1}}, \tag{B.13}$$

where

$$A_0 = \sum_{i=1}^{N_1-1}\frac{\log t_{0,i} + \log t_{0,i+1}}{2}(\log G_{0,i+1} - \log G_{0,i}). \tag{B.14}$$

Using TTSP, the creep compliance master curve at a reference temperature can be obtained by shifting individual short-term creep response data obtained at different temperatures; the master curve thus obtained usually extends for tens of logarithmic decades. Hence TTSP is a convenient way to obtain the creep responses at extreme time periods that are not practical to obtain from a single creep experiment at a fixed temperature.

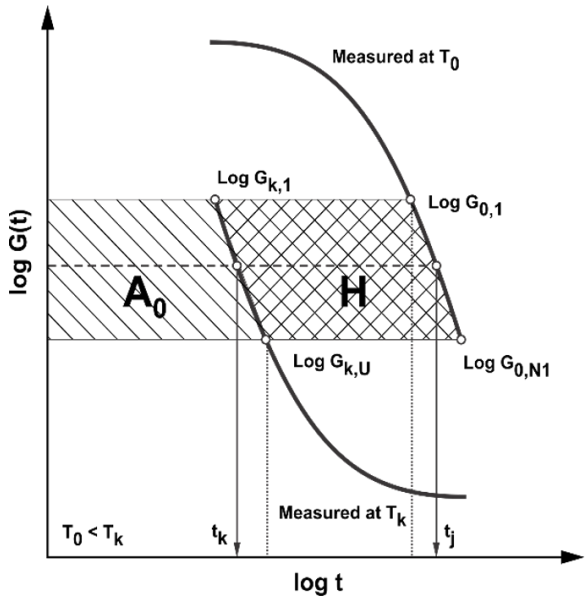

Figure B.2 Schematics of the CFS procedure for an example of shear relaxation modulus

For modeling of tow wrinkling, the creep response of the material at temperatures somewhat higher than 40 °C are of interest since the typical layup temperature is between 40 °C and 60 °C. Since thermoset tow samples experience accelerated aging and changes in mechanical properties at higher temperature, it is not possible to perform creep experiments using the DMA in this temperature range without causing significant changes to the mechanical properties. However, using the creep response at lower temperatures and the TTSP principle, creep response of tow at higher temperature is obtained without the problem of aging. The creep response thus obtained will be shifted towards shorter time periods, which is effective in modeling critical processes of interest such as compaction and wrinkling that occur within a short period of time.

B.3.3 William Landel Ferry (WLF) model

The shift factors for most polymers are observed to follow the WLF model given in Equation (B.15). The WLF equation is effective for obtaining the master curve

at a temperature outside the test temperatures (Williams, Landel, and Ferry 1955). Parameters for the WLF model are obtained by fitting the experimentally determined shift factors to the model using least square methods. The WLF fit and model parameters thus obtained are shown in section B.4.

$$\log a_T = -\frac{C_1(T - T_{ref})}{C_2 + (T - T_{ref})}, \tag{B.15}$$

where C_1 and C_2 are WLF parameters.

B.3.4 Arrhenius model

Another model for predicting shift factors is based on the Arrhenius equation in Equation (B.16). The Arrhenius model is commonly used to obtain shift factors below the glass transition temperature, T_g, of the material[3], whereas the WLF is used to obtain shift factors above T_g.

$$log a_T = \frac{\Delta E}{2.303\overline{R}}\left(\frac{1}{T} - \frac{1}{T_{ref}}\right), \tag{B.16}$$

where ΔE is activation energy and $\overline{R}$ is the universal gas constant.

B.4 RESULTS AND DISCUSSION

The measured average creep response of the tow material IM7/8552-1 for nine different temperatures is shown in Figure B.3. The vertical bars at the start and end of the creep curve show three standard deviations in the measurements for twenty different samples tested at each temperature. The master curve at 40 °C obtained using TTSP is shown in Figure B.4 and the corresponding shift factors are shown in Table B.1. The experimental shift factors are obtained by CFS algorithm explained in section B.3.2. Only a horizontal shifting along log time axis was sufficient to obtain

[3]Since T_g of the tow material is close to 0 °C, the WLF model is used in this work to obtain the shift factors for higher temperatures.

a master curve with good overlap between the creep data at different temperatures, indicating that the prepreg material is thermorheologically simple material (Knauss, Emri, and Lu 2008).

The WLF and Arrhenius models for the experimentally determined shift factors are shown in Figure B.5a and Figure B.5b, respectively. Both the WLF and Arrhenius models match the experimental shift data very closely. Coefficients for the WLF model parameters (C_1, C_2) and the activation energy (ΔE) obtained from least square fitting of the shift factors to the WLF and Arrhenius model are shown in Table B.2.

Table B.1 Experimentally determined shift factors (a_T) for a reference temperature of $T_{ref} = 40\,^{\circ}$C

$T - T_{ref}(^{\circ}\mathrm{K})$	$\log a_T$	$T - T_{ref}(^{\circ}\mathrm{K})$	$\log a_T$
0	0	-25	3.96
-5	0.53	-30	4.93
-10	1.13	-35	5.81
-15	1.85	-40	6.53
-20	2.83	-45	7.53

Table B.2 WLF constants and Arrhenius activation energy obtained from least square fitting of the experimental shift factor with the models

WLF parameters		Arrhenius activation energy
C_1	C_2	ΔE
26.78	202.1	268 KJ/mol

Using the WLF model shift factor, the master curve obtained at 40 °C (see Figure B.4) can now be shifted to a reference temperature of 50 °C. The shift factor for the master curve at reference temperature of 50 °C, a_T(T = 40 °C; T_{ref} = 50 °C) = 1.40. The creep compliance master curve at 50 °C thus obtained is shown in Figure B.6. It is noted that creep data at 50 °C is available up to a time period of 7.44 sec. Though extrapolation of the data beyond the experimental time period can be obtained from the Kelvin-Voigt model, it is usually not recommended (Emri

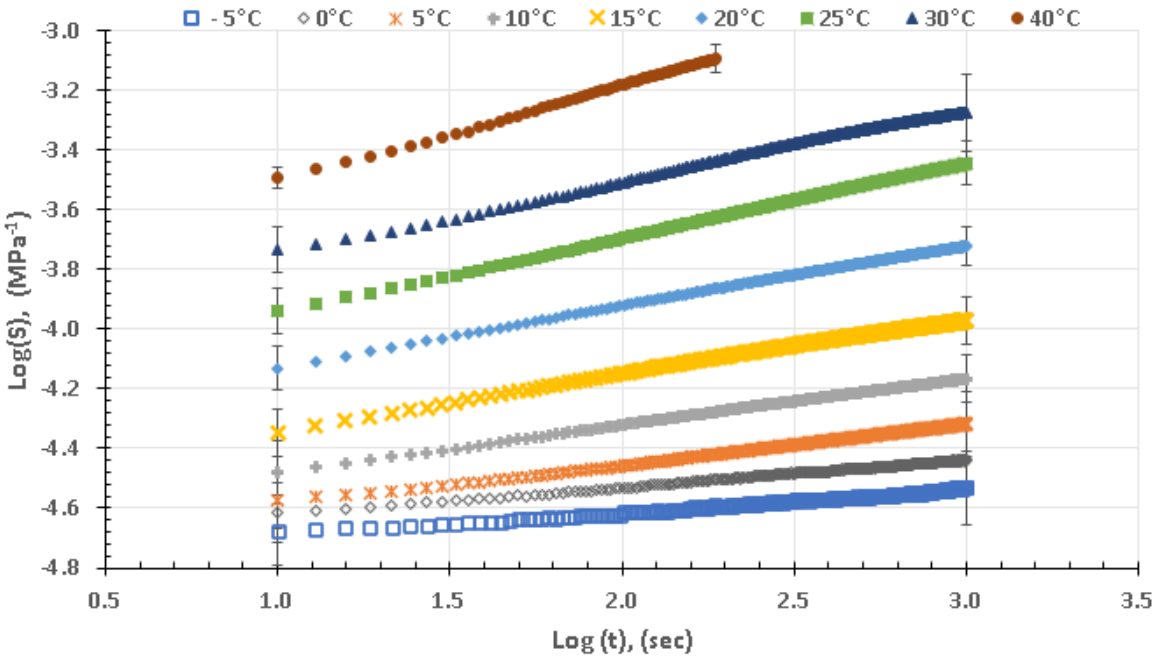

Figure B.3 Average value of short-term creep compliance curve from twenty different samples for nine different temperatures from −5 °C to 40 °C

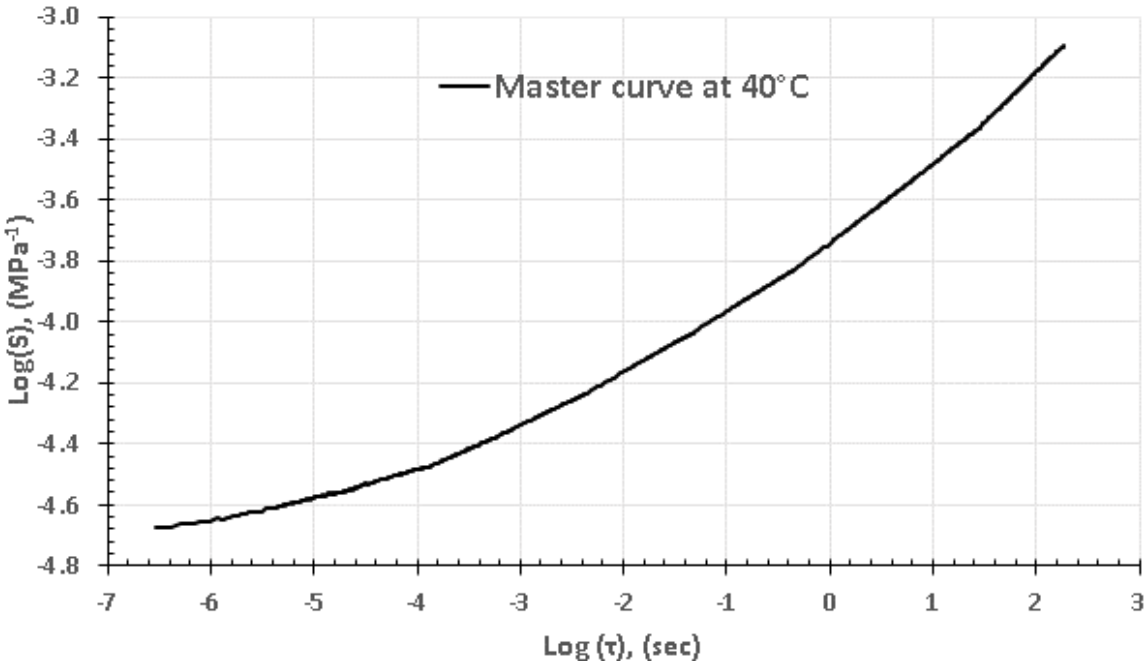

Figure B.4 Creep compliance master curve at 40 °C

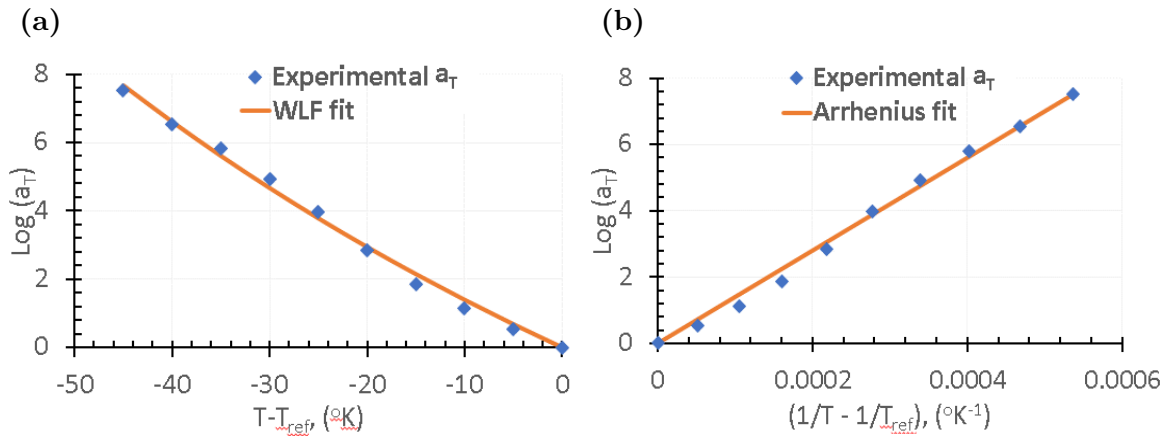

Figure B.5 Experimentally obtained shift factors with (a) WLF fit and (b) Arrhenius fit

and Tschoegl 1993). Further, due to aging of the material at higher temperature, modeling of the material response for longer periods using linear viscoelastic theory will not be an accurate representation of the actual material response. As mentioned in the previous section, the viscoelastic response for a short period of time is of interest since initiation of wrinkling is observed to occur almost instantaneously after the roller passes over the tow. Hence, the creep data reported in this work will be sufficient for modeling the initiation of wrinkling during AFP process.

B.4.1 Retardation spectra

The retardation spectra consist of the set of parameters of the Kelvin-Vogit model in Equation (B.8), i.e., (S_i, τ_i; $i = 1$ to N). Determination of the spectrum is essentially a curve fitting procedure. There are two ways that have been reported by investigators to obtain the spectra (Emri and Gergesova 2010). The first procedure, usually based on Tikhonov regularization, produces the very best mathematical fit but generally will produce negative spectrum lines that are physically unrealistic and can create problems in interconversion of retardation spectra to relaxation spectra. The second fit, called the windowing algorithm and developed by Emri and Tschoegl (1993), eliminates negative spectrum lines and has been shown to closely approach the

"true" distribution. Based on these findings, the windowing algorithm was adopted and used in this study to determine the shear creep retardation spectra. The iteration procedure for obtaining retardation spectra using the windowing algorithm is expressed in Equation (B.18). Procedural details for obtaining retardation spectra can be found in Rajan, Sutton, Oseli, Emri, and Matta (2017), where the authors obtained retardation spectra for two different classes of bituminous material. Eighteen discrete spectrum lines for our IM7/8552-1 tow material obtained by selecting two retardation times per decade in the iteration procedure are presented in Table 3. The normalized experimental creep data (M data points) can be expressed by an N parameter Prony series as shown in Equation (B.17).

$$S(t_j) = S(t_M) - \sum_{i=1}^{N} S_i e^{(-\frac{t}{\tau_i})} + \theta(t_j), \tag{B.17}$$

where normalization is performed by dividing the creep data by the difference in

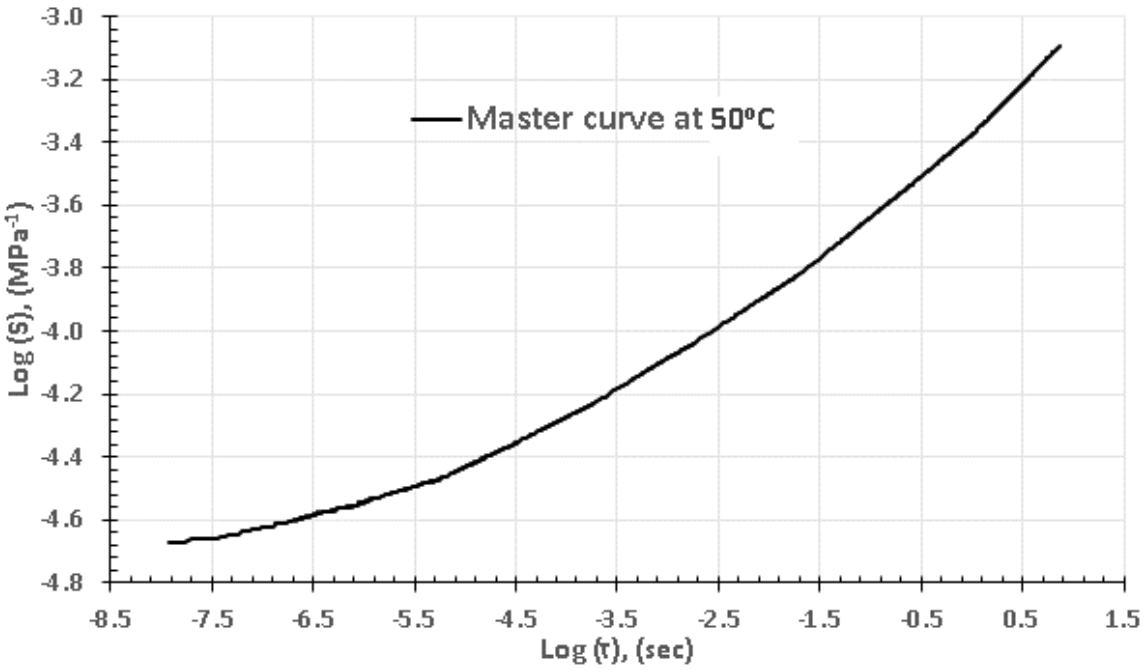

Figure B.6 Creep compliance master curve at 50 °C obtained by shifting the master curve at 40 °C using shift factor from WLF model

the last and first creep compliance data, i.e., $S(t_M) - S(t_1)$, and $\theta(t_j)$ accounts for experimental and approximation error. Approximation arises because of replacing normalized equilibrium compliance (S_∞) by $S(t_M)$. The k$^{\text{th}}$ normalized spectrum line, S_k, is obtained by minimizing the square of error in the region close to the retardation time (τ_k), as shown in Equation (B.18).

$$S_k = \frac{\sum_{j=l_k}^{u_k} \left[S(t_M) - S(t_j) - \sum_{i=m}^{k-1} S_i e^{(-\frac{t_j}{\tau_i})} - \sum_{i=k+1}^{N} S_i e^{(-\frac{t_j}{\tau_i})} \right] e^{(-\frac{t_j}{\tau_k})}}{\sum_{j=l_k}^{u_k} e^{(-\frac{2t_j}{\tau_k})}}, \qquad \text{(B.18)}$$

where $m = k - 2r - 1 \geq 1$, r is the number of spectrum lines per decade, and l_k and u_k are the first and last discrete points defining the window that contains the k$^{\text{th}}$ spectrum line. The windowing algorithm begins the computation with the N$^{\text{th}}$ spectrum line, S_N. In the first pass of the algorithm, the discrete retardation spectra are assumed to be zero. In the succeeding sweeps, retardation spectra are updated by using non-negative values of the previously determined spectrum and setting negative spectrum values to zero. The iteration is terminated when the difference between the previous and current spectrum lines is smaller than a pre-defined error tolerance. In our program, the predefined error tolerance is set at 1%.

Table B.3 Normalized discrete retardation spectra (Prony series parameters) of the prepreg tow at 40 °C

$\log(\tau_k)$(sec)	S_k	$\log(\tau_k)$(sec)	S_k
-5.5	0.0062	-1.5	0.0618
-5.0	0.0025	-1.0	0.028
-4.5	0.0057	-0.5	0
-4.0	0.003	0.0	0.1739
-3.5	0.0168	0.5	0.0649
-3.0	0.003	1.0	0
-2.5	0.0329	1.5	0.523
-2.0	0	2.0	0.0781

The creep compliance reconstructed from the retardation spectra shown in Figure B.7 matches very closely to the experimental creep data, showing the effectiveness of modeling viscoelastic response using Prony series representation. The retardation spectra for any other temperature can be obtained by determining the shift factor and shifting the retardation time (τ_k); the height of the spectra lines at corresponding reduced retardation times will not change.

The results obtained in this work are quite important in applications for several reasons. First, the uncured IM7/8552-1 material for which the viscoelastic characterization has been obtained is used in the manufacture of composite components, including aerospace applications. By obtaining the Prony series representation, the material behavior for different temperatures can be quantified to assess the importance of viscoelastic response of tows during manufacturing. Secondly, once a manufacturing temperature is confirmed for layup of a material, the experimental creep

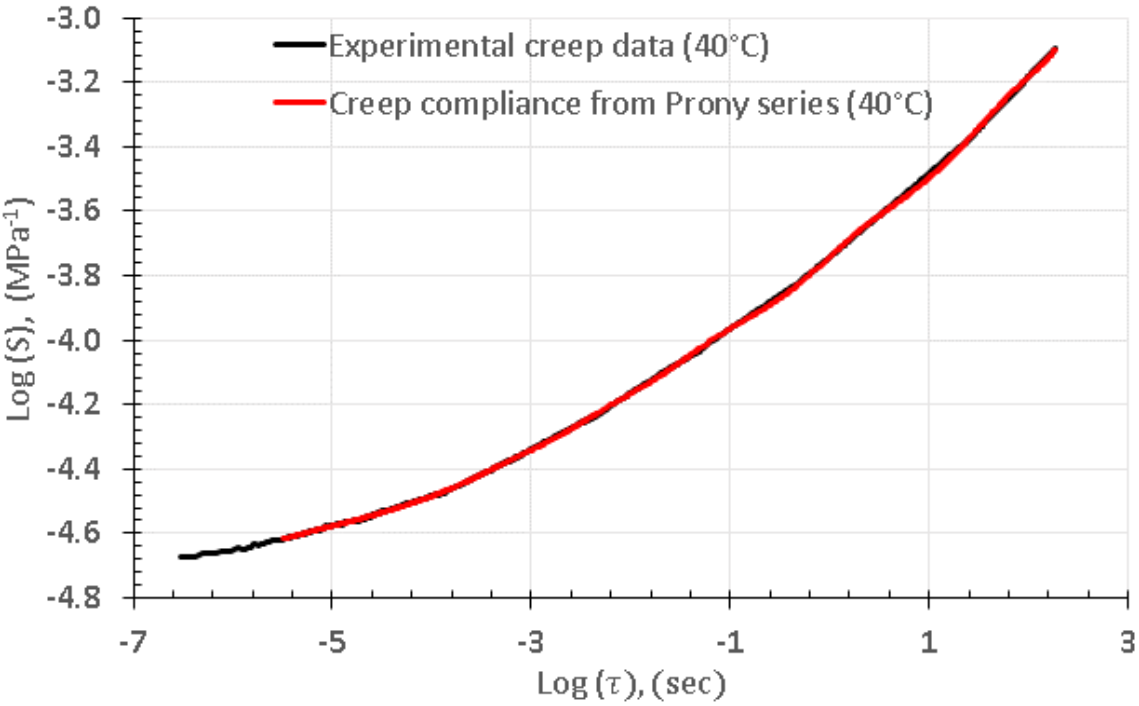

Figure B.7 Experimental creep compliance master curve and creep compliance reconstructed using Prony series at 40 °C

compliance curve provides a window into assessing the level of viscoelasticity to be expected in the early stages of layup and determining whether viscoelastic behavior is important for tow wrinkling (local debonding) during placement. As an example, consider the situation where IM7/8552-1 is to be bonded to a composite substrate along a curvilinear path. It has been shown in a previous study (Rajan et al. 2019b) that placement of unidirectional carbon-epoxy tows may result in buckling/tow separation along the compressive side of the tow during placement. The tow placement simulations performed at the commercially relevant laydown velocity of 2m/s used elastic properties for the tow and quasi-statically measured traction-separation relationships for cohesive interaction of the IM7/8551-1 material (Rajan et al. 2020a) with the substrate. Results from the simulations showed that tow separation and wrinkling occurred within 200μs after the roller forces were relaxed. Since the elastic properties and traction-separation relationship used in the simulations was assumed to be time-independent, the role of viscoelasticity during these early stages of processing was important to quantify, and the data obtained in this study provided an answer. According to Figure B.7, the bending compliance changed from the nearly elastic value of 2 x 10^{-5} to 3.5 x 10^{-5} Mpa^{-1}, a relatively small change that indicates the assumption of nominally elastic conditions during the onset of separation/debonding is quite reasonable.

B.5 CONCLUSION

The creep compliance of IM7/8552-1 tow is measured at nine different temperatures between $-5\,^{\circ}$C and $40\,^{\circ}$C via three-point bending experiments in a TA RSA III DMA. The master curve at $40\,^{\circ}$C obtained using time-temperature shifting procedure (TTSP) extends more than eight logarithmic decades. The shift factor for temperatures outside the experimental range are obtained using the WLF model. The WLF model parameters for the tow material are obtained using the experimental shift fac-

tors at 40 °C. Using the WLF equation, shift factors for 50 °C are determined and used to plot the creep compliance master curve at 50 °C. Using thirteen Prony series parameters to model the viscoelastic response of the material, the model predictions for creep compliance vs time are in excellent agreement with experimental measurements. Compliance-time results for 50 °C are shown to provide essential data for assessing the importance of viscoelastic behavior in the highly transient processes associated with rapid placement of tows on substrates.